Alma Mater Studiorum – Università di Bologna

DOTTORATO DI RICERCA IN

Meccanica e Scienze Avanzate dell'Ingegneria

Ciclo XXVIII

Settore Concorsuale di afferenza: 09/A3

Settore Scientifico Disciplinare: ING-IND/21

CAST ALUMINUM ALLOYS AND AL-BASED NANOCOMPOSITES WITH ENHANCED MECHANICAL PROPERTIES AT ROOM AND HIGH TEMPERATURE: PRODUCTION AND CHARACTERIZATION

Presentata da

Dott.ssa Stefania Toschi

Coordinatore Dottorato

Prof. Vincenzo Parenti Castelli

Relatore

Prof.ssa Lorella Ceschini

Correlatore

Prof. Alessandro Morri

Esame finale anno 2016

SUMMARY

The use of cast Al-Si-Mg and Al-Si-Cu aluminum alloys, widely diffused in the industrial field, is strongly limited in high temperature applications, in view of the tendency of β-Mg_2Si and θ-Al_2Cu strengthening precipitates to undergo coarsening after long term high temperature exposure (~200 °C). Aiming to exploit the high specific properties (strength and stiffness), the excellent oxidation resistance and the high castability of Al-Si based alloys also in high temperature applications, coarsening resistant strengthening phases are needed. Two main routes may be followed to this aim, namely: (i) chemical modification of Al-Si alloys to induce the formation of thermally stable strengthening phases; (ii) addition of micrometric or, more recently, nanometric ceramic dispersoids to the Al matrix, in the so called Al-based composites.

Aim of the present PhD work was, from one side, the study of quaternary Al-Si-Cu-Mg alloys, characterized by the concurrent presence of Cu and Mg, supposed to enhance the overageing resistance of the alloys in comparison to the ternary ones; from the other side, the production and characterization of Al-based composites both by ex-situ and in-situ routes.

As concerning quaternary alloys, two Al-Si-Cu-Mg alloys (A354 ad C355) have been characterized from the microstructural and mechanical point of view, to investigate the effect of chemical composition, solidification rate, heat treatment condition and high temperature exposure, on the tensile and fatigue behavior both at room and high temperature. Furthermore, the heat treatment of A354 alloy was studied, aiming to enhance mechanical properties derived from the industrial practice treatment applied in the previous activity. Both solution and ageing phases were studied to keep at a minimum treatment time and temperature, while inducing the maximum strengthening effect through precipitation hardening. The overageing behavior of the alloy in the optimized treatment condition was compared to that of C355 alloy and A356 ternary alloy, confirming the

higher coarsening resistance of strengthening precipitates present in quaternary alloys. A preliminary study towards further enhancement of high temperature resistance of A354 alloy was conducted, aiming to evaluate the effectiveness of Molybdenum as a possible alloying element. Heat treatment studies, associated to microstructural analyses and preliminary tensile tests, revealed that the addition of Mo to A354 alloy leads to the formation of Mo-rich intermetallic particles, while preventing from the formation of β-Fe phases, and enables to enhance mechanical properties of the alloy after high temperature long-term overaging, enhancing A354 thermal stability.

In the framework of metal composites, the first research activity was devoted to the implementation, at the laboratory scale, of casting processes for the production of Al-matrix composites. In particular, the stir-casting method assisted with ultrasonic treatment of the melt was applied to the ex-situ production of Al_2O_3-A356 micro and nanocomposites. On the other hand, an in-situ liquid state reactive technique aimed at the production of ZrB_2 particles from inorganic salts was tested. Experimental results showed that, despite up to 8 wt.% and 1 wt.% of micro and nano alumina particles were incorporated in the matrix, an even distribution of the reinforcing phase, in particular in the case of nanometric particles, is still challenging to be achieved. Good hardness enhancement was obtained, but the presence of casting defects associated to nanoparticles clusters was detected. The in-situ production route, on the other hand, was reported to be unsuccessful: no ZrB_2 particles were detected and a general decrease of hardness was observed, mainly due to the formation of irregular and detrimental phases. As a further research activity, Friction Stir Process (FSP) was evaluated as possible solid state processing route to: (i) enhance Al_2O_3 nanoparticles distribution in semisolid processed AA2024 based nanocomposite, and (ii) directly distribute Al_2O_3 nanoparticles into AA7075 alloy at the solid state. The research activity carried out on Al_2O_3-AA2024 system revealed that the semisolid processing technique alone does not allow to evenly distribute nanoparticles within the matrix; casting defects associated to nanoparticles clusters dominated the mechanical behavior of the composites. On the contrary, FSP allows enhancing particles distribution, leading also to microstructural refinement and homogenization. Mechanical properties (UTS, YS) and ductility (Elongation to failure) were strongly enhanced by the process, allowing the exploitation of nanoparticles strengthening effect. The direct incorporation of alumina nanoparticles into AA7075 matrix by FSP, was evaluated by microstructural and hardness characterization on composites processed by 1, 3 and 4 FSP passes. Large nanoparticles clusters were observed both in samples processed by 1 and 3 passes, while 4 FSP passes led to increased microstructural homogeneity and non-

detectable particles clusterization, associated to noticeable enhancement of the alloy microhardness. In conclusion, experimental activities confirmed the ability of FSP, both as primary and secondary solid state process, to induce good nanoparticles distribution, thus allowing the exploitation of their strengthening effect.

Keywords: Al-Si-Cu-Mg alloys, Microstructure, Overageing, Heat treatment, Tensile, Fatigue, Molybdenum, Al-matrix Microcomposites, Al-matrix nanocomposites; Casting routes, Friction Stir Processing.

RIASSUNTO

L'utilizzo delle tradizionali leghe ternarie Al-Si-Mg e Al-Si-Cu, ampiamente diffuse in ambito industriale, è fortemente limitato nel caso di applicazioni ad alta temperatura, a causa della tendenza all'ingrossamento dei precipitati β-Mg_2Si e θ-Al_2Cu a seguito di esposizione a temperature prossime ai 200 °C. Al fine di sfruttare le elevate proprietà specifiche (resistenza e rigidezza) e l'elevata colabilità di queste leghe anche in impieghi ad alta temperatura, è quindi necessario indurre la formazione di precipitati di rinforzo resistenti ai fenomeni di coarsening. A questo riguardo, vi sono principalmente due strategie: (i) la modifica compositiva, che tramite l'aggiunta di opportuni elementi alliganti mira all'ottenimento di precipitati caratterizzati da alta stabilità termica, (ii) l'aggiunta di particelle ceramiche micrometriche o, più recentemente, nanometriche, ad una lega Al-Si; è il caso dei compositi a matrice di alluminio.

Lo scopo della presente attività di ricerca è stato, da un lato, lo studio di leghe quaternarie Al-Si-Cu-Mg, in cui la presenza concomitante di rame e magnesio dovrebbe indurre la formazione di fasi caratterizzate da più elevata stabilità termica rispetto a quelle presenti nelle leghe ternarie; dall'altro lato, la produzione e la caratterizzazione di compositi a matrice di alluminio, tramite tecnologie ex situ ed in situ.

Per quanto riguarda lo studio delle leghe di alluminio quaternarie, sono state sottoposte a caratterizzazione microstrutturale e meccanica due leghe Al-Si-Cu-Mg (A354 e C355), per evidenziarne le correlazioni tra composizione chimica, velocità di solidificazione, trattamento e degrado termico sulle proprietà meccaniche (trazione e fatica) a temperatura ambiente e a caldo (200 °C). E' stato poi studiato il trattamento termico della lega A354, che nella precedente attività di ricerca era stata sottoposta a trattamento di derivazione industriale, caratterizzato da parametri non ottimizzati. Le principali fasi del trattamento termico, ossia la solubilizzazione e l'invecchiamento, sono state studiate al fine

di massimizzare l'azione di rinforzo esercitata dalla precipitazione di fasi intermetalliche, mantenendo tempi e temperature di trattamento il più contenuti possibile. E' stata poi valutata la risposta al degrado termico della lega a seguito di trattamento termico ottimizzato, comparando la suddetta lega alla simile C355 e alla tradizionale A356, Al-Si-Mg. Le analisi hanno evidenziato come le leghe quaternarie siano caratterizzate da una più elevata stabilità termica rispetto alla lega Al-Si-Mg, grazie alla presenza di precipitati intermetallici caratterizzati da maggior resistenza ai fenomeni di coarsening. Infine, è stato svolto uno studio preliminare volto all'ulteriore incremento della resistenza al degrado della lega A354 tramite modifica compositiva. In particolare, è stato valutato l'effetto del Molibdeno quale ulteriore elemento alligante. Le attività di caratterizzazione microstrutturale hanno evidenziato come l'aggiunta di molibdeno alla lega A354 induca la formazione di fasi intermetalliche ricche in Mo, evitando la formazione delle indesiderate fasi β-Fe; la preliminare caratterizzazione meccanica svolta sulla lega contenente 0.3p.%Mo, a valle dello studio del trattamento termico, ha evidenziato un incremento delle proprietà meccaniche a seguito di degrado termico prolungato, rivelando quindi un incremento della stabilità termica rispetto alla lega base.

Nell'ambito dei compositi a matrice di alluminio, la prima attività di ricerca è stata volta all'implementazione, su scala di laboratorio, di processi fusori per la produzione di micro e nanocompositi a matrice in lega A356. In particolare, per quanto riguarda le tecnologie ex situ, è stata applicata la tecnica di stir casting con trattamento ultrasonico del fuso, con l'obiettivo di disperdere particelle micrometriche e nanometriche di allumina all'interno della matrice allo stato fuso. Per quello che riguarda invece le tecnologie in situ, è stata testata una tecnica di tipo reattivo allo stato liquido, con lo scopo di formare particelle di ZrB_2 sfruttando opportune reazioni chimiche tra alluminio e alcuni sali inorganici. I risultati sperimentali hanno evidenziato come, nonostante sia stato possibile disperdere micro e nanoparticelle fino all'8% e 1% in peso, rispettivamente, sia comunque difficile ottenere una distribuzione uniforme delle particelle stesse, in particolar modo nel caso di quelle nanometriche. L'aggiunta di rinforzo ceramico ha portato a discreti incrementi di durezza; tuttavia, sono stati riscontati numerosi difetti associati alla tendenza all'agglomerazione delle particelle nanometriche, quali porosità e cluster. La tecnica in situ si è dimostrata infruttuosa all'ottenimento di particelle di ZrB_2 all'interno della lega A356; al contrario, è stato riscontrato un decremento di durezza rispetto alla sola matrice, a causa della formazione di fasi caratterizzate dalla morfologia irregolare e disperse in modo non uniforme nelle aree interdendritiche. Quale ulteriore attività di ricerca, è stata valutata l'adeguatezza della Friction Stir Processing (FSP) come possibile tecnica per distribuire

nanoparticelle di Al_2O_3 in compositi a matrice Al (i) prodotti tramite stir casting allo stato semi-solido e (ii) tramite distribuzione diretta allo stato solido tramite FSP.

L'attività svolta sul composito AA2024-Al_2O_3 ha mostrato come la sola tecnica fusoria allo stato semisolido non consenta di ottenere una distribuzione uniforme di nanoparticelle, a causa della scarsa bagnabilità delle stesse, con conseguente formazione di porosità e cluster. Al contrario, la tecnica di FSP ha consentito di distribuire più omogeneamente le particelle, eliminandone quasi completamente gli agglomerati, e di ottenere una maggiore uniformità microstrutturale, con conseguente aumento delle proprietà meccaniche (UTS, YS) e dell'allungamento a rottura, a confronto con la sola matrice processata allo stesso modo. L'efficacia dell'addizione diretta di nanoparticelle allo stato solito tramite FSP, realizzata tramite la deposizione delle stesse all'interno di un solco superficiale poi richiuso da una prima passata di utensile, è stata valutata tramite caratterizzazione microstrutturale del composito AA7075-Al_2O_3. Nel corso di tale attività è stato inoltre valutato l'effetto del numero di passate (1, 3 e 4) di utensile sulla distribuzione di particelle. Macro-cluster di allumina sono stati riscontrati nei campioni processati tramite 1 e 3 passate; al contrario, un incremento ulteriore del numero di passate (4) ha consentito di omogeneizzare la distribuzione di particelle, nonché di ottenere ulteriori incrementi di microdurezza rispetto al materiale base. In conclusione, le attività sperimentali hanno dimostrato come la tecnica di FSP consenta, in qualità di processo primario o secondario, di indurre buone dispersioni di nanoparticelle, consentendone lo sfruttamento dell'effetto di rinforzo.

Parole chiave: leghe Al-Si-Cu-Mg, Microstruttura, Degrado termico, Trattamento termico, Trazione, Fatica, Molibdeno, Microcompositi a matrice di Al, Nanocompositi a matrice di Al; Processi fusori; Friction Stir Processing.

Abbreviations

ADZ	Alumina Depleted Zones
AMC	Aluminum Matrix Composites
AS	Advancing Side
CNFs	Carbon Nanofibers
CNTs	Carbon Nanotubes
CTE	Coefficients of Thermal Expansion
DRA	Discontinuously Reinforced Aluminium composites
E%	Elongation to failure
EBSD	Electron backscattered diffraction
FSP	Friction Stir Processing
FSW	Friction Stir Welding
HPDC	High Pressure Die Casting
MA	Mechanical alloying
MMCs	Metal Matrix Composites
MMNCs	Metal Matrix Nanocomposites
MWCNTs	Multi Walled Carbon Nanotubes
NDZs	Nano-alumina Dispersed Zones
NG	Nugget
OM	Optical Microscopy
PM	Powder Metallurgy
RS	Retreating Side
SDAS	Secondary Dendrite Arm Spacing
SEM-EDS	Scanning Electron Microscopy equipped with Energy Dispersive Spectroscopy
TMAZ	Thermo-Mechanically Affected Zone
TMF	Thermomechanical Fatigue
UTS	Ultimate Tensile Strength
YS	Yield Strength

Index

page

INTRODUCTION 1

CHAPTER 1
CAST AL ALLOYS FOR HIGH TEMPERATURE APPLICATIONS 5

1.1 Damage Mechanisms at high temperature 5

1.2 Alloying elements for high temperature applications 8

1.3 Al-Si-Cu-Mg alloys 13

1.3.1 Heat treatment of Al-Si-Cu-Mg alloys 13

1.3.2 Dissolution of intermetallic phases 14

1.3.3 Incipient melting and multiple step solution treatment 16

1.3.4 Quenching 18

1.3.5 Aging 19

1.3.6 Coarsening resistance of Al-Si-Cu-Mg alloys 24

1.4 Mechanical properties of Al-Si-Cu-Mg alloys 27

1.5 Molybdenum addition to Al-Si alloys 29

REFERENCES – CHAPTER 1 32

CHAPTER 2
MATERIALS AND METHODS, AL-SI-CU-MG ALLOYS 37

PURPOSE OF THE WORK 37

2.1 Experimental procedure – PART 1
Characterization of Al-Si-Cu-Mg alloys 41

2.1.1 Samples production 41

2.1.2 Microstructural characterization 42

2.1.3 Tensile and hardness tests 43

2.1.4 Fatigue tests 44

2.2 Experimental procedure – PART 2
Optimization of A354 heat treatment 47

2.2.1 Samples production 47

2.2.2 Heat treatment optimization 47

2.2.3 Overageing behavior evaluation 49

2.2.4 Microstructural characterization 49

2.2.5 Tensile tests 50

2.3 Experimental procedure – PART 3
Mo addition to Al-Si-Cu-Mg alloys 51
2.3.1 Casting production 51
2.3.2 Heat treatment study 51
2.3.3 Microstructural characterization 52
2.3.4 Mechanical behavior 52
REFERENCES – CHAPTER 2 54

CHAPTER 3
RESULTS AND DISCUSSION, AL-SI-CU-MG ALLOYS 55

3.1 Results and Discussion – PART 1
Characterization of Al-Si-Cu-Mg alloys 57
3.1.1 Microstructural analysis 57
3.1.2 Tensile tests 68
3.1.2.1 Tensile properties 68
3.1.2.2 Fractographic analyses 73
3.1.3 Fatigue tests 76
3.1.3.1 Fatigue properties 76
3.1.3.2 Fractographic analyses 78
3.1.4 Conclusions 82
3.2 Results and Discussion – PART 2
Optimization of A354 heat treatment 85
3.2.1 Study of Solution treatment 85
3.2.2 Aging treatment optimization 93
3.2.3 Overaging behavior 95
3.2.4 Tensile properties 99
3.2.5 Fractographic analyses 102
3.2.6 Conclusions 103
3.3 Results and Discussion – PART 3
Mo addition to Al-Si-Cu-Mg alloys 105
3.3.1 Castings production 105
3.3.2 Preliminary heat treatment study 107
3.3.3 Microstructural characterization 110
3.3.4 Heat treatment study 114
3.3.5 Tensile properties 116
3.3.6 Fractographic analyses 117
3.3.7 Conclusions 119
REFERENCES -CHAPTER 3 120

CHAPTER 4
AL-MATRIX NANOCOMPOSITES 123

4.1 Overview on Metal Matrix Nanocomposites (MMNCs) 124

4.2 Strengthening mechanisms and modelling 126

4.3 MNCs processing routes 129

4.3.1 Stir casting 129

4.3.2 Compocasting 135

4.3.3 Ultrasonic assisted casting 136

4.3.4 Friction Stir Processing 140

4.4 General considerations on mechanical behavior 143

4.5 Conclusions 145

REFERENCES – CHAPTER 4 146

CHAPTER 5
MATERIALS AND METHODS, AL-MATRIX COMPOSITES 153

PURPOSE OF THE WORK 153

5.1 Experimental procedure – PART 1
Production of micro and nano Al-based composites 157

5.1.1 Samples production 157

5.1.2 Microstructural and hardness characterization 159

5.1.3 Mechanical characterization 160

5.2 Experimental procedure – PART 2
Characterization of AA2024-Al_2O_3 FSP nanocomposites 161

5.2.1 Samples production 161

5.2.2 Microstructural characterization 162

5.2.3 Mechanical characterization 162

5.3 Experimental procedure – PART 3
Characterization of AA7075-Al_2O_3 FSP nanocomposites 165

5.3.1 Samples production 165

5.3.2 Microstructural analyses 166

5.3.3 Mechanical characterization 166

REFERENCES -CHAPTER 5 167

CHAPTER 6
RESULTS AND DISCUSSION, AL-MATRIX COMPOSITES 169

6.1 Results and Discussion – PART 1
Production of micro and nano Al-based composites 171

6.1.1 Microstructural analysis - Ex situ technique 171

6.1.2 Hardness characterization - Ex situ technique 177

6.1.3 Microstructural analysis - In situ technique 178

6.1.4 Hardness characterization - In situ technique 181

6.1.4 Conclusions 182

6.2 Results and Discussion – PART 2
Characterization of AA2024-Al_2O_3 FSP nanocomposites 183

6.2.1 Microstructural analysis 183

6.2.2 Mechanical characterization 187

6.2.3 Tensile tests 189

6.2.4 Fractographic analyses 190

6.2.4 Conclusions 193

6.3 Results and Discussion – PART 3
Characterization of AA7075-Al_2O_3 FSP nanocomposites 195

6.3.1 Microstructural analysis 195

6.3.2 Mechanical characterization 208

6.3.3 Conclusions 212

REFERENCES – CHAPTER 6 213

CONCLUSIONS 215

INTRODUCTION

Cast aluminum alloys are widely employed in the transport field for the production of a large number of components. Al-Si alloys, in particular, thanks to the high specific strength and good castability, enable the production of complex-shape parts, such as engine blocks. It is well known that mechanical properties of heat treatable cast alloys (e.g. Al-Si-Mg), are negatively affected by long term high temperature exposure[1,2], as a result of strengthening precipitates coarsening induced by overageing processes. A noticeable reduction of hardness and tensile strength already occurs at temperatures close to 200 °C; applications of these alloys, mainly in the case of automotive and motorbike engine components, are therefore significantly limited. In recent years, increasingly restrictive regulations about air pollution have imposed the reduction of fuel consumptions and emissions, thus leading to the need of vehicles lightening. In view of this, the concept of *engine downsizing* has been introduced, consisting in the reduction of the engine dimensions, by adopting and evolving design solutions such as overfeeding or direct injection. Engine components are therefore subjected to higher operating temperatures and thermo-mechanical stresses than in the past. It is therefore clear that thermally stable materials are strongly required for this kind of applications.

Improving strength of Al alloys at elevated temperature has been a scientific and industrial goal for many years, aiming to the exploitation of their high specific properties (strength and stiffness) and relatively low cost for the production of low weight automotive components[3], such as engine parts. Aiming to enhance the high temperature resistance of Al alloys, efforts have been addressed to obtain fine dispersion of secondary phases characterized by Ostwald ripening resistance, acting as obstacle for dislocation movement. In view of this, since 80's, rapid solidification technique was evaluated as possible mean to produce high temperature alloys, mostly based on the eutectic Al-Fe system. Such

materials, containing elements as V, Si, Co, Zr, Ni, possess good thermal resistance in view of the formation of a high volume fraction of stable precipitates formed in the melt. Other techniques, such as powder processes, may present drawbacks such as brittleness, oxide layers and residual porosity. Nevertheless, solid state strengthening mechanisms, as precipitation hardening, confer a more even and dispersed distribution of nanometric strengthening phases, in comparison to the one formed in the melt. In this regard, traditional ingot metallurgy would allow the large volume production of sound, low cost and heat treatable components.

In the framework of casting techniques, chemical modification is one of the most studied and promising way to confer superior thermal stability to traditional Al-Si-Mg alloys. By adding proper alloying elements, it is possible to induce the formation of precipitates characterized by superior thermal stability in comparison to the typical β-Mg_2Si phase found in the heat-treated Al-Si-Mg alloys. Aiming to identify possible alloying elements, cost-effectiveness of the system alloy-production process should be taken into account. Recently, several researches were conducted on chemical modification of Al alloys, proposing, for example, Scandium or Hafnium as new alloying elements. Irrespectively of the real increase in mechanical properties, they lead to a strong increase of the material cost, and are therefore not suitable for high volume components production. More cost effective elements are therefore needed.

On the other hand, stable ceramic particles (i.e. oxides, carbides, etc.) may be used as reinforcing phases. Thanks to the isotropic behavior and to the possibility of employing traditional processing routes, discontinuously reinforced aluminium composites (DRA), have attracted research interest in the last three decades. Aiming to further enhance specific mechanical performance with respect to the unreinforced matrix[4,5], while conferring to the composite higher ductility[6], composites reinforced by nanometric particles have been studied in the last years. Despite the noticeable potential, processing techniques still need to be studied and optimized for achieving the successful exploitation of ceramic nanoparticles as reinforcing phase.

In view of the above, the research activities carried out during the PhD were mainly devoted to the study of Al-Si alloys for room and high temperature applications (T≤250 °C), exploiting the strengthening effect of (i) intermetallic phases induced by precipitation hardening and (ii) micro and nanometric ceramic reinforcing particles. The effect of Copper as low-cost alloying element meant to increase the thermal stability of Al-Si-Mg alloys was evaluated by microstructural and mechanical characterization of two Al-Si-Cu-

Mg alloys, namely A354 (Al-Si9-Cu1.5-Mg0.4) and C355 (Al-Si5-Cu1-Mg0.4). Static tensile and rotating bending fatigue tests were carried out both room and high temperature (200 °C), in the artificially aged condition and after overageing (i.e. long term exposure at 210 °C). The heat treatment of A354 alloy was optimized, aiming to maximize the strengthening effect induced by the alloying elements while maintaining treatment times and temperature as low as possible. Further, the effect of Molybdenum addition to A354 alloy was evaluated as possible alloying element for further increasing thermal stability of the alloy. In the framework of Al-based composites, liquid state routes were studied for the production of A356 (AlSi7Mg0.3) based composites, reinforced by Al_2O_3 micro and nano particles (ex situ routes) and by ZrB_2 particles by reactive casting (in situ route). Moreover, in view of the low wettability issues associated to nanoparticles, Friction Stir Processing (FSP) has been studied as possible mean for enhancing Al_2O_3 nanoparticles distribution in AA2024 and AA7075 matrix composites, produced by semisolid casting and nanoparticles direct addition by FSP, respectively.

Research activities were carried out at Bologna University – Department of Industrial engineering (DIN) under the supervision of Prof. Lorella Ceschini and Prof. Alessandro Morri. As described in Chapters 2 and 5, the research project was carried out in the framework of fruitful collaborations with the Department of Mechanical Engineering - Materials and Manufacturing of Jönköping University (Jönköping, Sweden), the Department of Metallurgy, Mining & Petroleum of Al-Azhar University (Cairo, Egypt) and the Department of Metallurgical and Materials Engineering of Suez University (Suez, Egypt).

References

[1] L. Mondolfo, *Aluminum Alloys: Structure & Properties*, Butterworths & Co, **1976**.

[2] B. Baradarani, R. Raiszadeh, *Mater. Des.* **2011**, *32*, 935.

[3] K. E. Knipling, D. C. Dunand, D. N. Seidman, *Zeitschrift für Met.* **2006**, *97*, 246.

[4] J.-Y. Lim, S.-I. Oh, Y.-C. Kim, K.-K. Jee, Y.-M. Sung, J. H. Han, *Mater. Sci. Eng. A* **2012**, *556*, 337.

[5] M. Karbalaei Akbari, O. Mirzaee, H. R. Baharvandi, *Mater. Des.* **2013**, *46*, 199.

[6] S. C. Tjong, *Adv. Eng. Mater.* **2007**, *9*, 639.

CHAPTER 1

CAST AL ALLOYS FOR HIGH TEMPERATURE APPLICATIONS

The high specific properties related to the low density, the good castability and the excellent thermal conductivity make Al–Si alloys good candidate materials for the production of complex shape components for lightweight applications (i.e. engine components). In view of the current increase in the maximum operation pressure/temperature of combustion engines, however, it is necessary to increase thermal resistance of aluminum alloys. Aiming to obtain creep resistant alloys and to improve the thermomechanical fatigue performance of Al–Si alloys, a uniform distribution of coarsening resistant phases, able to efficiently block dislocation movement, is therefore needed[1,2]. The principal mechanisms at the basis of high temperature damage will be described in the following paragraph, focusing also on coarsening mechanisms of the strengthening phases induced by aging treatment.

1.1 DAMAGE MECHANISMS AT HIGH TEMPERATURE

Cast components such as engine parts, in view of the operating conditions, may be subjected to complex phenomena as thermo-mechanical fatigue. Cyclic stresses causing fatigue failure at elevated temperature ($0.3Tm \leq T \leq 0.7Tm$) are not only induced by application of external loads, but may be the result of metal constrain resulting from cyclic thermal stresses[1]. As instance, during the engine heat-up, metal expansion in the inter-

valve region is constrained, subjecting the metal to compressive creep loading at 300 °C. On the other hand, during engine cool-down, contraction is prevented, therefore leading to tensile stresses within the temperature range of 150–300 °C[3]. This kind of alternating thermo-mechanical stresses may favour thermal fatigue crack nucleation.

Generally, thermomechanical fatigue (TMF) tests refers to two kinds of cycling: (i) in-phase cycles, if thermal and mechanical strain are in phase and (ii) out-of phase cycles, when the maximum mechanical strain corresponds to the minimum temperature. Out-of phase damage mechanisms[4] usually characterize engine components; among them, cylinder head is particularly subjected to failure by TMF, in view of its geometry and higher thermo-mechanical stresses (related to assembly load, combustion pressure and thermal load) in comparison to the engine block.

Interestingly, during this kind of thermo-mechanical loading, the cast component may be subjected to several processes: creep effects, crack nucleation and propagation, oxidation, hardening processes and plastic deformation[1]. Among them, fatigue, creep and oxidation are known to be the main source of damage in TMF.

Despite there is no a single property able to evaluate the thermal fatigue properties of a material, it is generally accepted that both tensile strength and ductility need to be optimized to prevent from TMF failure[1,2]. In particular, a high yield strength would enable to elastically accommodate stresses while high ductility could delay crack nucleation[2,5]. Together with these properties, good creep resistance should however be guaranteed[2].

Multiple factors are reported to enhance thermo-mechanical resistance of an alloy; in particular, beneficial features are: (i) high thermal conductivity, (ii) low thermal expansion, (iii) microstructural stability, (iv) fine secondary dendrite arm spacing (SDAS), (v) low porosity and low amount of casting defects (oxides, bi-film), (vi) low content of coarse intermetallic phases[6–13]. An indication of the thermo-mechanical fatigue resistance of an alloy subjected to temperature variations between minimum and maximum values, is given by mechanical fatigue properties at the intermediate cycle temperature[9]. As instance, if a component is subjected to cycles from room temperature to 300 °C, mechanical fatigue at 150 °C should be assessed.

Another fundamental aspect of high temperature mechanical behavior of metals is *creep*. Creep condition usually refers to a permanent and time-dependent deformation occurring when a metal is subjected to a constant stress at elevated temperature. Usually, the temperature threshold for occurrence of creep phenomenon is considered to be 0.3-0.5 Tm. For pure aluminum, in particular, this value is about 0.54 Tm[14]. Creep is strongly related to temperature since it is dominated by temperature-dependent diffusive

phenomena. While at room temperature dislocations may move only through *glide* mechanism or *cross slip* (in the case of edge dislocations), elevated temperature may activate also *climb* mechanism. Vacancies fluxes and diffusion induced by elevated temperature may in fact favor the climb of a dislocation towards a parallel plane. Dislocation motion becomes therefore a sequence of glide and climb. The creep curve, representing the variation of total strain with time, is usually composed by three regions, namely (i) transient creep stage, where the strain rate decreases with time in view of the metal strain hardening; (ii) steady state creep, characterized by constant strain rate as a result of opposed strain hardening and recovery phenomena; (iii) tertiary stage, in which the strain rate increases with time until failure[14]. Several damaging phenomena act in this phase, i.e. cavities nucleation and growth, cracks formation and necking. Stress continuously increases with reduction of cross-sectional area, until final fracture occurs.

Two main parameters are used for evaluating creep behaviors of an alloy. When creep life is of most importance, the most interesting parameter to be considered is time to rupture; on the other hand, when low stresses are applied, or when final rupture will not occur during the operating life of the component, steady-state or minimum creep rate parameter is usually taken into account. The latter may help in evaluating the accumulation of strain and to give some indication about the creep life of the component.

Different mechanisms are involved during creep phenomenon, somehow related to atoms movement within the metal lattice. Vacancy diffusion, as instance, involves the movement of vacancies from an atomic site to another one, with corresponding displacement of one atom in the opposite direction. Bulk diffusion occurs mainly by this mechanisms and by diffusion of interstitial atoms as well; grain boundary and dislocation core diffusion may occur. The dependence of creep rate on the applied stress is particularly complicated in solid-solution alloys. Similarly to creep of pure metals, glide and climb of dislocations occur in sequence. The following main phases may be identified: (i) high-stress regime characterized by power law breakdown; (ii.a) an intermediate-stress regime interval, where climb controls creep; (ii.b) a second region of the intermediate-stress regime, where creep is controlled by glide of dislocation; in this regime, climb is faster than viscous glide; (ii.c) third region of climb-controlled creep, where climb is the slowest mechanism and is rate controlling; (iii) low-stress regime, purely diffusive[14].

In view of the above, it appears clear that for applications involving creep phenomena, high melting point materials are preferred and reduction of dislocation mobility is of crucial importance.

Microstructures with large grain size are beneficial for creep resistance, since grain boundaries are reduced and a long diffusion path is necessary for grain-boundary diffusion. Moreover, grain-boundary sliding is strongly reduced. Nevertheless, the most efficient strategy to increase the low creep strength is to obtain a dispersion of fine and stable particles. Both precipitation on grain boundaries, aimed to prevent from grain-boundary sliding, and addition of stable oxides, carbides is reported to confer great enhancement in creep resistance. Many researches have been addressed in the last years, showing how creep resistance may be enhanced in Al based materials by dispersion of precipitates/intermetallics and ceramic dispersoids. In the field of cast aluminum alloys, among the most investigated alloying elements, Ni, Zr and Fe are found [3,15,16].

As previously mentioned, fatigue and creep phenomena may coexists in certain kind of applications, provided the elevated temperature is maintained for sufficient time. Generally, a noticeable reduction of fatigue life is observed, in such loading/temperature conditions[17].

At early holding time stages, failure may be related to the propagation of the main crack from nucleation sites, mainly superficial and intragranular; propagation is mainly transgranular. With increasing holding time, mixed-mode (inter/trans-granular) propagation is present and, for longer times, when creep damage dominates failure mechanisms, complete transgranular propagation is observed. However, interaction between fatigue and creep damage may also show more complex interdependence, taking into account temperature, stress and strain rate.

1.2 ALLOYING ELEMENTS FOR HIGH TEMPERATURE APPLICATIONS

While precipitation hardening is an efficient strengthening mechanism at room temperature, high operating temperatures may strongly reduce the ability of precipitates to hinder dislocation movement. As a result of long-term high temperature exposure, in fact, precipitates gradually undergo to coarsening.

The mechanism at the basis of precipitates coarsening with overaging is usually referred to as Ostwald ripening, consisting in the growth of precipitates at the expense of smaller ones. Ripening process is controlled by diffusion phenomena: shrinking precipitates gradually loose atoms, moving towards the growing ones. The variation of precipitates average size with time is modelled by the following equation, as described by Lifshitz-Slyozov-Wagner theory[18,19]:

$$\langle R(t)\rangle^3 - \langle R_0\rangle^3 = kt$$

Where $\langle R(t)\rangle$ represents the average precipitate radius and $\langle R_0\rangle$ is the average initial precipitate size (namely, at the onset of coarsening process), k is a material constant related to solubility and diffusivity as follows[20]:

$$k \propto \frac{D\sigma}{(C_e^{\beta} - C_e^{\alpha})^2}$$

D represents the diffusivity of the rate-controlling solute, σ is the interfacial free energy between precipitate and matrix; C_e^{α} and C_e^{β} stand, respectively, for the equilibrium solubilities of the solute within matrix and precipitate.

The aim of chemical modification is to induce, through the addition of proper alloying elements, the formation of coarsening resistant strengthening precipitates. Nevertheless, the development of casting aluminum alloys for traditional production techniques must take into account that only few alloying elements are characterized by relatively high solubility at equilibrium (>1 at.%); these elements are Zn, Ag, Mg, Li, Ga, Ge, Cu and Si[21]. As a result, a limited amount of precipitates (<1vol. %) may form in such systems. In this regard, Ni super-alloys may contain a precipitates volume fraction also two order of magnitude higher in comparison to Al alloys (even 70 vol.%), thanks to the high solubility of Al in Ni. Reinforcing phases, in this case, are mostly matrix-isomorphous and coherent $NiAl_3$ precipitates, conferring to these alloys excellent creep resistance[21].

On the basis of recent works, focusing on the development of new heat resistant Al-Si alloys, four criteria were identified to confer better thermal stability to such alloys. Alloying elements are required to (i) be able to form strengthening phases, (ii) present low solid solubility and (iii) low diffusivity in aluminium, (iv) conferring good castability to the alloy.

Alloying elements (M) that form trialuminides compounds (i.e. characterized by Al_3M stoichiometry), are reported to be suitable elements for the scope, presenting low density, high specific strength and good thermal resistance, due to the high melting point. In particular, the cubic $L1_2$ structure (Figure 1.1), due to its symmetry and coherency with the Al lattice, is thought to be the best reinforcing structure, maximizing the strengthening effect by allowing dislocation-matrix elastic interaction. As further benefit, lattice coherency minimizes surface interfacial energy, thus leading to increased coarsening resistance. Many elements are reported to form trialuminides compounds: groups 3-5 of transition elements may generate structures such as the cubic $L1_2$ (Sc), tetragonal $D0_{22}$ and $D0_{23}$ (Ti, V, Zr, Nb, Hf and Ta) or lower simmetry compounds (Fe, Co, Ni). A schematic of such structures is shown in Figure 1.1. Moreover, all rare earth (RE) elements (except

from Eu) form thermodynamically stable Al_3RE compounds (some of them, as Er, generating $L1_2$ structure). Further Al_3M trialuminides may exist, as the Al_3Li, usually found in high-strength Al-Li alloys, unfortunately characterized by metastability. Among alloying solutes forming $L1_2$ structures, Sc is the only transition element, and, so far, it attracted great research interest. On the other hand, $D0_{22}$ and $D0_{23}$ structures are characterized by low simmetry and tetragonal structure, and usually present high brittleness.

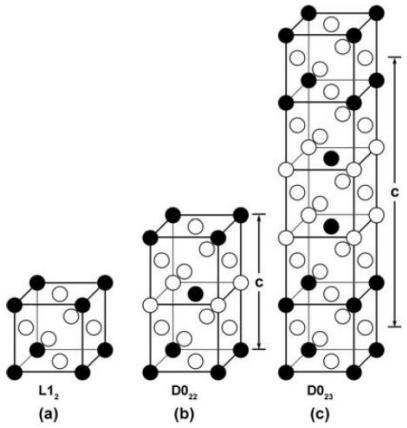

Figure 1.1. $L1_2$, $D0_{22}$ and $D0_{23}$ structures[21].

Being $D0_{22}$ and $D0_{23}$ related to $L1_2$ structure, many attempts were made by different investigators to transform such phases into $L1_2$, mainly by chemical modification. Al_3Ti and Al_3Zr were successfully modified to stabilize $L1_2$ structure. Moreover, $L1_2$ trialuminides (containing Ti, Zr, Hf), even if thermodynamically metastable, are reported to precipitate from supersaturated solid solution and show kinetic stability up to 400 C°.

As concerning precipitation hardening, a low solid solubility is needed to maximize the chemical driving force for nucleation, thus to induce the precipitation of a high amount of phases. Moreover, aiming to obtain a homogeneous distribution of supersaturated atoms after solution and quenching, high maximum solubility is needed. Solid solubility should also be limited at intermediate temperatures (~400 °C), aiming to prevent from Ostwald ripening. Further, low diffusivity in aluminium is required to reduce at a minimum diffusive phenomena leading to precipitates coarsening. Transition metals are reported to be suitable in this regard.

As concerning alloys castability, the kind of system generated by Al and solute atoms should be taken into account (i.e. *eutectic* or *peritectic,* Figure 1.2). As a matter of fact, the first phase to solidify in an alloy with peritectic composition, is the solute-rich pro-peritectic phase. As a consequence, if conventional casting processes are applied, a lot of solute

element is lost in such primary phases. It should also be taken into account that primary particles, acting as grain refiners during solidification, are undesired for creep applications, where grain boundaries should be kept at a minimum. Moreover, high temperatures are needed to reach the fully liquid state of peritectic compositions, thus to reach complete dissolution of primary phases (e.g. in Al-Ti, Al-Zr and Al-Nb systems).

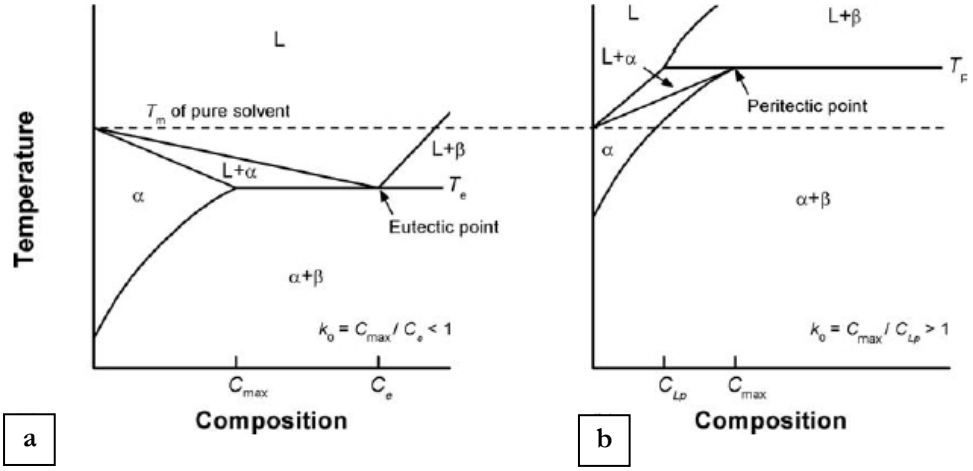

Figure 1.2: typical eutectic (a) and peritectic (b) phase diagrams[21].

Case studies. As previously mentioned, Sc presents a beneficial combination of properties: it is characterized by low solubility and diffusivity in aluminium, it generates nanometric stable Al_3Sc precipitates characterized by $L1_2$ structure and, lastly, forms with Al an eutectic system. Despite Al_3Sc precipitates are reported to be coarsening resistant[22], the very high cost of this alloying element make its use affordable only for a few niche applications. In view of this, attempts were aimed to partially substitute Sc with Zr, Hf and Ti[23,24]. Some research work was carried out to study the more cost-effective peritectic Al-Hf system, indicating that a certain amount of Si may be added to foster precipitation[25]. Good results in terms of creep behavior at 200 °C and 20 MPa were achieved by Hf addition[26]. Silicon content must however not exceed a threshold content (0,15 wt.%), to prevent from the formation of undesired ternary Al-Hf-Si phases, instead of Al_3Hf compounds. Together with silicon content, heat treatment (time and temperature) may influence shape, size and composition of intermetallics; Al_3Hf with spherical or elongated shape, as well as Si_2Hf nanobelts were observed[27]. Hafnium is commonly found in nature together with Zr, the latter showing the lowest diffusivity and low solid solubility in Al, among the transition metals. Several studies investigated Zr as possible alloying element, reporting increase of hardness, yield strength and elongation to failure at room temperature, not only in the aged

condition but also in the as cast state[28,29]. Some studies were also reported on Ni and Zr addition to Al-Si-Cu-Mg alloys, observing a remarkable increase of ultimate tensile strength (~30%) at 300 °C in the as-cast condition by adding simultaneously 0.2wt% Ni and 0.2wt% Zr[30,31]. Fine and semi-coherent ternary (Al–Zr–Si) dispersoids formed during solution treatment were observed within dendrites of A356 alloy containing Zr. On the other hand, the presence of Ni as alloying element may induce the formation of several coarse intermetallic phases, depending on the overall alloy composition (e.g. Ni:Fe and Ni:Cu ratios), such as the thermal resistant ε-Al_3Ni, δ-$Al_3(CuNi)_2$, γ-Al_7Cu_4Ni and T-Al_9FeNi[32] phases. Creep tests (300 °C – 20 MPa) carried out on AlSi12 alloy with and without Ni addition showed the positive effect of this alloying element, especially in the as-cast condition[33]. Ni addition, through the formation of such phases (especially the T phase), may anyway lead to embrittlement of the alloy and to a not negligible loss of ductility. Mn addition to such alloys was reported to reduce the embrittling effect of Fe and Ni, further enhancing creep behavior of high Ni content alloys[15]. Nickel-copper interaction should also be considered, since the formation of Cu-rich intermetallics lower the amount of copper for precipitation hardening through T6 heat treatment[31]. A very low diffusion kinetic in Al characterizes also Ti, which forms Al_3Ti precipitates with a $D0_{22}$ equilibrium structure. Ti and Al behave as peritectic system, and high Ti content (next to the maximum solid solubility) may lead to the formation of primary intermetallics in the liquid, therefore acting as grain refiners, which dissolve only at temperatures higher than the melting temperature of pure Al. On the other hand, a noticeable decrease of solid solubility of Ti in α-Al by decreasing the temperature may ensure a good response to solution and quench. The effect of Ti, V and Zr addition on Al-Si-Cu-Mg alloys was evaluated by Lee et al.[34] reporting an increase of the mechanical properties at high temperature. Dislocation movement was effectively hindered by dispersoids. In a similar alloying system, S-(Al_2CuMg), Al_3(Zr, V, Ti) $L1_2$ nanoprecipitates and Al_3(Zr, V, Ti) $D0_{23}$ phases were observed by TEM in the heat treated condition by Kasprak et al[35]. Zr, V and Ti addition improved static and cyclic yield strength at room temperature at the expense of ductility, reporting no significant increase on tensile strength at elevated temperature.

1.3 AL-SI-CU-MG ALLOYS

Aiming to identify suitable chemical compositions for cast aluminum alloys for high temperature applications (also above 250 °C in the case of diesel engines), the addition of Mg and Cu has been recently investigated[2,32,36]. The addition of Cu up to 0.5wt% to traditional Al-Si-Mg alloys, such as the A356, was reported to improve tensile strength at 150-250 °C, without loss of ductility and enhancing creep time to fracture at 200 °C and 120 MPa[10,16].

In particular, the concomitant presence of both copper and magnesium in Al-Si-Cu-Mg alloys should in fact enable the precipitation of more stable Cu-based intermetallic precipitates, leading to enhanced thermal stability of the T6 heat treated alloys[37]. Further than β' (Mg_2Si) and θ' (Al_2Cu) precipitates, present in ternary Al-Si-Mg and Al-Si-Cu alloys[37–42], reinforcing compounds such as the S' phase (Al_2CuMg)[41,43,44] and the Q' phase (whose general stoichiometry is $Al_5Cu_2Mg_8Si_6$) are found in quaternary Al-Si-Cu-Mg alloys. As recently investigated by Farkoosh et al. [2], the quaternary Q' phase is expected to give the most relevant contribution to thermal stability enhancement, being the only age-hardening stable phase after soaking at 300 °C for 100 h[2]. The mechanisms which confer higher coarsening resistance to Q phases are still however under discussion[2,45,46].

1.3.1. HEAT TREATMENT OF AL-SI-CU-MG ALLOYS

Heat treatment of Al-Si-Cu-Mg alloys generally consists of three main steps:

- Solubilization: this treatment phase is usually carried out at high temperature, (490-540 °C). The aim of this step is the microstructural homogenization and the dissolution of coarse intermetallic particles containing Cu and Mg formed during solidification.
- Quench, usually carried out in hot (~ 50-60 °C) or room temperature water; this phase is meant to obtain a supersaturated solid solution.
- Aging, to induce the precipitation of strengthening phases from the supersaturated solid solution. Aging can be natural or artificial, depending on the temperature. Artificial aging is usually carried out in the range 150-200 °C for times from ~ 1 h to 24 h, depending on the alloy chemical composition and on the treatment scope.

1.3.2 DISSOLUTION OF INTERMETALLIC PHASES

In general, it is possible to affirm that the time required to completely homogenize an Al-Si casting is strictly related to the nature of the diffusing atoms, to the solution temperature and to microstructural fineness (i.e. to SDAS)[47,48].

However, the different coarse intermetallic particles formed during solidification in Al-Si-Cu-Mg show different tendency to dissolution. β-Mg_2Si and θ-Al_2Cu phases are generally easy to dissolve; on the contrary, other Cu bearing phases, such as the Q-$Al_5Cu_2Mg_8Si_6$ are usually reported to be quite stable with solution treatment. Also Fe-rich phases are usually difficult to be dissolved, such as the α-$Al_{15}(Fe, Mn)_3Si_2$ phase or the typical needle like β-Al_5FeSi, which undergoes gradual dissolution only after long term solution at high temperature.

One of the most typical phases found in the as-cast microstructures of Cu containing cast alloys (both Al-Si-Cu and Al-Si-Cu-Mg) is the θ-Al_2Cu phase. θ particles may nucleate both around β-Al_5FeSi plates or coarse eutectic Si particles during the last solidification stages.

θ-Al_2Cu phases may form in two main morphologies: blocky and eutectic. Nevertheless, mixed morphologies may also be found[49,50]. It is reported that elevated solidification rate may promote the formation of eutectic morphology; on the other hand, the addition of Sr as chemical modifier may favor the formation of θ blocky phases[51].

Eutectic and blocky θ-Al_2Cu phases undergo dissolution through different mechanisms (Figure 1.3): the eutectic morphology is at first fragmented in smaller particles, which then gradually spherodize and undergo complete dissolution[49] by radial diffusion of Cu into the surrounding matrix. On the contrary, θ-Al_2Cu blocks are quite difficult to bring into solution in view of the compact morphology, which leads to gradual spherodization. This kind of dissolution mechanism requires higher times in comparison to the one involving eutectic particles. Mg containing alloys, may be characterized also by β-Mg_2Si phases; differently from θ particles, the dissolution of Mg_2Si is generally faster thanks to the high diffusion rate of Mg in Al; moreover, in Al-Si-Mg alloys, the quick dissolution of Mg_2Si is made possible also to the high solution temperature (~540 °C), which may be significantly higher than that employed in Al-Si-Cu-Mg, aiming to avoid the incipient melting. Mg content in Al-Si-Mg alloys and microstructural coarseness are also expected to influence the needed time for dissolution, as reported by different investigators[52–54].

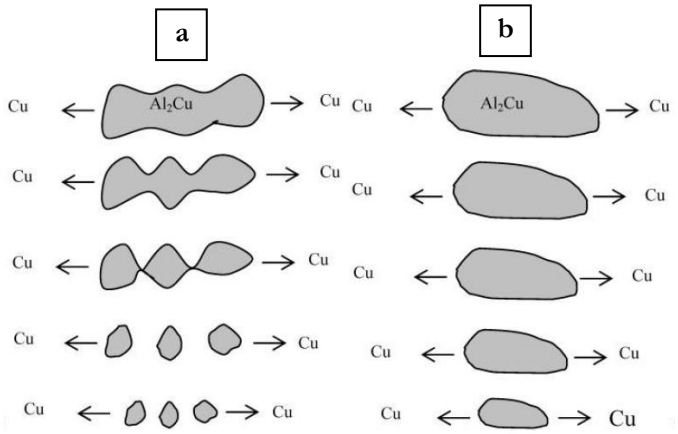

Figure 1.3. Al_2Cu dissolution mechanisms corresponding to (a) eutectic and (b) block like particles[50].

Fe-based phases generally presents a lower tendency to dissolution in comparison to the previous ones. Generally, the β-Al_5FeSi phase is reported to fragment and gradually dissolve only after long time and high temperature solution treatment[55]. On the other hand, the transformation of π-$Al_6Mg_3FeSi_6$ phase into the β-Al_5FeSi may occur in Al-Si-Mg alloys, depending on the Mg content. If a low fraction of Mg is present, the transformation is quick, while for higher Mg contents (0.6-0.7 wt%), the process may be reversed, leading to the formation of π-$Al_6Mg_3FeSi_6$ from the β-Al_5FeSi [56–58]; nevertheless, transformation of the β-Al_5FeSi into Al_7FeCu_2 phase was reported in Al-Si-Cu alloys with high Cu content.

Al-Si-Cu-Mg alloys are characterized also by the presence of quaternary Q particles, $Al_5Mg_8Si_6Cu_2$, whose size is reported to depend also on Mg content. The Q phases are often observed to nucleate in correspondence of Al_2Cu particles, during the last stages of solidification[59].

The response of Q phases to solution treatment is reported to be dependent on solution temperature and chemical composition of the alloy. Some authors documented the dissolution of Q phases at high solution temperature, i.e. 530 °C[60,61]. At lower temperatures, i.e. 490 °C, in high Cu alloys (~4wt%) the Q phase did not undergo dissolution, independently from the Mg content[50,62]. On the contrary, at the same temperature, if lower Cu content is present (~1.4wt%) and high Mg (1.3wt%), transformation of the binary Mg_2Si into the quaternary Q was observed, with a general increase of the total Q fraction[60]. Dissolution of Q phases after double step solution (500 °C + 530 °C) was observed in an Al-Si7-Cu0.5-Mg alloy by Farkoosh et al.[2]. The authors reported also dissolution of π-$Al_6Mg_3FeSi_6$ phase for low Mg (0.3wt%) and small amounts of undissolved particles for higher Mg content (0.7wt%). Also microstructural coarseness plays a fundamental role on intermetallics dissolution: in an Al-Si alloy containing 3wt% of

Cu, Q phases were reported to dissolve at 495 °C for fine microstructure (~9 μm), while no variation in the area fraction was registered in coarser microstructures (~28 and 49 μm)[63].

1.3.3 INCIPIENT MELTING AND MULTIPLE STEP SOLUTION TREATMENT

Differently from the traditional Al-Si-Mg alloys, particular attention should be made during solution treatment of quaternary Al-Si-Cu-Mg alloys. As a matter of fact, in these alloys the maximum solution temperature is limited by the incipient melting of Cu containing phases, which would lead to strong decrease of mechanical properties. In general, low solution temperatures do not allow maximizing the dissolution of solute atoms for subsequent aging treatment. The solution of Al-Si-Cu-Mg alloys needs therefore proper adjustments to fully exploit Cu and Mg for aging.

Most of the work found in the literature about incipient melting of quaternary alloys is focused on high Cu materials, e.g. the widely used A319 alloy. However, the last stage of solidification sequence from the liquid state in quaternary alloys occurs at about 507 °C, depending also on the actual alloy composition, following the reaction[64]:

$$L \rightarrow \alpha(Al) + Al_2Cu + Si + Al_5Cu_2Mg_8Si_6 \qquad (1)$$

The experimental observation of this low temperature reaction has been reported, for example, by Samuel et al.[65]. The authors, through DSC analyses carried out on an Al-Si-Cu alloy, observed the melting of Al_2Cu phase for heating above 520 °C; below this temperature, Al_2Cu particles were reported to undergo gradual dissolution in the Al matrix. By adding 0.5 wt% Mg, a marked shift in the melting point of the copper phases towards lower temperature (i.e. 505 °C) was observed. Incipient melting of $Al_5Mg_8Si_6Cu_2$ and Al_2Cu phases was observed in 319 alloy containing 0.5 wt% of Mg, by using solubilization temperatures above 505 °C for sufficiently long durations; distortion of the castings and deterioration of the mechanical properties were registered[65]. Melting of copper intermetallics starts at grain boundaries and in the interdendritic regions leading to the formation of spherical liquid droplets within the dendrites[65]. By increasing solution temperature up to 535 °C, the width of the grain-boundary melted zone increases, with consequent coalescence of interdendritic droplets to form a large network[65].

The presence of low melting phases is widely reported by several authors in high Cu content alloys[65–67]. On the contrary, different results are reported in the literature for low Cu alloys. Wang et al., for example, observed a low melting DSC peak only in alloys

containing more than 2 wt% of Cu[66]. Moreover, an increase of the mechanical properties, without any observable localized melting, was reported for a low Cu alloy solution treated at 520 ◦C[68].

In spite of this, some researchers suggested for low Cu alloys a solubilization temperature of 495 °C, consistent with the presence of the low melting peak[69,70]. However, it should be taken into account that the maximum affordable temperature, avoiding local melting, actually depends not only on the specific alloy composition, but also on solidification rate, which strongly influences the segregation of intermetallic phases[71].

It appears clear that the heat treatment of quaternary Al-Si-Cu-Mg alloys needs to be optimized: for low solution temperature and time, not all the solute atoms (i.e. Cu, Mg) would be available for precipitation hardening during aging, while too high solution temperature and time would lead to local melting and energy loss, respectively.

Solution heat treatment can be carried out in single or multiple steps. In view of the above, single-step treatment is usually limited to about 495 ◦C-500 °C[72]. Multiple steps solution treatment usually consist of two stages, the first step at ~490 °C aimed to dissolve the Cu-containing phases, while the second step at higher temperature (and usually for longer durations) allows the dissolution of Cu- and Mg- based intermetallics for precipitation hardening[73]. First studies on double-stage solution treatment were carried out by Sokolowski and coworkers[73,74] on 319 alloy. The authors found out that first stage holding time and second stage solution temperature are of primary importance. A double two-step solution treatment (2 h at 495 °C, then 4 h at 515 °C) induced the best combination of strength and ductility in comparison to a single-step solution treatment of 8 h at 495 °C[74].

Other studies on double stage solution were carried out by Mohamed et al. on 319 alloy[72]. These studies revealed that 505°C may be considered as safe temperature for single stage treatments; on the contrary, 530 °C leads to the melting of Al_2Cu particles. However, the authors pointed out that, even if melting of Al_2Cu occurred, the tensile properties still remained high. The authors hypothesized that competitive effects between dissolution of copper and aging precipitation, versus melting of Al_2Cu particles, could be present. Double solution treatment carried out at 505+520 °C on alloys containing less than 0.3 wt% Mg does not induce incipient melting, while additions of higher levels of Mg lower the melting point of the Al_2Cu phase. Moreover, by increasing the second stage solution temperature to 530 °C causes melting of the Al_2Cu phase even in the alloys containing low Mg.

Strontium was reported by some investigator to play a role on incipient melting; in particular, Sr was supposed to lead to segregation of copper-rich phases to areas free of eutectic Si particles. As a result of segregation, it was suggested that the blocky morphology

of Al_2Cu phase would form rather than the fine eutectic one. Since blocky phase presents a higher nucleation temperature (525 °C) than the eutectic one, the temperature corresponding to the melting of the copper-rich eutectic would be raised by the addition of strontium[75]. In this regard, different results were reported by Samuel, reporting no influence of 300 ppm of Sr on incipient melting reaction of Al-Si-Cu and Al-Si-Cu-Mg alloys [65]. Fe was reported not to play a significant effect on the formation temperature of complex eutectics in 319 alloy by Fuoco et al. [76]. The authors also suggested 500 °C as a maximum solution treatment temperature for Al–Si–Cu–Mg alloys, indicating also that in comparison to conventional heat treatment, a double step solutioning may improve both UTS and elongation to failure of the alloy. On the contrary, Mohamed et al. reported an interaction of Fe and Ni traces with Cu to induce the increase of incipient melting temperature[72].

1.3.4 QUENCHING

The aim of quenching phase is to create a supersaturated solid solution, thus to suppress the precipitation of solute atoms from the solution temperature. Precipitation kinetics during aging, in fact, are strictly related to the supersaturation degree. Quenching is usually carried out with high cooling rates aiming to retain in solid solution solute atoms and vacancies. As main drawback of fast cooling, thermal stresses may be present in the casting, also inducing failure. Low cooling rates, on the other hand, would lead to undesired precipitation with consequent lower amount of alloying elements available for aging. The most widely adopted quenching media is water (at room temperature or hot, i.e. ~50-60 °C). In certain cases, where a lower cooling rate is needed, other media may be used, such as polymeric solutions and salt baths. The influence of quench rate on mechanical properties has been mainly investigated on Al-Si-Mg alloys. In general, by decreasing the quench rate, yield strength decreases. Below 1 °C/s yield strength increases with quench rate, while for higher rates (up to 4 °C/s) the quench sensitivity is alloy dependent, increasing with Mg content. For quench rates higher than 4 °C/s sensitivity is reduced and is not dependent on Mg content[77–79]. As a general consideration, for such alloys, the decrease of mechanical properties with decreasing quench rate is due to the loss of excess Si in the supersaturated solution, determining a lower quantity of β" precipitates upon aging[78]. As concerning Cu containing alloys, depending on Mg content, alloys present two kind of behavior: for Mg ~ 0.6 wt%, elongation to failure increases by decreasing the quench rate; between 0.2 and 0.4 Mg wt%, elongation at first decreases with quench rate

(up to 4-40 °C/s); further quench rate decreases lead to an elongation increase[78–80]. The influence of quench rate on ductility is however related to the formation of different amount/morphologies of β'/ β" phases during aging[78,79]. Quench medium, therefore quench rate, was also reported to influence the hardness increase during aging, more pronounced in the case of water quenched alloys in comparison to air quench and time to peak as well[78,81].

1.3.5 AGING

Aim of the aging treatment is to enhance mechanical properties of the alloy, inducing a fine distribution of nanometric intermetallic precipitates acting as obstacles for dislocations movement[82–84]. Aging treatment may be natural (T4), if carried out at room temperature, or artificial (T6) if carried out at high temperature (150-210 °C).

During aging (Figure 1.4), the first step of precipitation sequence is the formation of GP (Guinier-Preston) zones, consisting of high fraction solute atoms clusters. GP zones are typically small, coherent with the matrix and evenly distributed in the α-Al. In view of the different size between solute and Al atoms, elastic stresses are present in the zones surrounding the clusters. As a result, GP zones hinder dislocations movement, leading to a general enhancement of mechanical properties. As concerning natural ageing, Al-Si-Mg alloys are reported to show rapid hardness increase at room temperature after quench, depending also on Mg content[85]. Al–Si–Cu alloys, on the contrary, are characterized by negligible natural ageing; their precipitation hardening is slow at room temperature, while, for small additions of Mg, a quicker response to natural ageing was reported[86].

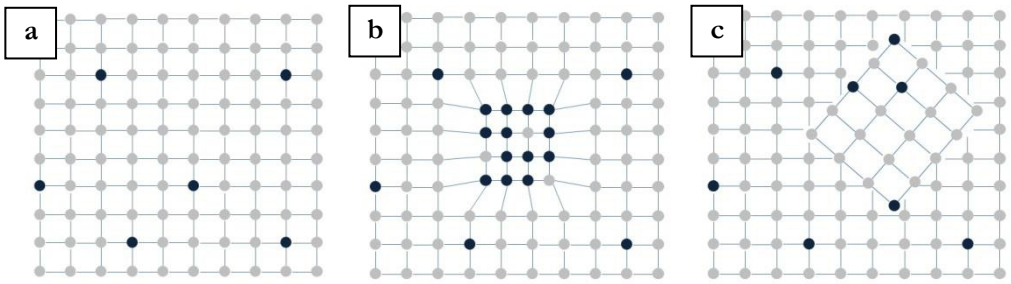

Figure 1.4. Evolution mechanisms of aging precipitates: (a) solid solution as a result of solution treatment, (b) formation of coherent phases and (c) evolution towards incoherent equilibrium precipitates.

Quaternary Al-Si-Cu-Mg alloys present the highest yield strength with direct artificial ageing after quench; nevertheless, if compared to the direct ageing, 3 weeks of natural

ageing was reported to induce a reduction of time to peak when ageing at 210°C; such influence depends however on ageing temperature[87]. Subsequently to GP zones formation, coherent metastable precipitates are generated in correspondence of GP zones, in the Al matrix or on lattice defects. By further aging, solute atoms precipitate from the supersaturated solid solution, resulting in the growth of such precipitates that become semi-coherent, then incoherent. At this stage, the alloy is in the overaged condition (usually referred to as T7). By coarsening, i.e. further increase in precipitates size, the coherency with the matrix lattice is lost, leading to non-coherent precipitates (Figure 1.4)[82,83,88]. At room temperature, dislocations may interact with precipitates mainly in two ways: (i) precipitates may be sheared by dislocations, more easily if they are fine and characterized by low interparticle spacing (*shear* or *Ashby* mechanism, Figure 1.5a); (ii) dislocations may bypass the precipitates by bowing, especially when particles grow and interparticle spacing is increased (*Orowan* mechanism, Figure 1.5b). At a fixed aging temperature, by increasing time, precipitates size increases, and interparticle spacing as well. As a result, the two mechanisms show opposite response to aging time: the maximum strengthening effect, i.e. the optimized aging condition, is realized when the energy required for shear and bypass is the same (Figure 1.5c)[89]. This condition is usually referred to as *peak aging*. Precipitates evolution during overaging follows the Lifshitz, Slyozov and Wagner theory[18] (known as the LSW theory), describing a diffusion-controlled coarsening process. The mechanism, based on Ostwald ripening model, involves the coarsening of larger precipitates at the expense of smaller ones, which undergo dissolution (see Paragraph 1.2 for coarsening modelling)[90].

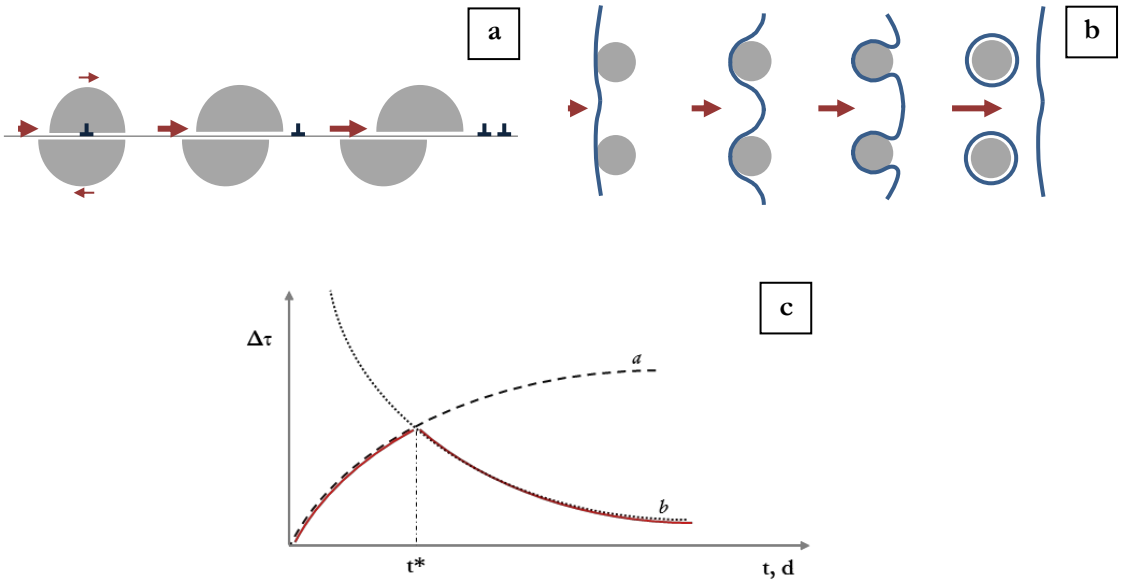

Figure 1.5. Schematic of (a) shear and (b) Orowan mechanism; (c) variation of necessary shear stress for dislocation movement with aging time and precipitates size.

As a consequence, precipitates lose their efficiency in hindering dislocation movement (at this stage only Orowan strengthening mechanism is possible) and strength of the alloy rapidly decreases.

Al-Si-Mg-Cu, if properly heat-treated, are characterized by superior mechanical properties in comparison to the more traditional ternary alloys, i.e. Al-Si-Mg and Al-Si-Cu.

Type, morphology and size of precipitates strongly depend on the alloy chemical composition and thermal treatment. The typical precipitation sequences which characterize Al-Si-Mg and Al-Si-Cu alloys, respectively, are the following[37–42]:

$$\alpha\ (SSS) \rightarrow \text{GP zones} \rightarrow \beta'' \rightarrow \beta'/B' \rightarrow \beta$$

$$\alpha\ (SSS) \rightarrow \text{GP zones} \rightarrow \theta'' \rightarrow \theta' \rightarrow \theta$$

where, β'', β', B' and θ'', θ' are the intermediate precipitates, while β and θ the stable incoherent phases.

Al-Si-Mg precipitation sequence usually starts with the formation of spherical GP zones, consisting in local enrichment of Si and Mg atoms; such clusters become, with further aging, acicular and coherent with the Al matrix (β''-Mg_2Si phase). Precipitates grow, becoming at first semi-coherent (β') then stable incoherent particles[85]. The time necessary to peak aging usually decreases with increasing aging temperature, unless too high temperatures (>210 °C) are used, leading to the formation of uncoherent precipitates inducing strength decrease. Composition of metastable precipitates was reported to vary, depending on the content of excess Si after quenching and during aging process itself[91]. Strength of the alloy generally increases for increase of Mg content up to 0.5 wt%[92]. As concerning Al-Si-Cu alloys, GP zones are characterized by agglomeration of Cu atoms. They are generated at room temperature on the dislocations formed during quenching, as a result of the differences in the thermal expansion coefficients of the Al matrix and eutectic Si. At high temperature, at first GP zones dissolve, leading to a strength decrease; subsequently, they are replaced by coherent θ'' phases (also named GP_2 zones), which transform in the metastable θ' (semi-coherent) and then in the θ incoherent stable phase. Different kinds of precipitates were observed by some authors on dislocations and Al-matrix. Coarse semi-coherent θ' particles and coherent, fine and evenly distributed θ'' phases were observed in correspondence of high density dislocation regions and dislocation free areas, respectively[93]. Peak hardness usually decreases with increasing aging temperature and longer times are needed to reach the peak condition in comparison to Al-Si-Mg and Al-Si-Cu-Mg alloys[93].

Due to the concurrent presence of Cu and Mg, the strength enhancement which can be achieved in quaternary Al-Si-Cu-Mg alloys is far superior in comparison to that of ternary alloys. Even if some author reported no variation in time to peak hardness between Al-Si-Mg and Al-Si-Cu-Mg alloys, inferring no variation in precipitates type[94], it is currently accepted that different precipitates may co-exist in these alloys[41,43,44,95,96]. The same time to peak was registered also by Reif et al. between Al-Si9-Cu3.5 and Al-Si9-Cu3.5-Mg0.5 alloys, showing sensible higher peak hardness values for the quaternary alloy[97]. On the other hand, most of the works found in literature reported longer times to peak for Al-Si-Cu alloys in comparison to Al-Si-Cu-Mg, due to acceleration and intensification of the precipitation-hardening processes owing to Mg addition. While θ' phases nucleate preferentially on dislocations located around Si particles, Q' phases have the capability to nucleate in lower surface energy locations, i.e. throughout the α-Al matrix. The more homogeneous distribution of the quaternary phase would lead to lower diffusion distance, therefore requiring shorter time to aging[93,95].

The type of intermetallics is supposed to be dependent on chemical composition (Cu and Mg content) and on heat treatment parameters. Beside the above mentioned β and θ phases, a quaternary phase (Q) may be present[41,43,44,95,96]. However, despite the presence of Q-phase precipitates in many heat treatable commercial Al alloys, the knowledge about this phase is still uncomplete, in particular about its chemical composition, in view of its small size, making its characterization very challenging [45,98].

In high Cu content alloys (~3wt%Cu), β", θ' and precursors of Q phase were observed, while alloys containing ≤ 1wt% Cu were characterized by absence of θ' phases[82,99]. The formation of θ' phase seems therefore to be somehow related to Cu content. A recent study on a ~3wt%Cu quaternary alloy reported a co-precipitation of Q and θ' phases[45]. DSC analyses revealed that Q phase act as heterogeneous nucleation sites for θ' platelets, suggesting the following precipitation sequence:

$$GP \rightarrow Q \rightarrow Q + \theta'.$$

Possible structural precursors of the Q-phase, QC and QP were also identified by Cayron et al.[96,100]. A metastable version of the Q phase, Q', was reported by Chakrabarti et al., showing smaller size, coherency with Al matrix and the same crystal structure and lattice parameters as the equilibrium Q[95]. Furthermore, evolution of chemical composition of the Q phase was documented: aging at low temperature leads to a Cu-rich Q-phase, poor in Mg and Si (44Al–22Cu–16Mg–16.5Si at.%). By increasing aging temperature the composition evolves to become Mg-rich (28Al–9Cu–37Mg–26Si at.%).

A ternary phase (S) was also reported by different works carried out on systems similar to Al-Si-Cu-Mg, characterized by the stoichiometry Al_2CuMg[41,43,44] and precipitation sequence

$$\alpha(SSS) \rightarrow \text{GPB zones} \rightarrow S'' \rightarrow S' \rightarrow S$$

where GPB indicates Guinier–Preston–Bagaryatsky zones. Despite the S phase is thought not to precipitate in high Si Al-Si-Cu-Mg alloys, it can be found in small amounts due to compositional heterogeneities[62]. In this regard, the S' phase was observed in the heat treated T5 condition in alloy 339[101] and in 0.5wt% containing Al-Si9-Cu3.5 alloy, together with θ' after aging at 160°C[97]. Coarse S phases were also observed in 319 alloy by Tavitas-Medrano et al.[88].

3D Atom Probe (3DAP) analyses were carried out by Hwang et al. on T6-319 alloy containing 0.45 wt% Mg. Local enrichment of Cu and Cu-Mg-Si were reported in strengthening precipitates, corresponding to θ' and finer Q' phases, respectively (Figure 1.6)[98]. A significant strengthening effect of Q' phase, also by favoring heterogeneous nucleation of the θ' phase, was registered: T6 heat treatment in this alloy induced a noticeable increase of UTS (+67%) in comparison to the as cast condition, while 319-Mg free alloy presented only 30 % of UTS increase after the same treatment. However, a much more pronounced decrease of ductility (elongation to failure) was reported in the Mg-rich alloy, likely due to the presence of Q' precipitates in the T6 condition. Decrease of ductility after T6 heat treatment was registered also by other investigators[102]

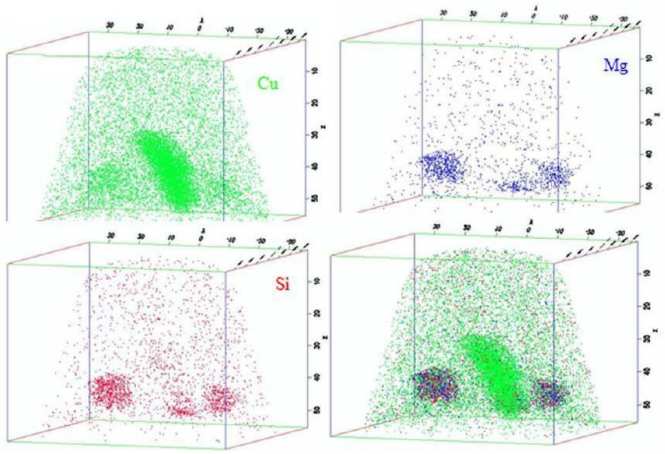

Figure 1.6. 3DAP data from 319-0.45wt%Mg alloy in the T6 condition, showing distribution of Cu, Si and Mg in green, red and blue, respectively. The Cu enrichment in the larger precipitate is supposed to correspond to a θ' phase, while the smaller particles containing Cu, Mg and Si should be Q' phases[98].

A different Mg content was reported by Farkoosh et al. to influence the quantity of Q and θ phases formed during aging of an Al-Si7-0.5Cu alloy: increasing Mg from 0.3 to 0.5 wt.%

led to an increase of Q phases and a decrease of θ phase. However, as a result of thermodynamic calculations, by further increasing Mg content up to 0.7 wt.%, the amount of Q phases does not change. From 0.5 to 0.7 wt.% Mg the maximum solubility of copper is in fact strongly reduced[2].

It should be pointed out that, despite it is not generally agreed, double aging peak has been sometimes observed in Al-Si-Cu-Mg alloys. Li et al.[103], in particular, reported such behavior for aging temperatures higher than 175 °C, the first peak being characterized by higher hardness values in comparison to the second one. Such behavior, not observed in ternary Al-Si-Cu and Al-Si-Mg alloys, was related to the formation and dissolution of GP zones, and subsequently to the formation of metastable phases.

1.3.6 COARSENING RESISTANCE OF AL-SI-CU-MG ALLOYS

The application of Al-Si-Cu-Mg alloys for high temperature applications has been investigated in recent years[2,32,36]. Aim of such studies is to optimize chemical composition and heat treatment for fully exploitation of strengthening effect of precipitates, both at room and high temperature (~250 °C), maintaining good ductility. Al-Si-Mg alloys, such as the A356, are characterized by good ductility, but lower mechanical properties in comparison to high Cu content alloys (e.g. A319), the latter showing very low elongation to failure. As a result, an optimal combination of strength and ductility should be achieved, being both crucial for thermal fatigue resistance. It is important to point out that, despite the great interest for industrial applications, few work has been addressed in the literature to investigate high temperature behavior of quaternary Al-Si-Cu-Mg alloys. Strengthening mechanisms are not well understood[2], and very limited studies were carried out to investigate on the overaging response of such alloys.

The effect of overaging (i.e. long term high temperature exposure) on Q and θ precipitates was recently studied by Farkoosh et al. on an Al-Si7-Cu0.5-Mg alloy[104]. Both Q and θ phases were found by TEM-EDS after solution and overaging at 200 °C for 450 h. On the contrary, after aging 100 h at 300 °C only rod shape, coarsened Q precipitates were identified (Figure 1.7).

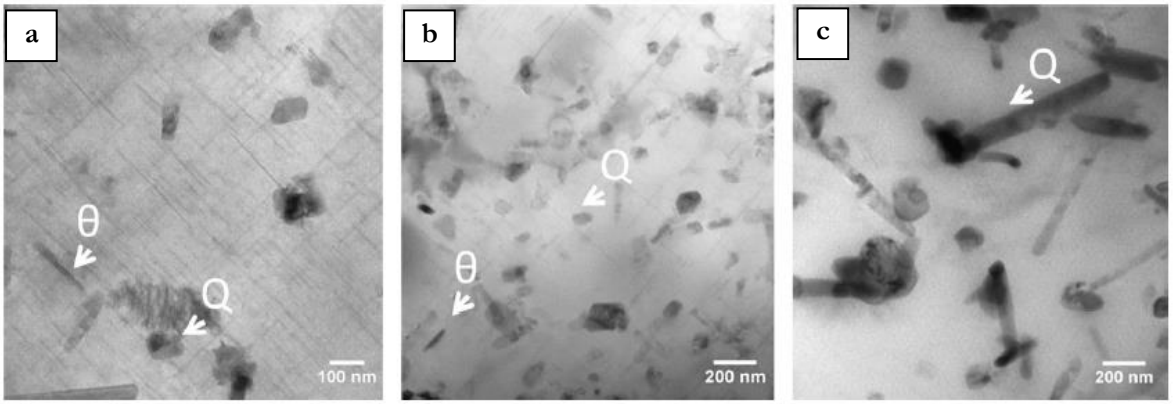

Figure 1.7. Bright field TEM images of Al-7Si-0.5Cu-0.3Mg alloy, showing coarsening evolution of strengthening precipitates after (a) 170 h and (b)500 h of aging at 200 °C, where both θ and Q phases are present; (c) after 5h at 200 °C and 240 h at 300 1 °C, where only coarsened Q precipitates were identified[104].

In particular, by increasing the Mg content from 0.3 to 0.5 wt.%, the fraction of Q-phases increased, suggesting this alloy to be a better candidate for high temperature applications. Coarsened particles are expected to strengthen the alloy at 300 °C by Orowan mechanism. Interestingly, particles overaged at 300 °C presented lower Cu contents in comparison to the one aged at 200 °C, as also observed by Biswas et al.[45]. Metallurgical mechanisms that confer to Q-phases higher thermal stability, i.e. better coarsening resistance, are still under debate. Some authors reported segregation of Cu at the interface between Q' and Al-lattice (Figure 1.8) in low Si alloys[46].

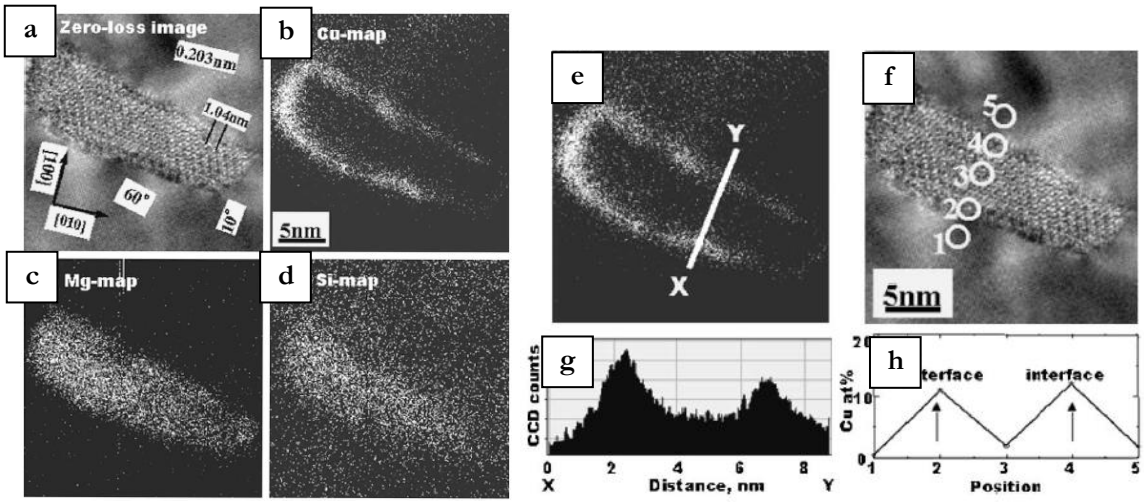

Figure 1.8. EFTEM images of (a) Q' phase showing distribution of (b) Cu, (c) Mg and (d) Si; (e) distribution of Cu atoms at the interface between Q' phase and matrix, (g) CCD intensity profile obtained from the line in (e), (h) EDS results obtained from points 1–5 marked in (f) [46].

Segregation of Cu could be related to the accommodation of misfit strains between Q phase and matrix, or to the shear component of the transformation strain during the first steps of precipitation. Such distribution of Cu atoms could be the reason of the higher thermal stability of Q' phases, limiting the diffusional growth of the Q' phase[46]. This finding, however, was not observed by other investigators[2,45], and the occurrence of Cu segregation at the Q interface is still uncertain.

Despite this, the beneficial effect of coarsening resistant Q phases on creep and high temperature tensile behavior was demonstrated[2]. Increasing the Mg content from 0.3 to 0.5 wt%, thus increasing the amount of Q phases, led to an increase of YS and UTS at 300 °C of about 30 and 50%, respectively; correspondingly, a decrease of about 20% in the elongation to failure was measured.

Creep tests carried out at 300 °C revealed that adding 0.5wt% of Mg leads to a noticeable decrease in the minimum creep rate and an increase of the threshold stress. The reason of the increased creep resistance has been related by the authors to the morphological evolution of Q phases upon overaging towards elongated rods, which could reduce the interparticle spacing, therefore leading to a greater Orowan mechanism contribution. Moreover, authors suggest that a higher amount of Q phases may also induce a delaying effect on interdendritic failure, which is strictly related to creep behavior, by slowing down slip within intragranular areas[2].

1.4 MECHANICAL PROPERTIES OF AL-SI-CU-MG ALLOYS

In the literature, most of the activity on tensile characterization has been devoted on high Cu content alloys (e.g. the widely used A319); only a few works were carried out on Al-Si-Cu-Mg alloys containing up to 1 wt% Cu. Effects of aging parameters on mechanical properties of C355 alloy were investigated by Mrowka-Nowotnik[105]. The authors reported continuous hardness increase with aging time at 150 °C, while at 220 °C, after reaching the aging peak (lower than that registered at 150 °C), hardness decreases. While UTS is reported to follow the trend of hardness curve, YS remained basically constant with increasing aging time after reaching the peak value, even at 220 °C; moreover, higher UTS values were achieved by aging at 220 °C in comparison to 150 °C. Ductility decreased with the aging time until a minimum was reached, then increased again. However, the authors gave no explanation of such behavior. Lower elongation to failure in A354 (Al-Si-Cu-Mg) alloy was observed by Seifeddine et al.[80], in comparison to A356 alloy (Al-Si-Mg). The authors related such behavior to the different content of Si and Cu content; moreover, A354 presented higher UTS and YS with respect to A356. The influence of aging parameters on tensile properties and ductility of Al-Si9-Cu1.8-Mg0.5 was studied by Ammar et al[106]. The most beneficial combination of strength and ductility was registered by aging at low aging temperature (155 °C); time to peak was reported to decrease from 155 to 245 °C. Further, the peak values of UTS and YS decreased from 155 °C to 245 °C aging temperature. Aging at the lowest temperature (155 °C) was reported to induce a continuous increase of tensile properties with time, while from 170 to 245 °C an increase of UTS and YS up to the peak followed by a decrease due to overageing was registered. The concurrent decrease of strength and increase in ductility upon overaging was related by the authors to softening, which would lead to the loss of coherency strain between Al matrix and precipitates, and to the increase of interparticle spacing induced by precipitates coarsening. Aging conditions influence also, to some extent, failure mechanisms. Low aging temperatures were reported to induce mixed brittle/ductile behavior, related to a dense population of fine strengthening precipitates, typical of a hard matrix; on the contrary, high aging temperature (245 °C) lead to completely ductile failure, as a result of matrix softening due to precipitates coarsening. The decrease of time to peak with increasing aging temperature was reported also by Sandoval et al[69], who registered the achievement of the maximum UTS (386 MPa) in a Al-Si9-Cu1.8-Mg0.4 alloy after 100 h at 155 °C, 10 h at 170 °C and 2 h at 190 °C. Increase of strength with aging at the expense of ductility was also confirmed. Long term exposure at 190 °C (i.e. overaging) led to a noticeable decrease of mechanical properties, being YS more affected (360 MPa after 10 h, 240 MPa after 1000 h)

than UTS, and a concurrent increase of plastic strain. As concerning fatigue behavior, once again most of the available literature data refer to high Cu content alloys, mainly characterized at room temperature[107–113]. However, in general, fatigue resistance of Al-Si-Cu-Mg alloys is strongly influenced by casting defects (i.e. porosities, interdendritic cavities, oxide films), similarly to Al-Si-Mg alloys. Brittle intermetallic compounds (especially Fe-based) are usually reported to act as crack nucleation sites and interacting with crack propagation[107,111]. Also eutectic Si particles are reported to play a role as crack initiator[108]. As instance, damage processes involved in B319 fatigue behavior in the T5 and T6 conditions consisted in cracking of Si and intermetallic particles ahead of the crack-tip and localized shear failure in the matrix, while in the T7 condition cracks propagated mainly in the Al-matrix without significant particles interaction[108]. As concerning high temperature fatigue behavior of low Cu Al-Si-Cu-Mg alloys, basically no work is available in the literature. Despite this, some research carried out to compare at room and high temperature 356 and 319 alloys to an Al-Si7-Cu0.5-Mg0.3, under low-, high-cycle and thermo-mechanical fatigue, showed that the investigated alloys present a very similar behavior under both isothermal low-cycle and thermo-mechanical fatigue, even if in different heat treatment conditions[109]. Fatigue life was not enhanced by the higher ductility of low Cu alloys, but the influence of casting defects was observed. A356-T6 and Al-Si7-Cu0.5-Mg0.3 alloys showed superior high cycle fatigue behavior up to 150 °C, if compared to A319 alloy. Such results, related to lower data scatter is thought to depend on the lower content of porosity in low Cu alloys[108]. The effect of 0.5-1.0 wt.% Cu on mechanical properties of an Al-Si8-0.3Mg-0.1Fe was evaluated by Feikus[10], reporting no significant improvement in YS at room temperature after T6, while enhancement of both tensile strength and creep resistance were observed in the temperature range 150-200 °C. Negligible variation in thermal expansion coefficient and thermal conductivity was reported[10].

1.5 MOLYBDENUM ADDITION TO AL-SI ALLOYS

Molybdenum has not been widely investigated as possible candidate for enhancing high temperature mechanical properties of cast Al alloys. Despite this, Molybdenum possesses good properties to allow efficient strengthening of cast aluminum alloys. It presents, in fact, low diffusivity in Al (2.3 x 10^{-26} m^2 s^{-1} at 300 °C) and solid solubility rapidly decreasing with the decrease of temperature (the maximum solid solubility is 0.25wt% at the peritectic reaction)[114]. Al-Mo phase diagram is reported in Figure 1.9.

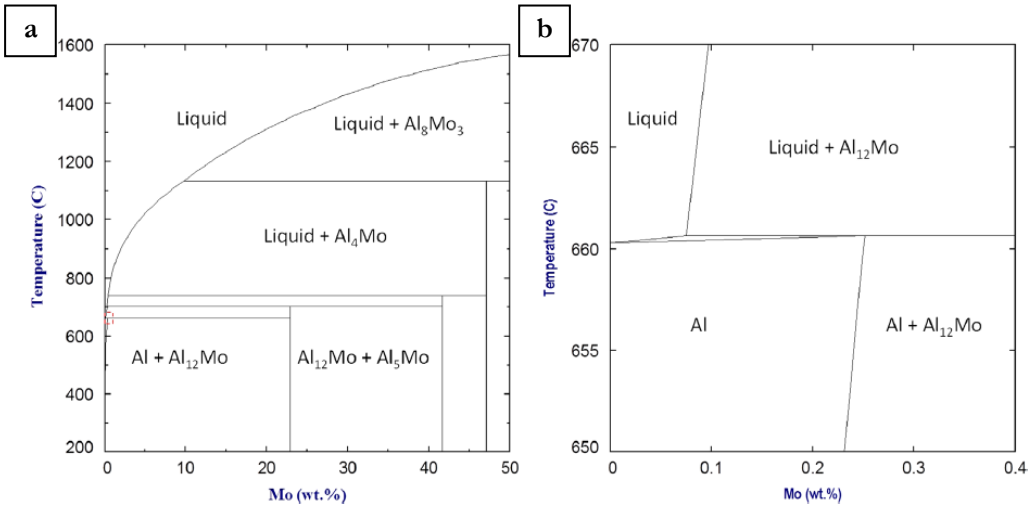

Figure 1.9. (a) Al-Mo diagram phase and (b) focus on Al-rich side[104].

Only a few works, by Farkoosh et al. [104,115], have been found in literature investigating the effect of Mo on high temperature behavior of Al-Si alloys. In particular, the authors investigated the possibility of inducing the formation of stable Mo-based dispersoids in an Al-Si alloy, through a conventional casting process and proper heat treatment.

Aiming to evaluate the effect of Mo addition on tensile and creep properties, 0.3wt% Mo was added to a traditional Al-Si7-Cu0.5-Mg0.3 alloy[104]. A double step heat treatment was proposed, to avoid incipient melting of the alloy. The first step, meant to homogenization of the alloy, was carried out at 500 °C; the second one, aimed to the formation of dispersoids containing Mo, was carried out at 540 °C. The authors indicate that, in view of the peritectic nature of the alloy, micro-segregation occurs during non-equilibrium cooling, thus leading to Mo supersaturation at the intradendritic regions. By subjecting the alloy to high temperature solution treatment (i.e. at 540 °C) in view of the low diffusivity of Mo in Al, a fine dispersion of Molybdenum containing phases can be achieved. TEM analyses combined with EDS spectra revealed that the dispersoids consist of quaternary Al-

(Fe,Mo)-Si phases (Figure 1.10). After 10 h of solution at 540 °C, dispersoids with average size of 120 nm were observed.

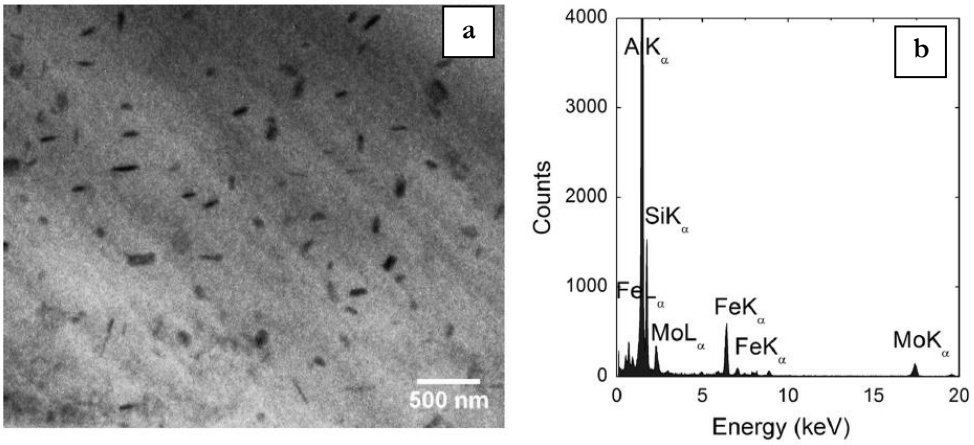

Figure 1.10. (a) Bright field TEM images of Al-Si7-Cu0.5-Mg0.3 alloy with 0.3 wt% Mo addition after solution treatment (540 °C – 10 h) showing Al–(Fe,Mo)–Si phases dispersed within the intradendritic region; EDS spectrum corresponding to Mo-based dispersoids[104].

The comparison of aging behavior at 200 °C of the base alloy with the Mo-alloyed one (Figure 1.11), revealed that the presence of Mo induced similar aging curves, with synchronous peaks, and slightly higher hardness values for the Mo-containing alloy, in particular in the first 3 aging hours, and for long term aging (from 2 weeks to 1 month at 200 °C). TEM analyses revealed that θ-Al_2Cu and Q-$Al_5Cu_2Mg_8Si_6$ undergo to coarsening and ripening at 200 °C for prolonged aging; only coarsened Q phases remained after overaging at 300 °C. On the contrary, Al-(Fe,Mo)-Si phases were observed unchanged upon aging at 200 °C and overaging at 300 °C. The Mo-rich alloy displayed significant enhancement in creep properties at 300 °C: the minimum creep rate decreased about 95% and the creep time to fracture increased about 30 folds in comparison to the base alloy. The effect of Mo-based dispersoids to strengthening was reported to be crucial after 100 h of thermal exposure at 300 °C, at the testing temperature of 300 °C.

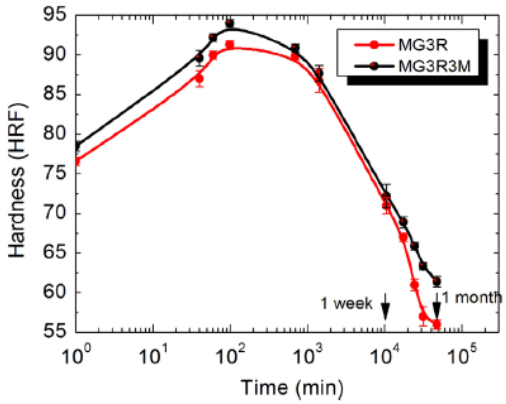

Figure 1.11. Hardness evolution during aging and overaging at 200 °C of Al-Si7-Cu0.5-Mg0.3 alloy (MG3R) and the same alloy with 0.3 wt% Mo addition (MG3R3M)[104].

While Cu and Mg based precipitates completely lost their efficiency due to coarsening, Al-(Fe,Mo)-Si phases allowed to obtain an enhancement of YS, UTS and elongation to failure of 25, 15 and 35% respectively, in comparison to the base alloy. The same authors investigated also the interaction between Mo and Mn on the formation of strengthening dispersoids and related effects on mechanical behavior[115]; an increase of the amount of Mo-based particles and the decrease of the average particles size was observed with Mn addition up to 0.5 wt%, leading to significant creep resistance enhancement. The presence of Mn was reported to induce a more uniform distribution of dispersoids, due to the different positioning of Mo and Mn atoms during solidification: Mn forms a terminal eutectic reaction with Al segregating in the interdendritic areas, while Mo, being a peritectic element, segregates to the dendritic cores. Mn, moreover, was also reported to substitute Fe atoms within the structure of α-Mo dispersoids. The total effect is the elimination of dispersoids-free zone. However, a decrease of creep time to fracture was registered for addition of Mn beyond 0.5 wt%, due to the formation of interdendritic intermetallics.

REFERENCES – CHAPTER 1

[1] M. Javidani, D. Larouche, *Int. Mater. Rev.* **2014**, *59*, 132.

[2] A. R. Farkoosh, M. Pekguleryuz, *Mater. Sci. Eng. A* **2015**, *621*, 277.

[3] M. Garat, G. Laslaz, *AFS* **2007**, 1.

[4] R. Minichmayr, M. Riedler, G. Winter, H. Leitner, W. Eichlseder, *Int. J. Fatiguenal J.* **2008**, *30*, 298.

[5] V. Firouzdor, M. Rajabi, E. Nejati, F. Khomamizadeh, *Mater. Sci. Eng. A* **2007**, *454-455*, 528.

[6] R. B. Gundlach, B. Ross, A. Hetke, S. Valtierra, J. F. Mojica, *AFS Trans.* **1994**, *102*, 205.

[7] T. Takahashi, K. Sasaki, *Procedia Eng.* **2010**, *2*, 767.

[8] S. C. Lee, L. C. Weng, *Met. Mater. Trans. A,* **1991**, *22*, 1821.

[9] G. E. Dieter, *Mechanical Metallurgy*, McGraw-Hill, London, UK, **1986**.

[10] F. Feikus, *AFS* **1998**, 1.

[11] H. Sehitoglu, T. Smith, X. Qing, H. Maier, J. Allison, *Met. Mater. Trans. A* **2000**, *31*, 139.

[12] J. Allison, J. Boileau, *Met. Mater. Trans. A* **2003**, *34*, 1807.

[13] J. Jang, Y. Jeong, C. Yoon, S. Kim, *Met. Mater. Trans. A,* **2009**, *40*, 1090.

[14] S. Spigarelli, in *TALAT (Lecture)*, **1999**.

[15] a. R. Farkoosh, M. Pekguleryuz, *Mater. Sci. Eng. A* **2013**, *582*, 248.

[16] L. Heusler, F. Feikus, M. Otte, in *AFS Trans.*, **2001**, pp. 215–223.

[17] E. Gariboldi, *Alta Temperatura e Comportamento a Fatica Dei Metalli: i Fenomeni Di Creep e Creep-Fatica*, **2011**.

[18] I. M. Lifshitz, V. V Slyozov, *J. Phys. Chem. Solids* **1961**, *19*, 35.

[19] C. Wagner, *Electrochemie* **1961**, *65*, 581.

[20] H. A. Calderon, P. W. Voorhes, J. L. Murray, G. Kostorz, *Acta Metall.* **1994**, *42*, 991.

[21] K. E. Knipling, D. C. Dunand, D. N. Seidman, *Zeitschrift für Met.* **2006**, *97*, 246.

[22] D. N. Seidman, E. a. Marquis, D. C. Dunand, *Acta Mater.* **2002**, *50*, 4021.

[23] R. a. Karnesky, M. E. van Dalen, D. C. Dunand, D. N. Seidman, *Scr. Mater.* **2006**, *55*, 437.

[24] Y. Harada, D. C. Dunand, **2002**, *331*, 686.

[25] H. Hallem, B. Forbord, K. Marthinsen, *Mater. Sci. Eng. A* **2004**, *387-389*, 940.

[26] *WO 2011/159169*, **2011**.

[27] Z. H. Jia, Z. J. Chen, L. Arnberg, P. Åsholt, Q. Liu, G. J. Huang, in *13th Int. Conf. Alum. Alloy.*, **2012**, pp. 1167–1172.

[28] P. Sepehrband, R. Mahmudi, F. Khomamizadeh, *Scr. Mater.* **2005**, *52*, 253.

[29] R. Mahmudi, P. Sepehrband, H. M. Ghasemi, *Mater. Lett.* **2006**, *60*, 2606.

[30] A. M. A. Mohamed, F. H. Samuel, S. Al Kahtani, *Mater. Sci. Eng. A* **2013**, *577*, 64.

[31] J. Hernandez-Sandoval, G. H. Garza-Elizondo, a. M. Samuel, S. Valtiierra, F. H. Samuel, *Mater. Des.* **2014**, *58*, 89.

[32] A. R. Farkoosh, M. Javidani, M. Hoseini, D. Larouche, M. Pekguleryuz, *J. Alloys Compd.* **2013**, *551*, 596.

[33] Z. Asghar, G. Requena, F. Kubel, *Mater. Sci. Eng. A* **2010**, *527*, 5691.

[34] J. A. Lee, P. S. Chen, *US Patent, 0192627 Al*, **2003**.

[35] W. Kasprzak, B. S. Amirkhiz, M. Niewczas, *J. Alloys Compd.* **2014**, *595*, 67.

[36] A. Farkoosh, X. Chen, M. Pekguleryuz, in *Mater. Sci. Technol. Conf. Exhib.*, Montreal, Canada, **2013**, pp. 1220–1227.

[37] J. Man, L. Jing, S. G. Jie, *J. Alloys Compd.* **2007**, *437*, 146.

[38] M. Murayama, K. Hono, M. Saga, M. Kikuchi, *Mater. Sci. Eng. A* **1998**, *250*, 127.

[39] L. Zhen, W. Fei, S. Kang, H. King, *J. Mater. Sci.* **1997**, *32*, 1895.

[40] W. F. Miao, D. E. Laughlin, *Scr. Mater.* **1999**, *40*, 873.

[41] D. G. Eskin, *J. Mater. Sci.* **2003**, *38*, 279.

[42] S. K. Son, M. Takeda, M. Mitome, Y. Bando, T. Endo, *Mater. Lett.* **2005**, *59*, 629.

[43] S. C. Wang, M. J. Starink, N. Gao, *Scr. Mater.* **2006**, *54*, 287.

[44] P. Ratchev, B. Verlinden, P. De Smet, P. Van Houtte, *Scr. Mater.* **1998**, *38*, 1195.

[45] A. Biswas, D. J. Siegel, D. N. Seidman, *Acta Mater.* **2014**, *75*, 322.

[46] K. Matsuda, D. Teguri, Y. Uetani, T. Sato, S. Ikeno, *Scr. Mater.* **2002**, *47*, 833.

[47] G. A. Edwards, K. Stiller, G. L. Dunlop, M. J. Couper, **1998**, *46*, 3893.

[48] E. Sjölander, *J. Mater. Process. Technol.* **2011**, *210*, 1249.

[49] Z. Li, A. Samuel, F. Samuel, C. Ravindran, S. Valtierra, *J. Mater. Sci.* **2003**, *38*, 1203.

[50] Y. M. Han, a. M. Samuel, F. H. Samuel, H. W. Doty, *Int. J. Cast Met. Res.* **2008**, *21*, 387.

[51] E. Samuel, A. Samuel, H. Doty, in *AFS Trans.*, **1996**, pp. 893–901.

[52] P. Rometsch, L. Arnberg, D. Zhang, *Int. J. Cast Met. Res.* **1999**, *12*, 1.

[53] D. Zhang, L. Zheng, D. St. John, *J. Light Met.* **2002**, *2*, 27.

[54] S. Shivkumar, J. S. Ricci, C. Keller, D. Apelian, *J. Heat Treat.* **1990**, *8*, 63.

[55] N. Crowell, S. Shivkumar, *AFS Trans.* **1995**, *107*, 721.

[56] A. Dons, L. Pedersen, S. Brusethaug, *Aluminium* **2000**, *76*, 294.

[57] J. Taylor, D. St. John, J. Barresi, M. Couper, *Mater. Sci. Forum* **2000**, *331*, 277.

[58] P. Rometsch, G. Schaffer, J. Taylor, *Int. J. Cast Met. Res.* **2001**, *14*, 59.

[59] A. Samuel, P. Ouellet, F. Samuel, H. Doty, *AFS Trans.* **1997**, *105*, 951.

[60] L. Lasa, J. Rodrigues-Ibabe, *J. Mater. Sci.* **2004**, *39*, 1343.

[61] S. Chaudhury, D. Apelian, *Met. Mater. Trans. A* **2006**, *37*, 2295.

[62] L. Lasa, J. . Rodriguez-Ibabe, *Mater. Charact.* **2002**, *48*, 371.

[63] E. Sjölander, S. Seifeddine, *Metall. Mater. Trans. A* **2013**, DOI 10.1007/s11661-013-2141-9.

[64] L. Mondolfo, *Aluminum Alloys: Structure & Properties*, Butterworths & Co, **1976**.

[65] F. . Samuel, *J. Mater. Sci.* **1998**, *33*, 2283.

[66] G. Wang, X. Bian, W. Wang, J. Zhang, *Mater. Lett.* **2003**, *57*, 4083.

[67] A. Samuel, H. Doty, S. Valtierra, F. Samuel, *Mater. Des.* **2013**, *52*, 947.

[68] P. Wang, S. Lee, J. Lin, *J. Mater. Res.* **2000**, *15*, 2027.

[69] J. H. Sandoval, A. M. . Mohamed, S. Valtierra, F. H. Samuel, *Mater. Sci. Forum* **2014**, *794-796*, 489.

[70] A. Mohamed, F. H. Samuel, S. Al Kahtani, *Mater. Sci. Eng. A* **2013**, *577*, 64.

[71] F. H. Samuel, A. M. Samuel, H. Liu, *J. Mater. Sci.* **1995**, *30*, 2531.

[72] A. Mohamed, F. Samuel, S. Al kahtani, *Mater. Sci. Eng. A* **2012**, *543*, 22.

[73] J. Sokolowski, X. Sun, G. Byczynski, D. Northwood, D. Penrod, R. Thomas, A. Esseltine, *J. Mater. Process. Technol.* **1995**, *93*, 385.

[74] J. Sokolowski, M. Djurdjevic, C. Kierkus, D. Northwood, *J. Mater. Process. Technol.* **2001**, *109*, 174.

[75] H. Beumler, A. Hammerstad, B. Wieting, R. DasGupta, *AFS Trans.* **1988**, *96*, 1.

[76] R. Fuoco, E. Corrêa, *AFS Trans.* **2002**, *110*, 1.

[77] E. Sjölander, S. Seifeddine, *J. Mater. Process. Technol.* **2010**, *210*, 1249.

[78] D. Zhang, L. Zheng, *Metall. Mater. Trans. A* **1996**, *27*, 3983.

[79] L. Pedersen, L. Arnberg, *Met. Mater. Trans. A* **2001**, *32*, 525.

[80] S. Seifeddine, G. Timelli, I. L. Svensson, **2007**, *59*, 2.

[81] M. Jeyakumar, M. Hamed, S. Shankar, in *Shape Cast. 3rd Int. Symp. Fr. CA. TMS,*, **2009**, pp. 87–95.

[82] G. Wang, Q. Sun, L. Feng, L. Hui, C. Jing, *Mater. Des.* **2007**, *28*, 1001.

[83] G. Wang, X. Bian, X. Liu, J. Zhang, *J. Mater. Sci.* **2004**, *39*, 2535.

[84] E. Sjölander, S. Seifeddine, *Mater. Sci. Eng. A* **2011**, *528*, 7402.

[85] D. Shivkumar, S., Keller, C., Apelian, *AFS Trans.* **1990**, *98*, 905.

[86] W. Reif, S. Yu, J. Dutkiewicz, R. Ciach, J. Krol, *Mater. Des.* **1997**, *18*, 253.

[87] E. Sjölander, S. Seifeddine, *Metall. Ital.* **2012**, *11*, 39.

[88] F. J. Tavitas-Medrano, a. M. a. Mohamed, J. E. Gruzleski, F. H. Samuel, H. W. Doty, *J. Mater. Sci.* **2009**, *45*, 641.

[89] G. M. Paolucci, *Lezioni Di Metallurgia, Vol. 1 - Struttura, Proprietà e Comportamento Dei Materiali Metallici*, **2002**.

[90] D. O. Ovono, I. Guillot, D. Massinon, *Scr. Mater.* **2006**, *55*, 259.

[91] N. Maruyama, R. Uemori, N. Hashimoto, M. Saga, M. Kikuchi, *Scr. Mater.* **1997**, *36*, 89.

[92] J. A. Taylor, D. H. St John, J. Barresi, M. J. Couper, *Int. J. Cast Met. Res.* **2000**, *12*, 419.

[93] H. G. Kang, M. Kida, H. Miyahara, K. Ogi, *AFS Trans.* **1999**, *27*, 507.

[94] Y. J. Li, S. Brusethaug, A. Olsen, *Scr. Mater.* **2006**, *54*, 99.

[95] D. . Chakrabarti, D. E. Laughlin, *Prog. Mater. Sci.* **2004**, *49*, 389.

[96] C. Cayron, P. a. Buffat, *Acta Mater.* **2000**, *48*, 2639.

[97] W. Reif, J. Dutkievicz, R. Ciach, S. Yu, J. Krol, *Mater. Sci. Eng. A* **1997**, *234-236*, 165.

[98] J. Y. Hwang, R. Banerjee, H. W. Doty, M. J. Kaufman, *Acta Mater.* **2009**, *57*, 1308.

[99] Y. J. Li, S. Brusethaug, A. Olsen, *Scr. Mater.* **2006**, *54*, 99.

[100] C. Cayron, L. Sagalowicz, O. Beffot, P. Buffat, *Philos Mag A* **1999**, *79*, 2833.

[101] R. K. Mishra, G. W. Smith, W. J. Baxter, A. K. Sachdev, V. Franetovic, *J. Mater. Sci.* **2001**, *36*, 461.

[102] P. Ouellet, F. H. Samuel, **1999**, *4*, 4671.

[103] R. Li, R. Li, Y. Zhao, L. He, C. Li, H. Guan, Z. Hu, *Mater. Lett.* **2004**, *58*, 2096.

[104] A. R. Farkoosh, X. Grant Chen, M. Pekguleryuz, *Mater. Sci. Eng. A* **2015**, *620*, 181.

[105] G. Mrowka-Nowotnik, J. Sieniawski, *Arch. Mater. Sci. Eng.* **2011**, *47*, 85.

[106] H. R. Ammar, a. M. Samuel, F. H. Samuel, E. Simielli, G. K. Sigworth, J. C. Lin, *Metall. Mater. Trans. A* **2011**, *43*, 61.

[107] Y. Kuroki, T. Tanaka, T. Sato, A. Kamio, *Mater. Trans.* **2001**, *42*, 2339.

[108] K. Chan, P. Jones, Q. Wang, *Mater. Sci. Eng. A* **2003**, *341*, 18.

[109] C. C. E. Jr, J. V Lasecki, J. M. Boileau, J. E. Allison, **2014**.

[110] L. Dietrich, J. Radziejewska, *Mater. Des.* **2011**, *32*, 322.

[111] L. Ceschini, a. Morri, G. Sambogna, *J. Mater. Process. Technol.* **2008**, *204*, 231.

[112] S. Sainis, A. Kalra, G. Babu, M. N. Rao, *Adv Mater Res* **2003**, *800*, 356.

[113] R. González, D. Martinez, J. González, J. Talamantes, S. Valtierra, R. Colás, *Int. J. Fatigue* **2011**, *33*, 273.

[114] N. van Chi, D. Bergner, *TransTechPublications* **1983**, 334.

[115] A. R. Farkoosh, X. G. Chen, M. Pekguleryuz, *Mater. Sci. Eng. A* **2015**, *627*, 127.

CHAPTER 2

MATERIALS AND METHODS

AL-SI-CU-MG ALLOYS

PURPOSE OF THE WORK

The main aims of the research activities carried out on Al-Si casting alloys for high temperature applications were the following:

- **PART 1 - Characterization of Al-Si-Cu-Mg alloys**

In the framework of Al-Si alloys for high temperature applications, the attention devoted from the industrial world to quaternary Al-Si-Cu-Mg alloys is constantly increasing. This interest is due not only to the high castability, but above all to the expected higher mechanical properties in comparison to the traditional Al-Si-Mg alloys, especially after prolonged exposure at high temperature.

The first research activity was therefore addressed to the microstructural and mechanical characterization of two Al-Si-Cu-Mg alloys, employed for automotive engine components: A354 alloy (Al-Si9-Cu1.5-Mg0.4) and C355 alloy (Al-Si5-Cu1-Mg0.4). The effect of chemical composition, solidification conditions (SDAS, microstructural fineness), secondary phases (intermetallic particles) and heat treatment conditions on tensile and fatigue behavior of both the alloys was evaluated. This research activity was carried out in the framework of a collaboration with the Department of Mechanical Engineering of Jönköping University (JTH), Sweden, under

the supervision of Prof. Salem Seifeddine. Experimental work and results are described in Par. 2.1 and 3.1, respectively.

- **PART 2 - Optimization of A354 heat treatment**

Heat treatment parameters employed for A354 alloy in the previous research activity derived from industrial practice and were not optimized. Aiming to exploit the potential of the A354 alloy, a dedicated research activity has been addressed to the study of solution heat treatment and aging of this alloy. In particular, the aim of the work was the determination of heat treatment parameters ensuring the maximization of the strength properties (HB, UTS, YS), by keeping at a minimum temperature and time of treatment. Solution and artificial aging parameters were studied by thermal and microstructural analyses, as well as by hardness tests. Tensile tests were then carried out to evaluate the differences between the new proposed heat treatment and the standard. Experimental work is described in Par. 2.2, while results are reported in Par. 3.2.

- **PART 3 - Mo addition to Al-Si-Cu-Mg alloys**

Among the possible alloying elements to increase the mechanical properties of Al-Si alloys at high temperature, poor attention has been devoted so far to molybdenum. Only a few works are found in the literature[1,2], indicating this element as a good candidate for increasing properties of cast aluminum alloys at elevated temperature. The main results on this research field were reported and summarized in Chapter 1. Molybdenum, as a result of the investigation of Farkoosh et al.[1,2] carried out on Al-Si7-Cu0.5-Mg0.3 alloy, is thought to promote the formation of thermally stable dispersoids, thus allowing to maintain good level of UTS, YS and elongation to failure even after prolonged exposure at high temperature (i.e. after 100 h at 300 °C), as well as to increase creep resistance in comparison to the base alloy.

In this framework, a research activity was aimed at the preliminary evaluation of molybdenum addition effect on the mechanical behavior of the A354 alloy. A354 alloy castings with different Mo contents (up to 0.8 wt %) were produced; as a result of a first research phase, 0.3 wt.% Mo composition was chosen as the most promising for heat treatment study and tensile characterization, carried out in the second research phase. Casting parameters were also optimized aiming to enhance the chemical

homogeneity of the produced castings. Experimental work and results are summarized in Par. 2.3 and 3.3, respectively.

2.1 Experimental procedure – PART 1

Characterization of Al-Si-Cu-Mg alloys

2.1.1 SAMPLES PRODUCTION

C355 and A354 alloys samples were produced at JTH facilities[1], using commercially available alloys. Both the alloys were melted in a resistance furnace at 710 °C; Ti and B were added as refiners, while Sr was added in the form of Al-Sr10 master alloy aiming to spherodize the eutectic silicon structure. Different quantities of Sr were added to the alloys, in view of the different Si content: 200 ppm and 250 ppm to C355 and A354 alloys, respectively. A copper die pre-heated at 200 °C was used for casting the alloys. Chemical composition of the cast C355 and A354 alloys was then evaluated through a mass spectrometer (Table 2.1).

Table 2.1. Chemical composition (wt.%) of the Sr-modified and refined C355/A354 alloys

	Si	Cu	Mg	Fe	Mn	Ti	B	Sr	Al
C355	4.99	1.050	0.470	0.138	0.021	0.133	0.001	0.0212	Bal.
A354	8.47	1.570	0.444	0.135	0.001	0.126	<0.0002	0.0240	Bal.

A gradient solidification equipment was then used to remelt the bars, aiming to produce samples with predetermined SDAS values. The equipment, exploiting the close relation SDAS-solidification time, and whose detailed description can be found elsewhere[3], works by holding the samples at high temperature (710 °C) until fully melting, and protecting the alloy from oxidation by an Ar gas shield. Specimens were maintained at 710 °C for 30 min. While the aluminum samples stay in a fixed position, the furnace can be raised at a prescribed speed. As a result, different microstructures can be obtained by simply changing the speed of the heating element and the cooling medium as well, thus obtaining different solidification rates.

[1] Specimens for tensile and fatigue characterization were produced at Jönköping University (JTH) at the Materials and Manufacturing, Department of Mechanical Engineering, in the framework of students Master Thesis, under the supervision of Prof. Salem Seifeddine.

In this work, two different values of furnace speeds were employed, namely 0.3 mm/s for the fine microstructure and 0.03 mm/s for the coarse one, corresponding to expected SDAS values of 20-25 μm (typical of die casting) and 50-70 μm (typical of sand casting), respectively. As concerning the cooling medium, air and water for coarse and fine SDAS specimens were used, respectively. Before heat treatment. samples were subjected to hot isostatic pressing (HIP), in order to eliminate internal porosity and shrinkage. Treatment parameters (temperature and pressure) are not exactly known, being a proprietary cycle (Densal® HIP). Holding temperature is however close to 490 °C. After HIP, samples were heat treated according to the parameters reported in Table 2.2. It must be pointed out that C355 alloy was subjected to an optimized T6 heat treatment, as a result of previous studies carried out by Metallurgy group. On the contrary, A354 alloy was heat treated following industrial standards, therefore using not optimized parameters. Anyway, for an easier understanding of the text, both the alloys in the heat treated condition will be hereafter indicated as "HT". Some samples were subjected to overaging (abbreviated as "OA") after heat treatment, as indicated in Table 2.3.

Table 2.2. Heat treatment parameters employed for C355 and A354 alloys

	C355	**A354**
solution treatment	530 °C - 24 h	515 °C - 10 h
quench	water - 60 °C	water - 60 °C
pre-aging	~25 min.	~25 min.
aging	180 °C - 6 h	210 °C - 6 h

Table 2.3. Overaging parameters for C355 and A354 alloys

	C355 - A354
Overaging	210 °C - 41 h

2.1.2 MICROSTRUCTURAL CHARACTERIZATION

C355 and A354 samples for microstructural characterization were obtained from tensile and fatigue specimens. Samples were prepared in a different manner depending on the aim. Metallographic preparation of samples for microstructural analyses (OM-SEM) and SDAS calculation was carried out according to ASTM E3-01[4], by etching the grinded and

polished specimens with 0.5% HF solution. On the other hand, samples for grain size measurement (carried out only on fatigue specimens) were etched using a double stage procedure, proposed by Rodriguez et al.[5] for microstructural analyses of Al-Si-Cu-Mg alloys, consisting of (i) 3 min immersion in a solution of 10 ml of phosphoric acid in 100 ml of distilled water, (ii) 10 s immersion in a solution of 2 g of sodium hydroxide and 8 g of potassium permanganate in 200 ml of distilled water.

The microstructure of the alloys was studied through optical microscopy (OM); image analyses was carried out using the ®Image Pro-Plus software to calculate the average SDAS value. Due to the different microstructural coarseness, optical micrographs at 25x and 50x magnifications were used to measure SDAS of coarse and fine specimens, respectively. Grain size was measured on fatigue specimen immediately after etching with the *linear intercept method* according to ASTM E112[6], by elaborating optical micrographs taken under polarized light.

The chemical composition of intermetallics was studied by scanning electron microscopy equipped with energy dispersive spectroscopy (SEM-EDS). Different microstructural features related to intermetallic compounds (average aspect ratio, average particle area and maximum size) were calculated on SEM micrographs through contrast image analysis on both HT and OA samples. In view of the different microstructural coarseness, the investigated area was normalized: 14 fields at 500X and 16 fields at 1500X were processed for coarse and fine SDAS microstructure, respectively. Aiming to assess possible variations in morphology and size of intermetallic precipitates induced by overaging, STEM analyses were also performed. These analyses were carried out at Linköping facilities, by Prof. Salem Seifeddine and Prof. Sten Johansson. STEM samples were prepared by electrolytic polishing in a Struers Tenupol 5 jet polishing equipment, using an electrolyte with 33% nitric acid in methanol. The thin foils were studied in a Hitachi SU70 at 30kV using a STEM detector. It should be mentioned that only fine SDAS samples, both of C355 and A354 alloy were analyzed through STEM microscopy.

2.1.3 TENSILE AND HARDNESS TESTS

C355 and A354 alloys were characterized in terms of hardness and tensile properties. Brinell hardness measurements were carried out according to ASTM E10-08 standard [7], employing a load of 62.5 kg and a 2.5 mm diameter steel ball (HB10 scale). Tensile specimens with round dog-bone shape (Figure 2.1) were machined from the hipped and treated bars (L_0=25mm and gauge diameter d_0=5 mm). Tensile tests were carried out both

at room and high temperature (200 °C) according to ISO standards at 5 MPa s^{-1} stress rate[8,9], using a servo-hydraulic testing machine equipped with a resistance furnace and an extensometer for high temperature testing. As concerning high temperature tests, the samples were maintained inside the furnace for 20 minutes at 200 °C before running the test. Testing conditions (microstructure of the tested samples, heat treatment condition and test temperature) are summarized in Table 2.4. SEM-EDS analyses were then carried out on fracture surfaces of the tested specimens, aiming to evaluate the failure mechanisms.

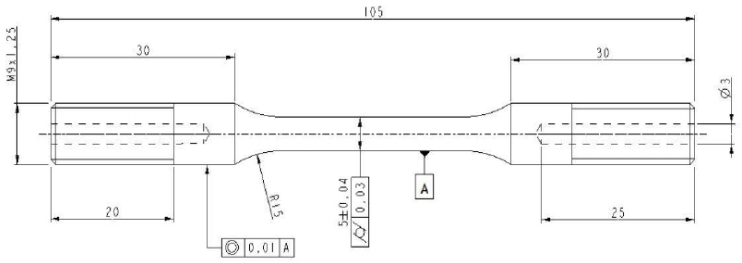

Figure 2.1. Tensile specimen geometry, dimensions in mm.

Table 2.4. Tensile testing conditions investigated on both C355 and A354 alloys.

Microstructure	Heat treatment condition	Tensile testing temperature
Fine SDAS	HT	Room T (RT)
	OA	
	HT	200 °C (200)
	OA	
Coarse SDAS	HT	Room T (RT)
	OA	
	HT	200 °C (200)
	OA	

2.1.4 FATIGUE TESTS

Fatigue specimens, whose shape and dimensions are shown in Figure 2.2, were machined from the treated bars. Rotating bending fatigue tests were carried out according to UNI 3964[10], using the *stair-case* method, at a frequency of 50 Hz, R=-1. The maximum number of cycles was set to $2x10^6$ (run-out condition). Fatigue tests were carried out at room temperature on the T6 heat-treated alloys and at 200 °C on the overaged (OA) alloys.

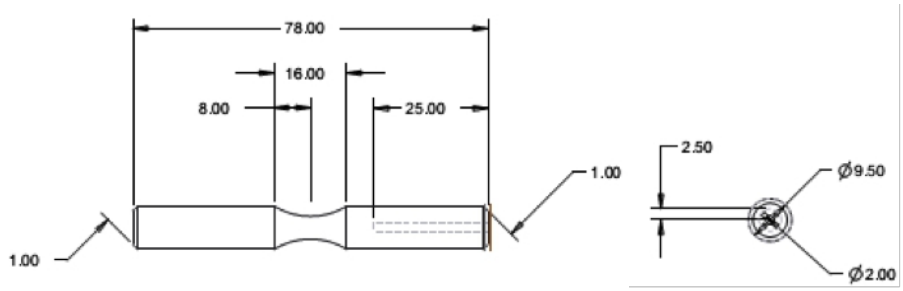

Figure 2.2. Fatigue specimen geometry, dimensions in mm.

For the high temperature fatigue tests, samples were maintained in the heating furnace for 2 h before applying the load, in order to reach a steady state thermal condition. Fatigue testing conditions (microstructure of the tested samples, heat treatment condition and test temperature) are summarized in Table 2.5.

Table 2.5. Fatigue testing conditions investigated on both C355 and A354 alloys.

Microstructure	Heat treatment condition	Fatigue testing temperature
Fine SDAS	HT	Room T (RT)
	OA	200 °C
Coarse SDAS	HT	Room T (RT)
	OA	200 °C

SEM-EDS analyses were then carried out on fracture surfaces of the tested specimens, aiming to investigate crack nucleation sites and to study propagation and final failure areas.

2.2 Experimental procedure – PART 2

Optimization of A354 heat treatment

2.2.1 SAMPLES PRODUCTION

Samples for heat treatment optimization of A354 alloy were produced from commercial ingots at Bologna University facilities. The alloy was melted in an induction furnace at 750 °C. Al-Sr10 master alloy was added in order to modify the eutectic structure, in such a quantity to have a Sr concentration of 300 ppm in the A354 melt. A slightly higher quantity of Sr was added in comparison to the casting for mechanical characterization (as described in Par. 2.1) due to the different stirring system employed, thus to avoid possible unmodified zones in the casting. In this experimental activity, in fact, a combination of electromagnetic and mechanical stirring system was used. The melt was then poured in a permanent steel die, pre-heated at 200 °C, and coated with boron nitride spray, aiming to prevent from Fe contamination at the interface between casting and die. Cylindrical bars for experimental activities were cut from the cast ingots. A354 alloy composition was verified through Glow Discharge Optical Emission Spectroscopy (GDOES). Results of chemical analyses are reported in Table 2.6. SDAS was calculated through image analyses on optical micrographs.

Table 2.6. Chemical composition of A354 alloy measured by GDOES (wt.%).

Si	Cu	Mg	Fe	Mn	Ti	Sr [ppm]	Al
8.608	1.746	0.467	0.113	0.003	0.122	88	Bal.

2.2.2 HEAT TREATMENT OPTIMIZATION

The optimization criteria adopted for the present research work was to identify treatment conditions that maximize hardness of the alloy, while keeping at a minimum treatment time and temperature. Samples for studying T6 heat treatment (small blocks of about 10x10x6 mm^3) were obtained from the cast bars.

A multiple stage solution treatment was studied, requiring thermal analyses to define temperatures and time of treatment.

Experimental activities were carried out in the following steps:

i) *1st Solution stage optimization*
ii) *2nd Solution stage optimization*
iii) *Artificial aging optimization*

i. The presence of eutectic phases, which could lead to localized melting during solution treatment, was evaluated through differential thermal analysis (DTA). The analyses were carried out on as cast material in Ar gas from room temperature to 700 °C, at a heating rate of 10°C/min. From the analysis of the eutectic reaction peak, the first solution treatment stage temperature was determined. On the basis of this result, A354 as-cast samples were solution treated at the identified temperature from different times (from 30 min to 6 h). The first stage of solution treatment was meant to eliminate the low melting peak through dissolution. Further DTA analyses were therefore carried out on the solution treated samples, aiming to evaluate the minimum time required for the homogenization and dissolution of the low melting eutectic phase, thus allowing to completely define the first stage parameters.
Brinell indentations were carried out on the solution treated samples, after quenching in water at 60 °C and artificial aging (200 °C – 2 h). These not optimized parameters were chosen to highlight differences in hardness induced by different solution temperatures and times. Hardness on the as-cast material was measured as well, for comparison. As concerning quench condition, at this experimental stage the same parameters adopted in commercial standard treatment (60 °C water) were used.

ii. A new set of samples was solution treated as defined in the previous research phase, then the temperature was raised to 515 or 530 °C. These values were chosen to cover, in a conservative way, the whole temperature range between the first stage temperature and the occurrence of the melting peak of the alloy. The second stage was carried out both at 515 and 530 °C for 2, 4, 6 and 8 h. Also in this case, to evaluate the hardness increase induced by different temperatures and times, samples were quenched in hot water (60 °C) and then aged at 200 °C – 2 h. Contrast image analyses was carried out on SEM micrographs, as described in Par. 2.1.2, to evaluate the evolution of the average area fraction covered by intermetallic particles with solution treatment.

iii. Next step in the heat treatment optimization of A354 was the study of artificial aging. In order to draw aging curves, samples were solution treated at the optimized conditions,

quenched in hot water (60 °C), then artificially aged at 160, 180, 190, 200 and 210 °C from 1 to 48 h. At predetermined time intervals, samples were extracted from the furnace and subjected to hardness measurement (HB10 scale). Optimal aging parameters (time/temperature) were defined as the ones allowing to maximize the hardness of the alloy, while preventing from the occurrence of overaging, at the same time.

2.2.3 OVERAGING BEHAVIOR EVALUATION

Once the optimal T6 heat treatment conditions were defined, the samples were subjected to further aging, aiming to evaluate the influence of temperature and time on coarsening of strengthening precipitates. Three temperature levels were chosen, namely 200, 245 and 290 °C. Soaking at these temperature was carried out from 1 h (10 min in the case of the highest temperature, 290 °C) to 168 h. Samples extracted from the furnace at prefixed times allowed to obtain overaging curves, representing the variation of hardness with soaking time. A354 overaging behavior was then compared to:

- A354-HT alloy (treated as described in Par. 2.1, therefore not optimized);
- C355-HT alloy (the overaging was carried out on C355 alloy in the non-optimized heat treatment condition; the curves were in fact obtained during past research activities carried out by Metallurgy group; initial hardness is in fact 115 HB, vs. 125 HB characterizing the optimized heat treatment);
- A356-T6 alloy (Al-Si-Mg alloy, treated at the peak aging condition), data were obtained from a past research activity carried by Metallurgy Group.

In all these research phases, HB10 measurements were taken on investigated samples, as previously described.

2.2.4 MICROSTRUCTURAL CHARACTERIZATION

To evaluate microstructural evolution during solution treatment (dissolution of intermetallic particles or their partial modification, eutectic silicon spherodization, etc.) both solution treated and aged samples were observed through Optical Microscopy (OM) and Scanning Electron Microscopy equipped with Energy Dispersive X-ray Spectroscopy (SEM-EDS). Metallographic preparation was carried out according to ASTM E3-01[4], by etching the grinded and polished specimens with 0.5% HF solution.

2.2.5 TENSILE TESTS

For comparison, the same testing procedures described in section 2.2.2 were adopted. Tensile samples were subjected to the optimized T6 heat treatment (summarized in Table 2.7). Part of them were subsequently overaged (OA) at 210 °C for 50 h. Tensile tests were carried out at room temperature both in the T6/HT condition and in the overaged condition. In this regard, the scope was to compare mechanical behavior of A354-T6 and A354-HT alloys at equal residual hardness (supposed to be reached after 50 h at 210 °C, on the basis of overaging curves presented in Chapter 3.2). In such a way, it was possible to investigate if, after a longer overaging, A354-T6 would have maintained the same mechanical properties of A354-HT. Testing conditions (heat treatment condition and test temperature) are summarized in Table 2.8.

Table 2.7. Optimized heat treatment parameters (T6) used for mechanical characterization

	A354
1st stage solution treatment	495 °C - 6 h
2nd stage solution treatment	515 °C – 2 h
quench	water - 60 °C
aging	180 °C - 6 h

Table 2.8. Tensile testing conditions

Heat treatment condition	**Tensile testing temperature**
T6	Room T (RT)
OA	Room T (RT)

Fracture surfaces of the tensile specimens were analysed through SEM, in order to evaluate the failure mechanisms in relation to the microstructure.

2.3 Experimental procedure – PART 3

Mo addition to Al-Si-Cu-Mg alloys

2.3.1 CASTINGS PRODUCTION

A first research phase was aimed to the set-up of casting process for the production of ingots of A354 alloy characterized by different Mo contents. A354 alloy was melted in an induction furnace at 800°C. Sr (300 ppm) was added to modify eutectic Si. Molybdenum was added in form of Al-Mo10 master alloy, in proper quantity to produce castings with the following Mo target content: 0.1, 0.3, 0.5, 0.8 wt%. The melt was processed through electromagnetic stirring. The melt was then poured in a permanent steel die, pre-heated at 300 °C, and coated with boron nitride spray, for avoiding iron contamination of the casting. Chemical compositions of the castings were analysed through Glow Discharge Optical Emission Spectroscopy (GDOES). On the basis of the obtained chemical composition, different casting parameters were employed for the production of ingots for successive research phases (as will be discussed in Chapter 3). In particular, aiming to induce better homogenization of the melt and to foster Mo diffusion, the A354 alloy was brought to 900 °C and maintained at this temperature for 30 min; subsequently, the temperature was decreased at 20 °C steps every 10 min until 800 °C, then the molten metal was cast. Only ingots of A354 alloy containing 0.3 wt% of Mo (hereafter referred to as A354-0.3Mo) were produced for further characterization, in view of the results of preliminary studies on overaging response after solution treatment.

2.3.2 HEAT TREATMENT STUDY

Aiming to evaluate the strengthening effect of Mo, the solution treatment phase was studied. Double stage solution treatment was adopted, aiming to dissolve the low melting compound previously identified in the A354 alloy. The occurrence of the same reaction was confirmed by differential thermal analyses (DTA) carried out on the as cast A354-0.3Mo alloy. A first solution step was therefore carried out at 495 °C for 6 h; while , at first, the second step was performed at 540 °C for 1 h in view of literature results[1]; the second step was meant to (i) further dissolve Cu and Mg based intermetallic particles and (ii) promote the formation of Mo-based dispersoids, which should occur during high

temperature solution treatment[1]. Overaging of alloys containing Mo from 0.1 to 0.8 wt.% was investigated, in three different post-solution treatment conditions: (i) air cooling, (ii) water quench at 60 °C, (iii) artificial aging at 180 °C – 4 h after 60 °C water quench. Samples were then overaged at 245 °C for times up to 300 h. Then, in order to assess the variation of hardness during solution treatment and evaluating the presence of stable dispersoids formed during solution, samples of A354-0.3Mo (the selected composition) were solution treated at 495 °C – 6 h, then subjected to a second step at 540 °C for different times, up to 24 h. Two cooling media from solution temperature were adopted: (i) air cooling and (ii) water quench at 60 °C. HB10 Brinell hardness was then measured to draw solution hardness curves.

2.3.3 MICROSTRUCTURAL CHARACTERIZATION

Microstructure of the produced castings was analysed through Optical Microscopy (OM) and Scanning Electron Microscopy equipped with Energy Dispersive X-ray Spectroscopy (SEM-EDS). The aim of the analyses was (i) to evaluate the influence of Mo addition on the formation of coarse intermetallic phases in the as cast microstructures; (ii) to identify possible segregation areas, (iii) to evaluate qualitatively the tendency of the different intermetallic particles to dissolution upon solution treatment. Metallographic preparation was carried out according to ASTM E3-01[4], by etching grinded and polished specimens with 0.5% HF solution. The analyses were carried out on the A354-0.3Mo alloy, in the as-cast condition and after solution treatment (540 °C – 1 h, 540 °C – 24 h). Contrast image analyses was carried out on SEM micrographs, as described in Par. 2.1.2, to evaluate the evolution of the average area fraction covered by intermetallic particles with solution treatment.

2.3.4 MECHANICAL BEHAVIOR

Preliminary tensile tests were carried out on A354-0.3Mo alloy following the same testing procedure described in Paragraph 2.1.3. Tensile samples were subjected to T6 heat treatment, whose parameters (identified as a result of the previous research phases) are reported in Table 2.9; after solution treatment, both water quench at 60 °C and air cooling conditions were used. All the samples were artificially aged. Samples for high temperature tensile testing were also subjected to overaging at the testing temperature (250 °C) for 100

h. For comparison, A354 alloy, processed and heat treated at the same manner of A354-0.3Mo, was tested as reference. Tensile testing conditions are summarized in Table 2.10.

Table 2.9. Optimized heat treatment parameters (T6) used for mechanical characterization of A354-0.3Mo and A354 alloys.

1st stage solution treatment	495 °C - 6 h
2nd stage solution treatment	540 °C – 1 h
quench	water - 60 °C
	air cooling
aging	180 °C - 6 h

Table 2.10. Tensile testing conditions

Heat treatment condition	Tensile testing temperature
T6	Room T (RT)
OA (T6+OA 250 °C-100 h)	250 °C (250)

Fracture surfaces of the tensile specimens were analyzed through SEM, in order to evaluate the failure mechanisms in relation to the microstructure.

REFERENCES – CHAPTER 2

[1] A. R. Farkoosh, X. G. Chen, M. Pekguleryuz, *Mater. Sci. Eng. A* **2015**, *620*, 181.

[2] A. R. Farkoosh, X. G. Chen, M. Pekguleryuz, *Mater. Sci. Eng. A* **2015**, *627*, 127.

[3] S. Seifeddine, Characteristics of Cast Aluminium–silicon Alloys: Microstructures and Mechanical Properties, Linköping studies in science and technology: Dissertations, **2006**.

[4] *ASTM E3-01 Standard Practice for Preparation of Metallographic Specimens*, ASM International, **2007**.

[5] A. Rodríguez, R. Torres, J. Talamantes-Silva, E. Velasco, S. Valtierra, R. Colás, *Mater. Charact.* **2012**, *68*, 110.

[6] *ASTM E112-13 Standard Test Methods for Determining Average Grain Size*, **2013**.

[7] *ASTM E 10-08 Standard Test Method for Brinell Hardness of Metallic Materials*, ASM International, **2007**.

[8] *ISO 6892-1:2009, Metallic Materials - Tensile Testing - Part 1: Method of Test at Room Temperature*, **2009**.

[9] *ISO 6892-2:2011, Metallic Materials - Tensile Testing - Part 2: Method of Test at Elevated Temperature*, **2011**.

[10] *UNI 3964 – 85, Mechanical Testing of Metallic Materials Fatigue Testing at Room Temperature*, **1985**.

CHAPTER 3

RESULTS AND DISCUSSION
AL-SI-CU-MG ALLOYS

In this chapter, the main results obtained from the experimental activities described in Chapter 2 will be presented and discussed. The hereafter described research activities resulted mainly in the following publications:

- **"Effect of microstructure and overaging on the tensile behaviour at room and elevated temperature of C355-T6 cast aluminum alloy"**, L. Ceschini, Al. Morri, An. Morri, S. Toschi, S. Johansson, S. Seifeddine; *Materials and Design, Vol. 83C, 2015, 626-634.*
- **"Microstructural and mechanical properties characterization of heat treated and overaged cast A354 alloy with various SDAS at room and elevated temperature"**, L. Ceschini, Al. Morri, S. Toschi, S. Johansson, S. Seifeddine, *Materials Science and Engineering: A, Vol. 648, 2015, 340–349*
- **"Room and high temperature fatigue behaviour of the A354 and C355 (Al-Si-Cu-Mg) alloys: role of microstructure and heat treatment"**, L. Ceschini, Al. Morri, S. Toschi, S. Seifeddine, *Materials Science and Engineering A, Vol. 653, 2016, 129–138*

The complete list of publications and conference proceedings is reported in the Appendix.

3.1 Results and Discussion – PART 1

Characterization of Al-Si-Cu-Mg alloys

3.1.1 MICROSTRUCTURAL ANALYSIS

Both C355 (Al-Si5-Cu1-Mg0.4) and A354 (Al-Si9-Cu1.5-Mg0.4) alloys are characterized by a typical hypoeutectic microstructure, consisting of α-Al dendrites surrounded by the eutectic structure. Representative optical micrographs of C355-HT and A354-HT alloys, with fine and coarse microstructures, are shown in Figure 3.1. At a macroscopic comparison, the two alloys present a different quantity of eutectic phase, due to the different Si content, about 5 and 9 wt.% for C355 and A354 alloys, respectively. At the same magnification, it is also possible to observe the different microstructural coarseness between fine (Figure 3.1a,c) and coarse (Figure 3.1b,d) SDAS samples.

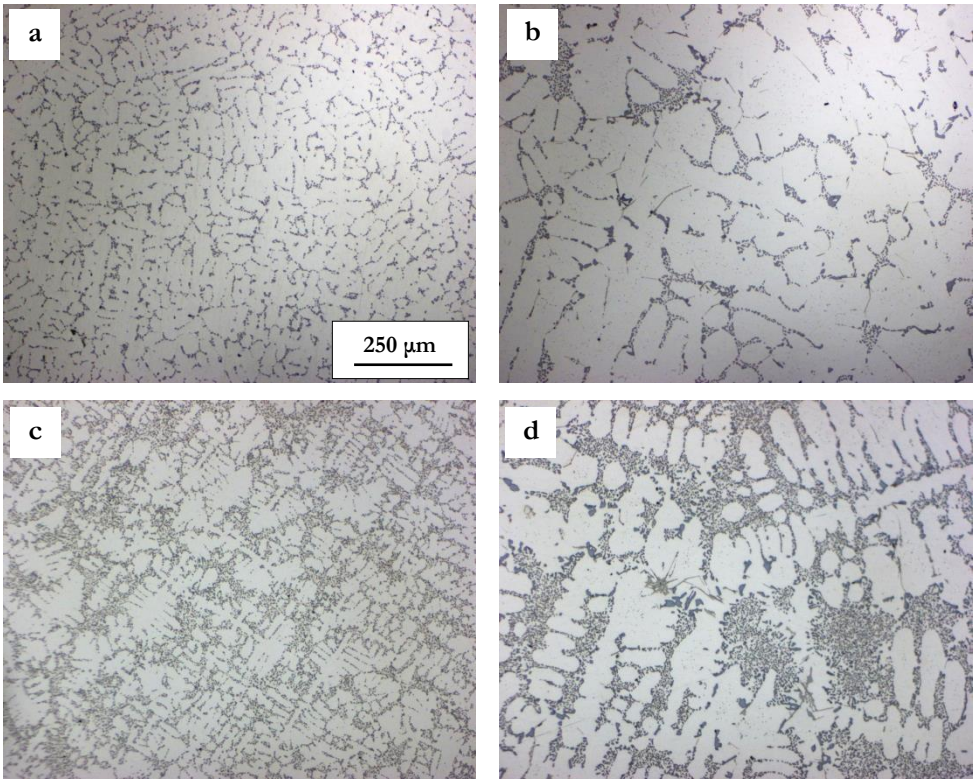

Figure 3.1. Optical images at the same magnification of C355-HT fine (a) and coarse (b) SDAS specimens, A354-HT fine (c) and coarse (d) SDAS specimens.

As expected, neither in C355 alloy, nor in the A354, appreciable differences were observed by optical microscopy between heat-treated and overaged samples. Soaking at 210 °C for

41 h influences the morphology of strengthening precipitates (as will be discussed in the next paragraphs) at the nanometric scale but it does not induce microstructural modifications that can be appreciated by OM. SDAS was calculated in all the tested alloys; the results well corresponded to the expected, nominal ranges. Results are summarized in Table 3.1. Overaged samples were characterized by similar SDAS values than heat-treated ones, as expected.

Table 3.1. Measured SDAS values on C355 and A354 samples for tensile and fatigue testing

		Fine SDAS [μm]	**Coarse SDAS [μm]**
Tensile samples	**C355**	24±1	64±0
	A354	20±2	44±3
Fatigue samples	**C355**	20±2	66±5
	A354	22±2	51±3
		Nominal 20-25[μm]	**Nominal 50-70[μm]**

Grain size of the alloys was evaluated by image analyses. As expected, both A354 and C355 fine SDAS samples were characterized by smaller grain size than the coarse ones, as summarized in Table 3.2. It is well known, in fact, that grain size is strongly related to solidification rate, as well as on the amount of refining elements, such as Ti and B. In this regard, it should be pointed out that, at a comparable SDAS range, A354 samples presented larger grain size (about two folds) in comparison to C355 alloy, as shown in Table 3.2.

Table 3.2. Grain size measured on fatigue samples of A354 and C355 alloys.

Alloy	**SDAS**	**Grain Size [μm]**
A354	Fine	875±144
	Coarse	1664±260
C355	Fine	454±82
	Coarse	1056±182

This difference should be related to the lower amount of Ti and B contained in A354 alloy, as shown in Table 2.1, but also to the effect of Si content on grain size. As reported in the literature, in fact, an increase of the Si content beyond 5 wt% may lead to grain coarsening[1–3]. Eutectic silicon was correctly modified, both in fine and coarse microstructures of the two alloys, characterized by fibrous eutectic Si particles.

Nevertheless, some partially unmodified areas were found in coarse microstructures of both A354 and C355 alloys (Figure 3.2). As fine and coarse SDAS samples contain the same Sr quantity, it should be inferred that, as reported by different investigators on Al-Si alloys[4,5], solidification rate plays a role on eutectic modification. Even if it is known that the effect of solidification rate on eutectic modification in Sr-modified alloys is less relevant in comparison to unmodified alloys[5], Si particles are generally refined by an increase of the cooling rate, changing their morphology from large plates to fine fibers. Further, it is worth noting that unmodified coarse Si particles were mostly adjacent to α-Al dendrites. As observed by Sjölander et al.[6], this could be related to back diffusion of silicon during cooling from the dendrites to the pre-existing eutectic particles.

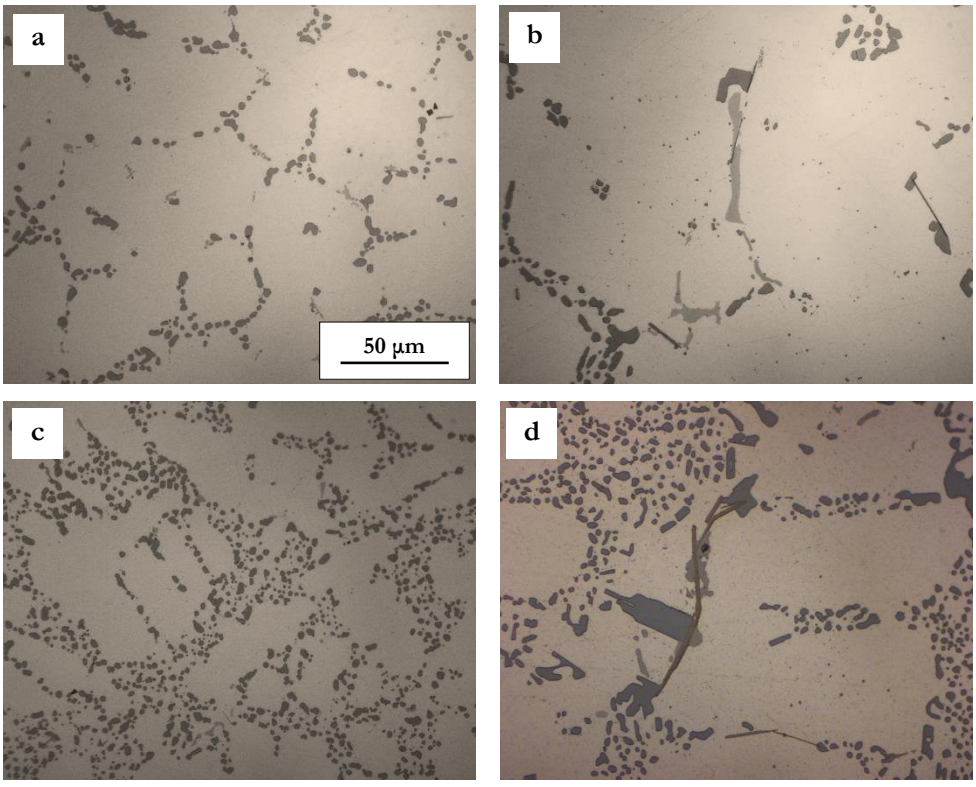

Figure 3.2. Optical images showing the morphology of eutectic Si particles in C355 alloy (a) fine and (b) coarse SDAS samples, and A354 alloy (c) fine and (d) coarse SDAS samples.

The core of microstructural analyses was focused on the observation and identification of large intermetallic particles formed during solidification. It is well known that not only alloying elements strongly influence composition and morphology of intermetallic particles, but also solidification rate plays an important role, especially on the size of intermetallic compounds[7]. SEM analyses revealed the effect of different solidification rates on intermetallics distribution in A354 and C355 alloys. SEM micrographs were elaborated and subjected to contrast image analyses (Figure 3.3) to highlight intermetallics features.

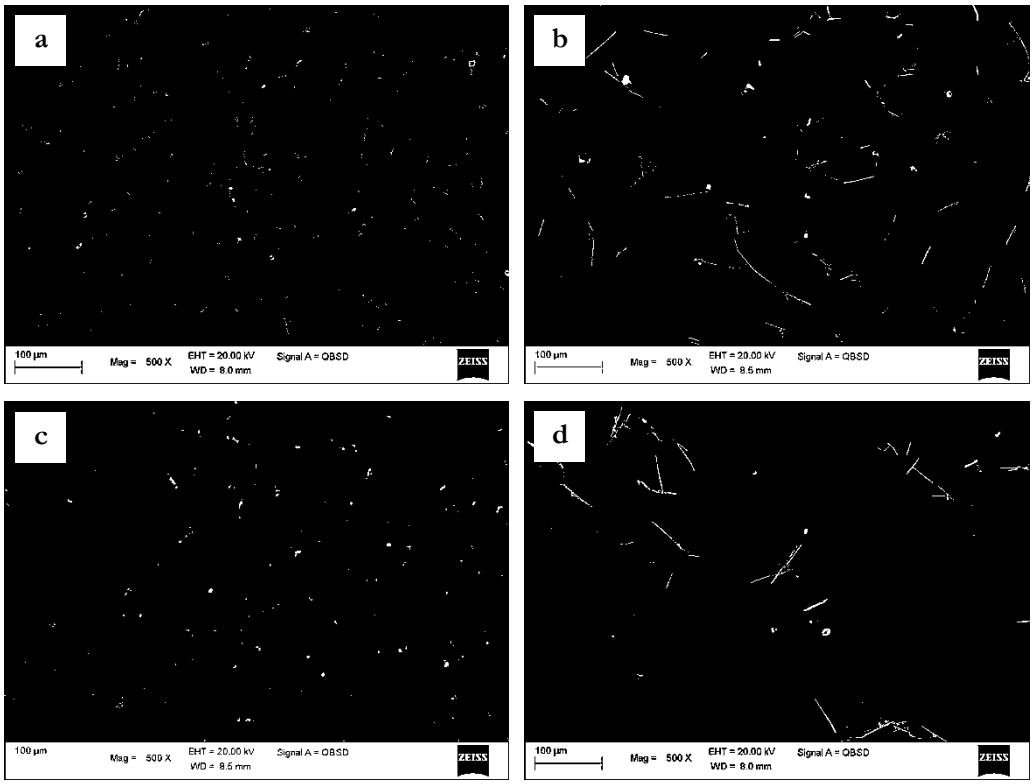

Figure 3.3. Contrast elaboration of SEM images of C355 (a) fine and (b) coarse SDAS samples, A354 (c) fine and (d) coarse SDAS samples showing differences in morphology, size and distribution of intermetallic phases induced by different solidification rates.

Image analysis on SEM micrographs was carried out to relate the global average area fraction covered by the intermetallic particles to the solidification rate. From analyses results reported in Figure 3.4, in both C355 and A354 alloys, fine and coarse microstructures presented similar intermetallic area fraction. Consequently, it was inferred that solidification rate does not influence the global area covered by intermetallic particles. Further, from the comparison it is possible to observe that the average area fraction is slightly higher in the case of C355 alloy. The reason of this difference still remains unexplained. Anyway, due to its higher Cu content, the A354 alloy could contain a higher quantity of θ-Al_2Cu particles in the as cast state, which are known to easily undergo dissolution after solution treatment. As a result, after solution treatment, this could result in a decrease of the total intermetallic area fraction.

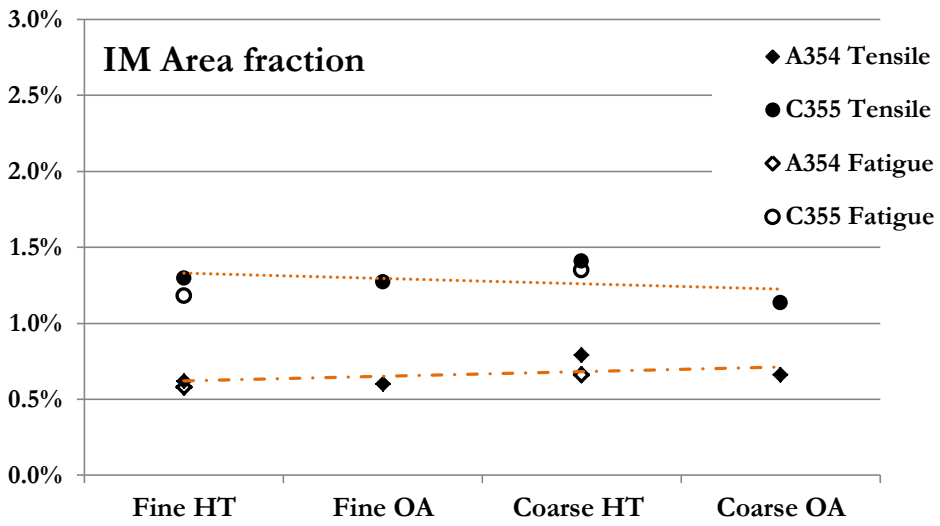

Figure 3.4. Average area fraction covered by intermetallic particles (IM) in heat treated (HT) and overaged (OA) fine and coarse A354 and C355 alloys.

Nevertheless, coarse microstructures were characterized by intermetallics with larger particle area, as depicted in Figure 3.5. Intermetallic particles, in fact, did not exceed 10 μm^2 of area in fine SDAS samples, whereas they ranged between 70 μm^2 and 100 μm^2 in coarse SDAS alloys. This could be related to the longer available time for growth in coarse microstructure. This kind of relationship has been reported also in different studies on Al casting alloys[4,8]. Interesting results were obtained also from the evaluation of the average intermetallic aspect ratio (Figure 3.6), which is strictly related to the particle morphology. A significant difference was reported between fine and coarse SDAS samples, both for C355 and A354 alloys: the average aspect ratio of particles contained in coarse microstructure was about three-fold the one measured in fine microstructure. Quasi-globular or slightly elongated particles were observed in fine samples (AR ≈ 1,7-3), while more elongated and acicular particles (AR ≈ 5.8-7.1) were observed in the coarse ones.

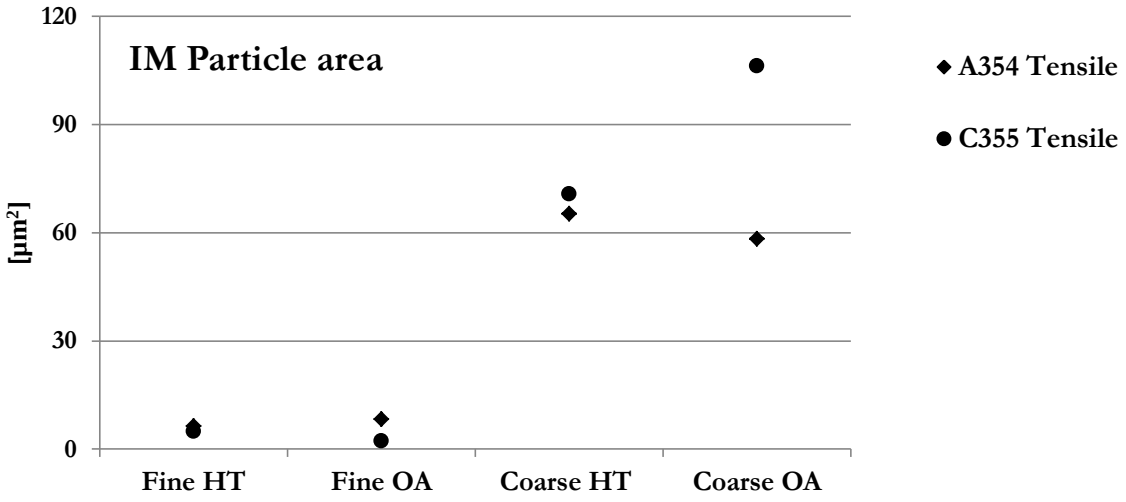

Figure 3.5. Average intermetallics (IM) particle area in heat treated (HT) and over-aged (OA) fine and coarse A354 and C355 tensile samples.

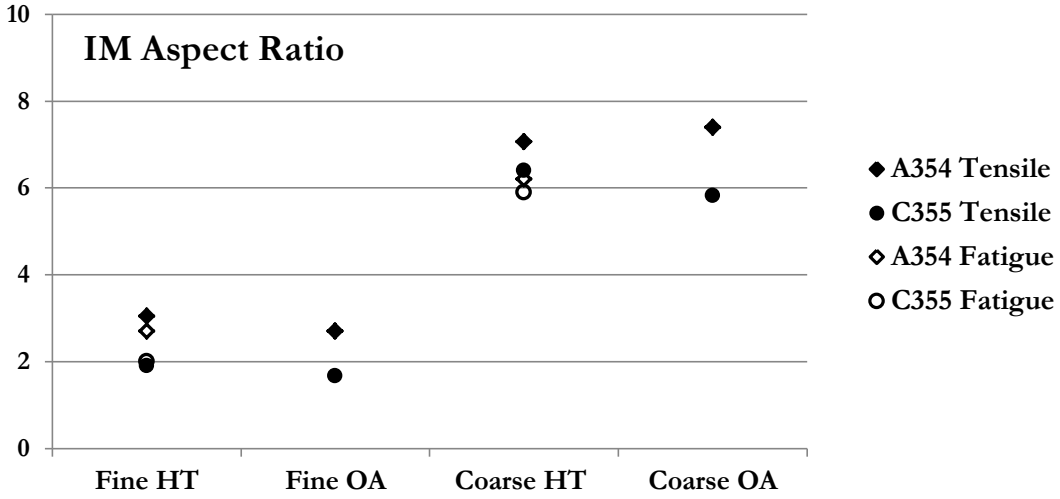

Figure 3.6. Average aspect ratio of intermetallic particles (IM) in heat treated and over-aged fine and coarse A354 and C355 on tensile and fatigue samples.

Table 3.3 summarizes the main intermetallic phases found on both fine and coarse C355/A354 samples. As a general observation, in both alloys no relevant difference was detected in the intermetallics composition between heat-treated and over-aged samples, either in fine or coarse SDAS samples. The main effect of soaking at 210 °C for 41 h is reflected on submicron precipitates, thus observable only at higher magnification, as will be discussed in the next paragraphs.

Table 3.3. Summary of the main intermetallic particles identified on A354 and C355 fine and coarse SDAS samples

C355		A354	
Fine	**Coarse**	**Fine**	**Coarse**
π-Fe	Q	π-Fe	π-Fe
β-Fe	π-Fe	β-Fe	Q
	β-Fe	Q	β-Fe
	(α-Fe)		(Al-Cu-Fe)

C355 fine samples contained mainly small blocky π-Fe ($Al_8Mg_3FeSi_6$) particles, about 10 μm in length. Typical acicular β-Fe particles (Al_5FeSi), about 10 μm in length, were also identified (Figure 3.7a). The same particles were observed also on A354 fine samples (Figure 3.7b). In both the alloys, also small particles containing Cu, Mn and even Ni besides Fe and Mg, were found. From the present analyses, the most relevant difference observed among the two alloys consisted in Q quaternary particles (whose most accepted composition is $Al_5Cu_2Mg_8Si_6$) found in A354 samples (Figure 3.7b). In order to explain this difference, two factors should be taken into account, namely (i) the different chemical composition of the two alloys, in particular the higher Cu content of A354 alloy if compared to C355 (1.5 vs. 1 wt.%), (ii) the different solution treatment parameters employed for the two alloys (especially the time, longer for C355 alloy: 530 °C - 24 h vs. 515 °C - 10 h). In view of the above, two hypothesis may be drawn to give an explanation to the different Q phase content: (a) no Q phases formed during solidification of fine C355 samples, due to the lower Cu content, or (b) the higher solution time (24 h vs. 10 h) employed for C355 with respect to A354, alloy may have taken into solution the Q particles present in the as cast microstructure. Aiming to solve this question, further microstructural analyses should be performed in the future on as cast C355 samples, processed with 0.3 mm/s furnace speed. The same intermetallic phases found in fine SDAS samples, were observed also in coarse microstructures, both in C355 and A354 alloys. Moreover, in C355 coarse SDAS samples also compact Q-$Al_5Cu_2Mg_8Si_6$ particles, often associated to β-Fe and occasionally to α-Fe phase ($Al_{15}(Fe,Mn)_3Si_2$), were observed. Similarly, several blocky Q phases nucleated in correspondence of elongated Fe-particles were found in A354 samples (Figure 3.7e,f).

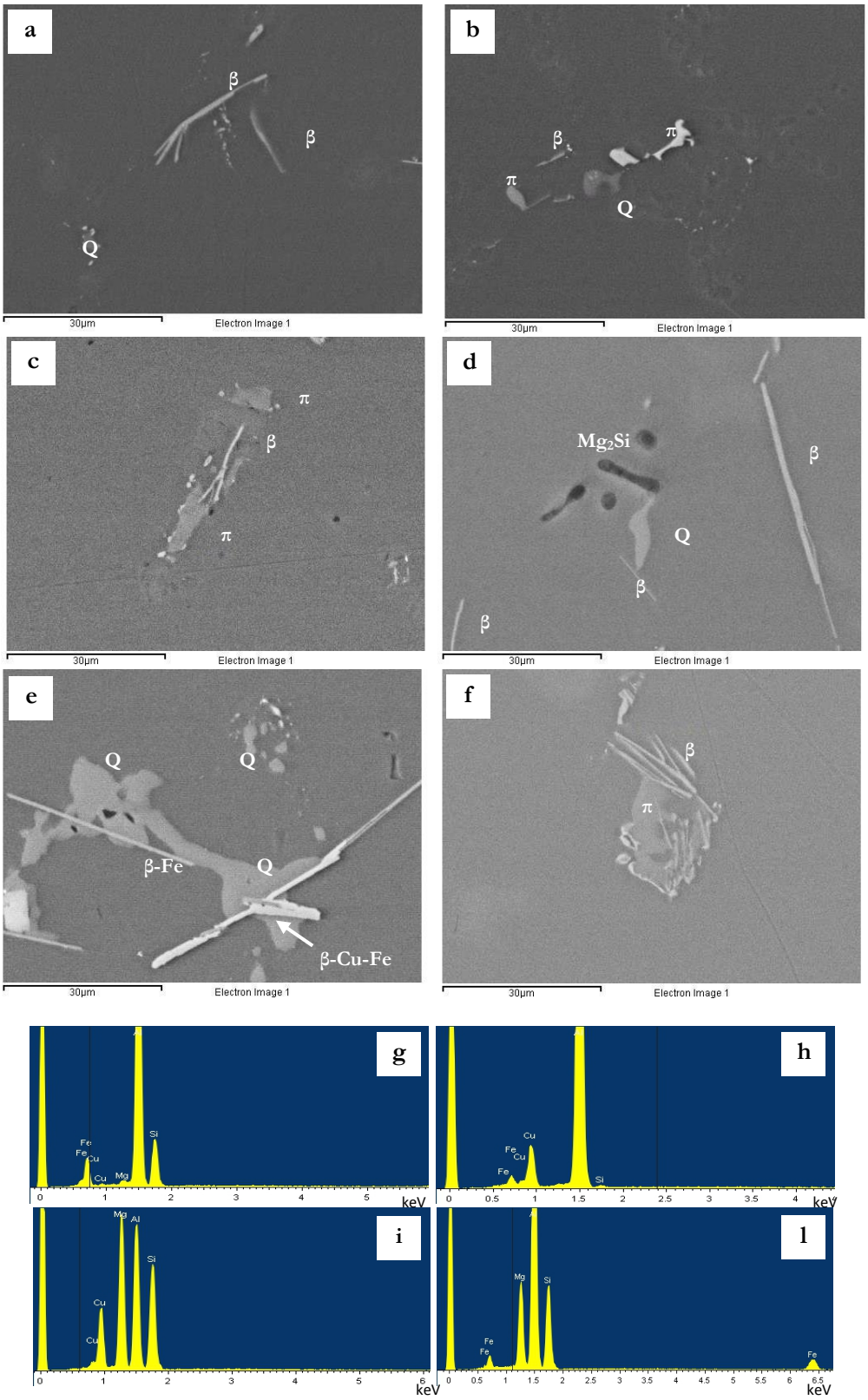

Figure 3.7. SEM images of coarse intermetallic particles formed during solidification, remained undissolved by solution heat treatment: (a) C355 fine SDAS, (b) A354 fine SDAS, (c,d) C355 coarse SDAS and (e,f) A354 coarse SDAS; EDS spectra of (g) β-Fe, (h) β-Cu-Fe, (i) Q and (l) π phases.

However, the most common phases detected by SEM-EDS in both C355 and A354 coarse samples were the needle-like Fe-based phases (Figure 3.7c-f). This finding well explains the higher value of average aspect ratio measured by image analyses on coarse specimens of A354 and C355 alloys, as reported in Figure 3.6. The remarkable effect of solidification rate on the size of acicular Fe-based particles between fine and coarse microstructure (Figure 3.3) is in accordance with different studies found in literature on Al-Si-Mg alloys[5,7]. EDS-analyses showed the presence of minor quantities of other alloying elements in elongated Fe-based phases, both in C355 and A354 alloys. β-Fe phases are known to contain also other alloying element as Mn, Cu and Mg, even though their most accepted chemical formula is Al_5FeSi[9]. Moreover, β-Fe phases transformation to π-Fe was reported in other works[10], for 0.35wt% addition of Mg. It should be however taken into account that EDS spot, due to the very small size of β-Fe phases, may have collected signals coming from the surrounding α-Al phase. Al-Cu-Fe elongated particles were often observed in coarse A354 samples, typically associated to Q and π-Fe phases (Figure 3.7e). In this regard, some studies reported also the transformation of β-Fe into Al_7FeCu_2 after solution treatment[11]. From the analyses of intermetallics contained in both the alloys, it is possible to infer that, as reported in the literature, the dissolution of Fe based particles (β-type, π-Fe) and Q-phases is particularly challenging and may require prolonged solution heat treatment times, as well higher solution temperatures[12]. Lastly, it is important to note that no θ-Al_2Cu phase was detected by SEM-EDS neither in fine nor in coarse SDAS samples of both the alloys. It is thought that this phase was dissolved by solution treatment, because (i) it is known to be present in as cast A354 alloy, from other experimental activities carried out in the present work (see Chapter 3.2) and (ii) it is known to easily undergo partial or total dissolution through solution heat treatment.

The strengthening precipitates morphology formed by heat treatment were observed through STEM microscopy (Figure 3.8). The analyses were meant mainly to evaluate, in both alloys, possible effects induced by overaging at 210 °C for 41 h. The analyses, carried out on fine SDAS samples, showed a fine and homogeneous precipitates distribution in the heat treated condition of both A354 and C355 samples (Figure 3.8a,e). On the contrary, coarsening of precipitates was observed in the overaged samples (Figure 3.8c,g). Relevant hardness decrease from the HT to the OA condition was in fact registered in both the alloys, as will be hereafter discussed. Differently, a lower effect on strengthening precipitates was induced by high temperature mechanical tests on heat treated and overaged samples[13], leading not to hardness variations (Figure 3.8b,f,d,h).

In A354 heat treated alloy, however, some of the precipitates (about 100 nm of maximum length) appeared darker and wider compared to the average morphology (Figure 3.8e). This observation, interpreted as a light precipitates coarsening effect, makes infer that the investigated aging treatment conditions (210 °C - 6 h) may lead to a partial overaging of the alloy. As previously explained in Chapter 2, heat treatment of A354 alloy has been extensively investigated in a dedicated research activity of the present PhD work, aiming to identify peak aging condition. Moreover, probably resulting from the combination of plastic deformation and high temperature, a slightly denser population of nano-sized dot-like precipitates was observed in tensile samples tested at 200 °C, in comparison to the ones tested at room temperature. A possible explanation is that precipitates growth and coarsening could have been stimulated during high temperature plastic deformation, as also observed by Kanesund[13]. Similarly, also in the overaged samples tested at high temperature, a higher quantity of fine rod-like precipitates was observed.

From the present investigations, the composition of heat treatment precipitates was not investigated, but further analyses will be addressed to understand whether if Al_2Cu, Mg_2Si, $CuAlMg_2$ or $Al_5Cu_2Mg_7Si_7$ phases are formed through heat treatment. Overaging was reported to induce coarsening of Al_2Cu precipitates[14]. Only Q phases were reported to be stable in a quaternary alloy with similar composition to that investigated in this work (Al-7Si-0.5Cu-Mg) after high temperature soaking, e.g. 300 °C[15]. Even if not widely accepted[15,16], the reason for the enhanced coarsening resistance of the Q phase could been related, as proposed by Matsuda [17], to the segregation of copper atoms at the interface between Q' precipitate and matrix (see Par. 1.3.6).

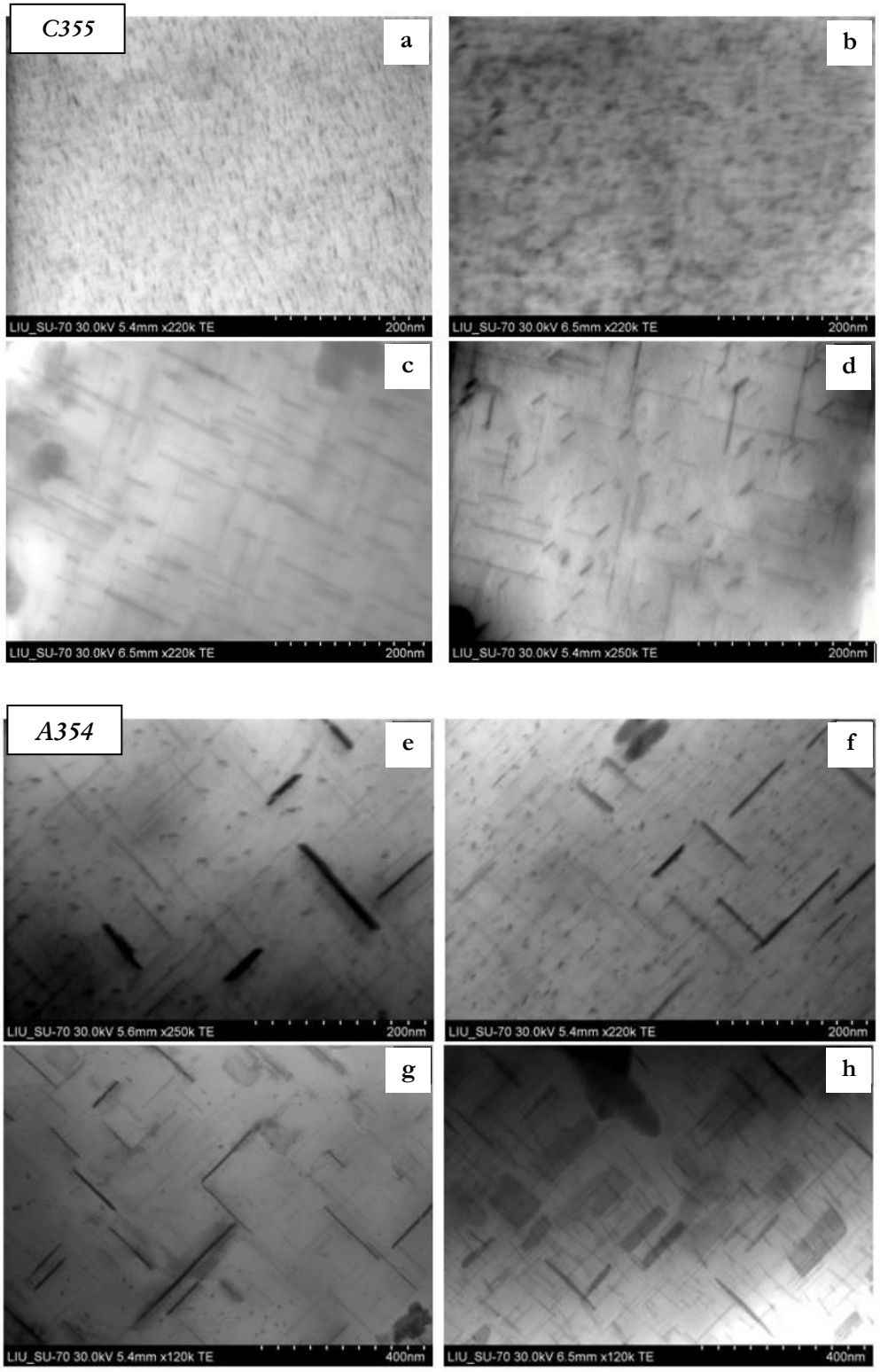

Figure 3.8. STEM images showing the evolution of heat treatment precipitates in C355 and A354 alloys, respectively, in the (a,e) heat treated condition at room and (b,f) high temperature; in the (c,g) overaged condition at room and (d,h) high temperature [18,19].

3.1.2 TENSILE TESTS

3.1.2.1 Tensile properties

As a result of hardness tests, summarized in Figure 3.9, no relevant effect of microstructural coarseness was observed on hardness values. However, both for A354 and C355 alloys, a slightly higher hardness value was registered in fine SDAS samples in comparison to the ones measured on coarse SDAS specimens. Morphological variation of heat treatment precipitates associated to overaging, as observed by STEM, was reflected on mechanical behavior of both the alloys with a strong reduction of hardness, related to the loss of efficiency of precipitates in hindering dislocation movement. Hardness decrease induced by overaging from the heat treated condition was more consistent in C355 alloy (about 15% in both fine and coarse samples) in comparison to A354 alloy (6 and 11% for fine and coarse microstructure, respectively). Furthermore, although in the heat treated condition C355 alloy presented the highest hardness value, after overaging the hardness of the alloy was even lower than that of A354. In view of this, it is possible to affirm that A354 alloy is characterized by a higher thermal stability in comparison to the C355 alloy. One explanation could be related to the different amount of Cu contained in the two alloys (1 wt.% and 1.5 wt.% for C355 and A354 alloys, respectively), which could lead to the formation of different amounts of Cu based precipitates (Q phases), more stable at high temperature than the θ-Al_2Cu or β-Mg_2Si, usually present in ternary alloys. Further studies should be addressed in this direction to evaluate differences in strengthening precipitates composition and morphology between the two alloys.

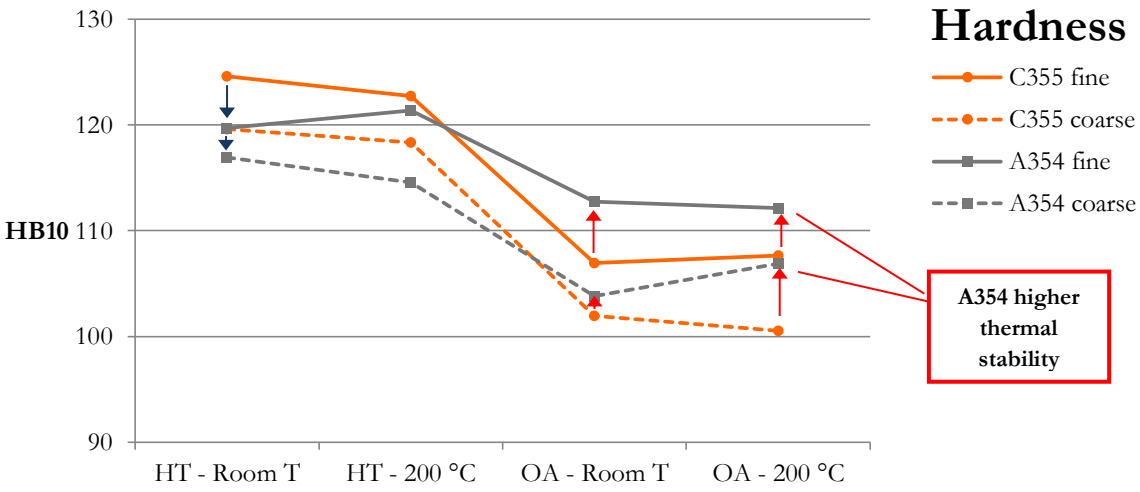

Figure 3.9. Hardness of fine and coarse A354 and C355 alloys in the heat treated (HT) and overaged (OA) condition, at room temperature and after tensile test at 200 °C

While long term exposure produced remarkable effects on hardness, the brief soaking time (≈20 min) at 200 °C did not lead to considerable effects. The higher density of precipitates appreciated on A354 samples tested at high temperature, induced no effect on the alloy hardness.

Yield strength of Al alloys is mainly influenced by precipitates nucleated during artificial aging[20,21]. As a result, a marginal influence of microstructural fineness on YS of both the alloys was expected (Figure 3.10). On the contrary, UTS (Figure 3.11) and elongation to failure (Figure 3.11) were observed to be strongly related to SDAS similarly to what has been reported for Al-Si alloys[5,22]. Decreasing the SDAS from 50-70 μm to 20-25 μm led to an increase of room temperature UTS of about 10% and 18% for C355-HT and A354-HT alloys, respectively.

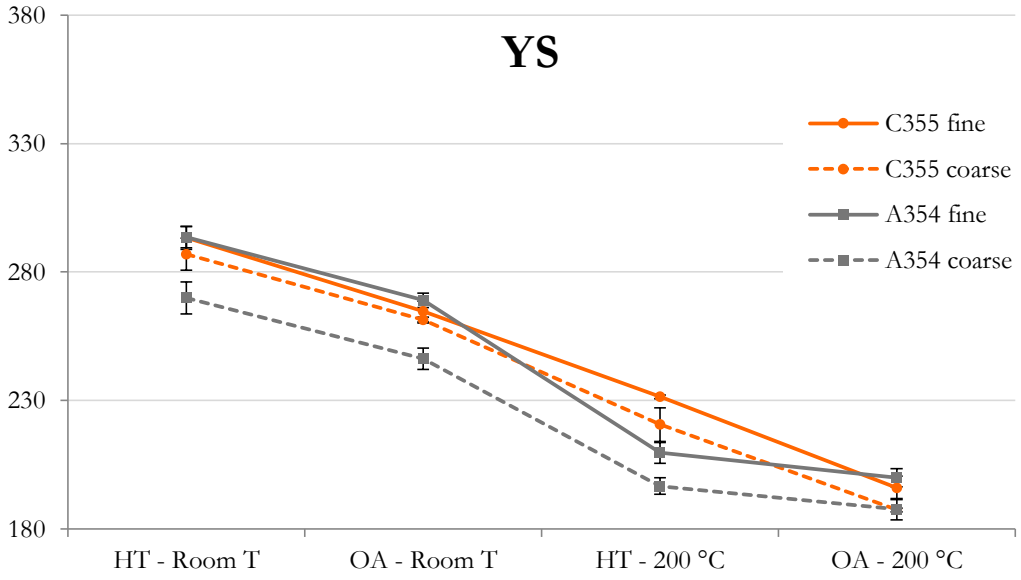

Figure 3.10. Yield strength of fine and coarse A354 and C355 alloys in the heat treated (HT) and overaged (OA) condition, at room temperature and after tensile test at 200 °C

The higher hardness of A354 alloy in the overaged condition is therefore reflected also on the tensile properties: with the exception of coarse SDAS at room temperature, A354 alloy exhibits superior UTS and YS in comparison to C355 alloy, irrespectively of microstructural fineness (Figure 3.10-11).

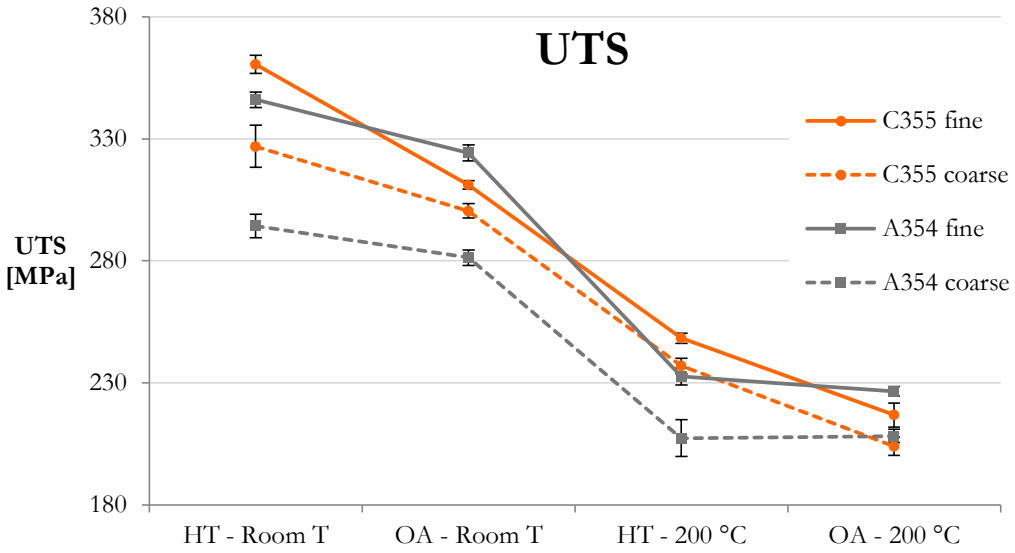

Figure 3.11. Ultimate tensile strength (UTS) of fine and coarse A354 and C355 alloys in the heat treated (HT) and overaged (OA) condition, at room temperature and after tensile test at 200 °C

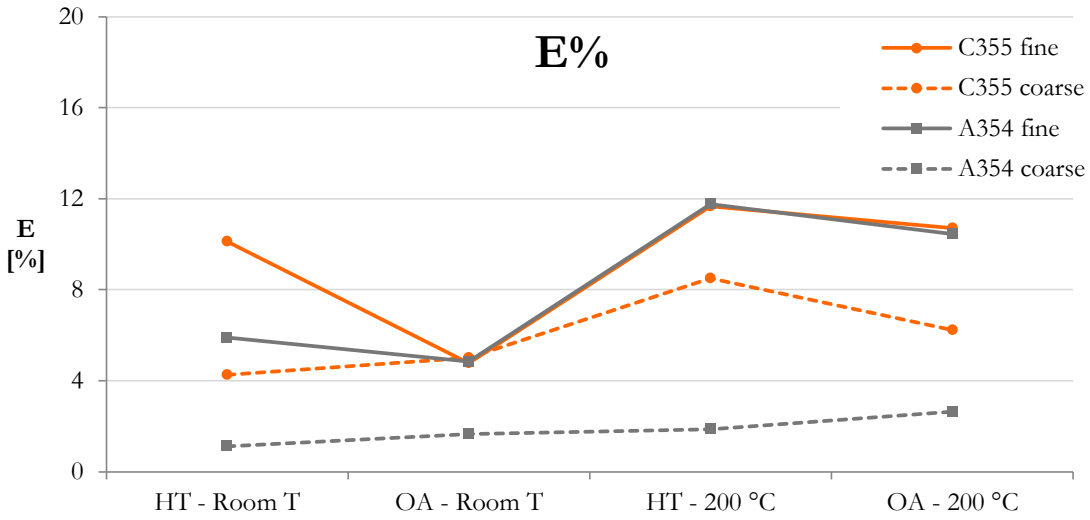

Figure 3.12. Elongation to failure of fine and coarse A354 and C355 alloys in the heat treated (HT) and overaged (OA) condition, at room temperature and after tensile test at 200 °C

Elongation to failure (Figure 3.12) was strongly influenced by microstructural fineness. At room temperature and in the heat treated condition, a significant increase of elongation was observed from coarse to fine microstructure (from 4.3 to 10.1% in the case of C355 alloy, from 1.1% to 5.9% for A354 alloy). Similar relationship between SDAS and elongation to failure of Al-Si alloys were reported also in the literature[4,5,22]. In both the alloys, the lower values of elongation to failure registered in coarse samples, often associated to higher

standard deviation, should be considered in strong relation with the larger intermetallic phases observed in such microstructures. The negative influence of brittle intermetallic particles such as the β-Al_5FeSi, α-$Al_{15}(Fe,Mn)_3Si_2$ and π-$Al_8Mg_3FeSi_6$ on the deformation behavior of Al-Si alloys are in fact well known[4,8], favoring crack initiation and propagation during plastic deformation. β-Al_5FeSi particle, in particular, due to the pronounced acicular morphology, are known to exercise a noticeable embrittling effect. By comparing the two alloys, the most relevant differences in elongation to failure were observed in the case of coarse microstructure: C355 alloy presented values higher than two fold that of A354. Anyway, it is thought that the very low values of elongation to failure of A354 coarse alloy are not only dependent on intermetallic particles, but also on the lower amount of the ductile α-Al phase, due to the higher Si content (about 5 and 9 wt.% for C355 and A354, respectively). Actually, the two alloys are characterized by intermetallics with similar average particle area, and slightly higher aspect ratio in the case of A354 alloy. On the contrary, as previously discussed, a slightly higher amount of intermetallic particles were measured in C355 samples. It is therefore clear that intermetallics are not the sole element to justify the lower ductility of A354 alloy.

Softening of the α-Al matrix becomes the predominant factor governing fracture process at 200 °C. In both the alloys and in all the investigated conditions, at high testing temperature lower values of strength and higher ductility were measured. An average 30% decrease of UTS in comparison to room temperature condition was registered both in A354 and C355 alloys. High temperature effect was found to be slightly less relevant on YS, which decreased of about 22% and 28% in C355 and A354 alloys, respectively.

Long term high temperature exposure induced precipitates coarsening, as previously discussed. Similarly to the effect on hardness, overaging induced a decrease on YS and UTS of both the alloys, more pronounced in the case of C355 alloy. Both in fine and coarse microstructure of A354 alloy, in fact, YS and UTS decreased of maximum 9 and 6%, respectively, from the heat treated condition at room temperature. In C355 alloy, reductions ranging from 8 to 14% were registered for UTS, while of about 9% for YS. Also these data suggest, as formerly discussed as concerning hardness, a higher thermal resistance of A354 alloy.

Mechanical properties of A354 and C355 alloy were compared to those of a typical ternary Al-Si-Mg alloy, the A356, in similar heat treatment conditions. Data on A356 alloy were derived from previous experimental investigations carried out at Metallurgy group, referred to an average SDAS value of ~25 μm. The comparison was therefore set only on fine

SDAS microstructures. Results of such comparison are summarized in Figure 3.13. Thanks to the presence of Cu-based precipitates, both the Al-Si-Cu-Mg alloys presented superior mechanical properties (HB, YS and UTS) at room temperature in comparison to A356 alloy, where the only strengthening precipitates are the Mg_2Si phases. After overaging and at high temperature, however, the superior thermal stability of Al-Si-Cu-Mg in comparison to Al-Si-Mg alloy is clearly outlined. A356 alloy, in fact, showed a marked decrease of mechanical properties from the heat treated condition; UTS and YS are reduced of about 50%. The decrease in Cu-containing alloys, on the contrary, is limited to about 30 %.

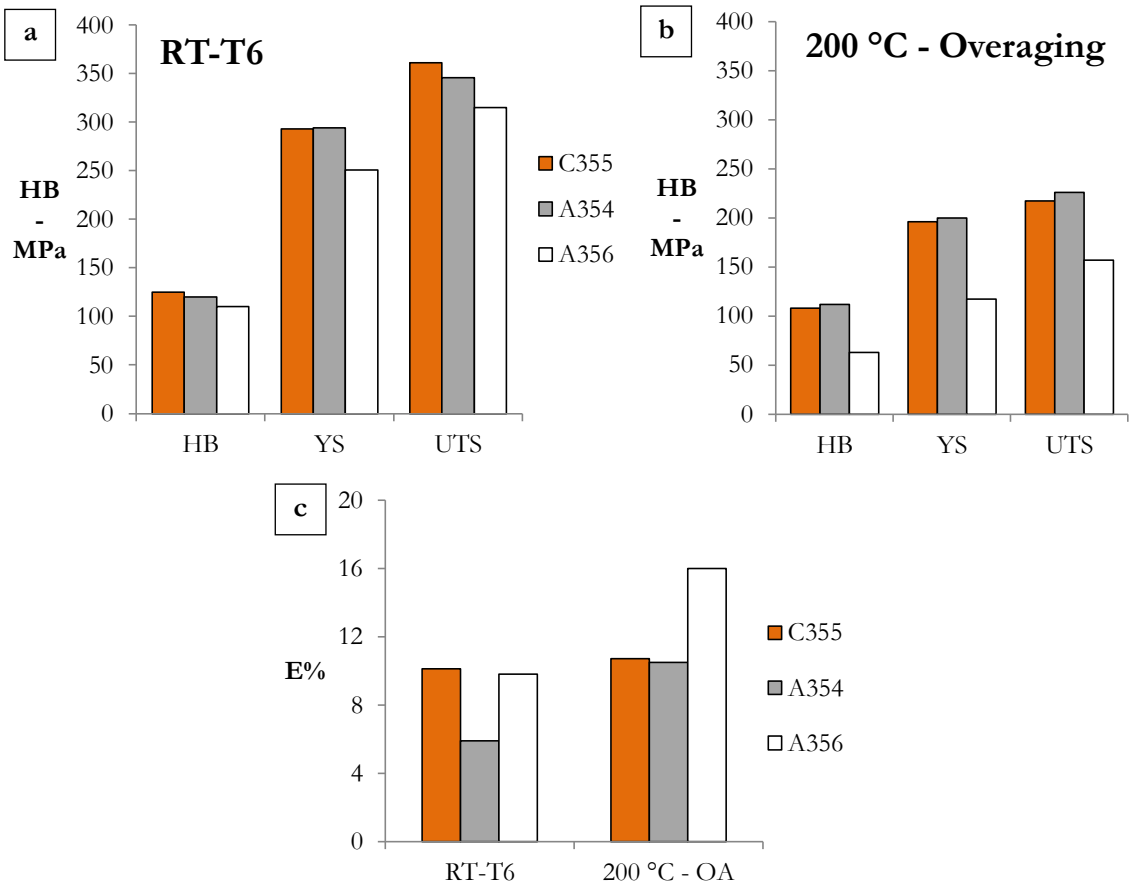

Figure 3.13. Comparison of hardness, yield strength and ultimate tensile strength between A354, C355 (Al-Si-Cu-Mg) alloys and A356 (Al-Si-Mg) alloy at (a) room temperature in the heat-treated condition and (b) at 200 °C testing temperature after overaging; (c) elongation to failure. Results refer to fine SDAS microstructures. Data referring to A356 alloy were obtained by past research activities carried out at Metallurgy group.

In conclusion, it is clear that Cu-based heat treatment precipitates possess higher coarsening resistance when compared to the Mg_2Si, therefore allowing to maintain high mechanical properties after high temperature exposure (210 °C – 41 h). From the comparative graph of elongation to failure, it is clear that, while at room temperature elongation to failure of C355 and A356 alloys were similar, at high temperature and after overaging A356 alloy showed a superior E% (16 %). This is likely related to the higher coarsening tendency of Mg_2Si in comparison to Cu-based precipitates, leading to a more ductile behavior in A356 alloy. The difference in elongation to failure between C355 and A354 alloys were already discussed in the previous paragraphs.

3.1.2.2 Fractographic analyses

Representative SEM images of the fracture surfaces of fine and coarse tensile specimens of C355 and A354 alloys are presented in Figure 3.14. SEM analyses revealed that, at equal SDAS value, both A354 and C355 alloys presented a similar fracture surface morphology at room and high temperature testing condition, as well as in the heat treated or overaged condition. As widely reported on previous works investigating the tensile behavior and deformation mechanisms of Al-Si alloys, fracture process under tensile loading generally starts with cracking of eutectic Silicon particles or with the decohesion at the interface between α-Al matrix and hard phases, such as Si particles or brittle intermetallics. Once generated, adjacent microcracks may connect with each other, thus leading to crack propagation and, lastly, to final failure[5,23,24]. Also in the present investigation, the above described mechanisms were observed on the fracture surfaces of A354 and C355 alloys. SDAS fineness was reported to play a role on the general aspect of the fracture surface.

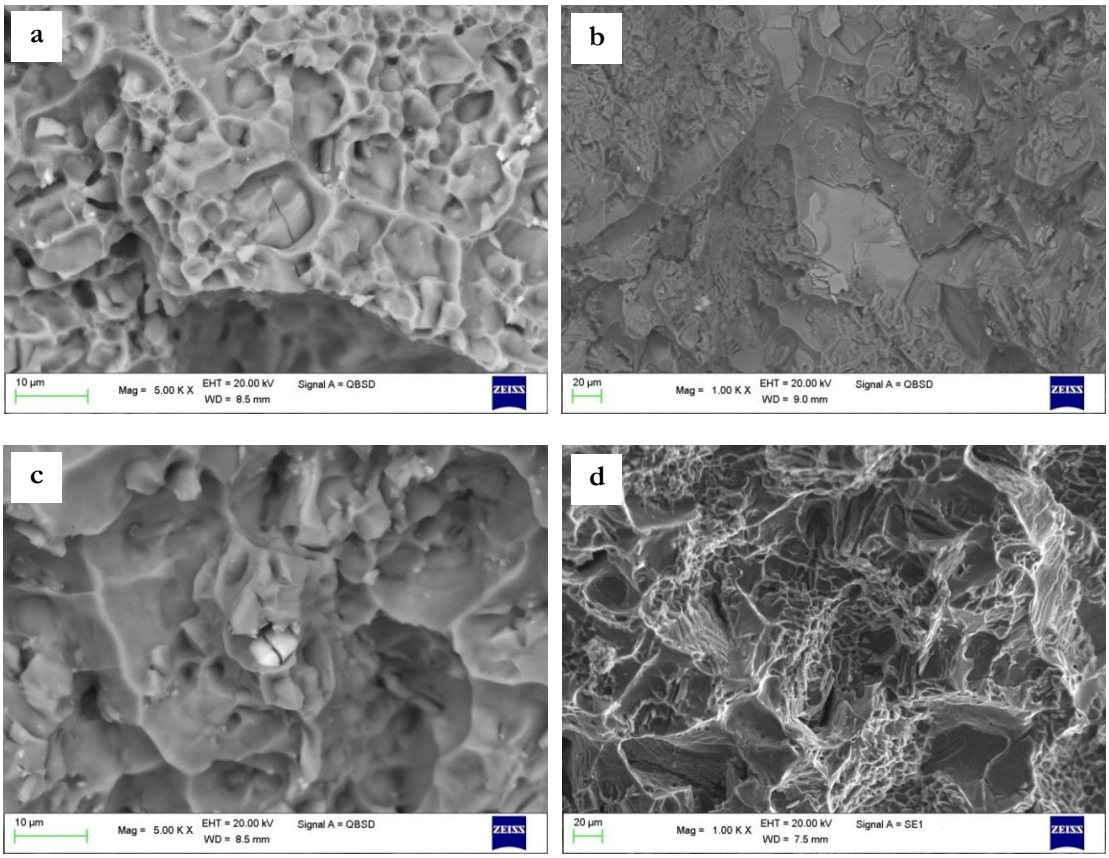

Figure 3.14. SEM images of fracture surfaces of A354 (a) fine and (b) coarse SDAS tensile samples, C355 (c) fine and (d) coarse SDAS tensile samples.

Fine SDAS samples of both the alloys, in fact, presented dimples characterized by small size and circular shape, evenly dispersed and generally developing around eutectic Si particles (Figure 3.14a,c). Despite coarse SDAS specimens presented similarly homogeneously dispersed dimples, a high number of large and fractured intermetallics was found on the fracture path. At the interface between intermetallic particles and α-Al matrix, cleavage-like regions with more pronounced brittle aspect were found. Together with coarse intermetallic phases, also the different eutectic Si particle size and morphology, registered between fine and coarse SDAS samples, may have influenced fracture behavior. Coarse SDAS samples were in fact characterized by bigger and sometimes even partially unmodified eutectic Si particles, thus maybe inducing a higher probability of particle fracture and higher stress concentration at the particle-matrix interface.

Large intermetallic particles were analysed by EDS, revealing that most of them were Fe-based. SEM images and corresponding EDS spectra carried out on fine and coarse SDAS samples are presented in Figure 3.15. The presence of such brittle phases is known to favour the linkage of microcracks under tensile loading, thus accelerating the damage process[4,5,15,25]. The harmful effect of Fe-based particles on crack propagation was

confirmed by the observation of three-dimensional intermetallics clusters on coarse SDAS surfaces: the fracture path appears thus to develop along particle-matrix interface (in case of decohesion) or along fractured particles. The low values of elongation to failure registered in the coarse SDAS alloys shall therefore be linked to the loss of deformation capacity of the α-Al matrix in correspondence of intermetallics-matrix interface.

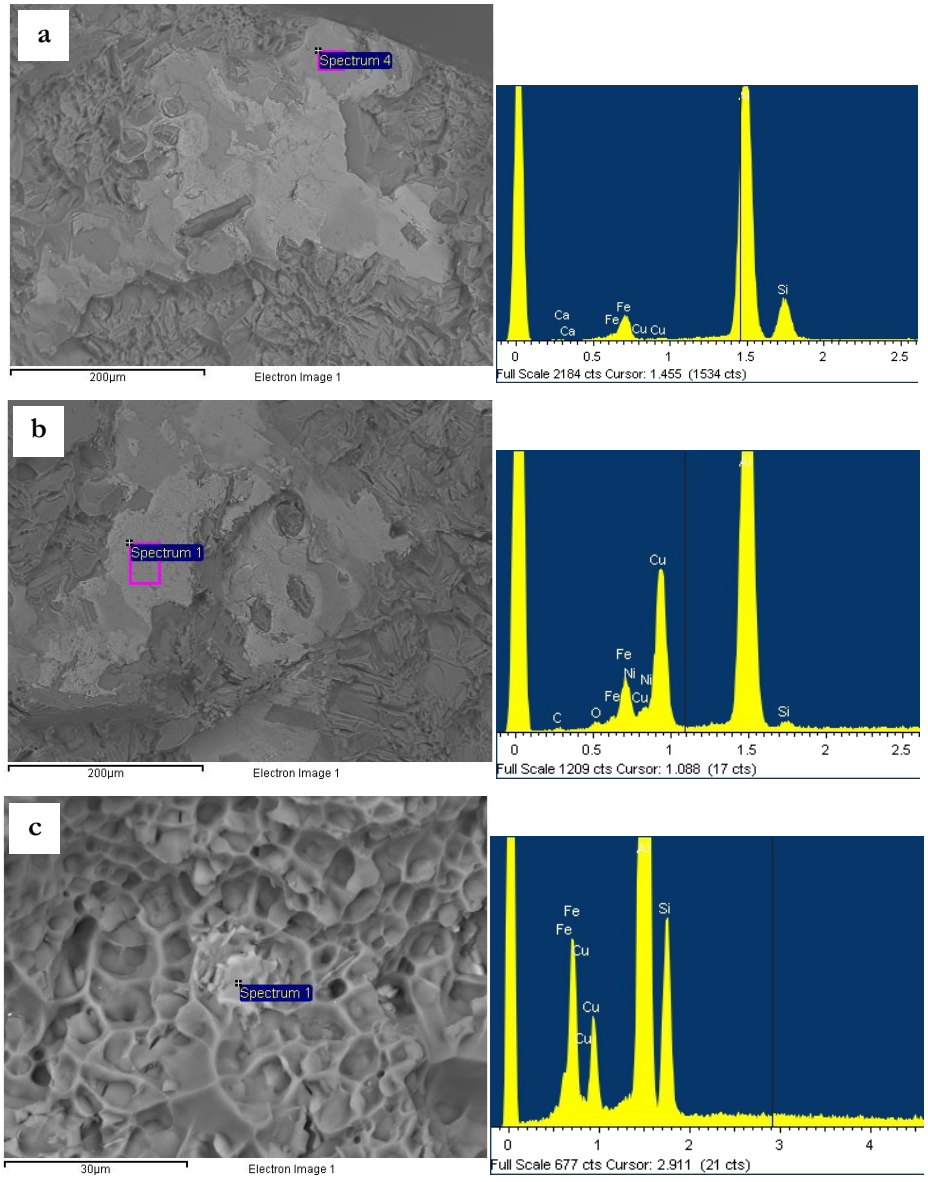

Figure 3.15. SEM images and EDS spectra showing the difference in size of Fe-based intermetallic particles observed on the fracture surface of (a, b) coarse SDAS samples and (c) fine SDAS samples.

3.1.3 FATIGUE TESTS

3.1.3.1 Fatigue properties

Aiming to reduce to a minimum the effect of casting defects (pores) on fatigue characterization, samples were subjected to HIP process. The beneficial effect on mechanical resistance of decreasing microstructural fineness, i.e. SDAS, was reflected also on rotating bending fatigue properties. As a matter of fact, in both the alloys fine microstructure presented higher fatigue resistance than the corresponding samples with higher SDAS. The data, shown in Figure 3.16, clearly show that, similarly to what has been reported in the literature for Al-Si-Mg alloys[4,7,26], fine SDAS induced an increase of fatigue resistance of about 10-15% in both the investigated Al-Si-Cu-Mg alloys. A negligible effect of SDAS on fatigue behavior was registered after overaging and at high temperature, where both the alloys presented comparable fatigue strength values.

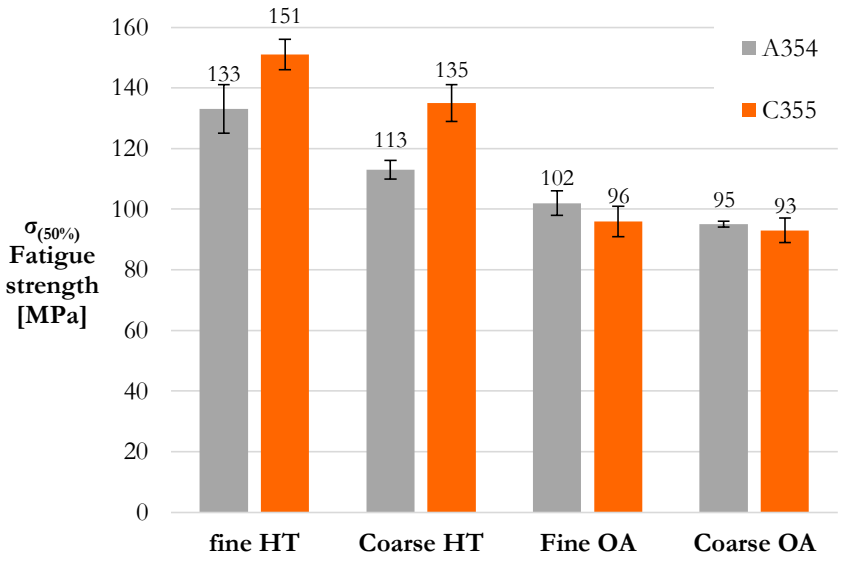

Figure 3.16. Fatigue resistance at $2 \cdot 10^6$ cycles of A354 and C355 alloys in the heat treated (HT) and overaged (OA) condition, tested at room temperature and 200 °C, respectively.

Interesting observations can be done by comparing the fatigue behavior of the two alloys. First of all, it appears clear the correlation between hardness, tensile strength and fatigue resistance: A354-HT alloy, being characterized by slightly lower hardness, tensile strength and elongation to failure, presents, correspondingly, a lower fatigue resistance in comparison to C355-HT alloy. Also fatigue behavior is strictly dependent on testing temperature and heat treatment condition: the two overaged alloys, tested at 200 °C presented a marked decrease of resistance in comparison to the room temperature-HT

behavior. Once again, the alloy which presented lowest strength loss was the A354 alloy. C355-OA, in fact, was characterized by a fatigue strength decrease of more than 30%, while A354-OA was subjected to a maximum strength loss of 23%, in the case of coarse microstructure. Percentage decreases in fatigue resistance from the heat treated to the over-aged condition are reported in Table 3.4.

Table 3.4. Calculated percentage loss of fatigue strength from the heat treated condition at room temperature to the overaged condition at 200 °C.

	C355	**A354**
Fine	-36%	-16%
Coarse	-31%	-23%

As a result, while in the heat treated condition C355 alloy showed higher resistance, in the overaged condition at 200 °C, the behavior of the two alloys resulted basically comparable.

It is interesting to observe that fatigue resistance and ultimate tensile strength are strictly related. In particular, as reported in Table 3.5, the ratio between UTS and fatigue resistance was reported to be similar for both the investigated alloys in all the testing conditions. The ratio was observed to be not dependent on SDAS value.

Table 3.5. Calculated ratios between fatigue resistance and ultimate tensile strength (UTS).

SDAS	**Room temperature**		**200 °C**	
	A354-HT	C355-HT	A354-OA	C355-OA
Fine	0.38	0.41	0.45	0.44
Coarse	0.38	0.41	0.45	0.45

The strong relationship between UTS and fatigue strength is well known, and several works reported the existence of linear dependence of fatigue resistance on ultimate tensile strength. In this regard, the slope of linear models is mainly dependent on fatigue deformation and fracture mechanisms[27–31] which are in turn strictly related to the microstructure. UTS and fatigue resistance are similarly affected by microstructural features such as SDAS, eutectic Si particles, intermetallic phases and solidification defects; as a result, among static properties, UTS is generally considered the most appropriate to predict the fatigue behaviour of aluminium alloys[4,5,7,26,30,32,33]. As confirmed by SEM analyses of fracture surfaces, the similar ratios in C355 and A354 alloys indicate that similar failure

mechanisms act in the two tested alloys, both at room and high temperature. It is possible to think that SDAS does not play a direct role on fatigue failure mechanisms; actually, it affects the size of the intermetallic compounds and, in turn, the absolute values of tensile and fatigue strength of the alloys, but does not influence their ratio.

3.1.3.2 Fractographic analyses

SEM analyses revealed that the fatigue behavior of the tested alloys was mainly governed by brittle Fe-based intermetallic particles. In particular, large solidification intermetallics resulted to be the main cause of crack nucleation, in correspondence of the sample surface, both in fine and coarse SDAS samples of A354 and C355 alloys. Some examples of the above mentioned nucleation sites are reported in Figure 3.17. Minor causes of crack nucleation were identified in small solidification defects, such as oxide films and superficial or sub-superficial pores. Despite the samples were subjected to HIP treatment, cavities located near the surface were only partially closed by the process, due to the lack of material around the void. However, the presence of such sub-superficial pores was linked in some cases to the presence of intermetallic particles, as shown in Figure 3.17, which are known to hinder the interdendritic flow during solidification.

As it is possible to observe in SEM images, particles cracking and/or interfacial decohesion between particle and Al matrix occurred during fatigue damage process, due to the action of Fe-containing particles. They are in fact known to hinder dislocation movement and causing their piling up, with a consequent stress concentration at the interface with the ductile Al matrix, thus causing crack nucleation. Size of intermetallic particles is thought to play a role on crack nucleation process: the larger the intermetallic, the faster the nucleation process. As a result, coarse SDAS heat-treated alloys presented generally lower fatigue resistance in comparison to the same alloy with fine SDAS microstructure, in view of the different intermetallic size.

As a general observation, it should be pointed out that, due both to the to the relatively short time exposure at 200 °C and high cycling frequency (50 Hz), no creep fracture morphologies were observed on overaged samples in specimens tested at high temperature[34,35]. Moreover, similarly to what has been observed for tensile fracture surfaces, no significant differences were appreciated by SEM analyses between the fracture surfaces morphologies of alloys tested at room and high temperature (200 °C).

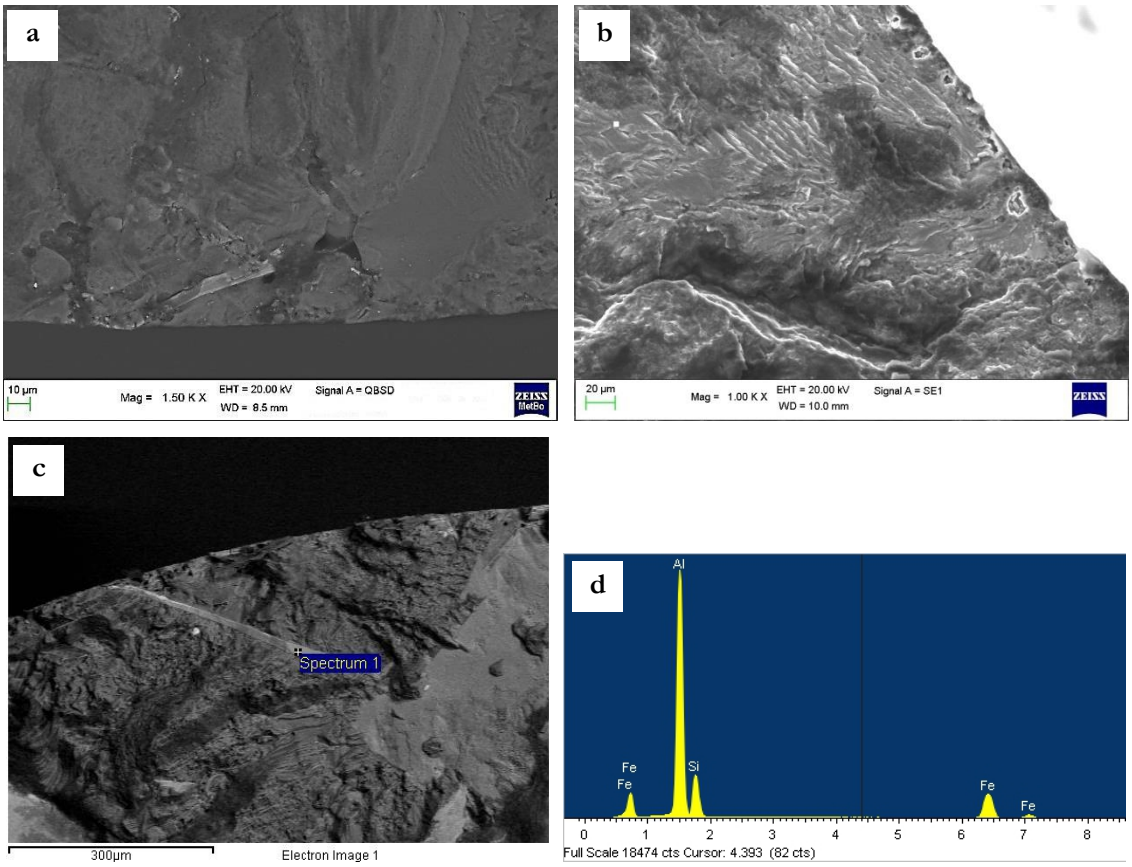

Figure 3.17. SEM images of crack nucleation sites, corresponding to: (a) Fe-based particle and (b) sub-superficial pores in C355 fine SDAS samples, and (c) β-Fe particle found in a A354 coarse SDAS sample and (d) corresponding EDS spectrum.

As discussed in the previous paragraph, despite in the heat treated condition fatigue resistance values were significantly different in fine and coarse SDAS samples, in the overaged condition the difference is reduced, and similar high temperature fatigue resistance values were reported for A354 and C355 alloys. In this regard, even though also on overaged samples tested at high temperature the same nucleation mechanisms were recognized, it is possible that the high testing temperature may have induced a local softening of the matrix, thus reducing the stress level at the interface between particle and α-Al matrix.

As concerning the crack propagation region (Figure 3.18), it is generally recognized that intermetallic particles act as an obstacle for the crack, often resulting in crack path deflection[4,36,37]. Despite large intermetallics are supposed to be more effective in this regard, thus reducing the crack growth rate, it should be taken into account that under low stress, the fatigue behaviour is mainly governed by the crack nucleation stage. Consequently, similarly to what has been reported in the literature[7,26,37], intermetallic

particles found in coarse SDAS microstructures, leading to crack nucleation, are supposed to induce a general decrease of the fatigue resistance.

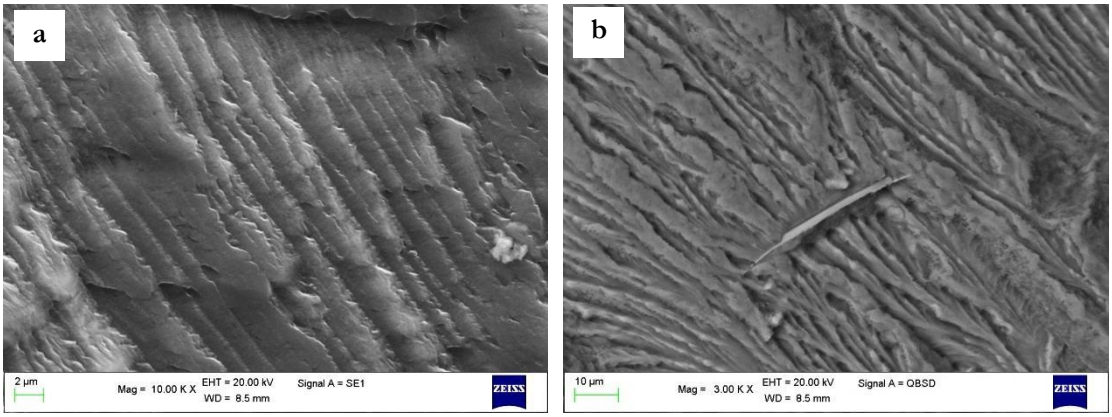

Figure 3.18. SEM images showing (a) fatigue striations on A354 coarse sample and (b) the interaction between a β-Fe intermetallic particle and crack propagation in a C355 coarse specimen.

Lastly, as a result of SEM analyses (Figure 3.19), the final failure region presented the typical ductile morphology, characterized by the presence of dimples.

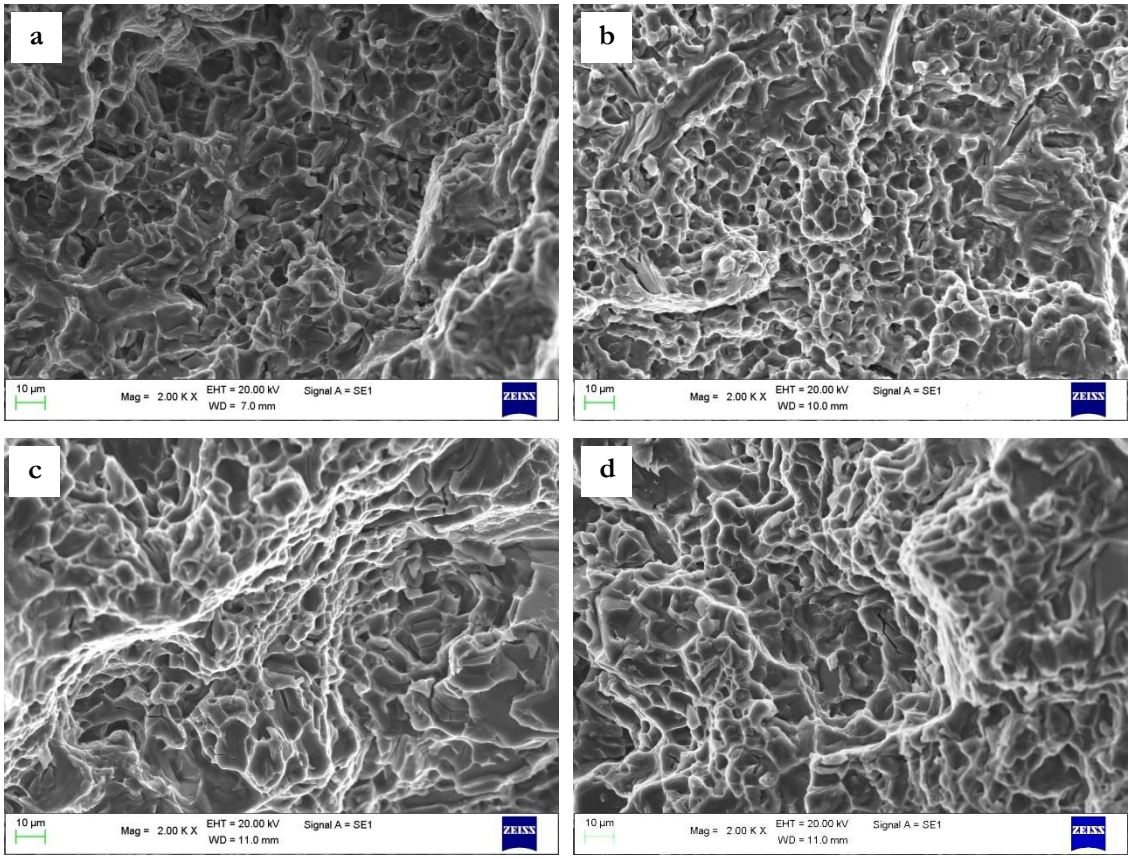

Figure 3.19. SEM images of the failure regions in (a) C355-HT and (b) A354-HT fine SDAS samples, tested at room T, (c) C355-OA with coarse SDAS tested at RT, (d) A354-HT with coarse SDAS tested at high temperature.

At high testing temperature, after overaging, the ductile aspect of the fracture surfaces appeared to be slightly more pronounced. Cracked intermetallic particles were observed both in the coarse and fine SDAS samples.

3.1.4 CONCLUSIONS

In recent years, increasing interest has been devoted to quaternary Al-Si-Cu-Mg alloys for high temperature applications. Not only the high castability, but above all the expected higher thermal stability and enhanced mechanical properties in comparison to the traditional Al-Si-Mg alloys, made such alloys particularly attractive for industrial applications, especially in the production of engine components.

Aiming to widen the knowledge on Cu-containing cast aluminum alloys, microstructural and mechanical characterization of two Al-Si-Cu-Mg alloys, suitable for motor racing components (A354 and C355), was carried out. The effect of chemical composition (in terms of Cu and Si content), solidification conditions (SDAS, microstructural fineness), secondary phases (intermetallic particles) and heat treatment conditions on room and elevated temperature tensile and fatigue behavior of the alloys was evaluated.

- SDAS was observed to play a role on mechanical behavior: fine SDAS alloys showed generally higher UTS and elongation to failure in comparison to the coarse ones, while the role on YS was less relevant. The same kind of influence was evaluated on fatigue behavior at room temperature; on the other hand, in the overaged condition microstructural fineness seemed not to influence fatigue resistance. A correlation between UTS and fatigue resistance for the two alloys was observed.
- Different types of intermetallic particles were observed in the alloys microstructures, mostly π- $Al_8Mg_3FeSi_6$, Q-$Al_5Cu_2Mg_8Si_6$ and β-Al_5FeSi. It should be noted that the type and size of intermetallic compounds are strongly influenced by the solidification rate: larger intermetallics were observed in the coarse SDAS microstructures; the global average area fraction of intermetallic compounds was not influenced by SDAS, therefore by solidification rate.
- The elongation to failure and fatigue resistance of the alloys was significantly affected by the presence of coarse intermetallic compounds, acting as cracks nucleation sites, especially at room temperature. At high temperature, on the contrary, the local softening of Al matrix reduced the detrimental effect of coarse brittle phases, lowering the difference in the fatigue resistance of fine and coarse SDAS alloys.
- Overaging, i.e. long term high temperature exposure, led to a decrease of mechanical properties (tensile and fatigue resistance) of the alloys, as a result of heat treatment precipitates coarsening. Such behavior was confirmed by STEM analyses, carried out on fine SDAS alloys. However, it should be stated that A354 alloy showed, in general,

higher thermal stability in comparison to C355 alloy, being characterized by relative lower loss of hardness, tensile and fatigue resistances after equal overaging time.

- Industrial T6 heat treatment of A354 alloy is thought to induce slight overaging in the alloy. In view of the above, a heat treatment optimization study is needed to better exploit the Cu content of the alloy, thus obtaining higher mechanical properties.

3.2 Results and Discussion – PART 2

Optimization of A354 heat treatment

3.2.1 STUDY OF SOLUTION TREATMENT

i) 1st stage

Castings for heat treatment study were obtained by remelting of A354 ingots, and addition of Al-Sr10 master alloy for eutectic Si modification. As expected, microstructure of A354 casting consisted in α-Al dendrites, surrounded by modified eutectic silicon particles (Figure 3.20a). Different intermetallic phases were found in the interdendritic region (Figure 3.20b, white arrows), with both blocky or acicular morphology (i.e. the typical β-Fe phases). The average SDAS of the castings was about 25 μm.

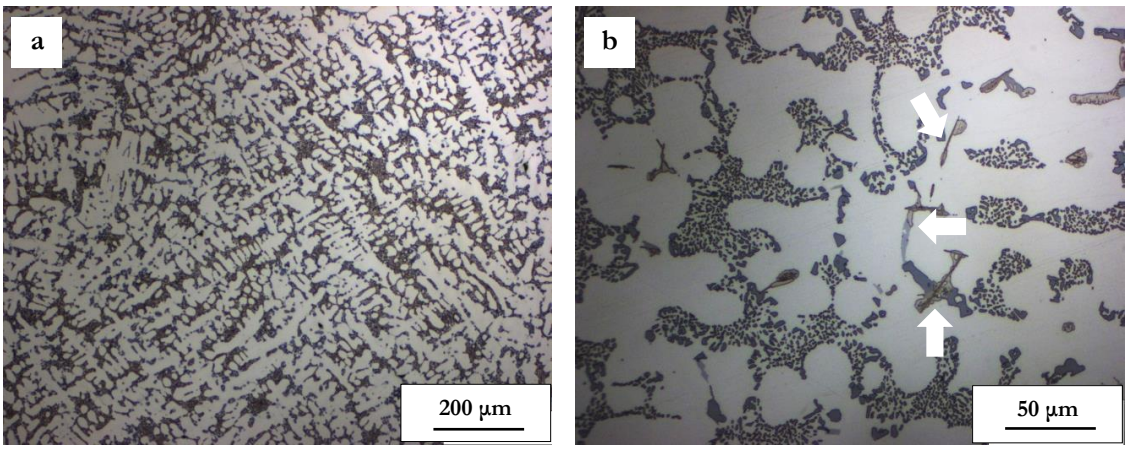

Figure 3.20. Optical micrographs of the as cast A354 alloy: dendritic structure surrounded by eutectic silicon at (a) low and (b) high magnification; intermetallics formed during solidification are highlighted by white arrows.

Composition of intermetallic phases was investigated by SEM-EDS, revealing the presence of both Cu and Fe based particles. The most diffused particle was the θ-Al_2Cu phase, characterized by both blocky (indicated as θ_b, Figure 3.21a) or eutectic (indicated as θ_e, Figure 3.21b)) morphology. Quaternary Q particles, usually characterized by regular blocks and smooth borders were also observed (Figure 3.21a). Q particles appeared usually in association to θ-Al_2Cu phases (Figure 3.21c), similarly to what has been reported also higher Cu content alloys by Hwang et al.[38], Han et al.[39] and Sjölander et al.[11], due to the fact that these phases are formed during the final eutectic reaction during solidification. In view of the small size of the particles, it was not always possible to determine by EDS

analyses the exact stoichiometry of Q phases. Compositional results however were consistent with the most widely accepted composition, i.e. $Al_5Cu_2Mg_8Si_6$[39–41].

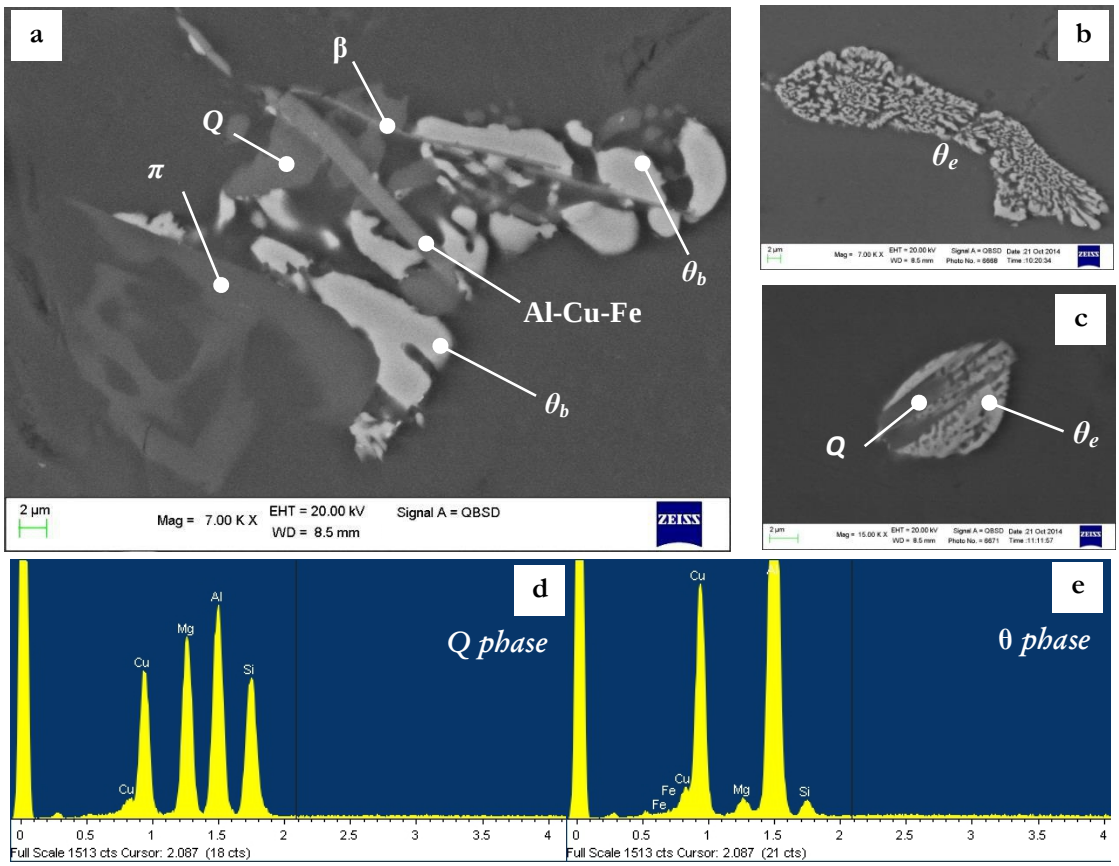

Figure 3.21. SEM images of intermetallic phases observed in the A354 as cast alloy: (a) different Cu-based intermetallics (blocky θ-Al_2Cu, indicated as θ_b and Q) and Fe-based particles (β-Al5FeSi, Al-Cu-Fe and π-$Al_8Mg_3FeSi_6$); (b) θ-Al_2Cu phase with eutectic morphology, indicated as θ_e; (c) θ-Al_2Cu associated to Q phase; (d, e) EDS spectra of Q and θ phases in Fig. 20c.

The as-cast material was subjected to differential thermal analyses (DTA) to identify the presence of low melting compounds. Results are shown in Figure 3.22. The first endothermic peak occurred at 509 °C, while the onset of the reaction was at 507 °C (Figure 3.22b).

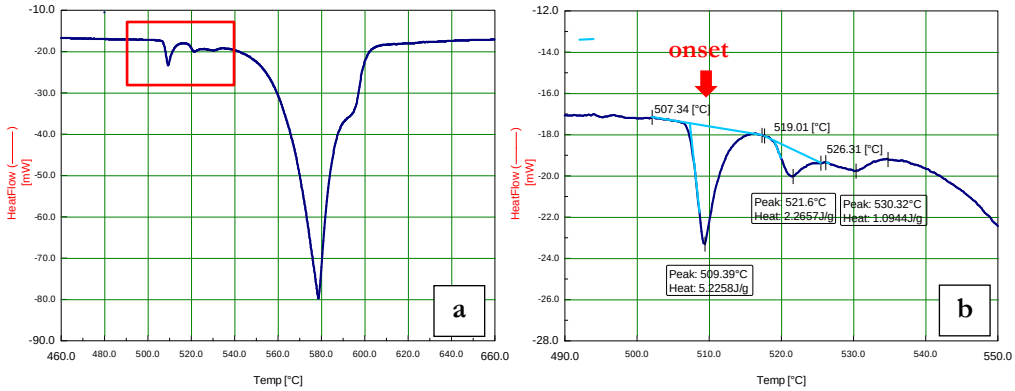

Figure 3.22. DTA thermographs obtained on the as-cast A354, highlighting (a) the presence of an endothermic peak due to incipient melting at 509 °C; (b) the onset of melting reaction was observed at 507 °C.

The presence of low melting phases (Al_2Cu, $Al_5Cu_2Mg_8Si_6$[42,43], see Chapter 1) is widely reported by several research works carried out on high Cu content alloys[43–45]. When copper is present in lower contents, on the contrary, alloys are not always observed to present such peak. Wang et al., for example, observed this reaction only in alloys with Cu content higher than 2%[44]. In spite of this, a solution treatment temperature of 495 °C is suggested by some authors for alloys similar to that investigated, consistently with the presence of such low melting peak[46,47]. However, it should be taken into account that the presence of the low melting phase depends not only on the specific alloy composition, but also on solidification rate, which strongly influences the segregation of intermetallic phases[48].

The experimental results of the present investigation suggest not to exceed, during solution heat treatment, the onset temperature of reaction (1) (see Par. 1.3.3), thus avoiding incipient melting of limited zones of the casting.

In view of this, a double step solution treatment was proposed, as previously done for alloys with higher Cu content by different authors[49,50]. The first solution stage is aimed at the dissolution of the low melting phase and to the homogenization of the alloy, while the second one is meant to maximize the dissolution of alloying elements (i.e. Cu and Mg) in the α-Al, making them available for precipitation hardening during artificial aging. The temperature of the first solution stage was therefore set to 495 °C, aiming to maximize homogenization while remaining conservatively far from the low melting peak, as well.

A354 cast samples were therefore solution heat treated at 495 °C from 30 min to 6 h. Solutionized samples were then subjected to differential thermal analyses (DTA), aiming to evaluate the minimum time required for complete dissolution of the low melting phase.

Thermal diagrams are reported in Figure 3.23. The endothermic peak at 509 °C gradually diminishes its amplitude by increasing solution time, disappearing after 6 h of treatment. It is therefore inferred that a first 6 h solution stage at 495 °C is needed to bring into solution the quaternary eutectic, therefore allowing to treat the alloy with a second – higher temperature – solution stage.

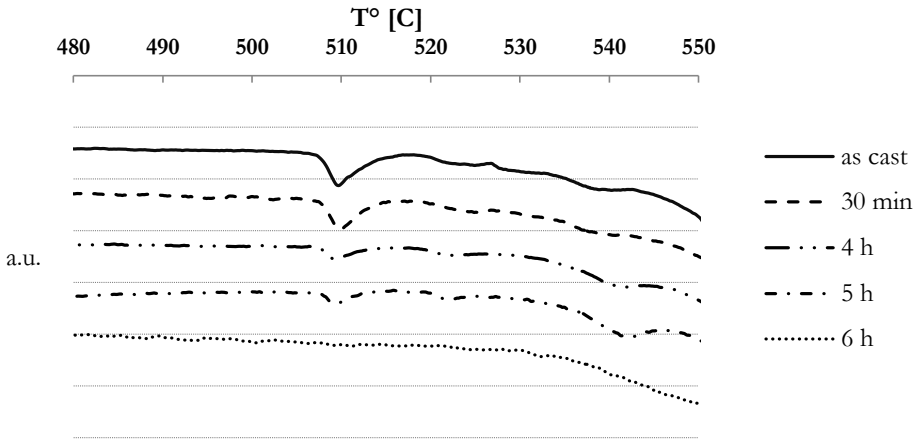

Figure 3.23. DTA thermographs obtained on A354 samples solution treated at 495 °C for 30 min, 4, 5 and 6 h. The endothermic peak associated to the melting of the eutectic phase at 509 °C disappears after 6 h of solution treatment; fluxes were normalized with the sample mass for comparison.

Optical micrographs of samples solution treated at 495 °C for 2 and 6 h are reported in Figure 3.24 a and b, respectively. After 2 h of treatment, θ-Al_2Cu particles appear basically unmodified if compared to the as cast microstructure, while they undergo fragmentation and partial dissolution after 6 h of treatment. In particular, from the present investigation, the eutectic θ is the phase which preferentially undergoes dissolution. SEM-EDS analyses, whose results are reported in Figure 3.25, confirmed the presence of a small amount of blocky θ particles and traces of eutectic Al_2Cu after 4 h solution, while after 6 h, most of the eutectic θ phase was dissolved. In this treatment condition, only small blocky Al_2Cu particles were still observed. The persistence of blocky θ phase after solution treatment was reported also by Paray et al.[51].

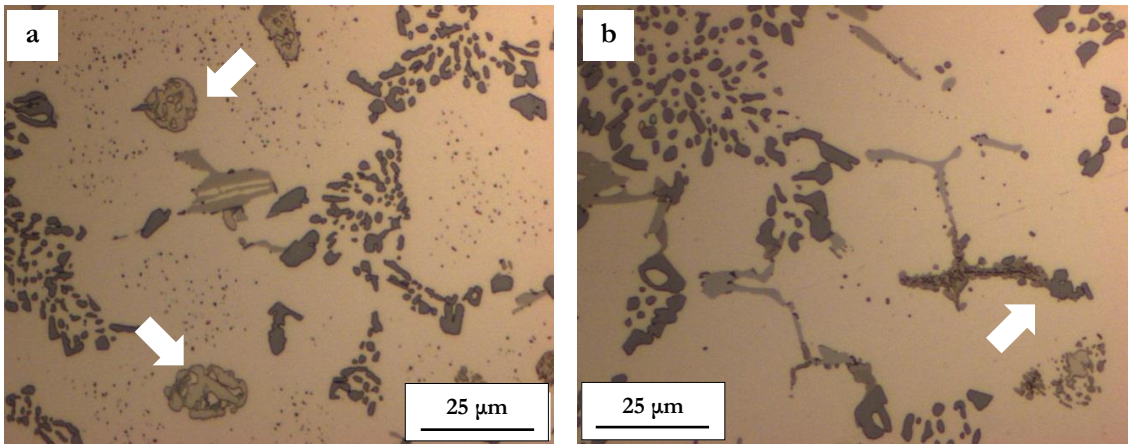

Figure 3.24. Optical micrographs of A354 samples solution treated at 495 °C for (a) 2 h and (b) 6 h; white arrows indicate θ phases.

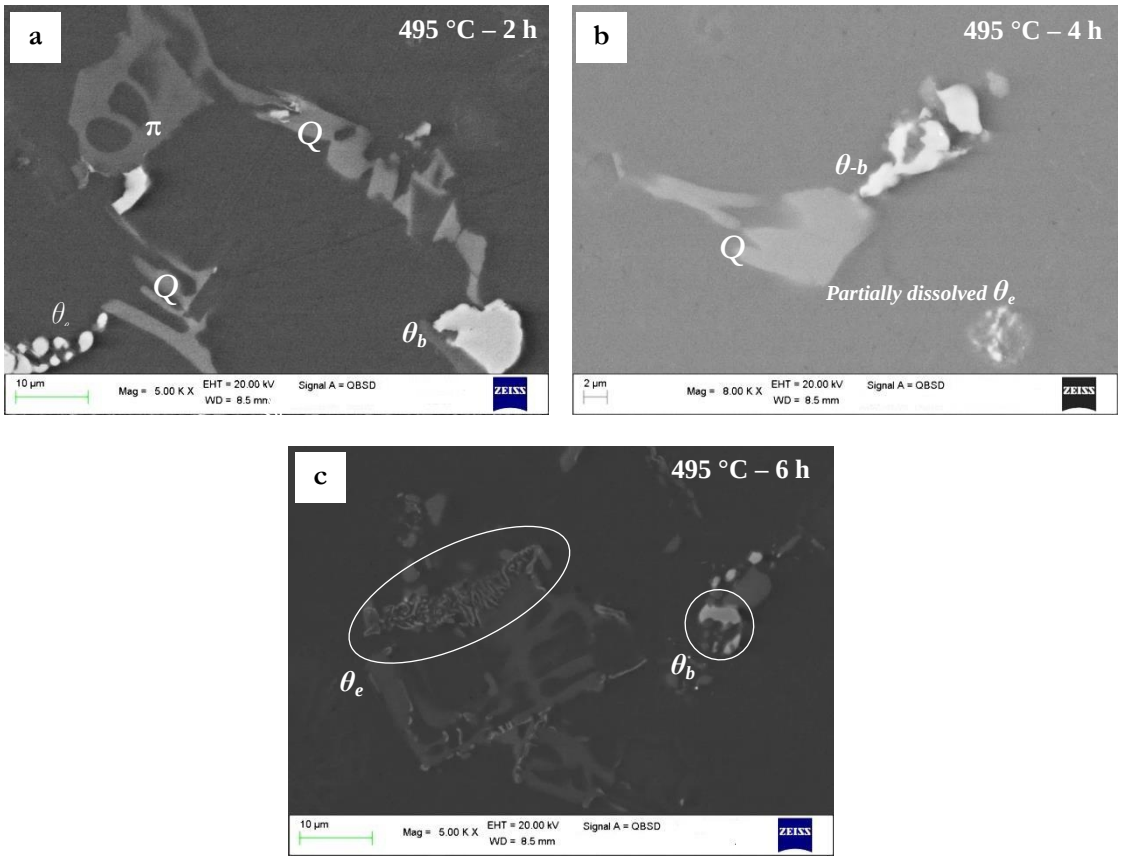

Figure 3.25. SEM images of A354 samples solution treated at 495 °C for (a) 2 h, (b) 4 h and (c) 6 h, showing the different dissolution behavior of eutectic and block-like θ-Al_2Cu particles.

The different dissolution behavior between eutectic and blocky particles was observed also in the study of Han et al.[39], who argued that, due to the shape of the particles, dissolution of eutectic Al_2Cu goes on by necking of the intermetallic in several points of its length, successive breaking into smaller fragments, than final spherodization and dissolution (see Figure 1.3). On the contrary, blocky particles undergo gradual dissolution, which therefore requires higher times and temperatures for complete solubilization. As concerning the

other intermetallic phases, from SEM observation, neither π-Fe nor Q phases underwent appreciable dissolution after the first step of solution treatment, as they were still observed in all the samples treated at 495 °C. In this regard, the presence of Q phases after solution treatment at 495 °C was reported also in high Cu content Al-Si-Cu-Mg alloys (Cu ~ 3 wt%)[52]. It should be however noted that the tendency of Q phases to dissolve or not strongly depends on microstructural coarseness, as reported by Sjolander[6], who observed a decrease in the area fraction of Q phases after 3 h of solution at 495 °C for a 3 wt.% Cu Al-Si-Cu-Mg alloy characterized by 9 μm SDAS, while no variation in the area fraction covered by Q particles was observed in coarser microstructures (24 and 49 μm SDAS, respectively).

ii) 2nd stage

In view of the previous analyses, a new set of A354 samples were solution treated at 495 °C for 6 h, then subjected to a second solution stage, at 515 or 530 °C for times ranging from 2 to 8 h. As a result of SEM-EDS analyses on treated samples, after 2 h at the lowest solution temperature (i.e. 515 °C), only a very small amount of Al_2Cu particles was still present, as a result of dissolution (Figure 3.27). The size of remaining Al_2Cu particles, however, was generally even too small (less than 1 μm) for clear identification by SEM-EDS analyses. Same findings were reported from observation of samples treated at 515 °C for longer durations. Furthermore, no relevant differences between 530 °C and 515 °C treated samples was appreciated by SEM in terms of Al_2Cu particles dissolution.

The qualitative analyses of intermetallics evolution during solution heat treatment was quantified by image analyses carried out on SEM micrographs. The average area fraction covered by intermetallic particles was calculated and compared among the different heat treatment conditions; results are shown in Figure 3.26. As a confirmation of visual interpretation of SEM images, it is possible to observe that the first solution stage at 495 °C favors particles dissolution; the area fraction in particular remarkably decreases from the as cast state (1.3 %) to 0.88% after 6 h at 495 °C. Further solution at higher temperature, i.e. 515 and 530 °C leads to further, but however limited, decrease of the intermetallics fraction, up to the minimum value of 0.61% after 8 h at 530 °C. This should be related to (i) the high dissolution rate of θ-Al_2Cu particles during the first solution treatment phase (495 °C) and (ii) to the slower dissolution rates of other phases, such as Q and π-Fe, even at higher temperatures (515-530 °C).

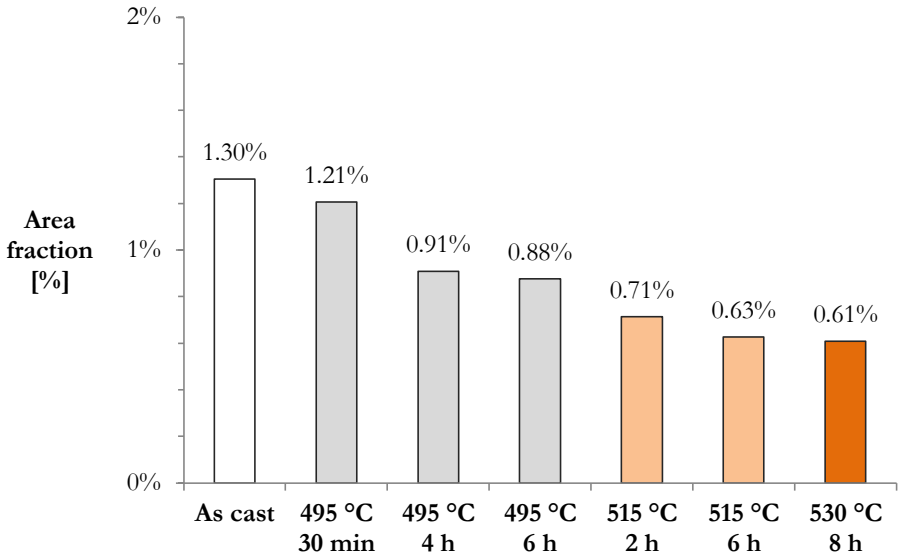

Figure 3.26. Average area fraction covered by intermetallic particles calculated by image analyses on A354 alloy samples in different heat treatment conditions.

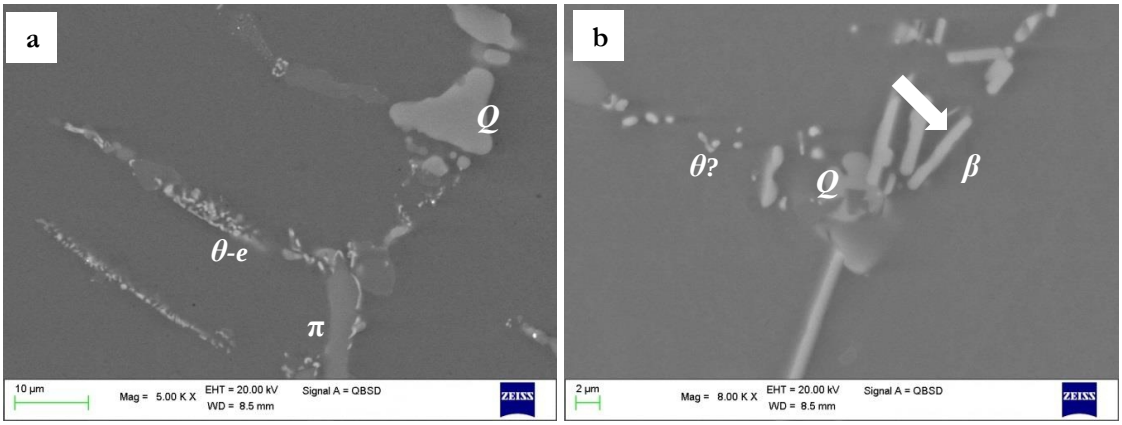

Figure 3.27. SEM images of A354 samples subjected to double step solution treatment: 495 °C - 6 h, then 515 °C - 2 h (a) and 530 °C - 8 h (b).

Differently from θ particles, neither π-Fe nor Q phases were apparently affected by solution treatment at both the investigated temperatures. This kind of behavior was observed also by different investigators: Q phase was reported to be insoluble in 319 alloy after a double step solution treatment (490 °C/8 h + 500 °C/4 h) by Han et al.[39]. Sjölander et al., as previously outlined, showed how the dissolution tendency of the Q phase is strongly affected by microstructural coarseness[6]. Further, the permanence of π-Fe phases after solution treatment was observed also by different authors, such as Taylor et al. and Mbuya et al.[53–55]. In the case of iron-based intermetallics, the complete particle dissolution is thought to be unlikely to occur, due to the low solubility of iron in the aluminum matrix; on the other hand, transformation of iron intermetallics from one phase

to another, partial fragmentation or spherodization is thought to be possible[53–56]. It is worth noticing that, especially in 530 °C solution treated samples, some β-Fe presented a slightly modified morphology, characterized by more rounded edges, if compared to the one observed in as cast samples (Figure 3.27b, white arrows). Further investigations are needed to understand if this effect could be related to dissolution phenomena induced by high temperature solution treatment.

Hardness measurements (Figure 3.28) were carried out after solution treatment at 515 and 530 °C, followed by quench in hot water and artificial aging at 200 °C for 2 h. The comparison aimed at evaluating the best combination of time/temperature for the second stage, aiming to maximize the increase of mechanical properties while maintaining at a minimum temperature and time of treatment.

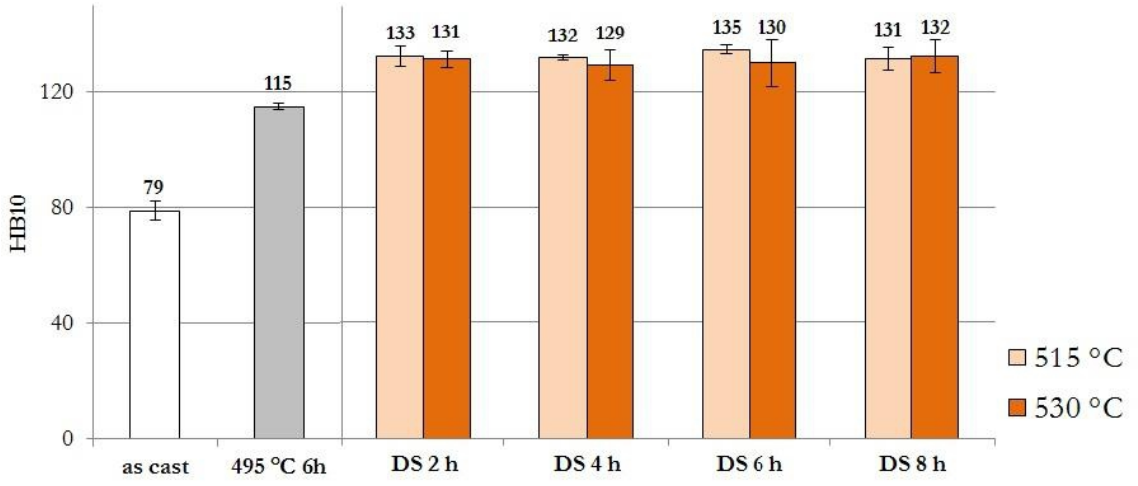

Figure 3.28. Hardness of A354 alloy in the as cast condition, after solution treatment at 495 °C – 6h and after Double Stage (DS) solution at 495 °C - 6 h + 515/530 °C – 2/8 h, followed by quench in hot water (60 °C) and artificial aging at 200 °C - 2 h.

The hardness increase registered after both the first and second solution treatment stage should be mostly related to the diffusion of Cu in the α-Al resulting from the dissolution of θ-Al_2Cu particles. After the first solution treatment stage (495 °C – 6 h), a 45 % hardness increase with respect to the as cast condition was registered (from 79 to 115 HB). As a result of double stage (DS) treatment, a further hardness increase was observed in all the investigated conditions, thanks to the enhanced dissolution of solute elements induced by the higher solution temperature. As observed by SEM-EDS analyses, the almost complete dissolution of Al_2Cu particles, enabled to bring into the α-Al even more Cu. It should be mentioned that, even if Mg containing phases appeared to be macroscopically unmodified

by the second stage solution treatment, a possible Mg and Cu atoms diffusion from π-Fe and Q particles may have contributed to the increase of hardness. The similar hardness values between 515 and 530 °C solution treated samples confirm the absence of appreciable microstructural variations among the DS treated samples, as observed by SEM. By comparing Fig. 3.26 and 3.28, perfect correlation was observed between hardness values and the average fraction of intermetallics in the different solution treatment conditions, as a result of the relationship between increased amount of Cu and Mg atoms in solid solution and increased hardness due to precipitation hardening.

From the present investigation, it is possible to affirm that, taking into account data standard deviation, hardness values are similar in all the investigated conditions (ranging from 130 to 135 HB). In view of this, aiming to the keep the heat treatment cost-effective, the lowest temperature and time (namely 515 °C – 2 h) were chosen for optimization of the solution treatment.

3.2.2 AGING TREATMENT OPTIMIZATION

Aging curves of A354 alloy, obtained as interpolation of hardness values measured on samples aged at 160, 180, 190, 200 and 210 °C, are presented in Figure 3.29. Samples were subjected to artificial aging after solution treatment according to the parameters previously identified (495 °C-6 h + 515 °C-2 h) followed by quench in hot water (60 °C). Differently from Al-Si-Mg alloys, whose aging behavior has been widely studied, the knowledge of age hardening of Al-Si-Cu-Mg, probably due to the intrinsic complexity of precipitation sequence, is not completely well understood. It is well known that Al-Si-Mg and Al-Si-Cu alloys are strengthened by β' (Mg_2Si) and θ' (Al_2Cu) precipitates[57–62], respectively. Quaternary alloys containing both Cu and Mg, as recently investigated, are reported to contain both containing both θ and Q phases, the latter characterized by general stoichiometry $Al_5Cu_2Mg_8Si_6$ (even if some different composition were proposed by different investigators)[63,64]. Minor phases, such as ternary precipitates (e.g. the S' phase, Al_2CuMg[61,65,66]), are also reported by some investigators.

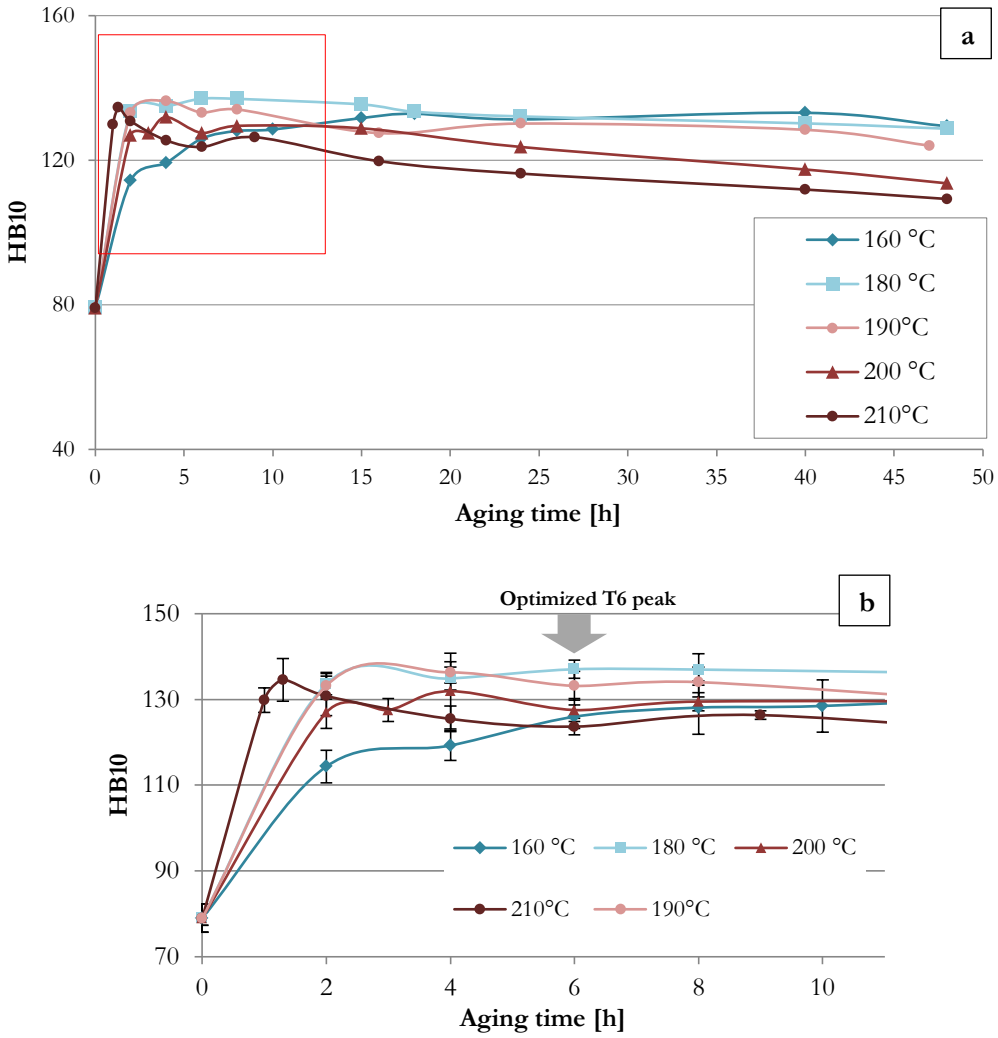

Figure 3.29. (a) Aging curves (HB10) of A354 alloy; samples were solution treated at 495 °C - 6 h, then 515 °C - 2 h, water quenched (60 °C) and aged at 160, 180, 190, 200 and 210 °C for maximum 48 h; (b) focus on the first 10 hours of aging.

From the analyses of the curves, it is clear that aging temperature plays an important role on precipitation hardening. At 160 °C, i.e. the lowest investigated temperature, the initial increase of hardness is slow, due to the low rate of atomic diffusion associated to low temperatures. In this condition, the hardness peak value (≈133 HB) is reached after 18 h of aging. By increasing aging temperature, i.e. 180 and 190 °C, kinetics of precipitation are faster, and a shorter time in comparison to the 160 °C curve is needed to reach the peak condition. At these temperatures, the peak value is basically the same, 135 HB, reached after 6 and 4 h of aging at 180 °C and 190 °C, respectively. At higher temperature, atomic diffusion mechanisms are further accelerated. As a result, at 210 °C, the initial slope of the aging curve is particularly steep. Time to peak (≈ 135 HB) is clearly decreased (about 90 min). Results obtained in the present investigation are in accordance to what has been

observed by other researchers, reporting decreasing time to peak by increasing the aging temperature[46,67]. Some authors report also that, by increasing the aging temperature, peak hardness and yield strength are generally reduced[52,68,69].

Aging temperature influences the alloy behavior after the peak condition. At the lowest temperatures (160, 180 °C), once the peak is reached, the hardness of the alloy remains basically constant, reaching a kind of plateau. Differently, at higher aging temperatures (190 – 210 °C), once the peak is reached, hardness decreases. In particular, at 210 °C, a loss of about 10 HB was registered after 2 h from the peak condition. Hardness decrease is the result of overaging, which involves coarsening of strengthening precipitates (Ostwald ripening). Kinetics of coarsening in Al-Si-Cu-Mg alloys has been investigated by Ovono et al.[70], who found that overaging of high Cu (3 wt%) Al-Si-Cu-Mg alloys can be described by the classical ripening theory. In particular, the authors observed that the evolution of strengthening precipitates is governed diffusion processes, well fitting the Lifshitz, Slyozov and Wagner (LSW) theory. The same kind of mechanism, based on Ostwald ripening model, is thought to be involved in the overaging of the investigated alloy. It should be mentioned that some authors reported for Al-Si-Cu-Mg alloys the presence of double aging peaks, for temperatures higher than 175 °C. The two aging peaks, documented by Li et al.[68] for an alloy with similar composition (9.35 Si-1.48 Cu-0.53 Mg) to the one investigated in the present work, were related to the formation of high-density GP zones and to θ' metastable phases, respectively. In the current investigation, no clear evidence of this phenomenon was observed.

As a conclusion, from the aging curves it was shown that the peak value of 135 HB is reached both at 180 °C and 190 °C, after 6 and 4 h, respectively. In view of the fact that at 190 °C coarsening phenomena lead to hardness decrease once reached the peak, the more conservative temperature of 180 °C was chosen as optimal temperature for aging treatment.

3.2.3 OVERAGING BEHAVIOR

The response of T6 heat-treated A354 alloy to high temperature exposure was investigated. A354 samples were T6 heat treated at the peak condition as described in the previous paragraph (DS solution treatment, quench in hot water at 60 °C and aging at 180 °C – 6 h), then subjected to soaking at different temperatures (200, 245, 290 °C) up to 168 h, i.e. 7 days. For comparison, other alloys were subjected to the same treatment conditions,

namely: A354 and C355 alloys, both in non-optimized heat treated condition (indicated as A354-HT and C355-HT*), and a typical Al-Si-Mg alloy, the A356-T6 (whose data were derived from previous experimental work carried out at Metallurgy Group), aiming to evaluate the influence of Cu on overaging response of Al-Si-Mg alloys. A356 alloy was heat treated according to the following parameters: solution treatment at 535 °C – 4.5 h, quench in water at room temperature and artificial aging at 160 °C for 4.5 h. It should be pointed out that, for similarity, samples with similar SDAS values (20-30 μm) were characterized, in order to avoid the influence of different microstructural fineness.

The overaging curves of A354 alloy, in the optimized and industrial heat treatment conditions (T6 and HT, respectively) are reported in Figure 3.30. A354-T6 and A354-HT present, as expected, similar overaging behavior at 200 °C. Initial hardness values are different (135 HB vs. 120 HB), due to the different heat treatment parameters applied. This gap is basically maintained during high temperature exposure; after about 120 h the difference between the two alloys is reduced to about 8 HB.

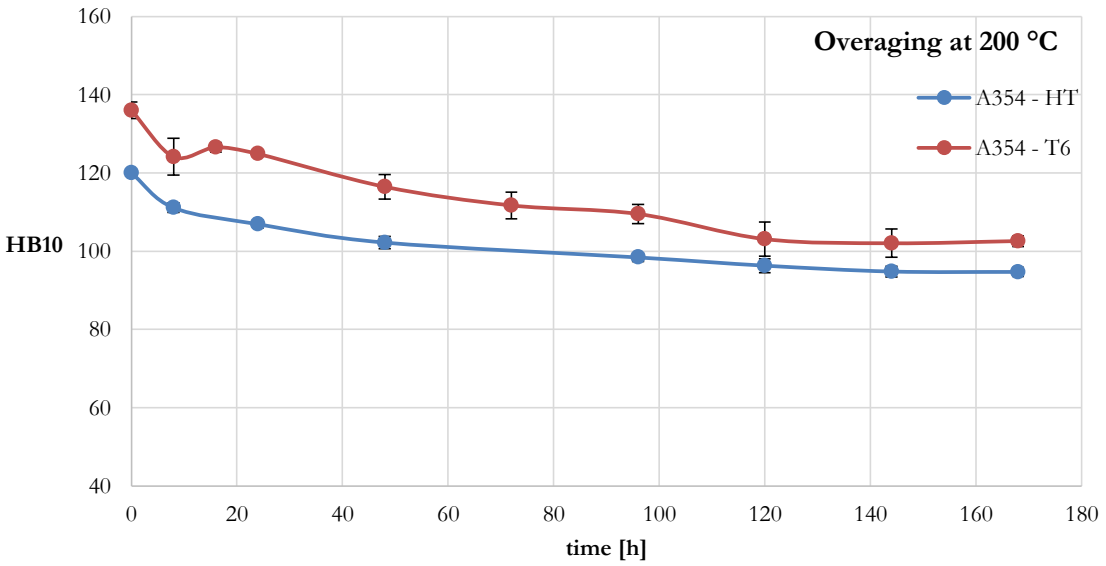

Figure 3.30. Comparison of the overaging curves of A354 alloy in the peak aging optimized heat treatment condition (A354-T6) and in the industrial heat treatment condition (A354-HT). Overaging temperature: 200 °C.

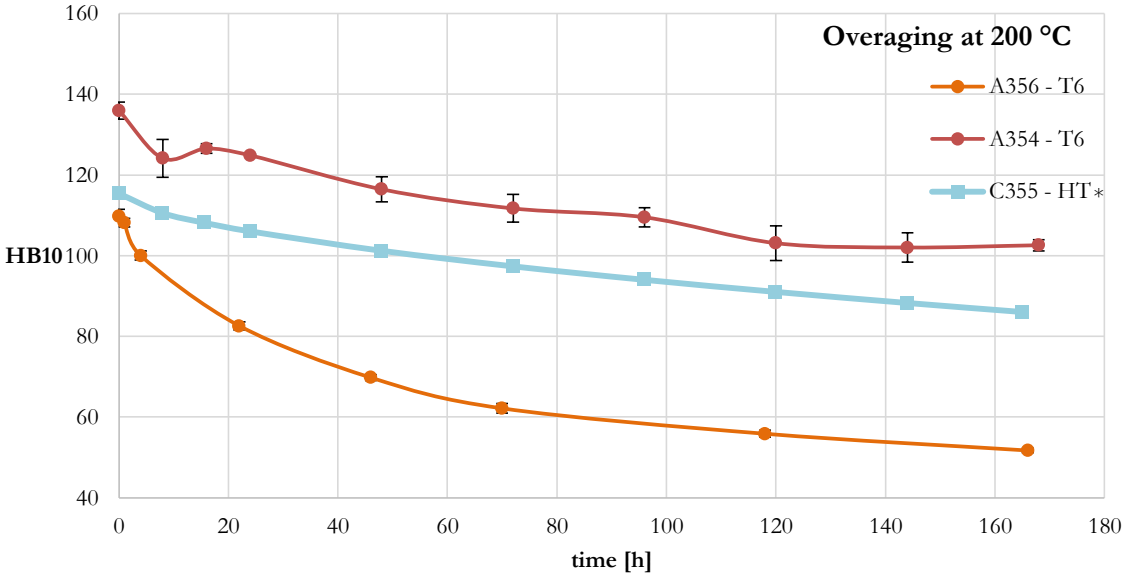

Figure 3.31. Comparison of overaging behavior of two Al-Si-Cu-Mg alloys (A354-T6, C355-HT*(not optimized heat treatment)) and an Al-Si-Mg alloy (A356-T6) characterized by comparable SDAS values (20-30 μm). Overaging temperature: 200 °C.

The effect of chemical composition on overaging response has been showed in Figure 3.31, where A354-T6, C355-HT* and A356-T6 are compared. First of all, it is clear that A356-T6 presents a different behavior in comparison to both A354 and C355 alloys. While Al-Si-Cu-Mg alloys maintain a certain stability even after 48 h of overaging, with a hardness decrease of about 12-15%, A356 is subjected to a more consistent hardness loss, of about 35%. With increasing overaging time, hardness of A356-T6 alloy further decreases, reaching the minimum value of 52 HB after 7 days (-52% of the initial value). At the same time, both the Al-Si-Cu-Mg alloys still maintain good level of hardness, with 86 and 102 HB for C355-HT* and A354-T6 alloys, respectively (-25 % of the initial hardness for both the alloys). In view of the differences in chemical composition between A354, C355 and A356 alloys, in particular for the Cu content (~1.5, 1 wt% and 0%, respectively), it is clear that copper strongly enhances the thermal stability of Al-Si-Mg alloys, by reducing precipitates tendency to coarsening.

A354-T6 and C355-HT* alloys behavior at higher temperatures is compared in Figure 3.32 and 33, where the overaging curves at 245 and 290 °C are reported. Once again, the two alloys show similar behaviors, both at 245 and 290 °C. The alloys mainly differ from the initial hardness value, 115 and 135 HB for C355 and A354, respectively. A gap between the curves of the two alloys is maintained also during overaging.

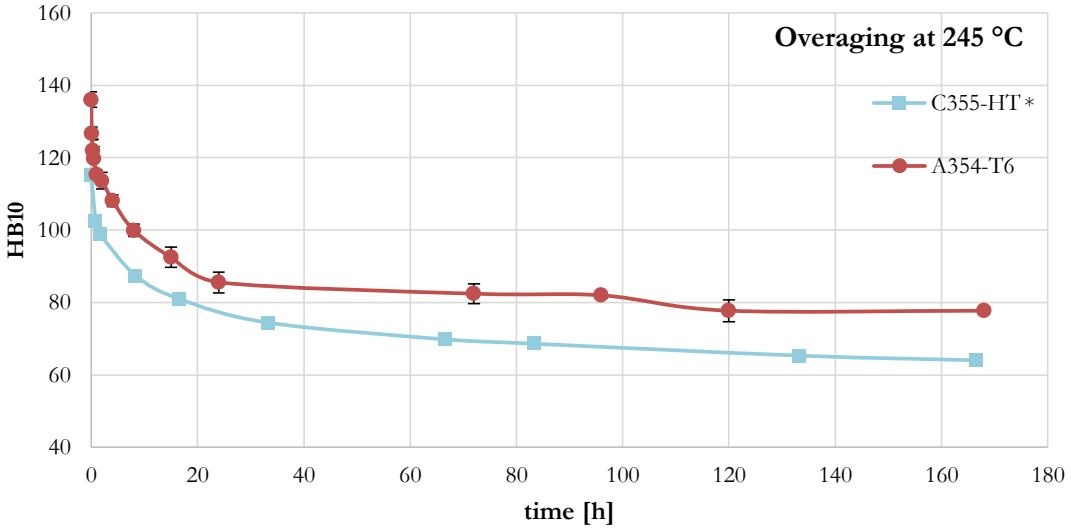

Figure 3.32 Comparison of overaging behavior of A354-T6 and C355-HT* alloys at 245 °C. Overaging temperature: 245 °C.

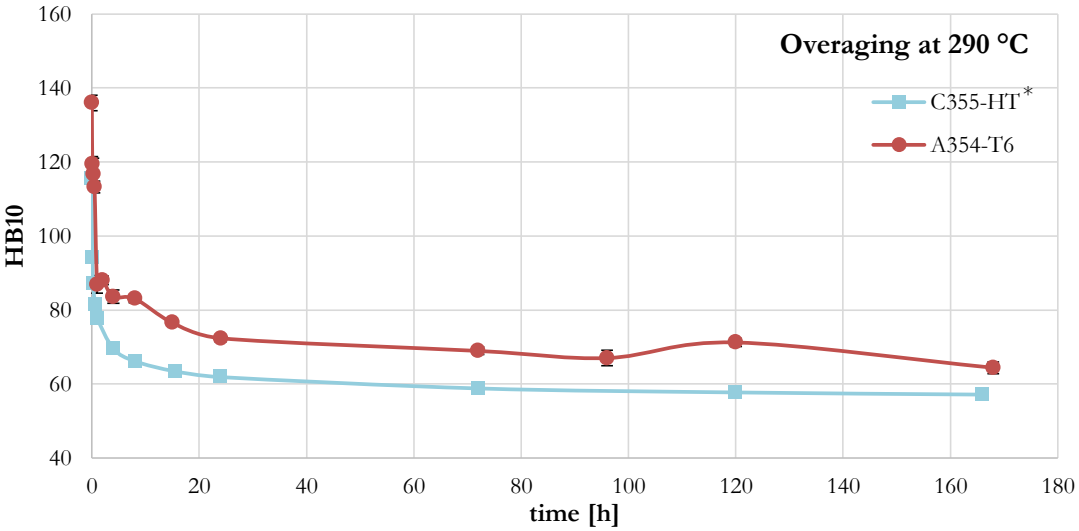

Figure 3.33. Comparison of overaging behavior of two A354-T6 and C355-HT* alloys at 290 °C. Overaging temperature: 290 °C.

By increasing the temperature, coarsening phenomena are even faster, and consequently the hardness drop is more pronounced. At 290 °C, in fact, after 4 hours of soaking, hardness of the two alloys is decreased of about 40 % in comparison to the initial value. Hardness plateau is reached after about 24 h of soaking, both at 245 and 290 °C. The noticeable hardness decrease registered at high temperature is strictly related to the Ostwald ripening induced by high diffusion rate and solid solubility of both Cu and Mg in the α-Al matrix. In particular, it is thought that at 290 °C, the only strengthening phase

remained is the quaternary Q phase, in view of the investigations reported by Farkoosh et al.[15] on an Al-7Si-0.5Cu-Mg alloy. After 100 h of soaking at 300 °C, the θ-Al_2Cu phases were in fact completely dissolved in the matrix and, thanks to the higher thermal stability, only the Q phase ($Al_5Cu_2Mg_8Si_6$) was observed by TEM to remain effective in hindering dislocation movement[71].

3.2.4 TENSILE PROPERTIES

Mechanical properties (UTS, YS, Elongation to failure) of A354 alloy in the optimized heat treatment condition were compared with C355–HT and A354–HT alloys; data are summarized in Figure 3.34 and 3.35. Tensile tests were carried out at room temperature, both in the T6/HT condition and in the overaged condition. The aim was to test A354-T6 and A354-HT alloys at equal residual hardness. In such a way, it was possible to investigate if, after a longer overaging, A354-T6 alloy would have maintained the same mechanical properties of A354-HT. Since A354-HT alloy in the overaged condition (210 °C – 41 h) presented 113 HB, an overaging of 210 °C – 50 h has been adopted for A354-T6 alloy, aiming to reach almost the same hardness level. Brinell hardness of the tested alloys are reported in Table 3.6.

Table 3.6. Brinell hardness of the materials under investigation, measured on tensile samples. T6 indicates the optimized heat treatment, while HT represents the industrial treatment.

	A354 - T6	**A354 - HT**	**C355 - HT**
HT/T6	130±2	120±2	125±1
Overaged	112±2	113±3	107±2

Enhanced tensile properties at room temperature were registered for A354 alloy in the optimized heat treatment condition, in comparison both to the same alloy, commercially heat treated, and to the C355-HT alloy. In particular, when compared to A354-HT alloy, UTS and YS increased about 10 % and 5 %, respectively. This enhancement should be related in particular to the optimization of artificial aging phase. As observed through STEM analyses on A354-HT samples, in fact, the commercial heat treatment, by aging the alloy at 210 °C for 6 h, was likely to induce a slight coarsening (i.e. overaging) of strengthening precipitates (Figure 3.8). This hypothesis was moreover confirmed by the evaluation of the aging curves of the alloy, as previously discussed in Paragraph 3.2.2 (Figure 3.29).

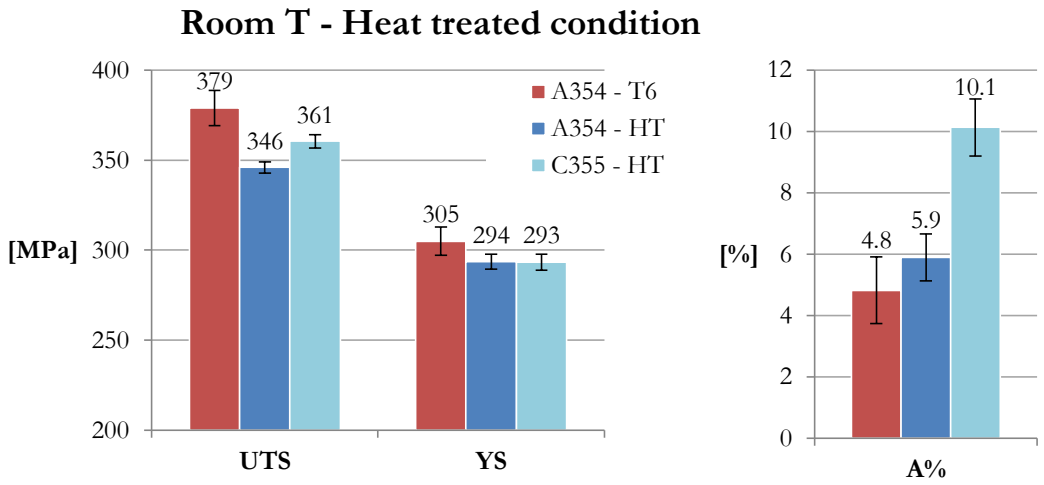

Figure 3.34. Comparison of room temperature tensile properties (UTS , YS and elongation to failure, E%) of A354-T6, A354-HT and C355-HT alloys.

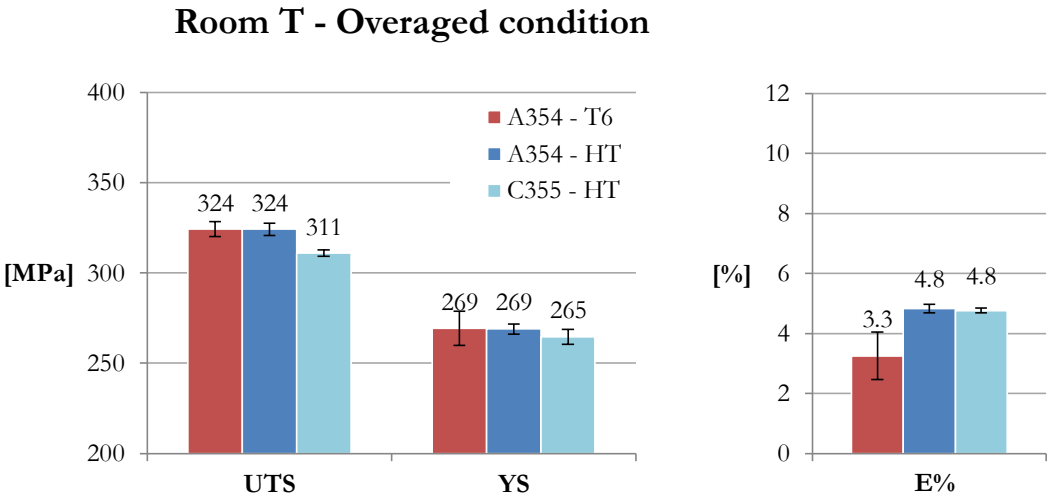

Figure 3.35 Comparison of room temperature mechanical properties of the overaged A354-T6, A354-HT and C355-HT alloys; UTS, YS and elongation to failure, E%. Overaging was carried out at 210 °C – 41 h for A354 and C355-HT alloys, while 210 °C – 50 h for A354-T6.

At 210 °C aging temperature, the hardening peak is reached after only 1 h, but then hardness of the alloy rapidly decreases, due to the coarsening mechanisms induced by diffusion processes. Also comparing A354-T6 properties with C355-HT alloy, an enhancement of UTS was observed. In particular, it should be pointed out that in the old heat treatment condition, even if C355 alloy contains a lower content of Si and, above all, Cu, it presented higher UTS in comparison to A354-HT. By optimizing heat treatment, the higher content of Cu and Si of A354 alloy has been exploited. Elongation to failure, as

previously observed, is lower in comparison to C355 alloy, due to the higher Si content, leading to higher eutectic fraction and lower ductile α-Al phase. Moreover, a slight decrease of elongation to failure was registered in the optimized heat treatment condition in comparison to A354-HT alloy. This behavior was anyway somehow expected; it is well-known in fact that mechanical properties enhancement induced by peak aging is generally at the expenses of ductility. Anyway, also in the proposed conditions, the alloy shows good levels of ductility (about 5 %). In the overaged condition, UTS and YS of A354-T6 alloy were the same measured for A354-HT alloy. This confirms that longer overaging at the same temperature (i.e. 210 °C) induces the same mechanical properties of A354-HT alloy in A354-T6. Small differences in elongation to failure were reported between the overaged A354-T6 and A354-HT alloys (3.3 vs 4.8 %, respectively).

As discussed in Paragraph 3.1.2, the superior thermal stability of A354 alloy in comparison to C355 was observed, both A354-HT and A354-T6 showing higher UTS and YS after overaging at 210 °C (41 and 50 h, respectively). Moreover, as summarized in Figure 3.36, it is therefore possible to affirm that the proposed heat treatment for A354 alloy allows to reduce treatment time and temperature, both in the solution and in the aging phases, while enhancing mechanical properties at room temperature and maintaining the same UTS, YS values after longer overaging at 210 °C (50 h vs 41).

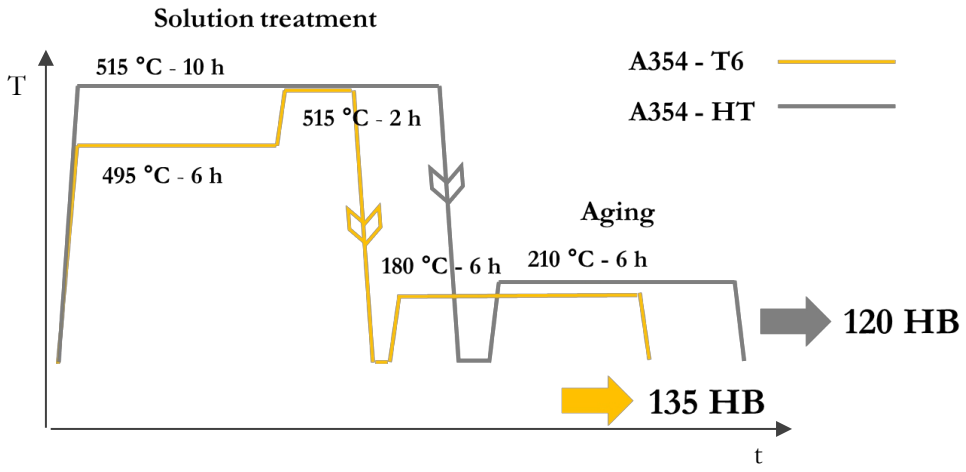

Figure 3.36. Comparison of times and temperatures parameters of industrial (HT) and optimized (T6) heat treatment for A354 alloy.

3.2.5 FRACTOGRAPHIC ANALYSES

SEM analyses revealed that, as expected, tensile fracture surfaces were characterized by a typical ductile behavior (Figure 3.37). Fine and uniformly distributed dimples were, in fact, observed both in the T6 heat treated and overaged samples, tested at room temperature. Fractured eutectic Si particles, as a result of load transfer from matrix to hard Si particles were also observed.

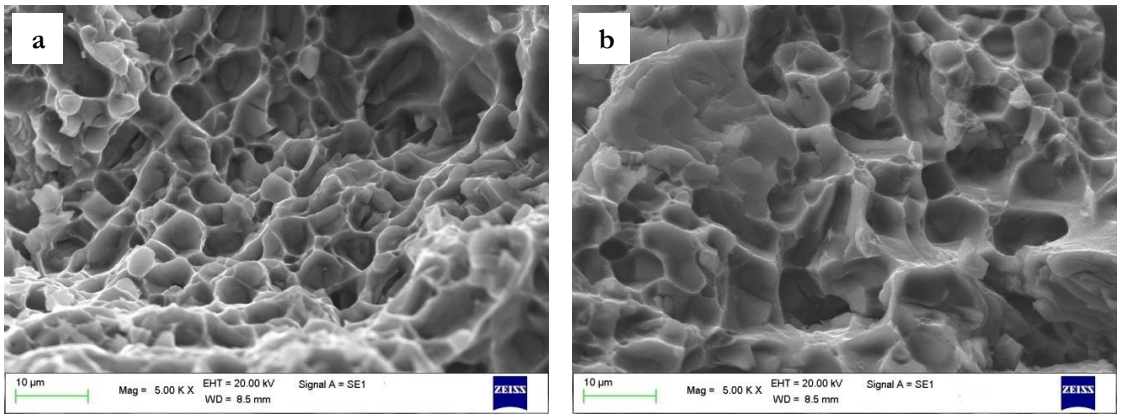

Figure 3.37. SEM images of fracture surfaces of A354 tensile samples in the (a) T6 and (b) overaged condition, tested at room temperature.

3.2.6 CONCLUSIONS

As a result of the research activities described in Paragraph 3.1, it was clear that heat treatment parameters employed for A354 alloy, derived from industrial practice, were not optimized. In particular, the alloys presented slight overaging. Aiming to fully exploit the potential of A354 alloy, a dedicated study on the optimization of its heat treatment was carried out. As optimization criteria, the aim of the work was the determination of heat treatment parameters ensuring the maximization of mechanical strength (HB, UTS, YS) while keeping at a minimum temperature and time of treatment. It should be mentioned that, for industrial exploitation of the treatment, good values of elongation to failure should also be maintained. The main results may be summarized as follows:

- Solution treatment was studied on the basis of thermal analyses associated to microstructural analyses. Aiming to avoid incipient melting, a first solution step at 495 °C – 6 h meant to dissolve the low melting compounds is needed. A second phase at higher temperature, 515 °C – 2 h, was the best choice to maximize hardness while maintaining treatment time and temperature as limited as possible. Quench condition was maintained fixed in hot water (60 °C).
- Artificial aging of the alloy was studied, by investigating aging curves from 160 to 210 °C. The peak hardness (135 HB) was obtained after 6 h at 180 °C.
- Overaging behavior of the alloy at 200, 245 and 290 °C was studied; the influence of Cu content on overaging behavior was investigated, by comparing the response to high temperature exposure of A354 alloy to that of C355 (Al-Si-Cu-Mg) and A356 (Al-Si-Mg) alloys. The analyses revealed that Cu-containing alloys present a higher thermal stability in comparison to the ternary Al-Si-Mg alloy. Such difference should be related to the presence of Cu-based precipitates induced by heat treatment, which are reported in the literature to possess higher coarsening resistance in comparison to the binary β-Mg_2Si and θ-Al_2Cu contained in traditional Al-Si-Mg and Al-Si-Cu alloys.
- The optimized heat treatment conferred to the alloy higher room temperature mechanical properties (HB, YS, UTS) in comparison to the not-optimized one; good level of ductility, i.e. elongation to failure, was maintained (E%=3.3%). Moreover, benefits of the optimized heat treatment in term of high temperature exposure resistance were confirmed by tensile tests in the overaged condition.

3.3 Results and Discussion – PART 3

Mo addition to Al-Si-Cu-Mg alloys

3.3.1 CASTINGS PRODUCTION

Al-Mo10 master alloy employed for the production of Mo-alloyed castings was analyzed by SEM to investigate the morphology of Mo-rich crystals and to evaluate their possible incomplete dissolution in the produced castings. The microstructure of the alloy was characterized by Al matrix and Mo-rich needle-like intermetallics (about 500~800 μm in length), shown at low and high magnification in Figure 3.38.

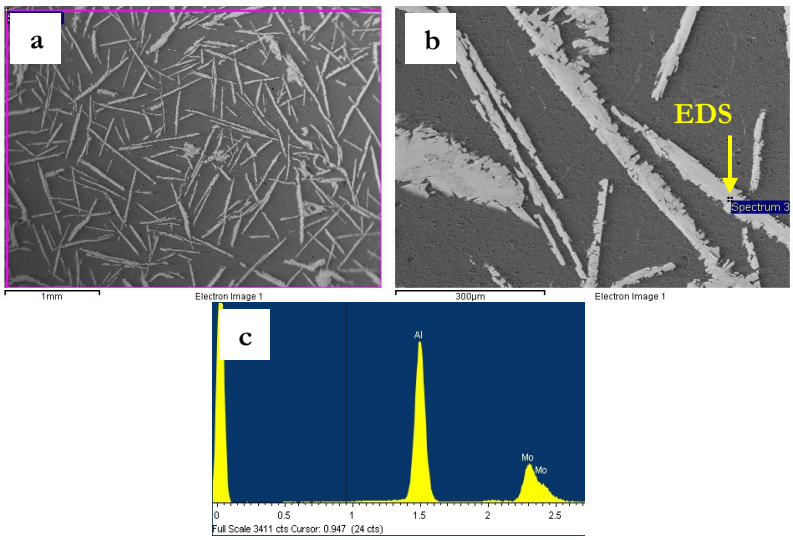

Figure 3.38. SEM images of Al-Mo10 master alloy at (a) low and (b) high magnification, and (c) corresponding EDS spectra.

Aiming to evaluate the effect of Mo addition on the overaging response of Al-Si-Cu-Mg alloys, castings of A354 alloyed with 0.1, 0.3, 0.5 and 0.8 wt% of Mo were produced. The first research phase was addressed also to the optimization of casting parameters for obtaining an even distribution of Mo throughout the casting. GD-OES analyses were carried out on the produced castings to assess the actual chemical composition, whose results are summarized in Table 3.7. Segregation of Mo was registered; in particular higher Mo content was found in the bottom part of the castings. This was due to the higher specific gravity of Mo in comparison to Al, (10.28 vs 2.70 g/cm^3), inducing settling of the Mo-rich phases to the lower part of the castings.

Table 3.7. Chemical composition (wt.%) of the produced A354-Mo castings, measured through GD-OES analyses.

		Si	Cu	Mg	Mo	Fe	Mn	Ti	Al (bal.)
0.1Mo	Top	8.91	1.895	0.532	**0.132**	0.126	0.014	0.126	87.907
	bottom	8.915	2.181	0.583	**0.142**	0.147	0.015	0.178	87.699
0.3Mo	Top	8.546	1.786	0.506	**0.329**	0.140	0.013	0.105	88.210
	bottom	8.864	1.867	0.500	**0.418**	0.132	0.012	0.121	87.904
0.5Mo	Top	8.718	1.732	0.480	**0.639**	0.121	0.013	0.111	87.901
	bottom	8.671	1.653	0.480	**0.810**	0.116	0.013	0.128	87.861
0.8Mo	Top	8.574	1.533	0.432	**0.781**	0.099	0.013	0.118	88.136
	bottom	8.728	1.488	0.42	**0.992**	0.096	0.012	0.142	87.82

The chemical inhomogeneity documented by GD-OES was also reflected in the microstructure of the castings, characterized by Mo-rich coarse (50~100 μm) and agglomerated particles (Figure 3.39). Most of them seemed to be segregated intermetallics formed during casting production (Figure 3.39a), but also undissolved Mo-based needles from the master alloy were observed (Figure 3.39b).

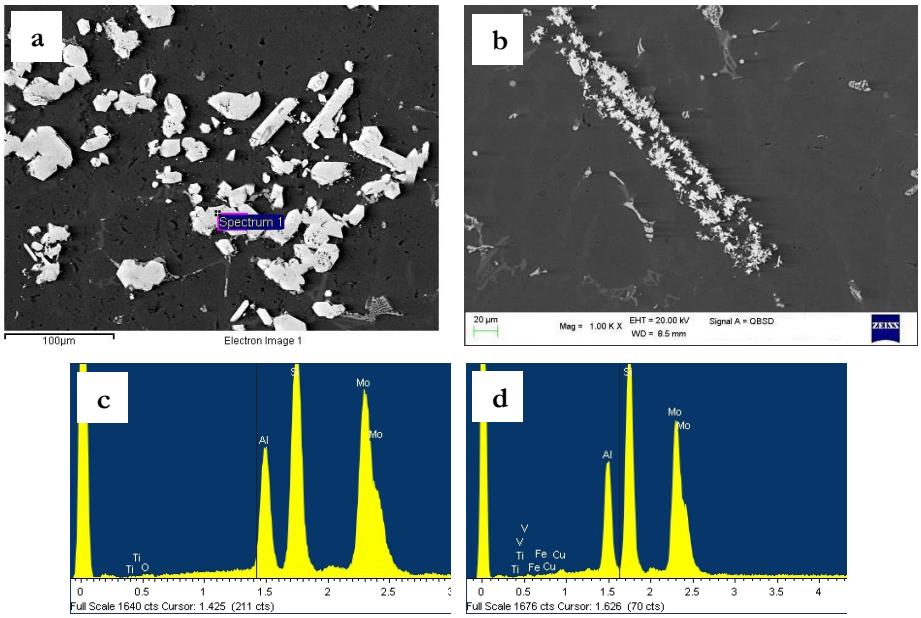

Figure 3.39. SEM images of cluster of Mo-rich particles observed in (a) A354-0.1Mo and (b) A354-0.3Mo castings with (c, d) corresponding EDS spectrum.

Aiming to obtain a more even distribution of Mo within the castings, the production process parameters were modified, as described in Paragraph 2.3.1. In particular, in order to favour Mo dissolution from the Al-10Mo master alloy and to promote diffusive phenomena to obtain a more homogeneous composition, a higher holding temperature and increased holding time were adopted (900 °C – 30 min); electromagnetic stirring of the melt was also applied during holding at 900 °C. It should be mentioned that, in view of the

preliminary study on heat treatment (described in the following Paragraph), Mo addition of 0.3% was considered the most promising one for the successive research phases (solution treatment and tensile properties study).

Chemical composition of the A354-0.3Mo castings produced with optimized process parameters is reported in Table 3.8. It is possible to observe that the modified casting technique allows to (i) obtain a more homogeneous composition between top and bottom of the casting, (ii) the actual amount of Mo (0.322-0.338 wt.%) well fits to the target value (0.3 wt.%).

Table 3.8. Chemical composition (wt.%) of A354-0.3Mo ingot produced by modified casting parameters, measured by GD-OES.

		Si	Cu	Mg	Mo	Fe	Mn	Ti	Al (bal.)
0.3Mo	Top	8.999	1.647	0.452	**0.322**	0.122	0.009	0.100	87.798
	bottom	9.057	1.676	0.467	**0.338**	0.126	0.009	0.099	87.731

3.3.2 PRELIMINARY HEAT TREATMENT STUDY

The preliminary evaluation of overaging response of the Mo-modified alloys was carried out, aiming to identify the most promising chemical composition for further studies. Samples of the four produced castings were heat treated by double step solution treatment, namely 6 h at 495 °C, then 1 h at 540 °C. The first solution phase at 495 °C was carried out since thermal analyses (Figure 3.40) revealed the presence of the low melting phase observed in A354 alloy, as shown in Par. 3.2.

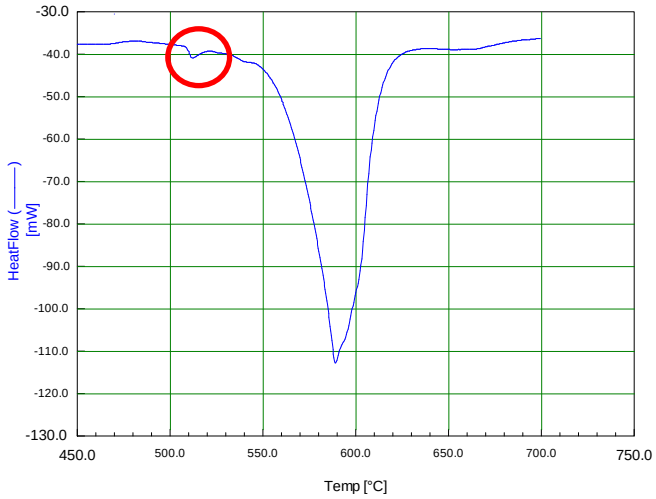

Figure 3.40. DTA thermograph obtained on the as-cast A354-0.3Mo, highlighting the presence the endothermic peak at ~509 °C (red circle), previously observed on A354 alloy.

Three different post-solution treatment conditions were then investigated and subjected to overaging, namely: (i) air cooling, (ii) water quench at 60 °C, (iii) artificial aging at 180 °C – 4 h after 60 °C water quench. The samples were simultaneously subjected to overaging at 245 °C, for up to 300 h. Overaging curves, showing the variation of hardness with time, are reported in Figure 3.41. It is possible to observe that, among the investigated Mo contents, the lowest Mo amount, 0.1 Mo wt.%, presents the lowest hardness values with overaging; on the other hand, no significant differences were registered among the curves corresponding to Mo contents from 0.3 to 0.8 wt.%. In this regard, it should be taken into account that, as shown in Paragraph 1.6, the maximum solid solubility of Mo into Al is 0.25wt% at the peritectic reaction (~660 °C).

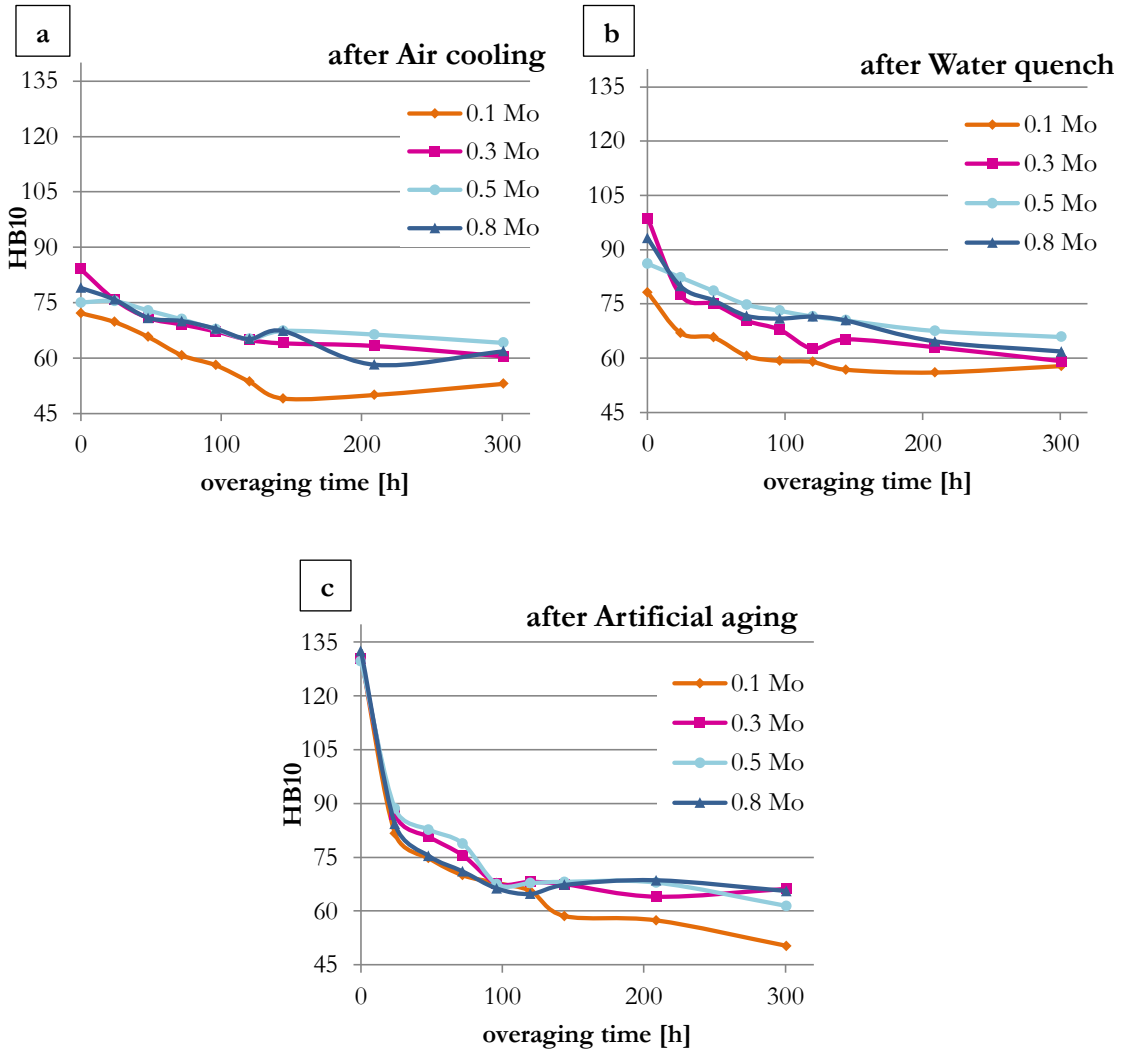

Figure 3.41. Overaging (245 °C) response of A354 alloy containing 0.1wt.%Mo (0.1 Mo), 0.3wt.%Mo (0.3 Mo), 0.5wt.%Mo (0.5 Mo) and 0.8wt.%Mo (0.8 Mo) after (a) air cooling and (b) water quench at 60 °C after double step solution treatment, (c) after artificial aging at 180 °C – 4 h.

In view of this, it is possible to think that additions of Mo weight fractions above this threshold (i.e. 0.3, 0.5 and 0.8%) result in the formation of higher amounts of coarse primary particles. For this reason, 0.3 wt.% Mo content was chosen for successive research steps (i.e. study of solution treatment and tensile testing). In the artificial aging condition, such difference was somehow hidden by the prevailing hardening effect of heat treatment Cu and Mg based precipitates; as a matter of fact, overaging curves appeared almost overlapped up to about 100 overaging hours. By comparing overaging behavior, it is possible to observe also that, as expected, cooling media plays a role on the alloys hardness: at t=0, quenched alloys present higher hardness values in comparison to the corresponding air cooling condition; such difference could be explained by a combined strengthening effect due to super-saturated solid solution generated by quench and natural aging, occurred before hardness test. With high temperature exposure during overaging, however, such reinforcing contribution is gradually lost due to diffusive phenomena, leading to equilibrium structure. The influence of cooling medium is even more clear in graphs of Figure 3.42a-d, where the overaging curves of each alloy are compared on the basis of the different treatment condition. It can also be observed that, by exposure at 245 °C, most of the strengthening effect of heat treatment precipitates is lost after 24 h of overaging (about 35% hardness decrease). However, after 300 h of overaging at 245 °C, in all the investigated materials, hardness is basically the same among the different heat treatment conditions; strengthening contribution of solid solution and heat treatment strengthening precipitates lost efficiency, resulting in a hardness plateau of about 66 HB10 (55 in the case of 0.1 wt.% Mo).

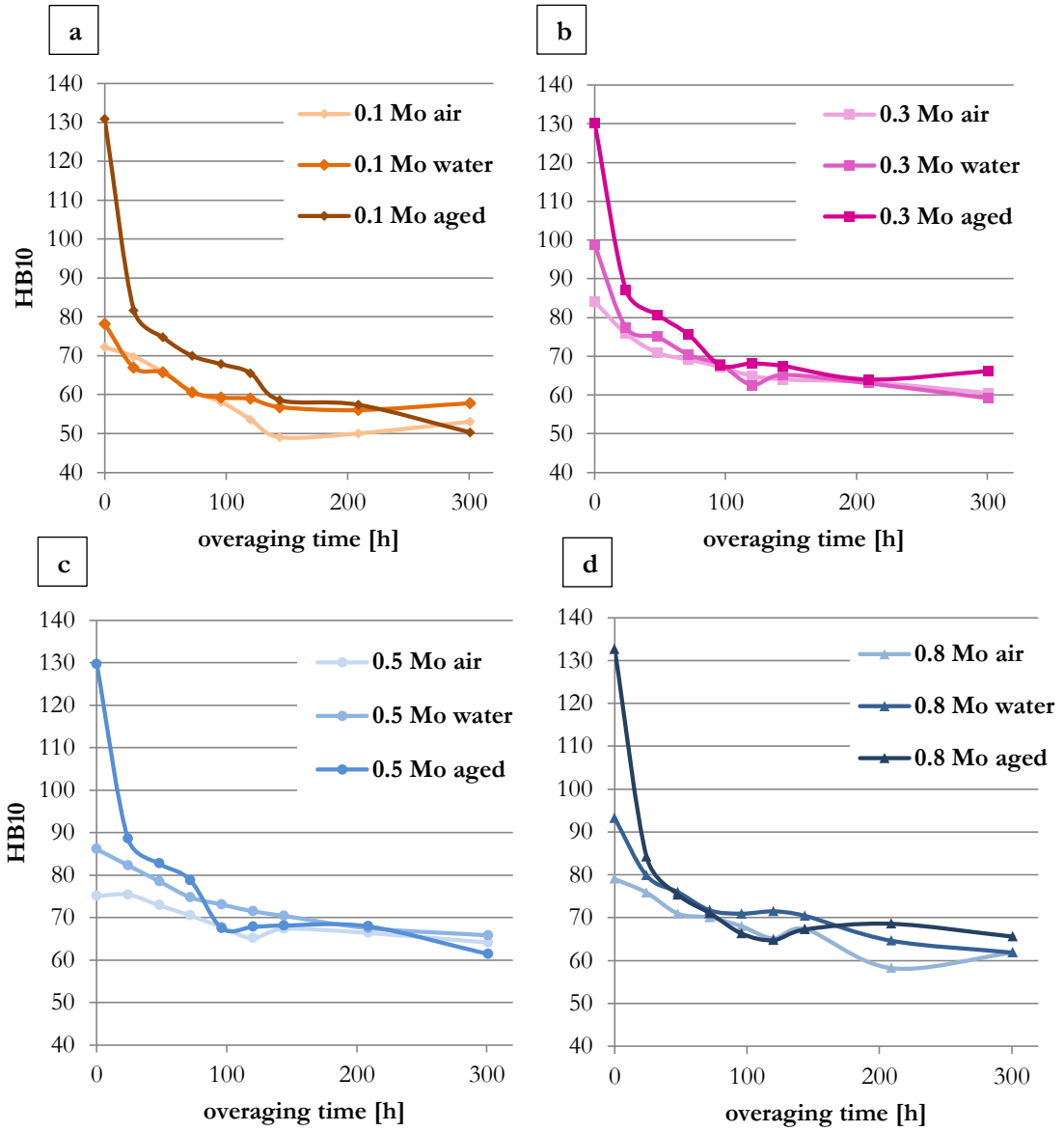

Figure 3.42. 245 °C overaging curves of (a) 0.1 wt. Mo, (b) 0.3 wt. Mo, (c) 0.5 wt. Mo and (d) 0.8 wt. Mo after air cooling, water quench at 60 °C and after artificial aging (180 °C – 4 h).

3.3.3 MICROSTRUCTURAL CHARACTERIZATION

In view of the preliminary study on overaging response, 0.3wt.%Mo amount was selected for further heat treatment study. Microstructural analyses were carried out on A354-0.3Mo ingots produced with modified casting parameters by optical (OM) and scanning electron microscopy (SEM-EDS). SDAS of the castings was 30±5 μm. Comparative optical images of the as cast condition and after solution treatment (in particular after the second solution step at 540 °C for 1 and 24 h) are presented in Figure 3.43a-f. In the as cast condition, the typical microstructure of A354 alloy was observed, characterized by the presence of α-Al dendrites surrounded by the eutectic structure. Eutectic silicon particles appeared partially unmodified, characterized by acicular morphology shown in Figure 3.43d. Since the casting

was modified by addition of 300 ppm Sr, it is possible to hypothesize that an interaction between Sr and Mo occurs, since no modification effect was observed in the casting. On the other hand, solution treatment at 495+540 °C played a role as thermal modifier: even though some unmodified particles were still present, eutectic Si presented more rounded edges after 1 h at 540 °C (Figure 3.43e), even more pronounced after 24 h (Figure 3.43f), in comparison to the as cast state.

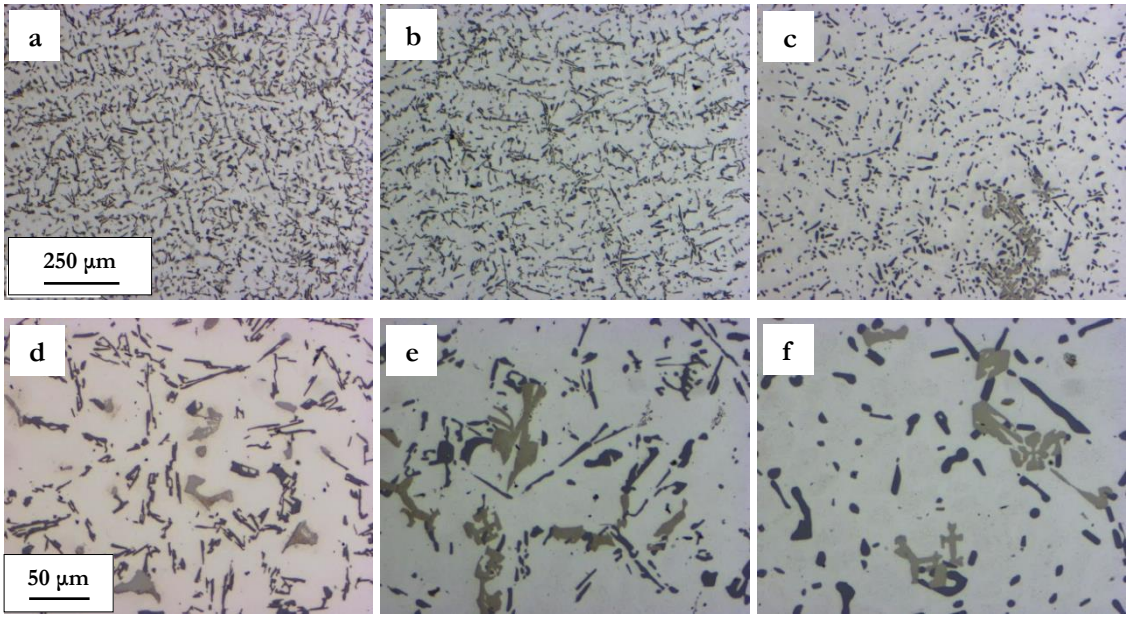

Figure 3.43. Optical images of A354-0. 3Mo alloy in the (a, d) as cast condition, after double step solution treatment consisting in the first step at 495 °C – 6 h followed by a second step at 540 °C for (b, e) 1 h and (c, f) 24 h.

As concerning intermetallic particles, both eutectic and block-like θ-Al_2Cu phases, π-$Al_8Mg_3FeSi_6$ and Q-$Al_5Cu_2Mg_8Si_6$ particles, typically found also in A354 alloy, were observed. A SEM overview of the as-cast microstructure was reported in Figure 3.44, while high magnification images of intermetallic particles are shown in Figure 3.45.

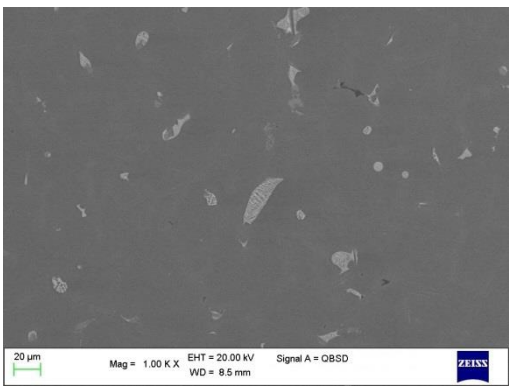

Figure 3.44. SEM image of A354-0.3Mo alloy in the as-cast condition, showing the overall microstructure.

Together with the previous phases, Mo-rich intermetallics were also observed; in particular, two different morphologies of Mo-based particles were found: (i) block-like particles, containing Al, Si, Fe and Mo, mostly observed in interdendritic regions (Figure 3.45a), in association with other intermetallics (in particular θ-Al_2Cu phases), (ii) polygonal or star-like particles, containing only Al, Mo and Si, observed within the α-Al region (Figure 3.45b).

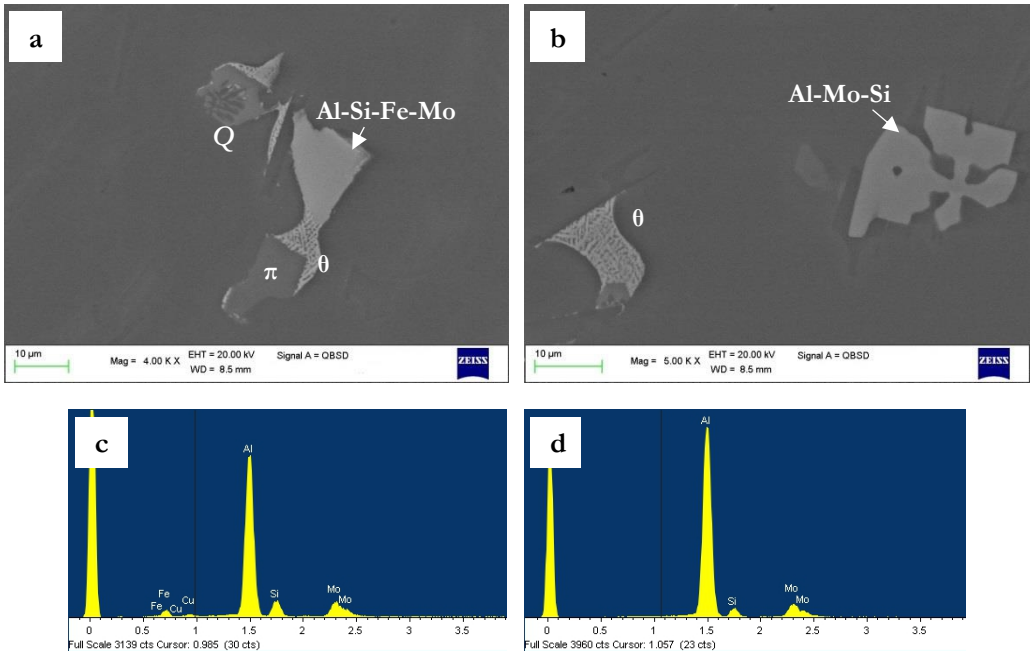

Figure 3.45. As-cast A354-0.3Mo SEM images of representative (a) Al-Si-Fe-Mo particle found in association with other coarse intermetallic phases in the interdendritic region, (b) Al-Si-Mo star-like phase observed within the α-Al matrix; (c, d) corresponding EDS spectra.

This fact could indicate that these two phases are formed in different moment during solidification, namely in the liquid metal as primary particles in the case of polygonal particles, while during the last stages of solidification in the case of Al, Si, Fe and Mo phases. The presence of Fe in such phases, in fact, could be due to the local iron enrichment in the liquid metal in interdendritic areas, due to its low solid solubility in α-Al. Interestingly, basically no β-Fe needles were observed. Probably, as suggested by Farkoosh et al., the presence of Mo induces the formation of the above mentioned Al-Si-Fe-Mo and Al-Mo-Si phases, therefore preventing from the nucleation of β-Al_5FeSi particles.

The investigated solution treatment condition was 495-6h followed by 540 °C for 1 and 24 h, both after quench in 60 °C water and after air cooling. From the microstructural point of view, no appreciable difference was observed between water quenched and air cooled samples. Solution treatment at 540 °C led to almost complete dissolution of Cu and Mg based phases, as it is possible to observe on low magnification SEM images reported in Figure 3.46. An image, corresponding to the as-cast condition, was reported as reference

(Figure 3.46a). After 1h of solution treatment at 540 °C (Figure 3.46b), most of the Al_2Cu particles disappeared, being dissolved by the high solution temperature; after 24 h of solution, even more particles were dissolved, and microstructure is basically characterized by very small particles (1~5 μm). Only Mo-rich phases appeared to be poorly affected or even undissolved by solution treatment, as shown in Figure 3.47.

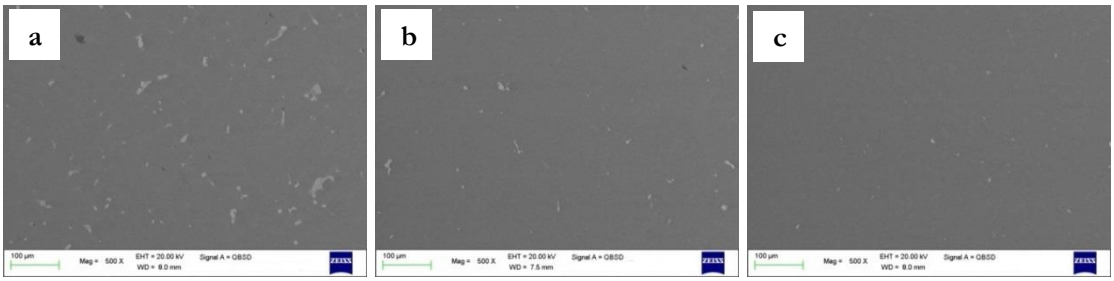

Figure 3.46. Evolution of (a) as cast microstructure after double step solution treatment: after 495 °C – 6 h followed by (b) 540 °C – 1 h and (c) 540 °C – 24 h.

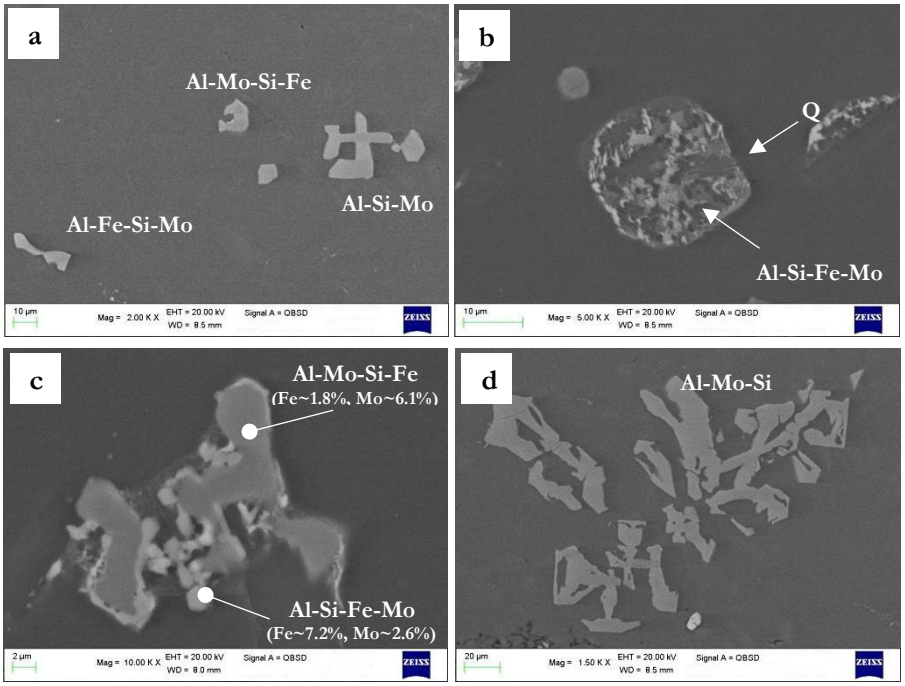

Figure 3.47. (a) Low magnification SEM images of Mo-rich undissolved particles after double step solution treatment, namely 495 °C-6 h and 540 °C-1 h; (b) a small Al-Si-Fe-Mo particle in association to partially dissolved θ and Q phases, (c) an Al-Mo-Si-Fe phase characterized by local enrichment of Fe at the boundary with Al matrix; (d) undissolved Al-Mo-Si particles after 24 h at 540 °C. Elements found in intermetallic particles are listed by decreasing wt.%, as resulted from EDS analyses.

The dissolution of intermetallic particles with increasing solution time was quantified by image analyses, carried out on SEM micrographs. The results are reported in Figure 3.48. The average area fraction covered by intermetallic particles decreased from 1.7 % in the as-cast alloy to 0.46% and 0.30% after solution treatment at 540 °C for 1 and 24 h, respectively, confirming the above visual considerations.

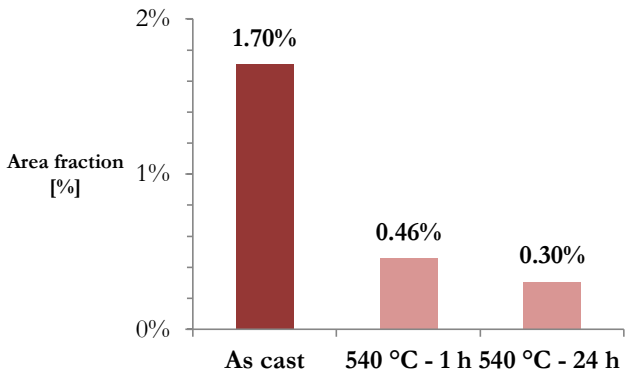

Figure 3.48. Average area fraction covered by intermetallic particles in A354-0.3Mo alloy in the as cast condition and after solution treatment at 540 °C for 1 and 24 h.

3.3.4 HEAT TREATMENT STUDY

Strengthening action of Mo should be related to the formation of stable dispersoids during high temperature solution treatment, as suggested by Farkoosh et al[71]. In particular, the authors claimed that, in a Al-Si7-Cu0.5-Mg0.3 alloy, the hardness peak related to the maximum strengthening effect induced by coherent Mo-based phases, was reached after solutioning 1 hour at 540 °C (after a first step at 495 °C-6h) Aiming to assess the variation of hardness during solution treatment and valuating the presence of stable dispersoids formed during solution, samples of A354-0.3Mo alloy were solution treated at 495 °C – 6 h, then subjected to a second step at 540 °C for different times. Two cooling media were adopted: (i) air cooling and (ii) water quench at 60 °C. Hardness curves are reported in Figure 3.49.

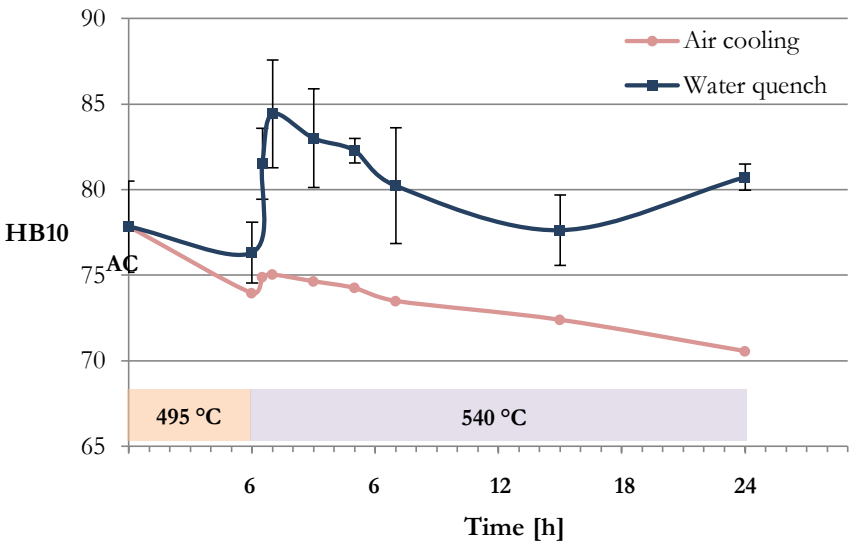

Figure 3.49. Hardness evolution during solution treatment; both air cooling and 60 °C water quench were used as cooling media before measuring hardness.

It is possible to observe that, in the quenched condition, hardness is remarkably increased after solution treatment at 540 °C. In particular, after 1 h at 540 °C (84 HB) the maximum hardness increase was registered in comparison to the as cast value (74 HB). A similar hardness trend was documented also by Farkoosh et al.[71]; it should be however pointed out that the authors used, as in this activity, water quench as cooling medium. Nevertheless, by comparing air and water cooling curves, it is clear that the effect of quench medium plays a significant role on hardness increase. In view of the obtained data, it is thought that, the hardness increase after quench is due both to solid solution contribution induced by non-equilibrium cooling and by partial natural aging induced possibly induced by the brief time occurred before hardness test. However, hardness decrease after 1 h at 540 °C is registered, which cannot be easily related to solid solution strengthening mechanisms. Other phenomena are therefore thought to be involved in hardness evolution. Farkoosh et al.[71] reported that for further solution time, Mo-based dispersoids undergo coarsening and loss of coherency, with consequent drop of hardness. This could explain the reason of the decrease of both the solution hardness curves, in particular also of the one corresponding to the air cooling condition, which should not be related to solid solution strengthening mechanisms. Moreover, a contribution to hardness drop in the water quenched alloy could be also due to the rapid coarsening of possible precipitates formed during natural aging. As a result of these analyses, according to Farkoosh et al.[71], the maximum strengthening effect is obtained after 1 h at 540 °C. In view of this, the solution treatment of tensile test samples was carried out in double stage,

consisting in a first phase at 495°C-6h to dissolve the low melting compound, and a second stage at 540 °C-1 h.

3.3.5 TENSILE PROPERTIES

Results of the tensile tests are summarized in Figure 3.50. A354-0.3Mo alloy was compared to Mo-free A354 alloy. Tensile tests were carried out at room temperature in the T6 condition and at 250 °C after overaging at 250 °C. The effect of different cooling media was investigated, since after double step solution treatment, A354-0.3Mo alloy was subjected to air cooling and quench, then to artificial aging.

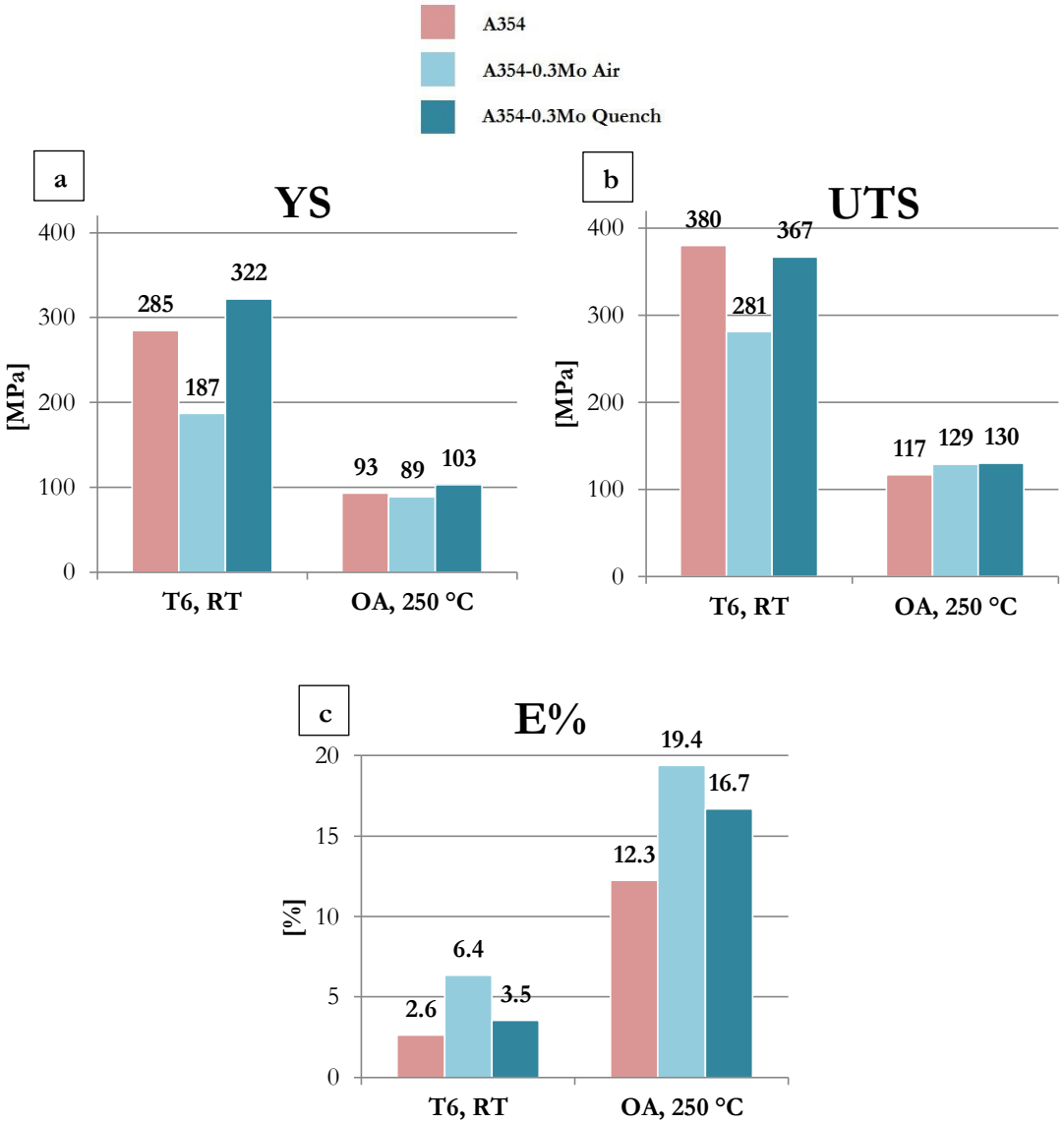

Figure 3.50. Comparison of (a) YS, (b) UTS and (c) elongation to failure (E%) between A354-0.3wt.%Mo and A354 alloys. Tensile tests were carried out at room temperature in the T6 condition and at 250 °C after overaging (100 h at 250 °C). A354-0.3Mo alloy was aged after solution treatment and air cooling (A354-0.3Mo Air) and water quench (A354-0.3Mo Quench).

The addition of 0.3wt.% Mo led to a sensible increase (+13%) of yield strength (YS) at room temperature, in comparison to A354; the two alloys were in fact treated at the same manner, and differ only for the presence of Mo. Such increase was not registered in UTS, but this evidence was related to the slightly higher amount of pores and cavities observed in Mo-rich samples. As previously stated, in fact, while YS depends mainly on strengthening heat treatment precipitates, UTS is strongly influenced by casting defects. Air cooling after solution treatment prevented from the formation of a supersaturated solid solution, thus strongly diminishing the Cu and Mg available for precipitation during artificial aging. As a result, both YS and UTS of A354-0.3Mo Air are sensibly lower than both A354 and A354-0.3Mo Quench. Correspondingly, elongation to failure, which is known to be strongly affected by artificial aging, is particularly high in A354-0.3Mo Air alloy (~6%). No decrease of E% was registered at room temperature, as a result of Mo addition. In the overaged condition and at high tensile testing temperature (250 °C), the beneficial effect of heat strengthening precipitates was lost, due to coarsening phenomena. The presence of Mo, however, enabled to maintain higher YS and UTS in comparison to A354 alloy (about +10%). Similarly to room temperature, A354-0.3Mo Air alloy presented the highest elongation to failure.

3.3.6 FRACTOGRAPHIC ANALYSES

The facture surfaces of the investigated alloys presented similar morphology, at the same heat treatment and testing temperature. In particular, mixed fracture morphology was observed in the samples tested at room temperature (Figure 3.51a); softening of the matrix induced by the high temperature tensile testing, resulted in a typical ductile morphology, characterized by small and regular dimples (Figure 3.51b).

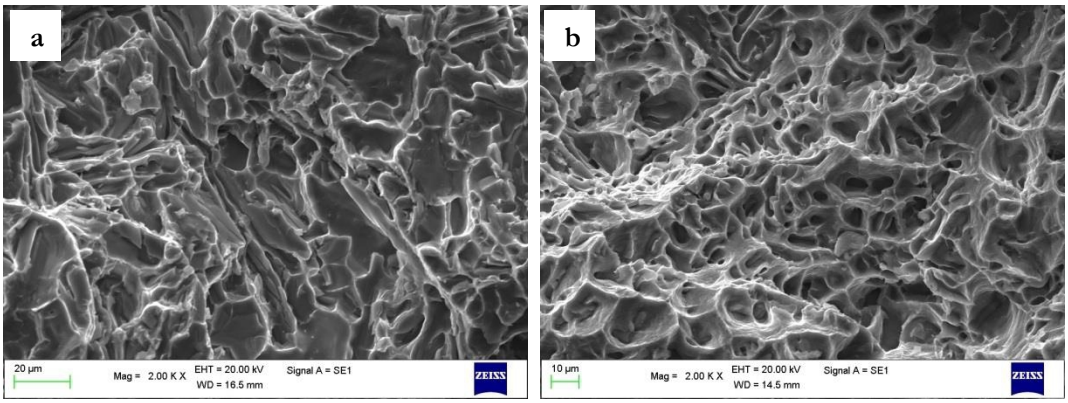

Figure 3.51. Fracture surfaces of A354-0.3Mo alloy subjected to double step solution treatment, water quench and artificial aging (A354-0.3Mo Quench), tested at (a) room temperature in the T6 condition and (b) at 250 °C after overaging at 250 °C for 100 h.

Representative casting defects found in A354-0.3Mo water quenched alloy, influencing UTS of the alloy, are shown in Figure 3.52a,b. Mo-rich intermetallics were oberserved on fracture surfaces of both A354-0.3Mo Water and Air samples (Figure 3.52c,d).

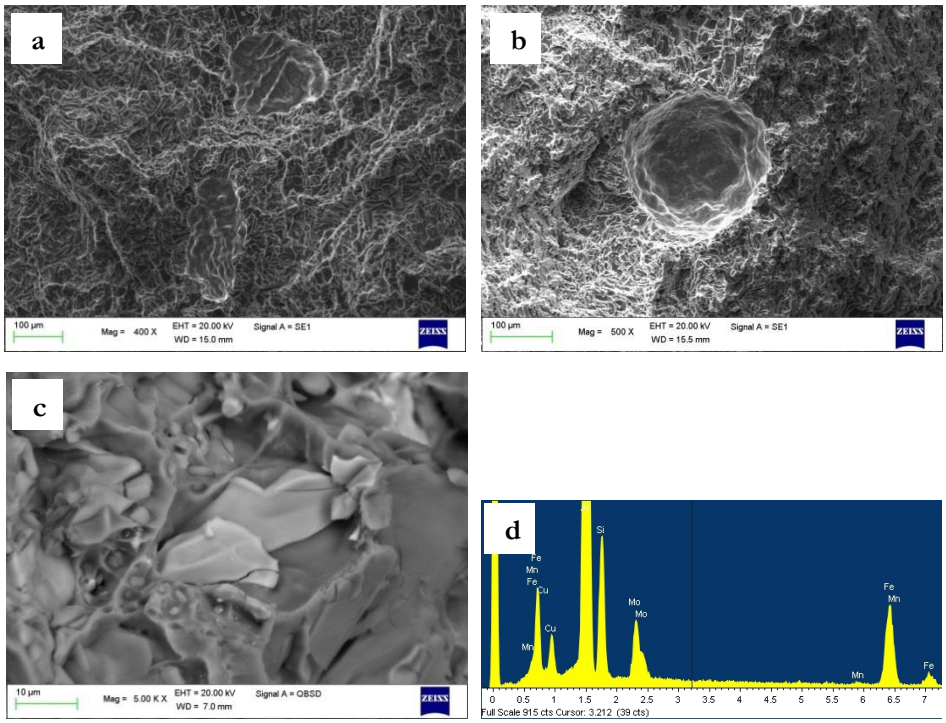

Figure 3.52. (a) Cavities and (b) pore found in A354-0.3Mo Quench sample, tested at room temperature in the T6 condition; (c) Mo-rich fractured intermetallics found on A354-0.3Mo Air sample and (d) corresponding EDS spectrum .

3.3.7 CONCLUSIONS

Aiming to further enhance the thermal stability of quaternary Al-Si-Cu-Mg alloys, the addition of Mo as alloying element has been investigated, on the basis of some recent works[71,72]. As reported in such works, Molybdenum is supposed to induce the formation, during solution treatment, of intermetallic phases stable up to 300 °C. The present, preliminary, investigation was mainly focused to evaluate the effects induced by 0.3 wt.% Mo addition on microstructure and overaging response of A354 alloy. The following main conclusions were drawn:

- Aiming to produce castings characterized by homogeneous distribution of Mo, holding temperature and time were set to 900 °C and 30 min, respectively, aiming to foster Mo dissolution from the Al-10Mo master alloy.
- A354-0.3Mo alloy presented a microstructure similar to that of A354 alloy, consisting in α-Al dendritic structure, eutectic Si and typical intermetallics (such as π-Fe, θ, Q). As a result of Mo addition, block-like particles (Al-Si-Fe-Mo), mostly present in interdendritic regions, and star-like phases (Al-Mo-Si) within the α-Al region were found. No β-Fe phases were observed, probably due to the presence of Mo, which reacts with Fe to form the above mentioned phases.
- Solution treatment parameters of A354-0.3Mo alloy were identified: a first phase at 495 °C-6 h to dissolve the low melting phase present also in A354 alloy, and a second phase at 540 °C – 1 h. The latter treatment stage was determined after investigating the variation of hardness during high temperature solution treatment, which should induce the formation of Mo-based precipitates.
- From the preliminary tensile tests, carried out at room temperature in the T6 condition and at 250 °C after long term overaging, the presence of Mo beneficially influences mechanical properties of A354 alloy, conferring higher YS at room temperature and increased strength (YS, UTS) after overaging, thus confirming a potential contribution to enhance thermal stability of the alloy. It should also be mentioned that, as a result of coarsening phenomena related to aging precipitates (θ, Q), after 100 h of permanence at 250 °C, the same mechanical properties were registered between samples artificially aged after water quench and air cooling.

REFERENCES – CHAPTER 3

[1] Y. Birol, *Mater. Sci. Technol.* **2012**, *28*, 385.

[2] J. a. Spittle, *Int. J. Cast Met. Res.* **2006**, *19*, 210.

[3] Y. C. Lee, A. K. Dahle, D. H. Stjohn, J. E. C. Hutt, **1999**, *259*, 43.

[4] L. Ceschini, I. Boromei, A. Morri, S. Seifeddine, I. L. Svensson, *J. Mater. Process. Technol.* **2009**, *209*, 5669.

[5] Q. G. Wang, *Metall. Mater. Trans. A* **2003**, *34A*, 2887.

[6] E. Sjölander, S. Seifeddine, *Metall. Mater. Trans. A* **2013**, DOI 10.1007/s11661-013-2141-9.

[7] Q. G. Wang, D. Apelian, D. A. Lados, *J. Light Met. 1* **2001**, *1*, 85.

[8] S. Seifeddine, S. Johansson, I. L. Svensson, *Mater. Sci. Eng. A* **2008**, *490*, 385.

[9] E. Samuel, a. M. Samuel, H. W. Doty, S. Valtierra, F. H. Samuel, *Int. J. Cast Met. Res.* **2014**, *27*, 107.

[10] A. M. Samuel, *AFS Trans.* **1997**, *105*, 951.

[11] E. Sjölander, S. Seifeddine, *Mater. Des.* **2010**, *31*, S44.

[12] M. A. Moustafa, F. H. Samuel, H. W. Doty, *J. Mater. Sci.* **2003**, *38*, 4523.

[13] J. Kanesund, S. Johansson, in *13th Int. Conf. Alum. Alloy.*, Pittsburgh, **2013**.

[14] F. J. Tavitas-Medrano, a. M. a. Mohamed, J. E. Gruzleski, F. H. Samuel, H. W. Doty, *J. Mater. Sci.* **2009**, *45*, 641.

[15] A. R. Farkoosh, M. Pekguleryuz, *Mater. Sci. Eng. A* **2015**, *621*, 277.

[16] A. Biswas, D. J. Siegel, D. N. Seidman, *Acta Mater.* **2014**, *75*, 322.

[17] K. Matsuda, D. Teguri, Y. Uetani, T. Sato, S. Ikeno, *Scr. Mater.* **2002**, *47*, 833.

[18] L. Ceschini, A. Morri, A. Morri, S. Toschi, S. Johansson, S. Seifeddine, *Mater. Des.* **2015**, *83*, 626.

[19] L. Ceschini, A. Morri, S. Toschi, S. Johansson, S. Seifeddine, *Mater. Sci. Eng. A* **2015**, *648*, 340.

[20] L. Ceschini, A. Morri, A. Morri, G. Pivetti, *Mater. Des.* **2011**, *32*, 1367.

[21] P. . Rometsch, G. . Schaffer, *Mater. Sci. Eng. A* **2002**, *325*, 424.

[22] A. M. Samuel, F. H. Samuel, *Metall. Mater. Trans. A* **1995**, *26A*, 2359.

[23] S. G. Shabestari, H. Moemeni, *J. Mater. Process. Technol.* **2004**, *153-154*, 193.

[24] C. H. Caceres, C. Davidson, J. Griffiths, *Mater. Sci. Eng. A* **1995**, *197*, 171.

[25] S. Seifeddine, Characteristics of Cast Aluminium–silicon Alloys: Microstructures and Mechanical Properties, Linköping studies in science and technology: Dissertations, **2006**.

[26] Q. G. Wang, D. Apelian, D. A. Lados, *J. Light Met.* **2001**, *1*, 73.

[27] L. Tóth, S. Y. Yarema, *Mater. Sci.* **2006**, *42*, 87.

[28] J. C. Pang, S. X. Li, Z. G. Wang, Z. F. Zhang, *Mater. Sci. Eng. A* **2013**, *564*, 331.

[29] J. C. Pang, S. X. Li, Z. G. Wang, Z. F. Zhang, *Fatigue Fract. Eng. Mater. Struct.* **2014**, *37*, 958.

[30] Z. Li, Q. Wang, A. a. Luo, P. Fu, L. Peng, *Int. J. Fatigue* **2015**, *80*, 468.

[31] J. A. Bannantine, J. J. Comer, J. L. Handrock, *Fundamentals of Metal Fatigue Analysis*, Prentice Hall, Englewood Cliffs, New Jersey, **1990**.

[32] M. Tiryakioglu, J. Campbell, J. Staley, *Scr. Mater.* **2003**, *49*, 873.

[33] D. L. Shu, *The Mechanical Properties of Engineering Materials*, China Machine Press, Beijing, **2007**.

[34] K. Nikbin, G. Webster, *Prediction of Crack Growth Under Creep –fatigue Loading Conditions*, **n.d.**

[35] J. Zrnik, J. Semeak, V. Vrchovinsky, P. Wangyao, *Mater. Sci. Eng. A* **2001**, *A319-321*, 637.

[36] K. Chan, P. Jones, Q. Wang, *Mater. Sci. Eng. A* **2003**, *341*, 18.

[37] L. Ceschini, I. Boromei, A. Morri, S. Seifeddine, I. L. Svensson, *Mater. Des.* **2012**, *36*, 522.

[38] J. Y. Hwang, R. Banerjee, H. W. Doty, M. J. Kaufman, *Acta Mater.* **2009**, *57*, 1308.

[39] Y. M. Han, a. M. Samuel, F. H. Samuel, H. W. Doty, *Int. J. Cast Met. Res.* **2008**, *21*, 387.

[40] L. Lasa, J. Rodrigues-Ibabe, *J. Mater. Sci.* **2004**, *39*, 1343.

[41] T. Lu, J. Wu, Y. Pan, S. Tao, Y. Chen, *J. Alloys Compd.* **2015**, *631*, 276.

[42] L. Mondolfo, *Aluminum Alloys: Structure & Properties*, Butterworths & Co, **1976**.

[43] F. . Samuel, *J. Mater. Sci.* **1998**, *33*, 2283.

[44] G. Wang, X. Bian, W. Wang, J. Zhang, *Mater. Lett.* **2003**, *57*, 4083.

[45] A. Samuel, H. Doty, S. Valtierra, F. Samuel, *Mater. Des.* **2013**, *52*, 947.

[46] J. H. Sandoval, A. M. . Mohamed, S. Valtierra, F. H. Samuel, *Mater. Sci. Forum* **2014**, *794-796*, 489.

[47] A. Mohamed, F. H. Samuel, S. Al Kahtani, *Mater. Sci. Eng. A* **2013**, *577*, 64.

[48] F. H. Samuel, A. M. Samuel, H. Liu, *J. Mater. Sci.* **1995**, *30*, 2531.

[49] J. H. Sokolowski, M. B. Djurdjevic, C. A. Kierkus, D. O. Northwood, **2001**, *109*, 174.

[50] Y. Han, a. M. Samuel, H. W. Doty, S. Valtierra, F. H. Samuel, *Mater. Des.* **2014**, *58*, 426.

[51] F. Paray, B. Kulunk, J. Gruzleski, *Int. J. Cast Met. Res.* **2000**, *13*, 17.

[52] E. Sjölander, S. Seifeddine, *Mater. Sci. Eng. A* **2011**, *528*, 7402.

[53] J. A. Taylor, *The Effect of Iron in Al-Si Casting Alloys*, **2000**.

[54] J. Taylor, D. St. John, L. Zheng, G. Edwards, J. Barresi, M. Couper, *Al Trans* **2001**, *45*, 95.

[55] T. Mbuya, B. Odera, S. Ng'ang'a, *Int. J. Cast Met. Res.* **2003**, *16*, 451.

[56] M. F. Ibrahim, E. Samuel, a. M. Samuel, a. M. a. Al-Ahmari, F. H. Samuel, *Mater. Des.* **2011**, *32*, 2130.

[57] J. Man, L. Jing, S. G. Jie, *J. Alloys Compd.* **2007**, *437*, 146.

[58] M. Murayama, K. Hono, M. Saga, M. Kikuchi, *Mater. Sci. Eng. A* **1998**, *250*, 127.

[59] L. Zhen, W. Fei, S. Kang, H. King, *J. Mater. Sci.* **1997**, *32*, 1895.

[60] W. F. Miao, D. E. Laughlin, *Scr. Mater.* **1999**, *40*, 873.

[61] D. G. Eskin, *J. Mater. Sci.* **2003**, *38*, 279.

[62] S. K. Son, M. Takeda, M. Mitome, Y. Bando, T. Endo, *Mater. Lett.* **2005**, *59*, 629.

[63] D. . Chakrabarti, D. E. Laughlin, *Prog. Mater. Sci.* **2004**, *49*, 389.

[64] C. Cayron, P. a. Buffat, *Acta Mater.* **2000**, *48*, 2639.

[65] S. C. Wang, M. J. Starink, N. Gao, *Scr. Mater.* **2006**, *54*, 287.

[66] P. Ratchev, B. Verlinden, P. De Smet, P. Van Houtte, *Scr. Mater.* **1998**, *38*, 1195.

[67] H. R. Ammar, a. M. Samuel, F. H. Samuel, E. Simielli, G. K. Sigworth, J. C. Lin, *Metall. Mater. Trans. A* **2011**, *43*, 61.

[68] R. Li, R. Li, Y. Zhao, L. He, C. Li, H. Guan, Z. Hu, *Mater. Lett.* **2004**, *58*, 2096.

[69] E. Cerri, E. Evangelista, S. Spigarelli, P. Cavaliere, F. Dericcardis, **2000**, *284*, 254.

[70] D. O. Ovono, I. Guillot, D. Massinon, *Scr. Mater.* **2006**, *55*, 259.

[71] A. R. Farkoosh, X. G. Chen, M. Pekguleryuz, *Mater. Sci. Eng. A* **2015**, *620*, 181.

[72] A. R. Farkoosh, X. G. Chen, M. Pekguleryuz, *Mater. Sci. Eng. A* **2015**, *627*, 127.

CHAPTER 4

AL-MATRIX NANOCOMPOSITES

Part of the research activity carried out during the PhD course was devoted to the study of Aluminum based composites. Most of the attention was given to Al-based nanocomposites, i.e. reinforced with particles below 100 nm average size. Nevertheless, some experimental activity was also addressed to the study of processing routes for both micro and nano reinforced composites. Experimental activity was accompanied by a careful bibliographic research, focusing mainly on Al-based nanocomposites, characterized by higher novelty from the theoretic and practical point of view in comparison to the more traditional micro-sized composites.

In this chapter, a general overview on Aluminum matrix nanocomposites will be given. A summary of the main results coming up from the literature will be presented, describing strengthening mechanisms involved by nanometric reinforcement phases, mechanical modelling, processing techniques and general overview on mechanical behavior. Since liquid-state production attempts were carried out in the framework of experimental activity (as will be shown in Chapter 5 and 6), bibliographic summary will be addressed mainly on liquid/semi-solid state routes for bulk production of nanocomposites castings. Moreover, since characterization activities on Al-based nanocomposites processed by Friction Stir Processing (FSP) were carried out as experimental work, a brief description of friction stir welding technique and its application to nanocomposites will be given.

4.1 OVERVIEW ON METAL MATRIX NANOCOMPOSITES (MMNCS)

In the last decades, a great attention has been devoted towards the reduction of fuel consumption and emissions, both in ground and aerospace transportation sector. As a result, an increasing trend in using light alloys (i.e. aluminium, magnesium) for the production of structural components was observed. Consequently, properties such as specific strength and stiffness became key parameters for the design of new materials.

A first attempt to enhance aluminium and magnesium specific properties was made from the 1980's, by all major aluminum producers, through the addition of hard and dispersed reinforcing phase (typically ceramic). As possible reinforcing phase for the so-called metal matrix composites (MMCs)[1–3], fibers, whiskers or particles were proposed. Among them, thanks to the isotropic behavior and to the possibility of employing relatively traditional processing routes, Discontinuously Reinforced Aluminium composites (DRA) attracted most of the interest. MMCs found different applications, from the automotive to the aeronautical field, and also electronic packaging[4]. Anyway, even though micrometric particles actually led to an increase of matrix hardness and strength, MMC were usually characterized by very low ductility and toughness due to the presence of high volume fraction of hard ceramic particles (10-20%)[5]. Micrometric particles (above 1.5 μm), in fact, could act as micro-concentrators of stress leading to cleavage, or also to the loss of interfacial cohesion, thus to formation of cavities in the case of smaller particles (200 nm - 1.5 μm)[5,6]. Moreover, due to the presence of both hard and soft phases (reinforcing particles and matrix), machinability of MMCs was reported to be particularly low[7,8]. As a consequence, only very hard and expensive materials, or non-traditional processes characterized by low cost-effectiveness and slow machining rates were thought to be suitable for machining of MMC[9,10].

Furthermore, poor weldability was reported for MMCs[11,12], due to the high volume fraction of reinforcing particles: particle segregation, high melt viscosity and detrimental reactions between matrix and reinforcement were reported as consequence of the most traditional welding techniques (i.e. TIG, MIG)[13]. Excessive wear damage of the counter-material in tribological application[14] was observed as additional drawback of MMCs; a clear example is the case of MMC pistons, which were reported to cause strong damage of cylinder lines[14].

In view of this, in recent years, the reinforcing phase was brought to the nanometric scale (Metal Matrix Nanocomposites, MMNCs), aiming to further enhance specific mechanical performance with respect to the unreinforced matrix[15,16], while conferring to the composite good ductility and higher thermal stability in comparison to unreinforced Al

alloys[17–19]. Both aluminum and magnesium alloys were investigated as matrix. The advantages of using nano-sized particles rather than microparticles were demonstrated by comparative studies, such as Sajjadi et al.[20], Ma et al.[21] and Kang and Chan[5], which reported nanoparticles to confer comparable or even higher YS, UTS and compressive strength in comparison to higher weight/volume fractions of micro-sized reinforcing phases.

Most of the research studies proposed as reinforcement phase Al_2O_3, SiC and AlN ceramic particles, although in the last years more attention was given to carbon based reinforcements (e.g. CNTs, MWCNTs)[15,22,23]. In all these cases, however, the volume fraction of reinforcement never exceeded 5wt%, due both to the more efficient reinforcing action of nanoparticles compared to microparticles, and to the bigger challenges posed by the addition of high volume fractions of nano-sized phases to Al matrix.

Different production processes, both *ex situ* and *in situ* were explored in the academic field. In the first ones, the reinforcing phase is formerly produced and added to the composite matrix, while in the latter, nano-sized reinforcement is generated during the production of the composite itself. Depending on the matrix state, ex situ methods may also be defined as solid, semi-solid or liquid processes. A good reinforcing action may be obtained only if particles are well dispersed within the matrix and if the interface between the two phases is sound. Even if more attractive for the relative simplicity and potential possibility of obtaining bulk cast components, liquid state routes present bigger challenges in terms of nanoparticles dispersion with respect to solid state processes. Nano-sized particles present in fact a low wettability and a strong tendency to agglomeration, when added to the liquid matrix, as reported by several investigators[2,20,24–27].

Despite the very high potential, as described by most of literature works, Al-based MNCs are still not exploited at the industrial level. In the field of casting processes, potentially characterized by high production volumes, the biggest challenges are related to the low wettability of particles, therefore leading to critical difficulties in obtaining a homogenous particle distribution. Attempts to enhance particles distribution both at the liquid/semisolid state or at the solid state through secondary processes are currently under study for fully exploitation of the materials potential.

4.2 STRENGTHENING MECHANISMS AND MODELLING

Different reinforcing mechanisms are involved in metal matrix nanocomposites, namely (i) Orowan strengthening, (ii) enhanced dislocation density, (iii) load bearing effect and (iv) grain refinement.

Orowan reinforcing mechanisms is related to the hindering effect on dislocations movement induced by hard particles within the matrix. While this effect has limited influence on mechanical properties of micro-sized reinforced composites, due to the large interparticle spacing[28,29] it is thought to have a major effect when particles are finely distributed in the matrix, such as in nanocomposites[30,31]. The second reinforcing mechanism involved, the *Enhanced dislocation density,* is due to the different coefficients of thermal expansion (CTE) between matrix and reinforcing phase (usually ceramic): stresses produced during cooling, as a result of the different CTE may cause plastic deformation at the matrix/reinforcement interface[32], with consequent increase in dislocation density[33–35]. *Load bearing effect* involves the transfer of load from the matrix to the hard ceramic particles. This mechanism, clearly, may be exploited only if a strong cohesion at the matrix/reinforcement interface is guaranteed[36]. *Grain refinement* mechanism is due to nanoparticles acting as heterogeneous nucleation sites[37], not only while casting, but also during high temperature plastic deformation, by hindering grain growth and inducing grain refinement during dynamic recrystallization[37,38]. Different studies carried out in the last years were aimed at building models for predicting mechanical behavior of nanocomposites, on the basis of reinforcing phase, matrix and processing route. Arithmetic summation methods were firstly developed, taking into account the addition of different strengthening mechanisms[39]. Summing methods were however reported to over-predict composites' properties[40]. In 1996, Ramakrishnan[41] proposed an analytical model to compute the yield strength (YS) of composites by taking into account both additive and synergistic effects related to load bearing effect and enhanced dislocation density:

$$\sigma_{yc=}\sigma_{ym}(1+f_l)(1+f_d)$$

where σ_{yc} and σ_{ym} represent YS of the composite and unreinforced matrix, respectively, while f_l and f_d are the improvement factors associated to the load-bearing effect and dislocation density. The model proposed by Ramakrishnan was integrated with Orowan contribution (relevant in the case of MNCs) by Zhang et al.[29], through its corresponding improvement factor f_{Orowan}:

$$\sigma_{yc=}\sigma_{ym}(1+f_l)(1+f_d)(1+f_{Orowan})$$

Contributions of the different reinforcing mechanisms were taking into account into a new *quadrature method*, as proposed by Kim[42]:

$$\Delta\sigma = \sqrt{(\Delta\sigma_{load})^2 + (\Delta\sigma_{CTE})^2 + (\Delta\sigma_{EM})^2 + (\Delta\sigma_{Orowan})^2 + (\Delta\sigma_{HP})^2}$$

Contributions reported in the above expression are expresses as follows:

- load bearing effect[41]:

$$\Delta\sigma_{load} = 0.5 V_p \sigma_{ym}$$

load bearing therefore depends on the particle volume fraction (V_p) and on the matrix yield strength, σ_{ym}.

- enhanced dislocation density[40]:

$$\Delta\sigma_{CTE} = \sqrt{3}\beta G_m b\sqrt{\rho_{CTE}}$$

Which, by expressing dislocation density as a function of CTE mismatch, may be written as follows[43]:

$$\Delta\sigma_{CTE} = \sqrt{3}\beta G_m b\sqrt{\frac{12 V_p \Delta\alpha \Delta T}{b d_p}}$$

Here, the strengthening coefficient β is 1.25, Δα is the difference between CTE of matrix and particles, while ΔT represents the temperature variation when the composite is cooled from its processing temperature; reinforcing particles features such as volume fraction (V_p) and diameter (d_p) are also taken into account.

- modulus mismatch contribution[42]:

$$\Delta\sigma_{EM} = \sqrt{3}\alpha G_m b\sqrt{\rho_{EM}}$$

where α is a the coefficient related to the specific material, G_m and b are the shear modulus of matrix and the magnitude of Burgers vector, respectively; the density of geometrically necessary dislocations ρ_{EM} around reinforcement particles may then be expressed as[43].

$$\rho_{EM} = \frac{6 V_p}{b d_p}\varepsilon$$

where ε is the bulk strain of the composite.

- Orowan contribution[37]:

$$\Delta\sigma_{Orowan} = \frac{0.13 G_m b}{\lambda} ln\frac{d_p}{2b}$$

The inter-particle spacing, *λ*, may be expressed as:

$$\lambda = d_p \left[\left(\frac{1}{2V_p} \right)^{1/3} - 1 \right]$$

- grain refinement[44,45]:

$$\Delta\sigma_{HP} = \frac{K}{\sqrt{d_m}}$$

The well-known Hall-Petch relation was used to introduce the strengthening effect of grain refinement: K is Hall-Petch coefficient and d_m is the matrix grain size.

It should be pointed out that, as observed by Kim, there is no general agreement on the model best representing the real behavior of MNCs[42]. However, different studies proved that the quadratic method shows good agreement with experimental data[40,46]. The most relevant contribution to nanocomposites yield enhancement was observed to the be the CTE mismatch[40]. However, nanometric size of the reinforcement, cluster tendency and low particle volume fraction may confer different relevance to each single factor in MMNCs in comparison to MMC. As previously stated, a strong mechanical properties enhancement may be obtained only if particles are well dispersed within the matrix. If nanoparticles are agglomerated into cluster, therefore presenting higher inter-particle spacing than the nominal or expected value, Orowan contribution may be strongly reduced or becoming negligible. If distribution of particles is efficient, however, by decreasing particle size the Orowan factor was observed to increase, until to a critical particle value. Further decrease may lead to the effect breakdown. In general, however, Orowan strengthening effect was reported to gain efficiency below the particle critical size of 100 nm[29]. This value is therefore commonly adopted as the threshold for considering a composite properly "nano". Further, due to the low volume fraction of nanoparticles (usually ≤ 2%), load bearing factor is thought to be not particularly relevant for MNCs, even negligible by some author[37,40].

Grain refinement mechanism is probably the most discussed one: it was reported to confer limited increase of yield strength from some studies and sometimes also negligible[29,40,47]. On the other hand, some investigators observed significant influence of grain refinement action on the material overall increase of strength[37]; grain refinement was reported by Kim et al.[42] to be the most relevant strengthening factor in Mg-based nanocomposites. Grain size decrease was documented also by Wang[48] in a $TiC_{0.7}N_{0.3}$ reinforced Al-based composites processed by ultrasonic processing. The same alloy was similarly refined by addition of Ti-B, but no relevant enhancement in UTS and ductility was reported, as a confirmation of reinforcing action played by nanoparticles.

4.3 MNCS PROCESSING ROUTES

As previously stated, the different production techniques for Al-MNCs may be classified depending on the matrix state: liquid, solid or semi-solid processes may therefore be employed. If compared to other methods, liquid state MMNCs processing techniques are particularly attractive since they are potentially scalable to industrial level, for the high volume production of near-net shape components[20,24,49]. Stir casting and ultrasonic assisted casting are the most widespread and studied processes; infiltration techniques and disintegrated melt deposition processes are still less diffused. On the other hand, solid-state processes are mainly based on powder metallurgy (PM), with consequent reduction of matrix/reinforcement wetting issues in comparison to liquid and semi-solid routes[50]. The main advantage of such techniques is the possibility of introducing higher volume fraction of particles, but the application field is restricted to the production of small sized components[51]. Nevertheless, the high cost of the powders, together with the high porosity content make production routes based on powder metallurgy still not applicable, unless secondary processes are applied to the compacted components (extrusion, rolling, forging, Cross Accumulative Roll Bonding-CARB)[52–55]. While in traditional PM processes the aim of powders blending is simply to mix the particles without inducing material transfer between the mixed components, high energy mixing makes possible to incorporate hard ceramic particles into the matrix powders through a solid-state bonding, thus eliminating voids between the matrix and reinforcing phase[52]. This technique, involving cold welding, fracturing, and re-welding of matrix/reinforcement particles, is usually referred to as *mechanical alloying* (MA)[50,56,57]. Moreover, during the continuous severe plastic deformation, refinement of powders structure to the nanometric scale may occur, resulting in the production of nanostructured powders[56,58]. Reinforcement/matrix particles processed by this method may also be employed as particles source in casting processes[16,24,49,59,60].
In the following paragraphs, the main liquid and semi-solid state routes will be described, by summarizing the results of recent case studies. A brief description of secondary processes for enhancing particles distribution, such as Friction Stir Processing, will be also given.

4.3.1 STIR CASTING

Stir casting technique consists in adding nano-sized reinforcing phase to the molten matrix (above its liquidus temperature), then distributing the particles by mechanically stirring the

molten composite (Figure 4.1). The stirring action is carried out by a stirrer (single or multiple stage[59,61]), which is dipped into the melt, then put into rotation, generating a vortex in the liquid matrix inducing particles distribution (this technique is usually referred to as *vortex method*). Particles are often added when the vortex is formed, since this is thought to facilitate incorporation of particles. Once the particles are dispersed, the composite is generally cast through gravity casting.

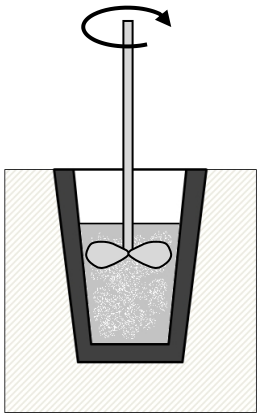

Figure 4.1. Schematic of stir casting technique, consisting in distributing nanoparticles within the molten matrix by rotation of a mechanical stirrer.

Advantages of MNCs stir casting are clear: low cost processing, relative simplicity and potential high volume production of bulk components[24]. For this reason, the method is really attractive for the industrial exploitation. However, even though it has been used for the production of micro-metric reinforced composites[27], it poses challenges for the application to nano-size particles, mainly due to the low wettability associated to such dimensions. Several drawbacks are related to this technique, such as agglomeration tendency and clusters-related entrapment of gas[16,20,27,49,62–64] (Figure 4.2). Moreover, matrix and reinforcement are characterized by different density; as a result, sinking or floating tendency has been reported[65–67]. Air entrapment may also be linked to the stirring action itself[24], and undesired chemical reactions at the interface between matrix and reinforcement may occur[20,26].

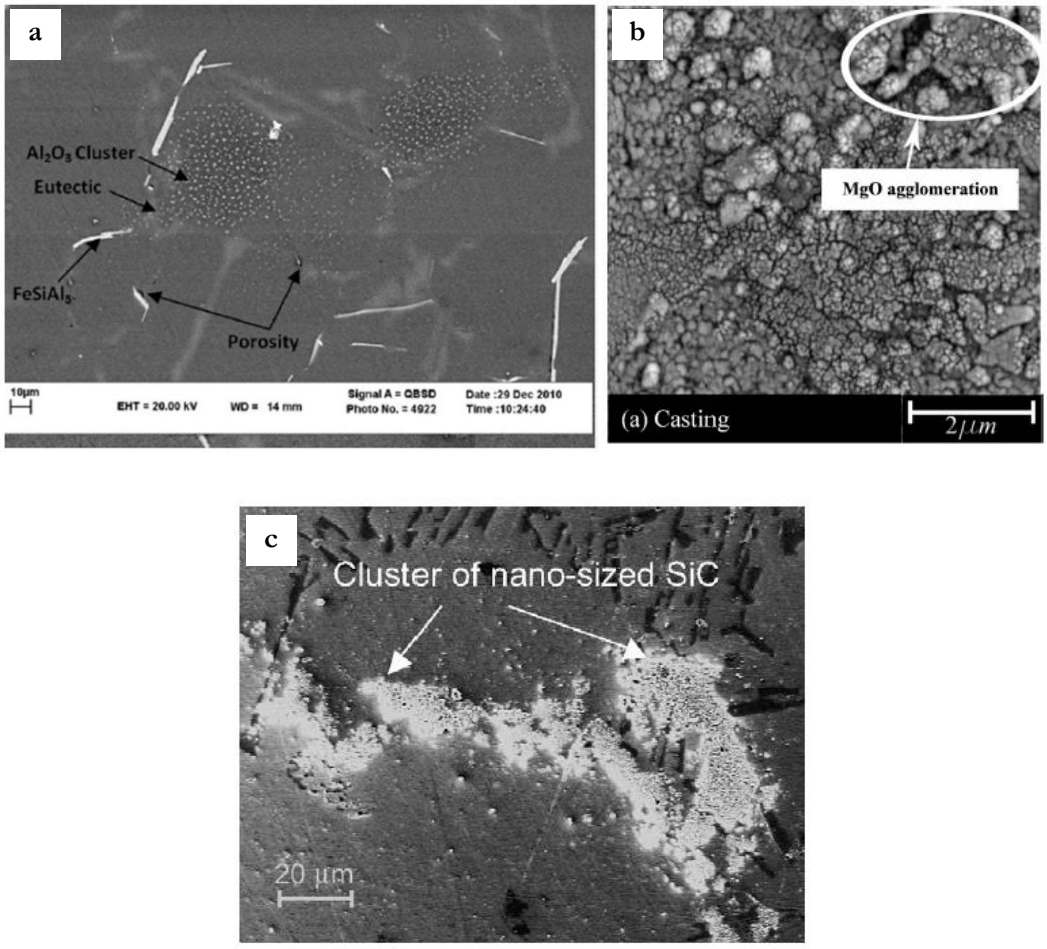

Figure 4.2. Literature SEM images showing (a) Al_2O_3 nanoparticles clusterization and associated small sized porosities; (b) MgO nanoparticles agglomerates and (c) SiC agglomeration observed in A356-based composites, produced by stir casting technique[20,64,68].

Aiming to enhance the distribution of particles within the matrix, different feeding methods were proposed and studied. Some authors reported, as instance, the use of an inert carrier gas to disperse particles, during the bubbles raise up in the melt[20,69]. Nevertheless, ways to enhance wettability of particles have been investigated. Pre-heating of the ceramic reinforcement, for example, was observed to eliminate, at least partially, absorbed gases from the particles surface, together with impurities[20,69,70]. In the last years, a lot of research was focused on the pre-milling of nanoparticles together with metallic powders, aiming to exploit plastic deformation of the matrix powders to obtain a master powder rich of reinforcing particles, but free from gas layers and with improved wettability[15,16,22–24,49,59,60,66,71]. Chemical modification of the melt through the addition of Mg was also proposed as possible way to enhance particles wettability by decreasing the surface tension of the matrix[65,72]. Also stirring processing parameters are reported to influence particle distribution, namely: stirrer shape and position, stirring temperature, rotational speed and duration of stirring[27,67].

Even if the first attempt to distribute nano-sized SiC through a vortex method was carried out by Kawabe et al. in 1999[73] at the semi-solid matrix state, the liquid application of the method is more recent. Stir casting was applied by Ansary Yar et al.[25] to produce an A356-based composite reinforced with 50nm MgO particles. In this study, the particles were added to the matrix in 1.5, 2.5 and 5vol% by wrapping them in aluminum foils to be fed into the melt during mechanical stirring (this method is usually referred to as *capsulate feeding method*). Increasing particles content and processing temperature led to an increased tendency to agglomeration. Similar findings were reported also by Abdizadeh et al.[68], observing that by adding up to 1.5 vol.% of 70nm MgO particles to A356 matrix induced an increase of compressive strength, while further increase (up to 5 vol.%) led to an increase of porosity content and strength decrease. A comparison between stir cast and powder metallurgy processes was carried out, highlighting that thanks to a better continuity between matrix and particles, stir casting method is able to confer high values of strength in comparison to powder metallurgy process. Interesting comparative studies were carried out also by Sajjadi et al.[20] and Mazahery et al.[74] analysing micro/nano stir cast composites, and liquid/semi-solid state processed nanocomposites, respectively. In the first study, a gas (Ar) feeding technique was used to inject particles in the melt, after pre-heating them in inert atmosphere. The comparison between micro (20 μm) and nano (50 nm) Al_2O_3 particles revealed that, due to the higher surface area and surface energy, nanoparticles show a higher tendency to agglomeration in comparison to micro-sized particles and increased porosity content by increasing particle content. Nevertheless, 3wt.% nanocomposite was reported to present same hardness and noticeably higher compression strength of a 10wt% micro-composite. Stirring speed was observed to be an important process parameter: while 200 rpm was not sufficient for distributing alumina, 450 rpm led to wastage of particles and increased porosity content. A comparative study between stir casting at the liquid and semi-solid state (compocasting), conducted by Mazahery et al.[74] highlighted that semisolid-processed composites present higher mechanical properties in comparison to those processed by stir casting, thanks to a lower porosity content and finer grains. The higher viscosity related to the semisolid state is thought to be the reason for the enhanced particle distribution, also related to their restricted movement during solidification. As observed by other studies, porosity was reported to increase with increasing the nanoparticle content. A decrease of ductility, together with an increase of hardness, UTS and YS was observed, reaching the maximum enhancement for 3.5vol% nanoparticles addition. The efficiency of Mg to improve wettability of nanoparticles (*reactive wetting* technique) was studied[75], revealing that different reactions may play a role

contributing to reactive wetting[76], such as the oxidation reaction between Mg and oxygen present in nanoparticles surface gas layers[75].

As a result of the bibliographic survey, one of the most promising methods for mitigating low wettability issues related to nanoparticle addition, is the so called *master powder feeding*. This technique, involving the pre-milling of ceramic particles to metallic powders (Figure 4.3), is thought to help in eliminating gases from nanoparticles surface. Surface gas layers in fact, may result in the total rejection of the particles by liquid aluminum, in particular if a critical amount of nanoparticles is added, resulting in the formation of a gas bridge. By pre-milling, hard ceramic reinforcing particles are pressed into the ductile metallic powders, usually Al, thanks to the milling media action Figure 4.3b,c.

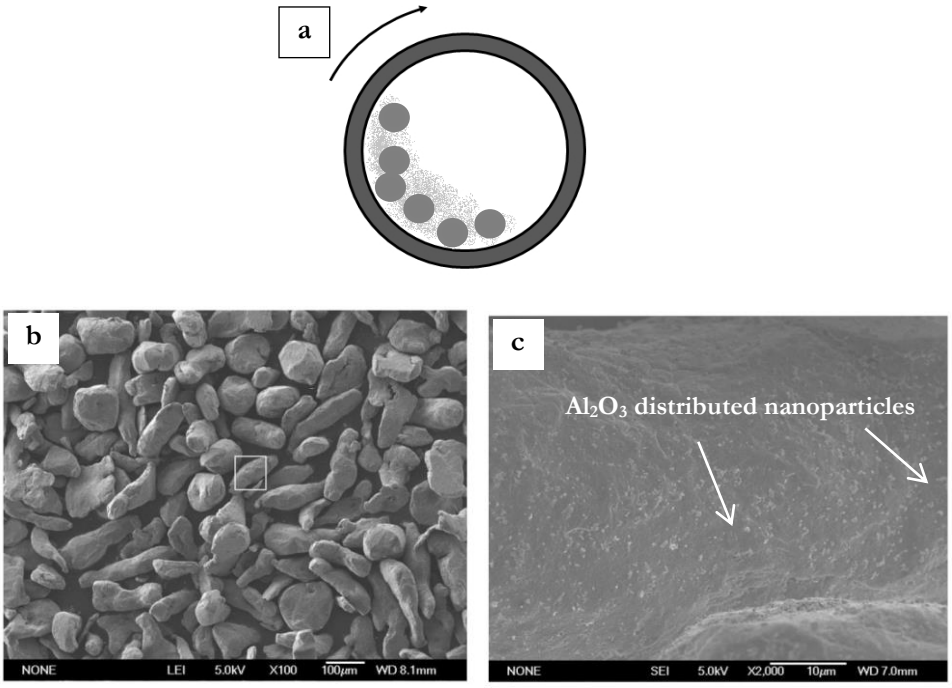

Figure 4.3. (a) Schematic of ball milling process, consisting in the production of reinforcement/matrix feedstock powders by pre-milling of ceramic nanoparticles and metallic powders; literature SEM images showing ball milled nano-Al_2O_3/Al composite powders at (b) low and (c) high magnification[61].

The milled powders are then added to the matrix, allowing a gradual release of particles within the molten metal[59,65,77]. Several studies are present in the literature about this technique[16,23,24,49,59–61,78]. It was demonstrated that for equal content of nanoparticles, composites produced with master powders presented higher tensile properties in comparison to pure-Al_2O_3 reinforced ones[24]. Nevertheless, also in this case, a critical particles content was found: further particles addition above 1.5vol.% induced more agglomeration/porosity, consequently decreased YS and UTS.

The better feeding efficiency of master-powder method in comparison to the traditional stir casting was confirmed also by other studies on AA2024-Al_2O_3 system[59]. YS, UTS and hardness of a 0.6wt% reinforced nanocomposite were found to be respectively 59, 58 and 16% higher in comparison to an equal reinforced composite processed by simple stir casting. Similar findings were reported also on A206-Al_2O_3 system[66], where Al-Mg-Al_2O_3 powders were cold pressed. Comparison with similar composites produced with pure alumina through simple stir casting highlighted an increase of mechanical properties in the case of master-powder composite. Pre-milled powders, especially when cold pressed, were reported in fact to induce in the composite lower porosity and clusters contents. The effect of different nanoparticles content in master-powders was investigated by Hamedan et al.[49], by adding to A356 matrix Al–20 wt.% SiC and Al–40 wt.% SiC pre-milled powders. The highest mechanical properties were obtained with the lowest content of nanoparticles (Al-20 wt.% SiC). As concerning the effect of stirring rate, according to Sajjadi[20], the optimal rotational speed balances two opposite effects: (i) enhancement of particle distribution with increasing speed due to the higher forces involved, (ii) increased porosity due to air entrapment through turbulent flow. Also by increasing temperature, a more turbulent flow and higher porosity content was observed. Milled master-powders may be produced also by metallic particles different from Al[16,79]. Al_2O_3 particles (20 nm) were milled with aluminium and copper micro-sized powders and added through stir casting to A356 alloy. Even if inducing in the composite a equal porosity content, Al_2O_3/Cu master-powders led to higher reinforcing effect in comparison to both pure Al_2O_3 and Al_2O_3/Al powders. Al_2O_3/Cu powders were thought to present higher tendency to be captured by the solid front in comparison to Al_2O_3/Al powders. As a secondary effect, dissolution of Cu and related strengthening effect should be considered. Increasing milling time was observed to induce higher oxidation of milled powders and higher porosity.

A certain number of studies were conducted on Al-MNCs with Carbon-based reinforcement, such as carbon nanofibers (CNFs), nanotubes (CNTs) and multi walled carbon nanotubes (MWCNTs). Some interesting solutions to enhance wettability of such particles were adopted. Carbon nanofibers (CNFs) were used by Oh et al.[22] and Lim et al.[15] to reinforce A1050 and Al-Zn-Mg matrix, respectively. In such studies, to increase particles wettability and avoid Al_4C_3 phase formation, CNFs were firstly coated with Cu by electroless plating. Button-shaped CNF-Al feedstocks were added to the matrix and subjected to stir casting. Even though with decrease of elongation to failure, after hot extrusion and T6 heat treatment, relevant increase in mechanical properties of composites containing 0.065 - 0.58 wt.% of CNFs was reported. A different solution for increasing

particles wettability was proposed by So et al.[23], who produced MWCNT-A356 stir cast composites. A SiC interfacial layer was coated on MWCNT surface, with the aim to improve the matrix/reinforcement interfacial strength through the formation of covalent bonds. Improvements of 15% in tensile strength and 79% in Young's modulus were achieved by adding 0.84 wt% Si powder and 1 wt% CNTs. MWCNTs were employed also by Li et al.[80], for the production of composites through High Pressure Die Casting process (HPDC) In this study, the turbulent flow obtained by pushing the AlSi10Mg molten alloy at 250 m/s in to the die, was exploited to disperse MWCNTs. As claimed by the authors, only 0.05wt% of MWNTs enabled to obtain an increase of tensile stress and elongation to failure of 8% and 27%, in comparison to the unreinforced matrix. Such process, thanks to the very brief contact time between MWCNT and molten matrix, is thought to help avoiding the formation of detrimental carbide phases.

4.3.2 COMPOCASTING

Aiming to facilitate nanoparticles distribution within the matrix, semi-solid state processing (usually referred to as *Compocasting*) has been investigated by many authors. This process is thought to allow a relatively uniform distribution of the reinforcing particles, increase wettability between particles and matrix, and confer finer microstructure and higher mechanical properties than stir casting[10,55,66,74,81,82]. By processing the matrix at temperatures below liquidus, viscosity is sensibly increased, helping to prevent from nanoparticles floating or settling[83]. Further, also superficial reactions, such as nanoparticles oxidation, are reduced, with a beneficial effect on matrix/particle interface[83].

Nevertheless, even if comparison studies show that compocast MNCs contain lower porosity than stir cast composites[66,74,82], a certain amount of porosity and clustering is still observed, thus requiring further processing (i.e. ultrasonic treatment[83–88]) or secondary processes (e.g. forging, extrusion) to achieve microstructural homogenization[55,88–91]. Recent studies were addressed to investigate on efficiency of both micro and nanoparticles distribution at the semisolid state. Sajjadi et al.[92] added to semi-solid A356 pre-heated micro (3-7.5 wt.%) and nano (1-4 wt.%) Al_2O_3 particles, by Ar gas injection. Microstructure was characterized by non-dendritic structure (as a result of dendrites fragmentation induced by semisolid state stirring); particles were observed to move towards inter-dendritic regions. The process allowed to add up to 3 wt.% and 5 wt.% of nano and micro particles, respectively. As reported for liquid processes, beyond a critical content threshold, agglomeration of particles and hardness decrease occur. Nanoparticles, once again, induced

better mechanical performances in comparison to micro-sized ones. MWCNTs-A356 composite was produced by Abbasipour et al.[81], by deposition of MWCNT on Al powders by a Ni-P electroless plating technique. A reduction of the average equivalent diameter of α-Al globular areas (related to semi-solid process) was registered, as a result of grain refining effect of nanoparticles. Good ductility and strength increase in comparison to liquid processed composite and unreinforced matrix were reported. Similar refining action was reported also by El Mahallawi et al.[10] in A356/Al_2O_3 composite. Differently from the previous study, Al_2O_3 particles were added at the semisolid state through capsulate method. It is interesting to note that in this work, even though an increase of UTS and elongation was reported in comparison to the matrix, a lower hardness value was reported for the T6-composite with respect to the matrix. As a result of EDS, nanoparticles were thought to interact with the formation of Mg_2Si strengthening precipitates.

4.3.3 ULTRASONIC ASSISTED CASTING

Ultrasonic treatment of the melt has been under study in metal processing for microstructural refinement and degassing of castings since many years[93]. One of the first attempts to exploit ultrasonic waves for helping in nanoparticles distribution within liquid and semisolid aluminium matrix was carried out by Li in 2004, followed by many researchers both on Al and Mg matrix[62–64,94–98]. Even though the mechanisms involved in ultrasonic treatment are still under discussion, according to the most accepted theories, acoustic streaming and transient cavitation are the main non-linear effects involved[99,100]. A schematic of ultrasonic process and its action on clusters disaggregation is presented in Figure 4.4. A sensible contribution to stirring is given by acoustic streaming, consisting in a macroscopic flow effect due to acoustic pressure gradient within the melt[101]. On the other hand, ultrasonic cavitation is produced by pressure cycles inside the melt, generated by ultrasonic waves. Small gas bubbles are formed in the melt and grow, pulse and collapse during negative and positive pressure cycles. Collapse occurs in less than 10^{-6} s, leading to the formation of transient micro hot-spots of about 5000 °C, 1000 atm and heating/cooling rates above 1000K/S[102]. Gas contained inside nanoparticles clusters is thought to act as cavitation nuclei, therefore leading to disgregation of cluster during pressure cycles and homogeneous distribution of particles through acoustic streaming action[94].

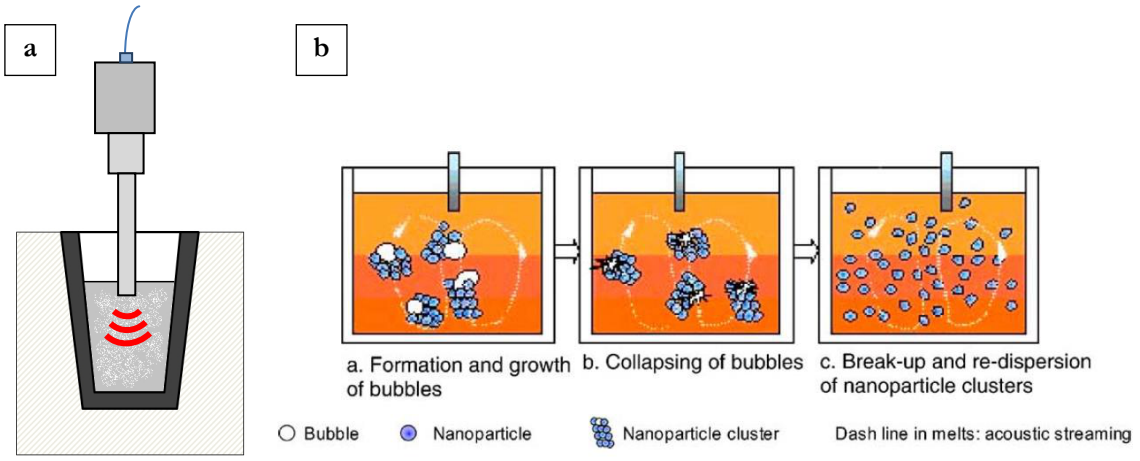

Figure 4.4. (a) Schematic of ultrasonic processing of Al-based nanocomposite at the liquid state; (b) schematic of cavitation and acoustic streaming effects involved in nanoparticles clusters disaggregation during ultrasonic treatment of composite melt[94].

Furthermore, enhancement of wettability is obtained through the elimination of gases or impurities from the surface of particles, thanks to the action of both pressure impacts and local hot-spots related increase of temperature[101]. The most widespread ultrasonic processing techniques consists in transmitting ultrasonic waves to the melt through a metallic waveguide (usually referred to as sonotrode), by dipping it into the melt (Figure 4.4). The sonotrode is usually made of titanium alloy, but some studies proposed the more expensive niobium, both for acoustic properties and ability to withstand to high processing temperature with minimum ultrasonic cavitation-induced erosion[103,104]. The frequency generally employed for this kind of application is 20 kHz, as commonly reported by different investigators[61,64,104,105]. Nanoparticles addition together with ultrasonic processing leads to globular α-Al dendrites refinement, as observed and discussed in a recent study by Su et al.[61], as a result of the interaction between ultrasonic vibration and primary α-Al and nanoparticles as well. Ultrasonic acoustic flows, facilitates the extraction of latent heat therefore decreasing the temperature gradient in the solidification front. As a result, instability at the liquid/solid interface is induced[106]. Further, ultrasonic vibrations break dendrites and clusters as well. Fragmented dendrite arms and de-clusterized particles are then carried away from their original site, acting as nuclei for new grains generation[94]. A microstructural evolution model during solidification and ultrasonic processing was proposed by Su et al.[61] (Figure 4.5).

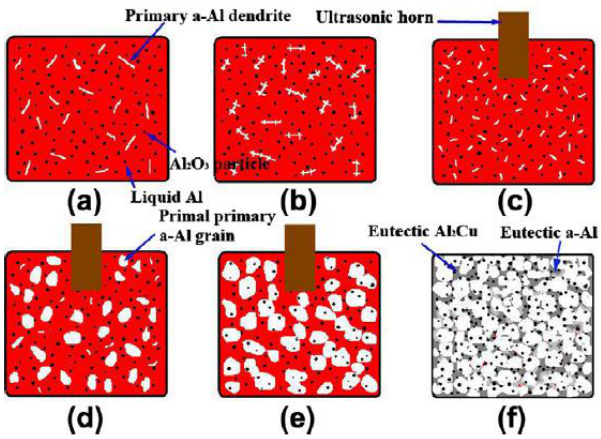

Figure 4.5. Microstructural evolution model during ultrasonic processing and solidification proposed by Su et al.; (a) formation of primary α-Al dendrites, (b) formation of dendrite arms, (c) breakage of dendrites induced by the ultrasound field; (d, e) growth of α-Al grains and (f) last stage of solidification[61].

α-Al dendrites are formed when temperature drops near the liquidus temperature. At this stage, nanoparticles are pushed away by the solidification front. The process continues, as secondary and tertiary dendrite arms are formed. Ultrasonic treatment of the composite induces breaking of dendrites and removal of the gas layer from the nanoparticles surface improving their wettability, thus enabling their entrapment in the growing grains. By decreasing temperature till the solidus, inter-granular eutectic reactions occur; particles which are pushed away by growing grains are therefore surrounded by the eutectic phase. As a conclusion, composite microstructure consists in nanoparticles mostly distributed in the inter-granular regions, while some particles located inside the α-Al grains.

Up to 2wt.% 30 nm SiC particles were added by Li et al. to A356 matrix[64]. The particles, introduced from the top of the crucible, were reported to be well entrapped by Al melt, as a result of both acoustic streaming and cavitation. Although small clusters were still observed, the technique allowed increasing YS more than 50% by adding 2wt% of SiC. Also wrought aluminum alloys were processed by ultrasonic treatment, as reported by Murthy et al., who incorporated up to 3 wt% of fly ash (composed usually mainly by quartz, mullite and hematite) in AA2024 matrix[105]. Composites with increased hardness and compression strength were obtained, by adding pre-milled Al-fly ash powders, mechanical stirring and ultrasonic processing (20 kHz) by a Ti sonotrode. Different feeding techniques were evaluated by Yang et al.[103], who proposed the use of a niobium-based sonotrode to disperse SiC into A356 matrix. Results of this study are particularly interesting: both master powder technique and inert gas spraying methods were reported to be ineffective in nanoparticles distribution. Oxidation of Al phase and difficulties in

melting the compacts were reported from the first method, while formation of large clusters, not able to penetrate the melt surface were induced by gas injection. The most efficient technique, even if requiring long ultrasonic processing time, was manual handling and mechanical delivery. Double-capsulate feeding method was used by Choi et al.[104]. In this study, a composite based on Al-7Si-0.3Mg-0.5Cu alloy reinforced with 1wt.% of γ-Al_2O_3 nanoparticles was produced. Nano-alumina was wrapped into double rolled-shape Al foils, allowing gradual release of nanoparticles during melting. Each capsule required 15 min of ultrasonic processing (20 kHz - 600 W) through a niobium sonotrode at 700 °C. Even though micro-clusters were observed, the authors claimed significant increase in yield, tensile strength and ductility, as a result of refinement of primary α-Al and modification of eutectic Si and θ-Al_2Cu phases.

Even though most of the published works claim satisfactory results in feeding nanoparticles to Al melt, some authors, more realistically, report some difficulties and challenges in obtaining uniform distribution of particles. Such observations were made for example by Kandemir et al.[87], who tried to apply ultrasonic treatment to thixoforming, aiming to produce A356-SiC nanocomposites. In this study, double capsulate method and crucible placement approach (consisting in placing the particles on the crucible bottom) were applied. Mechanical stirring was carried out to force nanoparticle clusters to pass underneath the sonotrode action field. Both the two methods did not lead to good dispersion, due to the oxide layers formation on the Al-foil, which prevented from capsule melting, and to the fact that particles tended to remain at the bottom of the crucible.

All the above discussed studies employed contact ultrasonic processing. However, in some studies, a non-contact method has been developed[95,107]. Aiming to avoid contact with Al melt, the mold is placed into a ultrasonic vibrating chamber partially immersed into the water, in order to effectively transmit ultrasonic waves to the mold. This kind of equipment, working at 35 kHz of frequency, was used by Mula et al. to produce 2 wt.% 10 nm Al_2O_3 composite with pure Al as matrix[95]. Microstructure of the composite consisted in continuous nano-alumina dispersed zones in proximity of grain boundaries, encapsulating alumina depleted zones. Nevertheless, hardness and tensile strength enhancement (92% and 48%, respectively) and ductility reduction was observed, in comparison to equally processed unreinforced Al. Despite the reported efficiency in distributing nanoparticles, ultrasonic treatment poses some challenge towards its exploitation at industrial scale. While a fully developed cavitation occurs when a ultrasonic density threshold of 80 W/cm^2 is achieved[108], high-intensity ultrasonic vibration requires 100 W/cm^2. As a result, it is clear that very high power is needed to successfully treat

molten composites in high casting volumes. In this regard, some research studies are trying to enlarge application field of the technique, for example by continuous processing of composite flow[109].

4.3.4 FRICTION STIR PROCESSING

In view of the difficulties encountered in nanoparticles incorporation into molten matrix, in recent years research efforts were addressed to identify possible alternative techniques to enhance nanoparticles distribution. Friction Stir Processing (FSP), based on friction stir welding (FSW), was proposed as possible method to produce surface-reinforced composites in 2003 by Mishra et al.[110]. It should be mentioned that FSW has been investigated in the last decades for joining of aluminum based composites (AMCs), characterized by micrometric reinforcement. In this regard, many matrix-reinforcement systems have been investigated, e.g. 6092–SiC, 6061–B_4C, A339–SiC, 6061–Al_2O_3[111]. As a matter of fact, sound and efficient joints in AMC could not be achieved by welding techniques based on material fusion, due the formation of brittle phases due to matrix/particles reaction, porosity generation and reinforcement decomposition.
FSW process (Figure 4.6) was invented in 1991 by The Welding Institute (TWI), aiming to join at the solid state aluminium alloys. FSW technique uses non-consumable rotating tools, made of two parts, namely pin and shoulder.

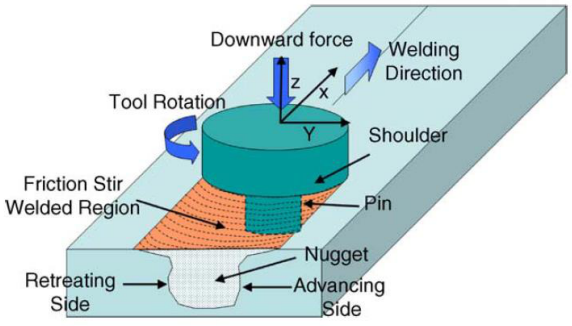

Figure 4.6. Schematic of Friction Stir Welding (FSW) processing[111].

During FSW processing, the rotating pin is plunged into the surface of the workpiece and moved along the joint line (Figure 4.6). Heat generation and mechanical sweeping of the softened metal are the main actions induced by the interaction between tool surface and workpiece. The metal around the pin is softened by heat and through severe plastic deformation the material is swept from the advancing side (AS; where pin moves in the

same direction of the tool linear movement) to the retreating side (RS, where relative direction of the pin is opposite to that of the linear movement) of the joint. Severe plastic deformation and high-temperature exposure inside the stirred zone during FSW/FSP leads generally to dynamic recrystallization and generation of fine equiaxed grains within the stirred zone, together with intermetallics fragmentation and precipitates dissolution and coarsening[111]. Process parameters such as tool geometry, tool rotation rate, temperature, vertical pressure, active cooling play an important role size of the recrystallized grains within the nugget zone[111]. FSW joints are usually characterized by four different zones (Figure 4.7): the nugget zone (NZ), thermo-mechanically affected zone (TMAZ), heat affected zone (HAZ) and base materials (BM). The most typical features that can be observed within a FSW joint are the shape of the nugget (basin or elliptical[111]), the presence of onion ring structures and process defects such as tunnels. Onion rings are characterized by swirl patterns on the joints cross sections, and are thought to be generated by softened matrix flow and differences in dislocation density during the joining process[112,113].

Figure 4.7. Representative macrostructure of FSP processed zone, characterized by the presence of the nugget zone, at the weld center, thermo-mechanically affected zone (TMAZ), heat affected zone (HAZ) and base materials (BM). Retreating and Advancing side are defined on the basis of relative rotating and linear motion direction of the pin[111].

Speed of pin rotation influences the formation of defects such as tunnels, in particular due to insufficient heat or inappropriate metal flow[114,115].

Many studies conducted on FSP application to aluminum based microcomposites reported that the stirring action related to the process may induce break up of clustered particles and homogenous distribution of reinforcing phase within the nugget zone, as a result of metal mixing and severe plastic deformation mechanisms[116–118]. Moreover, size and aspect ratio of micrometric particles was reported to decrease, due to the interaction/abrasion between tool (pin and shoulder) and reinforcing particles[113,116,119]. As a result of particles distribution and grain refinement, it is generally accepted that hardness increases within the nugget zone, then gradually diminishing towards the base material[120]. Generally, FSW allows the

processing of high-quality joints in AMC reinforced with up to 30 vol.% particles, free from macroscopic defects and interfacial reactions. Despite no general trend can be identified between mechanical properties and processing parameters, it is reported that the efficiency of AMC weld joints (namely the ratio between UTS of joint and base metal) is usually between 60% and 97%; it is strongly influenced by process parameters, such as rotation rate, traverse speed and axial force[111,120]. Severe wear of the processing tool due to the abrasive action of hard ceramic phases is a critical issue that needs to be taken into account during FSP of composites reinforced by micro-sized particles[111,120].

FSP has been recently proposed for the processing of surface composites reinforced by nanometric particles. Both Al- [121–123] and Mg- [124,125] based nanocomposite have been produced by FSP, aiming to distribute ceramic or carbon based nano-reinforcement. The most diffused particles deposition process involves the preparation of superficial grooves, to be filled with nanoparticles. A first tool pass is usually carried out to cover the particles-rich processing zone[126]. Successive tool passes are then applied to induce particles distribution. Hardness and strength enhancement has been reported in different studies; the process however is still under study, also in view of the difficulties in obtaining an even dispersion of nanoparticles. Attempts to apply FSP to nanocomposite production were made by Liu et al.[123], who distributed up to 6 vol.% of MWCNT in A1016 alloy through multiple FSP passes. Sensible increase of UTS in comparison to the unreinforced matrix (+100%) was registered in the 6vol.% nanocomposite. Tensile strength and microhardness of the composites were found to gradually increase by increasing MWCNT content. On the other hand, decrease of ductility was observed. A recent study by Hosseini et al.[127] was carried out to incorporate in AA5083 matrix, through surface groove, a mixture of MWCNT and CeO_2 particles, aiming to fabricate surface composites characterized by improved mechanical properties and corrosion resistance. The authors reported multiple passes effective in decreasing reinforcing clusterization. Grain size reduction, enhanced distribution of reinforcing phase and intermetallics fragmentation were observed in the nugget zone; sensible strength enhancement was observed in FSPed material in comparison to the unreinforced alloy similarly processed. Reduction of grain size was reported also by Shafiei-Zarghani et al. [121], investigating on 6082-Al_2O_3 system. The authors suggest nano-sized Al_2O_3 particles induced pinning effect thus retarding grain growth of dynamically recrystallized grains. Multiple FSP passes were reported to increase microhardness; moreover, enhancement in wear resistance against steel was observed. Despite the technique is still not widely diffused, these case studies depict FSP as a good process candidate to produce surface composites characterized by nanometric reinforcing phases.

Similarly to AMC, the influence of process parameters on particles distribution and mechanical properties of the composite strictly depends on the system under investigation; as a result, more investigation are needed to widen the knowledge on such process.

4.4 GENERAL CONSIDERATIONS ON MECHANICAL BEHAVIOR

Research works generally agree on reporting mechanical properties enhancing of room temperature mechanical properties by nanoparticles addition. Noticeable enhancement of hardness, YS and UTS have been reported[20,22,66,82,128,129], while Young's modulus improvement is limited by the low volume fraction of ceramic reinforcement which is generally used[16,23,79]. Researchers usually agree also on the existence of a critical reinforcing fraction which leads, if exceeded, to the decrease of mechanical performance[24,71,82,129], as a result of porosity/defects associated to nanoparticles agglomeration. Similarly, also ductility of the composite is strongly influenced by nanoparticles distribution and related porosity. By increasing the volume fraction of nanoparticles, decrease of ductility is usually observed[16,24,74,104]. Generally, semi-solid state processing leads to higher levels of ductility than stir casting, also in combination to master powder feeding technique[49,66,74]. Increase of ductility in comparison to the unreinforced matrix was reported also for ultrasonic processed composites[10,16,48,64,79,104]. The increase in ductility is usually related by authors to grain refinement, low level of porosity and partial modification of eutectic Si phases, as a result of nanoparticles addition[10,104]. Ductile fracture surfaces have been reported together with good values of elongation to failure (however lower than the unreinforced matrix) by Mazahery on A356-Al_2O_3 composite[71]. Micro-cracks were generally observed to propagate in the interdendritic region, characterized by segregation of nanoparticles by the solidification front[16,79] and high pore content[79]. Enhancement of ductility was also linked by some authors to primary and eutectic silicon refining effect acted by nanoparticles, in hypereutectic and hypoeutectic alloys[96,104]. Ductile dimpled fracture surfaces, even if becoming less pronounced by increasing reinforcing content, were observed, also in carbon reinforced composites, processed by stir cast and extrusion[22,71].

Even if Al-based nanocomposites are expected to present better mechanical properties at high temperature in comparison to the unreinforced matrix, very few works were carried out in this kind of investigation. However, it was demonstrated that addition of 2vol.% of MWCNT and semisolid processing allows to maintain at 300 °C 90% of the room temperature YS[130]. Also, creep resistance is enhanced by incoherent non-shearable phases such as ceramic particles. Some works carried out on micrometric reinforced composites

relate this to the limitation of dislocations climb or gliding processes[131], as well as by the ability to carry higher load in comparison to the unreinforced matrix[132,133]. A further improvement of creep resistance is expected by addition of nanoparticles, thanks to the lower interparticle spacing. Enhancement of creep resistance were however reported for a Al/4.5 vol.%MWCNT composite sheet fabricated by hot-rolling ball-milled powders[19]. Moreover, as a result of some study on solid processed nanocomposites, nanometric particles are thought to be more effective in dislocation pinning in comparison to micrometric particles[18,134,135].

Enhancement in wear behaviour of Al-based MMNC in comparison to unreinforced matrix was reported in recent works using ceramic[78,136–138] and carbon-based[139–142] reinforcement. Mazahery et al.[78] investigated the wear behaviour of a SiC reinforced Al–Si matrix produced by stir casting. The authors reported significant improvement of dry sliding wear resistance against hardened steel. Higher wear resistance and lower friction coefficient in comparison to the unreinforced alloy was observed also by Al-Qutub, investigating on 1 wt.% CNTs-AA6061 composite under mild wear conditions[139]. Different results were obtained under severe wear conditions, where high wear rate and friction coefficient were observed. A comparative study was also carried out to assess differences in tribological behavior between similar micro and nano composites[138]. The study, carried out on TiC-Al-Cu composites, showed that not only wear resistance of the nanocomposite is higher than both the unreinforced matrix and the corresponding microcomposite.

4.5 CONCLUSIONS

Different production routes have been studied so far for manufacturing of Al-based nanocomposites. In the framework of liquid state techniques for the production of bulk parts, stir casting process is particularly attractive for the relative simplicity and possibility to work on large scale productions. Nevertheless, several difficulties related to nanoparticles incorporation within the molten matrix have been reported. Air entrapment, porosity and particles agglomeration due to the low wettability of nanosized reinforcing phase are main drawbacks of this method. Alternative or additional processing steps for enhancing particles wettability and favouring their even distribution have been proposed in the literature, such as semi-solid state processing and ultrasonic treatment of the melt. It was demonstrated that compocasting assisted with mechanical stirring may potentially facilitating nanoparticles incorporation in comparison to fully liquid routes. Such processes are industrially attractive in view of the fact that no special feedstock is required; the semi-solid slurry is simply generated from the liquid state by cooling the molten composite during the casting process. Ultrasonic-assisted casting is generally considered as a method which provides sound matrix–particle interface, helps in disaggregation of nanoparticles clusters, further eliminating impurities from the particles surface. Even though the method potential is clear, industrial scale up still needs some evaluation; main limitations are related to power of the ultrasonic source, thus to the ultrasonically processed volume. Secondary processes have been investigated in the literature for improvement of nanoparticles dispersion. Friction Stir Processing, deriving from the well-known Friction Stir Welding technique, has been recently proposed to produce sound surface Al-based nanocomposites. Thanks to severe plastic deformation mechanisms and grain refinement induced by dynamic recrystallization processes, FSP seems to be a promising technique for enhancing nanoparticles distribution and mechanical properties in Al-based composites.

Despite in the literature drawbacks of such techniques are somehow reported (particles clusterization, cavities and porosity generation, undesired reaction between reinforcement and matrix), the vision on nanocomposites production by liquid or semi-solid state routes seems however quite optimistic, generally reporting extraordinary enhancement of mechanical properties (strength, hardness), together with good values of ductility. Even though most of the above mentioned techniques have been investigated and tested at the laboratory scale, industrial scale up of such processes seems still far to come.

REFERENCES – CHAPTER 4

[1] T. W. Clyne, P. J. Withers, *An Introduction to Metal Matrix Composites*, Cambridge University Press, **1995**.

[2] H. Ye, X. Y. Liu, *J. Mater. Sci.* **2004**, *9*, 6153.

[3] J. N. Fridlyander, *Metal Matrix Composites*, Springer, **1994**.

[4] D. Miracle, *Compos. Sci. Technol.* **2005**, *65*, 2526.

[5] Y.-C. Kang, S. L.-I. Chan, *Mater. Chem. Phys.* **2004**, *85*, 438.

[6] M. Besterci, M. Slesar, G. Jangg, *Powder Met. Int.* **1992**, *24*.

[7] L. Cronjäger, D. Meister, *CIRP Ann. - Manuf. Technol.* **1992**, *41*, 63.

[8] C. J. . Andrewes, H.-Y. Feng, W. . Lau, *J. Mater. Process. Technol.* **2000**, *102*, 25.

[9] T. Ozben, E. Kilickap, O. Cakir, *J. Mater. Process. Tech.* **2008**, *198*, 220.

[10] I. El-Mahallawi, H. Abdelkader, L. Yousef, A. Amer, J. Mayer, A. Schwedt, *Mat. Sci. Eng. A* **2012**, *556*, 76.

[11] M. Taya, R. J. Arsenault, *Metal Matrix Composites, Thermomechanical Behavior*, Pergamon Press, **1989**.

[12] D. B. Miracle, S. L. Donaldson, in *ASM Handb. Vol. 21, Compos.*, ASM International, **2001**, pp. 3–17.

[13] M. B. D. Ellis, *Int. Mater. Rev.* **1996**, *41*, 41.

[14] R. L. Deuis, C. Subramanian, J. M. Y. Yellup, *Compos. Sci. Technol.* **1997**, *57*.

[15] J.-Y. Lim, S.-I. Oh, Y.-C. Kim, K.-K. Jee, Y.-M. Sung, J. H. Han, *Mater. Sci. Eng. A* **2012**, *556*, 337.

[16] M. Karbalaei Akbari, O. Mirzaee, H. R. Baharvandi, *Mater. Des.* **2013**, *46*, 199.

[17] S. C. Tjong, *Adv. Eng. Mater.* **2007**, *9*, 639.

[18] J. Cadek, K. Kucharova, V. Sustek, *Scr. Mater.* **1999**, *40*, 1269.

[19] H. J. Choi, D. H. Bae, *Scr. Mater.* **2011**, *65*, 194.

[20] S. A. Sajjadi, H. R. Ezatpour, H. Beygi, *Mater. Sci. Eng. A* **2011**, *528*, 8765.

[21] Z. Y. Ma, Y. L. Lia, Y. L. F. Zheng, J. Bi, S. C. Tjong, **1996**, *219*, 229.

[22] S.-I. Oh, J.-Y. Lim, Y.-C. Kim, J. Yoon, G.-H. Kim, J. Lee, Y.-M. Sung, J.-H. Han, *J. Alloys Compd.* **2012**, *542*, 111.

[23] K. P. So, J. C. Jeong, J. G. Park, H. K. Park, Y. H. Choi, D. H. Noh, D. H. Keum, H. Y. Jeong, C. Biswas, C. H. Hong, Y. H. Lee, *Compos. Sci. Technol.* **2013**, *74*, 6.

[24] A. Mazahery, H. Abdizadeh, H. R. Baharvandi, *Mater. Sci. Eng. A* **2009**, *518*, 61.

[25] A. Yar, M. Montazerian, H. Abdizadeh, H. R. Baharvandi, *J. Alloys Compd.* **2009**, *484*, 400.

[26] W. Zhou, Z. M. Xu, *J. Mater. Process. Technol.* **1997**, *63*, 358.

[27] J. Hashim, L. Looney, M. S. J. Hashmi, *J. Mater. Process. Technol.* **1999**, *93*, 1.

[28] D. J. Lloyd, *Int. Mater. Rev.* **1994**, *39*, 1.

[29] Z. Zhang, D. Chen, *Scr. Mater.* **2006**, *54*, 1321.

[30] L. Thilly, M. Véron, O. Ludwig, F. Lecouturier, *Mater. Sci. Eng. A* **2001**, *309-310*, 510.

[31] P. M. Hazzledine, *Scr. Metall. Mater.* **1992**, *26*, 57.

[32] R. U. Vaidya, K. . Chawla, *Compos. Sci. Technol.* **1994**, *50*, 13.

[33] S.-M. Choi, H. Awaji, *Sci. Technol. Adv. Mater.* **2005**, *6*, 2.

[34] D. Dunand, A. Mortensen, *Mater. Sci. Eng. A* **1991**, *144*, 179.

[35] R. J. Arsenault, N. Shi, *Mater. Sci. Eng.* **1986**, *81*, 175.

[36] H. Zhang, N. Maljkovic, B. S. Mitchell, *Mater. Sci. Eng. A* **2002**, *326*, 317.

[37] M. Habibnejad-Korayem, R. Mahmudi, W. J. Poole, *Mater. Sci. Eng. A* **2009**, *519*, 198.

[38] R. K. Davies, V. Randle, G. J. Marshall, **1998**, *46*, 6021.

[39] R. J. Arsenault, *Mater. Sci. Eng.* **1984**, *64*, 171.

[40] C. Goh, J. Wei, L. Lee, M. Gupta, *Acta Mater.* **2007**, *55*, 5115.

[41] N. Ramakrishnan, *Acta Mater.* **1996**, *44*, 69.

[42] C.-S. Kim, I. Sohn, M. Nezafati, J. B. Ferguson, B. F. Schultz, Z. Bajestani-Gohari, P. K. Rohatgi, K. Cho, *J. Mater. Sci.* **2013**, *48*, 4191.

[43] L. H. Dai, Z. Ling, Y. L. Bai, *Compos. Sci. Technol.* **2001**, *61*, 1057.

[44] E. O. Hall, *Proc. Phys. Soc. Lond.* **1951**, *64B*, 747.

[45] N. J. Petch, *J. Iron Steel Inst.* **1953**, *174*, 25.

[46] A. Sanaty-Zadeh, *Mater. Sci. Eng. A* **2012**, *531*, 112.

[47] Z. Zhang, D. L. Chen, *Mater. Sci. Eng. A* **2008**, *483-484*, 148.

[48] D. Wang, M. P. De Cicco, X. Li, *Mater. Sci. Eng. A* **2012**, *532*, 396.

[49] A. Dehghan Hamedan, M. Shahmiri, *Mater. Sci. Eng. A* **2012**, *556*, 921.

[50] C. Suryanarayana, N. Al-Aqeeli, *Prog. Mater. Sci.* **2013**, *58*, 383.

[51] J. Cintas, F. G. Cuevas, J. M. Montes, E. J. Herrera, *Scr. Mater.* **2005**, *53*, 1165.

[52] J. Ye, J. He, J. M. Schoenung, *Metall. Mater. Trans. A* **2005**.

[53] Y. B. Liu, S. C. Lim, L. Lu, M. O. Lai, *J. Mater. Sci.* **1994**, *29*, 1999.

[54] S. Bera, S. G. Chowdhury, Y. Estrin, I. Manna, *J. Alloys Compd.* **2013**, *548*, 257.

[55] M. R. Kamali Ardakani, S. Khorsand, S. Amirkhanlou, M. Javad Nayyeri, *Mater. Sci. Eng. A* **2014**, *592*, 121.

[56] C. Suryanarayana, *J. Alloys Compd.* **2011**, *509*, S229.

[57] C. Suryanarayana, *Prog. Mater. Sci.* **2001**, *46*, 1.

[58] H. J. Fecht, *NanoStructured Mater.* **1995**, *6*, 33.

[59] H. Su, W. Gao, H. Zhang, H. Liu, J. Lu, Z. Lu, *Mater. Sci. Technol.* **2012**, *28*, 178.

[60] A. Mazahery, M. O. Shabani, *Trans. Nonferrous Met. Soc. China* **2012**, *22*, 275.

[61] H. Su, W. Gao, Z. Feng, Z. Lu, *Mater. Des.* **2012**, *36*, 590.

[62] G. Cao, H. Choi, J. Oportus, H. Konishi, X. Li, *Mater. Sci. Eng. A* **2008**, *494*, 127.

[63] S. Donthamsetty, **2009**, *2*, 27.

[64] Y. Yang, J. Lan, X. Li, *Mater. Sci. Eng. A* **2004**, *380*, 378.

[65] J. Hashim, L. Looney, M. S. J. Hashmi, *J. Mater. Process. Technol.* **2001**, *119*, 324.

[66] S. Tahamtan, a. Halvaee, M. Emamy, M. S. Zabihi, *Mater. Des.* **2013**, *49*, 347.

[67] J. Hashim, L. Looney, M. S. J. Hashmi, *J. Mater. Process. Technol.* **2002**, *123*, 251.

[68] H. Abdizadeh, R. Ebrahimifard, M. A. Baghchesara, *Compos. Part B Eng.* **2014**, *56*, 217.

[69] H. Beygi, H. R. Ezatpour, S. A. Sajjadi, S. M. Zebarjad, in *18th Int. Conf. Compos. Mater.*, **2011**.

[70] J. Hashim, L. Looney, M. S. J. Hashmi, *J. Mater. Process. Technol.* **2001**, *119*, 329.

[71] a. Mazahery, M. Ostadshabani, *J. Compos. Mater.* **2011**, *45*, 2579.

[72] K. Sukumaran, S. G. K. Pillai, R. M. Pillai, V. S. Kelukutty, B. C. Pai, K. G. Satyanarayana, K. K. Ravikumar, *J. Mater. Sci.* **1995**, *30*, 1469.

[73] A. Kawabe, A. Oshida, T. Toda, Kobayashi Hiroyuki, *J. Japan Inst. Light Met.* **1999**, *49*, 149.

[74] A. Mazahery, M. . Shabani, *Strength Mater.* **2012**, *44*, 686.

[75] B. F. Schultz, J. B. Ferguson, P. K. Rohatgi, *Mater. Sci. Eng. A* **2011**, *530*, 87.

[76] A. D. Mcleod, C. M. Gabryel, *Metall. Trans. A* **1992**, *23A*, 1279.

[77] W. Zhou, Z. M. Xu, *J. Mater. Process. Tech.* **1997**, *63*, 358.

[78] A. Mazahery, M. O. Shabani, *Powder Technol.* **2012**, *217*, 558.

[79] M. Karbalaei Akbari, H. R. Baharvandi, O. Mirzaee, *Compos. Part B Eng.* **2013**, *55*, 426.

[80] Q. Li, C. a. Rottmair, R. F. Singer, *Compos. Sci. Technol.* **2010**, *70*, 2242.

[81] B. Abbasipour, B. Niroumand, S. M. Monir Vaghefi, *Trans. Nonferrous Met. Soc. China* **2010**, *20*, 1561.

[82] S. a. Sajjadi, H. R. Ezatpour, M. Torabi Parizi, *Mater. Des.* **2012**, *34*, 106.

[83] L.-Y. Chen, J.-Y. Peng, J.-Q. Xu, H. Choi, X.-C. Li, *Scr. Mater.* **2013**, *69*, 634.

[84] K. B. Nie, X. J. Wang, K. Wu, L. Xu, M. Y. Zheng, X. S. Hu, *J. Alloys Compd.* **2011**, *509*, 8664.

[85] K. B. Nie, X. J. Wang, L. Xu, K. Wu, X. S. Hu, M. Y. Zheng, *J. Alloys Compd.* **2012**, *512*, 355.

[86] K. B. Nie, X. J. Wang, L. Xu, K. Wu, X. S. Hu, M. Y. Zheng, *Mater. Des.* **2012**, *36*, 199.

[87] S. Kandemir, A. Yalamanchili, H. V. Atkinson, *Key Eng. Mater.* **2012**, *504-506*, 339.

[88] M. J. Shen, X. J. Wang, C. D. Li, M. F. Zhang, X. S. Hu, M. Y. Zheng, K. Wu, *Mater. Des.* **2013**, *52*, 1011.

[89] K. Deng, C. Wang, X. Wang, K. Wu, M. Zheng, *Mater. Des.* **2012**, *38*, 110.

[90] K. K. Deng, X. J. Wang, Y. W. Wu, X. S. Hu, K. Wu, W. M. Gan, **2012**, *543*, 158.

[91] K. K. Deng, K. Wu, Y. W. Wu, K. B. Nie, M. Y. Zheng, *J. Alloys Compd.* **2010**, *504*, 542.

[92] S. a. Sajjadi, M. Torabi Parizi, H. R. Ezatpour, a. Sedghi, *J. Alloys Compd.* **2012**, *511*, 226.

[93] T. T. Meek, Q. Han, *Ultrasonic Processing of Materials - Final Technical Report*, U.S. Departiment Of Energy, **2006**.

[94] J. Lan, Y. Yang, X. Li, *Mater. Sci. Eng. A* **2004**, *386*, 284.

[95] S. Mula, P. Padhi, S. C. Panigrahi, S. K. Pabi, S. Ghosh, *Mater. Res. Bull.* **2009**, *44*, 1154.

[96] H. Choi, H. Konishi, X. Li, *Mater. Sci. Eng. A* **2012**, *541*, 159.

[97] H. Puga, J. Barbosa, S. Costa, S. Ribeiro, a. M. P. Pinto, M. Prokic, *Mater. Sci. Eng. A* **2013**, *560*, 589.

[98] G. Cao, H. Konishi, X. Li, *Mater. Sci. Eng. A* **2008**, *486*, 357.

[99] K. S. Suslick, Ed., *Ultrasound: Its Chemical, Physical, and Biological Effects*, VHC, New York, **1988**.

[100] O. Abramov, *Ultrasound in Liquid and Solid Metals*, CRC Press, Boca Raton, FL, **1994**.

[101] L. Ma, F. Chen, G. Shu, *J. Mater. Sci. Lett.* **1995**, *14*, 649.

[102] K. S. Suslick, Y. Didenko, M. M. Fang, T. Hyeon, K. J. Kolbeck, W. B. McNamara, M. M. Midleleni, M. Wong, *Phil. Trans. R. Soc. Lond. A* **1999**, 335.

[103] Y. Yang, X. Li, *J. Manuf. Sci. Eng.* **2007**, *129*, 252.

[104] H. Choi, M. Jones, H. Konishi, X. Li, *Metall. Mater. Trans. A* **2011**, *43*, 738.

[105] I. Narasimha Murthy, D. Venkata Rao, J. Babu Rao, *Mater. Des.* **2012**, *35*, 55.

[106] X. Liu, Y. Osawa, S. Takamori, T. Mukai, **2008**, *62*, 2872.

[107] S. Mula, S. K. Pabi, C. C. Koch, P. Padhi, S. Ghosh, *Mater. Sci. Eng. A* **2012**, *558*, 485.

[108] Z. Liu, Q. Han, J. Li, *Compos. Part B Eng.* **2011**, *42*, 2080.

[109] H. Choi, W. Cho, X. C. Li, D. Hoefert, D. Weiss, **2013**, 1.

[110] R. S. Mishra, Y. Ma, Z, I. Charit, *Mater. Sci. Eng. A* **2003**, *341*, 307.

[111] R. S. Mishra, Z. Y. Ma, *Mater. Sci. Eng. R Reports* **2005**, *50*, 1.

[112] P. Cavaliere, E. Cerri, L. Marzoli, J. Dos Santos, *Appl. Compos. Mater.* **2004**, *11*, 247.

[113] L. Ceschini, I. Boromei, G. Minak, A. Morri, F. Tarterini, *Compos. Part A Appl. Sci. Manuf.* **2007**, *38*, 1200.

[114] F. Cioffi, R. Fernández, D. Gesto, P. Rey, D. Verdera, D. González-Doncel, *Compos. Part A Appl. Sci. Manuf.* **2013**, *54*, 998.

[115] P. Periyasamy, B. Mohan, V. Balasubramanian, *J. Mater. Eng. Process.* **2012**, *21*, 2417.

[116] D. R. Ni, D. L. Chen, D. Wang, B. L. Xiao, Z. Y. Ma, *Mater. Des.* **2013**, *51*, 199.

[117] K. Kalaiselvan, I. Dinaharan, N. Murugan, *Mater. Des.* **2014**, *55*, 176.

[118] Y. Bozkurt, H. Uzun, S. Salman, *J. Compos. Mater.* **2011**, *45*, 2237.

[119] D. Storjohann, O. M. Barabash, S. S. Babu, S. A. David, P. S. Sklad, E. E. Bloom, *Met. Mater. Trans. A* **2005**, *36*, 3237.

[120] O. S. Salih, I. Hengan Ou□ , W. Sun, D. G. McCartney, *Mater. Des.* **2015**, *86*, 61.

[121] a. Shafiei-Zarghani, S. F. Kashani-Bozorg, a. Zarei-Hanzaki, *Mater. Sci. Eng. A* **2009**, *500*, 84.

[122] Y. Morisada, H. Fujii, T. Nagaoka, K. Nogi, M. Fukusumi, *Compos. Part A Appl. Sci. Manuf.* **2007**, *38*, 2097.

[123] Q. Liu, L. Ke, F. Liu, C. Huang, L. Xing, *Mater. Des.* **2013**, *45*, 343.

[124] C. Lee, J. Huang, P. Hsieh, *Scr. Mater.* **2006**, *54*, 1415.

[125] G. Faraji, P. Asadi, *Mater. Sci. Eng. A* **2011**, *528*, 2431.

[126] K. Sun, Q. Y. Shi, Y. J. Sun, G. Q. Chen, *Mater. Sci. Eng. A* **2012**, *547*, 32.

[127] S. A. Hosseini, K. Ranjbar, R. Dehmolaei, A. R. Amirani, *J. Alloys Compd.* **2015**, *622*, 725.

[128] Y. Yang, X. Li, *J. Manuf. Sci. Eng.* **2007**, *129*, 497.

[129] H. R. Ezatpour, S. A. Sajjadi, M. H. Sabzevar, Y. Huang, *Mater. Des.* **2014**, *55*, 921.

[130] B. Abbasipour, B. Niroumand, S. Monirvaghefi, *Suppl. Proc. Mater. Process. Interfaces* **2012**, *1*, 733.

[131] S. Purushothaman, J. K. Tien, *Acta Metall.* **1978**, *26*, 519.

[132] R. Fernández, G. González-Doncel, *Acta Mater.* **2008**, *56*, 2549.

[133] Y. Li, F. A. Mohamed, *Acta Mater.* **1997**, *45*, 4775.

[134] a. H. Monazzah, a. Simchi, S. M. S. Reihani, *Mater. Sci. Eng. A* **2010**, *527*, 2567.

[135] Z. Lin, Y. Li, F. a Mohamed, *Mater. Sci. Eng. A* **2002**, *332*, 330.

[136] a. Alizadeh, E. Taheri-Nassaj, *Mater. Charact.* **2012**, *67*, 119.

[137] M. Sameezadeh, M. Emamy, H. Farhangi, *Mater. Des.* **2011**, *32*, 2157.

[138] N. Nemati, R. Khosroshahi, M. Emamy, a. Zolriasatein, *Mater. Des.* **2011**, *32*, 3718.

[139] a. M. Al-Qutub, a. Khalil, N. Saheb, a. S. Hakeem, *Wear* **2013**, *297*, 752.

[140] I.-Y. Kim, J.-H. Lee, G.-S. Lee, S.-H. Baik, Y.-J. Kim, Y.-Z. Lee, *Wear* **2009**, *267*, 593.

[141] H. J. Choi, S. M. Lee, D. H. Bae, *Wear* **2010**, *270*, 12.

[142] S. Zhou, X. Zhang, Z. Ding, C. Min, G. Xu, W. Zhu, *Compos. Part A Appl. Sci. Manuf.* **2007**, *38*, 301.

CHAPTER 5

MATERIALS AND METHODS
AL-MATRIX COMPOSITES

PURPOSE OF THE WORK

The growing interest on metal matrix composites for industrial applications, related to the potentially high specific properties and thermal stability of such materials has been extensively discussed in Chapter 4. Aiming to widen the knowledge on Al-based composites, different research activities were addressed to the production and characterization of both micrometric and nanometric reinforced composites. The purpose of each activity may be summarized as follows:

- **PART 1 – Production of Al based composites via ex situ and in situ routes**

Focusing the attention on casting routes for Al-matrix composites, some attempts were made at the laboratory scale to evaluate the feasibility of liquid-state ex situ and in situ techniques to produce sound Al based composites.

As concerning the *ex situ* production route, attempts were made to produce composites characterized by micrometric and nanometric reinforcing phase (Al_2O_3 particles) and A356 alloy as matrix; the composites were processed through liquid state casting method assisted with ultrasonic stirring of the melt. Different weight fractions of micro and nanoparticles were added to the melt to evaluate (i) the efficiency of the method to incorporate micro and nanoparticles to the matrix and (ii) the effect of different micro and nanoparticles content on the composite hardness.

On the other hand, an *in situ* technique was tested to produce A356 based composites reinforced with ZrB_2 particles. The technique, exploiting proper chemical reactions between Al and KBF_4/K_2ZrF_6 inorganic salts, is expected to induce the formation of in-situ ZrB_2 particles. Ex situ and in situ processed composites were subjected to microstructural and preliminary mechanical characterization. Experimental activities and main results obtained from the present investigation are described in Paragraphs 5.1 and 6.1.

- **PART 2 – Characterization of FSP rheo-cast AA2024-Al_2O_3 nanocomposites**

The second part of the research activity on Al-based composites was carried out in the framework of a collaboration with the Department of Metallurgy, Mining & Petroleum of Al-Azhar University (Cairo, Egypt) and the Department of Metallurgical and Materials Engineering of Suez University (Suez, Egypt), aiming to evaluate the application of Friction Stir Processing (FSP) as possible method for enhancing particles distribution and mitigating casting defects associated to the semi-solid processing of Al based nanocomposites.
In this context, AA2024-Al_2O_3 nanocomposites were produced by rheo casting technique at Cairo University[1], where cast bars were subjected to FSP at fixed processing conditions (linear and rotational speed, tilt angle). Characterization activities were then carried out at Bologna University on the unreinforced matrix and nanocomposite, both in the as cast and FSP state, aiming to evaluate the effect of FSP process on the composite microstructure and mechanical behavior. Experimental activities and main results are summarized in Paragraphs 5.2. and 6.2.

- **PART 3 – Characterization of FSP AA7075-Al_2O_3 nanocomposites**

In the framework of the above mentioned cooperation project, a research activity was addressed to the evaluation of Friction Stir Processing (FSP) as possible solid-state mean of nanoparticles distribution to produce surface Al-based nanocomposites. It is known, in fact, that both liquid state processing of Al based nanocomposites are unavoidably associated to casting defects such as porosities, cavities and oxide films; FSP is thought to be a good candidate method to allow the incorporation of Al_2O_3 particles at the solid state by exploitation of severe plastic deformation. The research activity was carried out in

[1] AA2024-Al_2O_3 composites were produced by Dr. Wael Hoziefa, under the supervision of Prof. Iman El-Mahallawi, at Al-Azhar University facilities.

collaboration with the Department of Metallurgical and Materials Engineering of Suez University (Egypt).

AA7075-Al_2O_3 surface nanocomposites were processed at Suez University[2] through FSP, at the same linear and rotation speed. In particular, the present study was aimed at the evaluation of the effect of FSP passes number on particles distribution. Composites processed with 1, 3 and 4 FSP passes were produced. Microstructural and preliminary mechanical characterization activities were carried out at Bologna University. Experimental procedure and results are summarized in Paragraphs 5.3 and 6.3.

[2] AA7075-Al_2O_3 composites were produced by Prof. Mohamed Mohamed Zaky Ahmed at Suez University.

5.1 Experimental procedure – PART 1

Production of micro and nano Al-based composites

5.1.1 SAMPLES PRODUCTION

Composites production attempts followed two main routes, i.e. an ***ex situ*** route, based on stir casting process and an ***in situ*** route, exploiting the chemical reaction between Al matrix and proper additive powders to form thermally stable dispersoids.

Ex situ technique

For the ex situ production route, A356 alloy was used as matrix (chemical composition is reported in Table 5.1). As reinforcing phase, alumina (Al_2O_3) particles with micrometric and nanometric size[3] were used. Size of the reinforcing particles is summarized in Table 5.2.

Table 5.1. Chemical composition of A356 matrix alloy measured by GD-OES.

Element	Si	Mg	Ti	Fe	Mn	Zn	Al
wt%	7.018	0.405	0.138	0.065	0.006	0.075	Balance

Table 5.2. Size of Al_2O_3 particles employed as reinforcing phase

Particle	Size
Micrometric Al_2O_3	1-20 μm
Nanometric Al_2O_3	~80 nm

The composites were produced through the stir casting method assisted with ultrasonic treatment of the melt (Figure 5.1). Alumina particles were added to the matrix by the layer-feeding method, consisting in the deposition of alternating layers of A356 pieces (100 g) and Al_2O_3 particles into a ceramic crucible. The temperature was raised to 800 °C in order to bring the matrix at the fully liquid state. Mechanical stirring at 120 rpm of the melt was performed by using a coated steel stirrer for 10 min, in order to distribute particles within the matrix and to preliminarily disgregate clusters. The ultrasonic probe, made in Ti6-Al4-V alloy, was pre-heated at 300° C and dipped into the melt at 730 °C. The ultrasonic treatment was then carried out for 3 minutes, by subjecting the melt to ultrasonic

[3] The particles were produced through plasma synthesis at the Research Group for Industrial Applications of Plasmas, University of Bologna, coordination Prof. Vittorio Colombo.

vibrations at 20 kHz and 38 μm of amplitude. The probe was then removed from the composite melt and the crucible was extracted from the furnace for solidification.

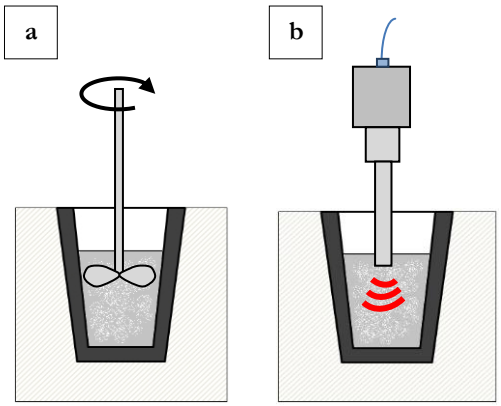

Figure 5.1. Schematic of the composites ex-situ production process steps: (a) mechanical stirring and (b) ultrasonic treatment of the melt.

Following the same production route, composites reinforced with micrometric, nanometric and mixed particles were produced. For comparison, unreinforced samples with and without ultrasonic treatment were produced (indicated as A356 and A356+US, respectively). Weight fraction and type of reinforcing phase used for the production of composites are summarized in Table 5.3.

Table 5.3. Summary of the composites produced through stir casting technique: designation, reinforcing phase size and weight fraction.

Sample code	Al_2O_3 size	Weight fraction
A356	-	-
A356-US	-	-
M2	Micrometric	2 %
M5	Micrometric	5 %
M8	Micrometric	8 %
N1	Nanometric	1 %
M3N1	Micrometric + Nanometric	3 μ% + 1 n%

In situ technique

For the in situ production route, attempts were made to produce particle reinforced composites by a molten reaction technique meant to form ZrB_2 particles. In particular, A356 alloy (chemical composition shown in Table 5.1) was used as matrix; 200 ppm of Sr was added to the melt in form of AlSr10 master alloy to modify the eutectic structure. K_2ZrF_6 and KBF_4 salts powders were used as reactants. Salts powders were dehydrated at 300 °C for 2 h before being added to the molten matrix at 800 °C. The amount of salts powders was calculated to reach KBF_4:K_2ZrF_6 mole ratio of 2:1, according to some studies reported in the literature[1]. A slightly higher mole fraction in comparison to the nominal value (i.e. ~2.4:1), was suggested to avoid the formation of needle-like brittle Al_3Zr, corresponding to KBF_4/K_2ZrF_6 weight ratio of 1,06. According to these calculations, two samples were produced by adding in total 5 and 10 wt% of salts to A356 matrix. Weight of reactants and matrix are shown in Table 5.4. At first, the salts were mixed in the molten matrix through mechanical stirring to favor powders distribution, then electromagnetic stirring of the melt was applied. After removing the slag, the composite melt was poured into a pre-heated metal mold.

Table 5.4. Amount of reactant salts added to A356 matrix

Salts tot. wt% ratio	Salts weight [g]	K_2ZrF_6 weight [g]	KBF_4 weight [g]	Total A356 weight [g]
5	27,5	13,31	14,19	550
10	100	48,5	51,5	1000

5.1.2 Microstructural and hardness characterization

Samples for microstructural analyses were cut from the castings; metallographic samples were then prepared by grinding and polishing up to 1 μm diamond suspension. Optical, scanning (SEM) and field emission electron microscopes (SEM-EDS and FE-SEM, respectively) were used for the evaluation of particles distribution and microstructures.

5.1.3 MECHANICAL CHARACTERIZATION

The effect of particles addition on mechanical properties was preliminary investigated by hardness measurement. Brinell hardness indentations were performed on the composites by applying a load of 62.5 kg and 2.5 mm diameter steel ball (HB10 scale).

5.2 Experimental procedure – PART 2

Characterization of AA2024-Al_2O_3 FSP nanocomposites

5.2.1 SAMPLES PRODUCTION

AA2024/Al_2O_3 nanocomposites were produced at the Department of Metallurgy, Mining & Petroleum, Faculty of Engineering of the Al-Azhar University (Cairo, Egypt), in the framework of a cooperation project aimed at the production and characterization of Al based nanocomposites. The composites were produced by semi-solid casting technique, in particular by rheo-casting process. AA2024 alloy, whose composition is reported in Table 5.5, was used as matrix, while alumina (Al_2O_3) nanoparticles (average particle diameter 50 nm) were used as reinforcing phase. Aiming to avoid particle clustering, nano-Al_2O_3 powders were ball milled and heat treated at 200 °C for 2 h. Particles were then added to the matrix (previously degassed) at ~600 °C by the capsulate feeding method, consisting in wrapping up nanoparticles in aluminum packages, to be added one by one to the Al melt. The melt was then mechanically stirred (1 min, 800 rpm) for enhancing particles distribution. The amount of added alumina was calculated to obtain 1 wt% of reinforcing phase fraction. The melt was then cast in a stainless steel mold. For comparison, the unreinforced AA2024 matrix was similarly processed and cast.

Table 5.5. Chemical composition (wt. %) of the AA2024 matrix measured by GD-OES

Element	Cu	Mg	Mn	Fe	Si	Zn	Al
wt%	3.984	1.502	0.404	0.143	0.194	0.064	Bal.

The produced nanocomposite and unreinforced alloy were then subjected to Friction Stir Processing (FSP). FSP was performed at 400 rpm of rotation rate, 20 mm/min linear speed with a tilt angle of 3°. The tool (6 mm probe diameter, 10 mm probe length and 20 mm diameter shoulder) was made of heat treated H13 steel. In this experimental activity, only one FSP pass was performed. Samples designation has been summarized in Table 5.6.

Table 5.6. Samples designation

Material	condition	Sample code
AA2024	As cast	A
	FSPed	A-FSP
AA2024-1wt%nAl_2O_3	As cast	N
	FSPed	N-FSP

5.2.2 MICROSTRUCTURAL CHARACTERIZATION

Microstructural analyses were carried out on the as cast and FSPed materials, for comparison, through multifocal microscopy (Hirox), optical microscopy (OM), scanning electron microscopy equipped with energy dispersive spectroscopy (SEM-EDS) and electron backscattered diffraction (EBSD). Representative cross sections of the investigated materials were cut from the FSPed and as cast plates, then grounded and polished with diamond suspension up to 1 μm. Keller's reagent was used for etching samples for OM and SEM analyses, while samples for EBSD analyses were electro-polished with a solution of 30% nitric acid in methanol for 20 s at 14 V and −15 °C. A further polishing phase with colloidal SiO_2 was aimed to eliminate small superficial second phase particles, possible causing a shadowing effect during EBSD data acquisition. The EBSD analyses were conducted with a FEI-Nova NanoSEM 450 field-emission gun scanning electron microscope (FEG-SEM) equipped with Bruker e-Flash1000 system, operating at 20 kV. FE-SEM/EBSD analyses allowed evaluating the average grain size in the stirred zone.

5.2.3 MECHANICAL CHARACTERIZATION

Vickers microhardness and tensile tests on the investigated materials were carried out at room temperature. Vickers hardness profiles were carried out on the cross section of the processed samples, as shown in Figure 5.2 at different depth from the FSPed surface (0.5, 2.5 and 5 mm). 20 indentations with linear step of 500 μm were carried out with 4.9 N of load and 10s of dwell time.

Tensile tests were carried out with an electromechanical testing machine, on flat tensile samples extracted from the FSPed plates along the processing line, aiming to have the whole gauge section in the stirred zone. Samples geometry (according to ISO6892-1[2]) and the extraction zone are depicted in Figure 5.3. All the investigated materials were subjected

to tensile testing, namely: i) the as cast 2024 alloy, ii) the as cast AA2024-Al_2O_3 nanocomposite, iii) the FSPed 2024 alloy and iv) the FSPed AA2024-Al_2O_3 nanocomposite.

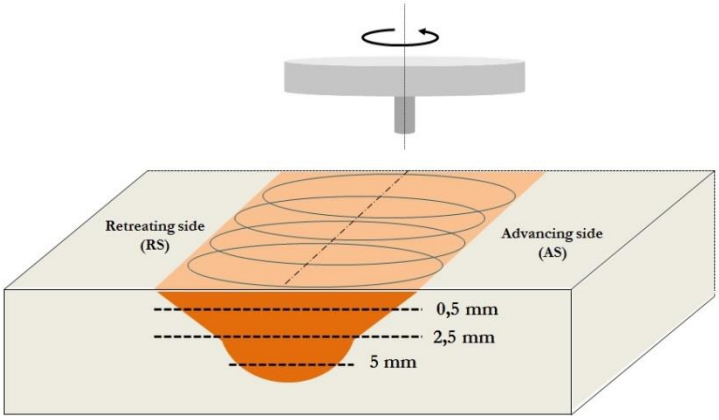

Figure 5.2. Positioning of Vickers microhardness profiles carried out on the cross sections of FSPed materials.

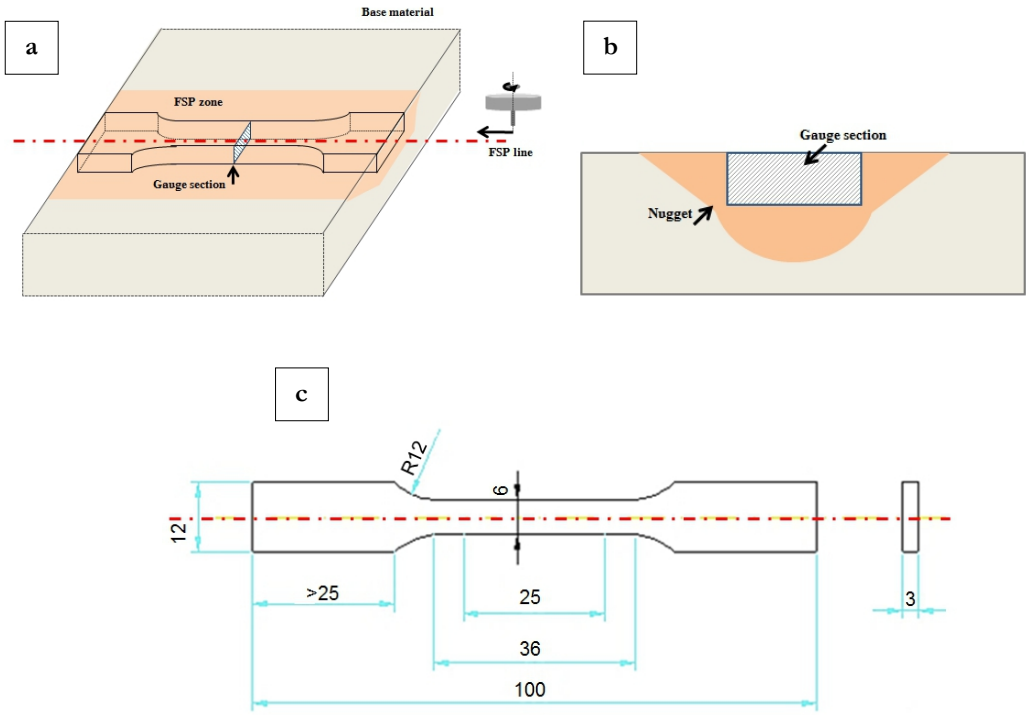

Figure 5.3. Tensile samples extraction zone: (a) position with reference to the FSP line, (b) position of the gauge section within the nugget zone and (c) geometry and size [mm] of the tensile sample.

5.3 Experimental procedure – PART 3

Characterization of AA7075-Al_2O_3 FSP nanocomposites

5.3.1 SAMPLES PRODUCTION

AA7075-Al_2O_3 nanocomposites were produced at the Department of Metallurgical and Materials Engineering of Suez University (Egypt), in the framework of a cooperation project aimed at the production and characterization of Al based nanocomposites. AA7075-O alloy (chemical composition reported in Table 5.7) was used as matrix and Al_2O_3 nanoparticles (average particle size 50 nm) as the reinforcing phase. Aiming to add nanoparticles to the aluminum matrix, a groove was realized on the surface of an AA7075 plate; particles were pushed inside it; then, in order not to disperse outside particles before FSP, a preliminary FSP pass with a flat tool was carried out, thus enabling to close the surface of the composite.

Table 5.7. Chemical composition (wt.%) of the AA7075-O composite matrix, evaluated through GD-OES.

Element	Zn	Mg	Fe	Cr	Cu	Si	Ti	Mn	Ni	Al
wt%	5,178	2,224	0,176	0,149	1,259	0,054	0,042	0,021	0,012	Bal.

The plate (Figure 5.4) was processed by 1, 3 and 4 FSP passes, with 100 % of overlapping. After each pass, the rotational direction of the tool (clockwise or counter-clockwise) was changed, as summarized in Figure 5.4. Rotational and linear speed were kept constant at 500 rpm and 40 mm/min, respectively.

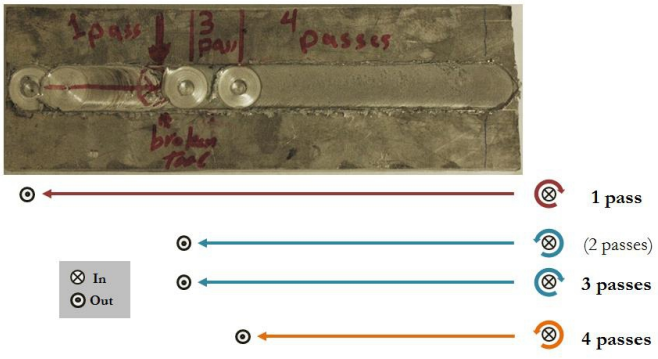

Figure 5.4. AA7075-Al_2O_3 composite plate after 1, 3 and 4 FSP passes.

5.3.2 MICROSTRUCTURAL ANALYSES

Cross sections of the plate were cut from areas processed with 1, 3 and 4 FSP passes and polished up to 1 μm diamond suspension. Samples for metallographic analyses were electro-chemically etched with Barker's reagent (HBF_4 5% vol.) at 30 V. Macrographs of the cross sections were taken by multifocal microscope (Hirox). Microstructural analyses were carried out by optical microscopy (OM) and scanning electron microscopy equipped with energy dispersive spectroscopy (SEM-EDS), aiming to highlight the presence of processing defects, particle clusterization, and the evolution of grain structure, induced by FSP-induced severe plastic deformation. The average grain size of the stirred zone (SZ) was measured on optical images, according to the linear intercept method[3].

5.3.3 MECHANICAL CHARACTERIZATION

In order to evaluate the combined effect of friction stir processing and nanoparticles addition on the material strength, Vickers microhardness measurements were carried out on the mounted cross sections. In particular, microhardness profiles were carried out at different depth from the FSP surface (2, 4, 6 and 8 mm), with 4.9 N of load and dwell time of 10s (Figure 5.5). Profiles at 2, 4 and 6 mm depth consisted of 60 indentations with linear step of 500 μm. Due to the nugget shape (narrowing by increasing distance from the FSPed surface), the last profile (at 8 mm) depth consisted of only 40 indentations, with same linear step.

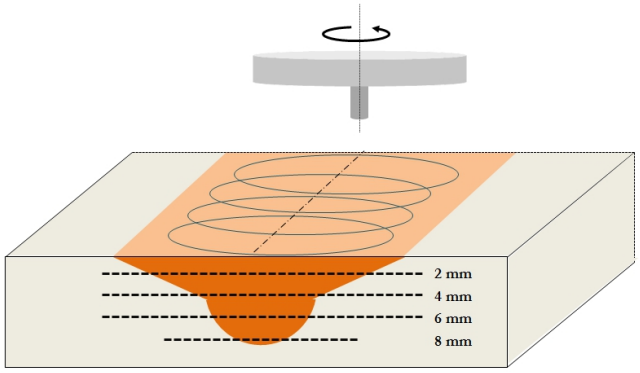

Figure 5.5. Position of Vickers microhardness profiles carried out on the cross sections of the FSP AA7075-Al_2O_3 plate.

REFERENCES – CHAPTER 5

[1] I. Dinaharan, N. Murugan, S. Parameswaran, *Mater. Sci. Eng. A* **2011**, *528*, 5733.

[2] *ISO 6892-1:2009, Metallic Materials - Tensile Testing - Part 1: Method of Test at Room Temperature*, **2009**.

[3] *ASTM E112-13 Standard Test Methods for Determining Average Grain Size*, **2013**.

CHAPTER 6

RESULTS AND DISCUSSION

AL-MATRIX COMPOSITES

6.1 Results and Discussion – PART 1

Production of micro and nano Al-based composites

6.1.1 MICROSTRUCTURAL ANALYSES - EX SITU TECHNIQUE

Micro and nano Al_2O_3 particles employed as reinforcing phase were analysed by SEM-EDS. Representative SEM images at low and high magnification and corresponding chemical composition of micro Al_2O_3 particles are reported in Figure 6.1 and Table 6.1. Microparticles were characterized by a size ranging from a few microns to about 20 μm and by regular, spherical morphology; EDS analyses revealed the nominal atomic Al:O ratio.

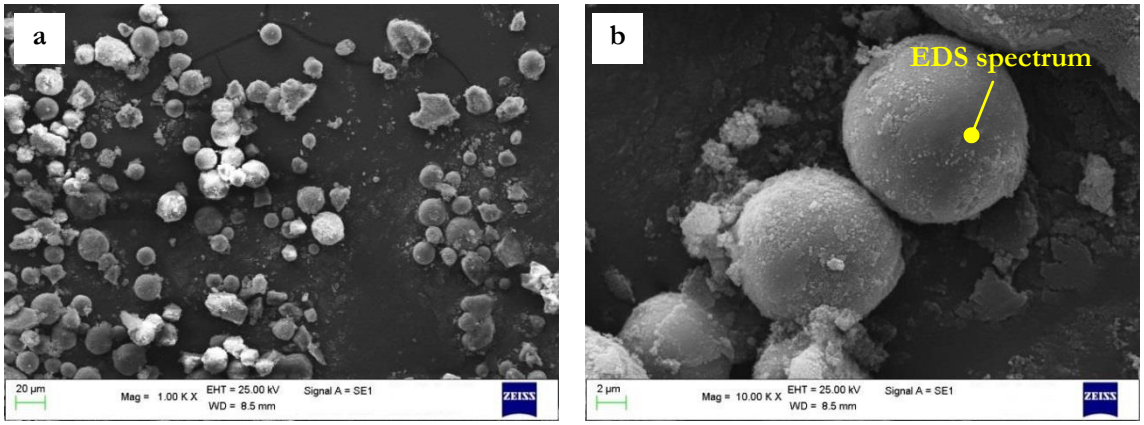

Figure 6.1. SEM images at (a) low and (b) high magnification of Al_2O_3 microparticles employed as reinforcing phase for the production of Al-based composites.

Table 6.1. Chemical composition of Al_2O_3 microparticles measured by EDS; the analyses was carried out on a single Al_2O_3 particle, as indicated in Figure 6.1b.

Element	Weight%	Atomic%
O K	47.34	60.25
Al K	52.66	39.75
Total	100.00	100.00

On the other hand, due to the nanometric size, it was not possible to quantify by SEM the actual dimension of Al_2O_3 nanoparticles (Figure 6.2). The average size was however compatible to the nominal value of ~80 nm. Chemical analyses, also in this case, well reflected Al_2O_3 chemical composition, as shown in Figure 6.2b.

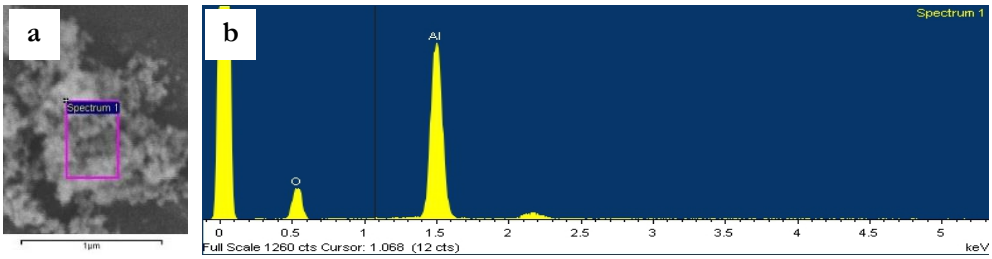

Figure 6.2. (a) SEM image of Al_2O_3 nanoparticles and (b) corresponding EDS spectrum.

Resulting from microstructural analyses carried out by optical microscopy, an increasing quantity of particles was observed in M2, M5 and M8 microcomposites, containing 2, 5 and 8 wt% of micro-sized particles, respectively (Figure 6.3). Microparticles were effectively distributed throughout the samples; it should be however pointed out that most of the particles were engulfed in the eutectic region. Therefore, in this case, the pushing action of solidification front seems to govern particles distribution. The even distribution of microparticles was observed also by SEM; representative images of M2 and M8 composites are reported in Figure 6.4.

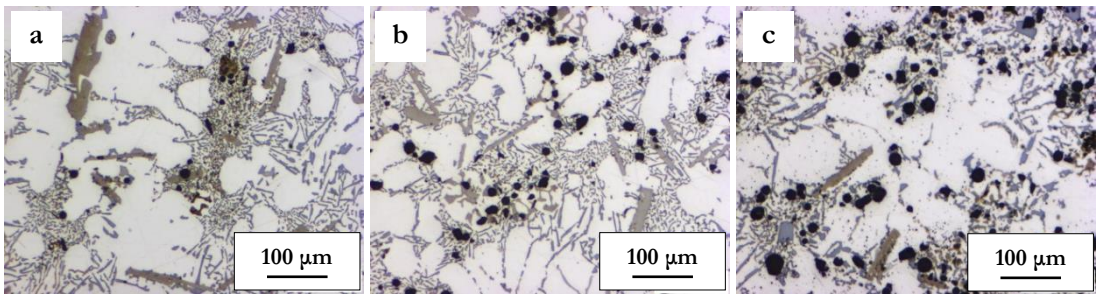

Figure 6.3. Optical images of A356 based composites containing (a) 2 wt.%, (b) 5 wt.% and (c) 8 wt.% of Al_2O_3 microparticles as reinforcing phase.

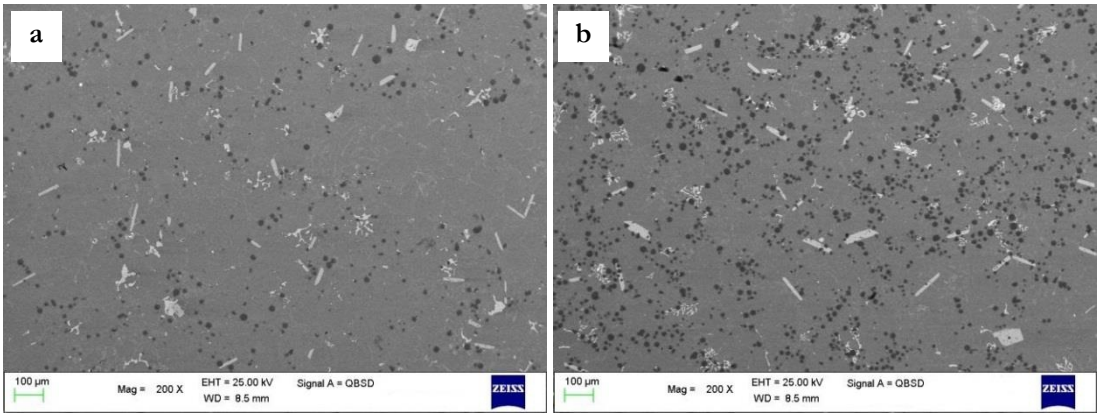

Figure 6.4. SEM images showing particles distribution in (a) M2 and (b) M5 microcomposites.

SEM analyses revealed also a good interface between matrix and Al_2O_3 microparticles (Figure 6.5). It is thought that the spherical shape of microparticles may have helped in preventing from the formation of interfacial micro-voids.

Nevertheless, despite the generally homogeneous microstructure achieved, casting defects associated to the low wettability of microparticles and clusterized particles with loss of particle/matrix coherency were observed in the composites microstructures. Representative images of such defects are reported in Figure 6.5 b,c.

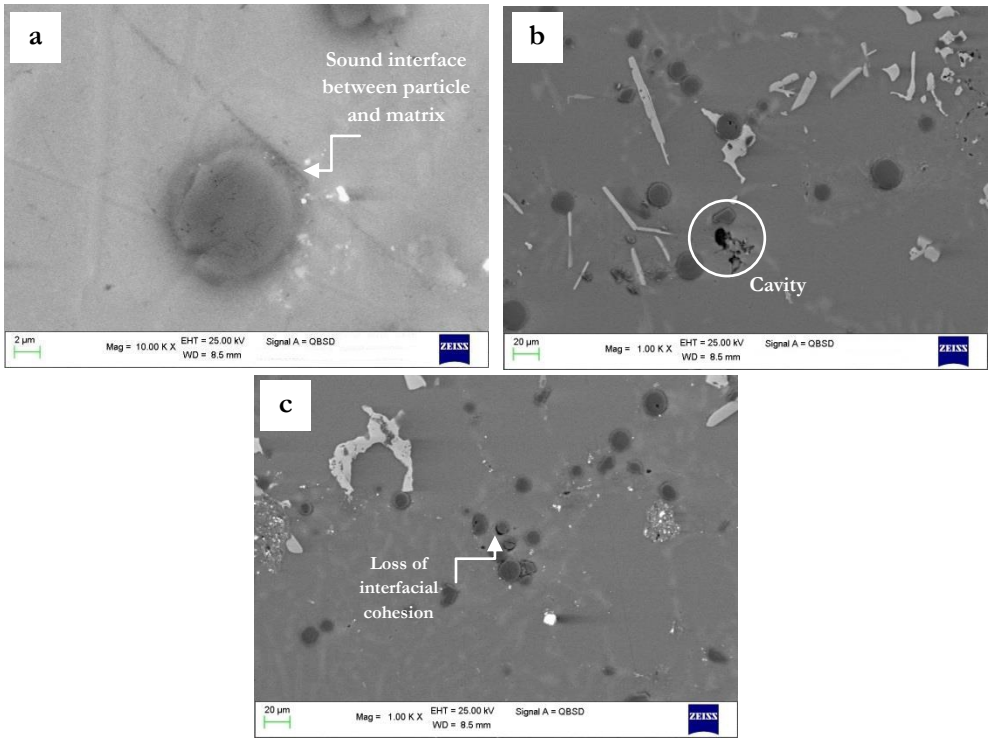

Figure 6.5. SEM images showing (a) good interface between microparticles and A356 matrix, (b) casting defect (cavity) associated to the poor wettability of Al_2O_3 particles in the eutectic region, (c) clusterized particles showing internal cracks and partial loss of interfacial cohesion with the matrix.

As further microstructural inhomogeneity, together with clusterized Al_2O_3, also some particles-depleted zones were observed, as a result of local lack of sufficient stirring action. Moreover, a large and localized amount of rod-like intermetallics (Figure 6.6a) was registered in all the samples processed with ultrasonic treatment of the melt (both in the unreinforced matrix and in the composites). A high magnification SEM image is reported in Figure 6.6b, together with EDS analyses.

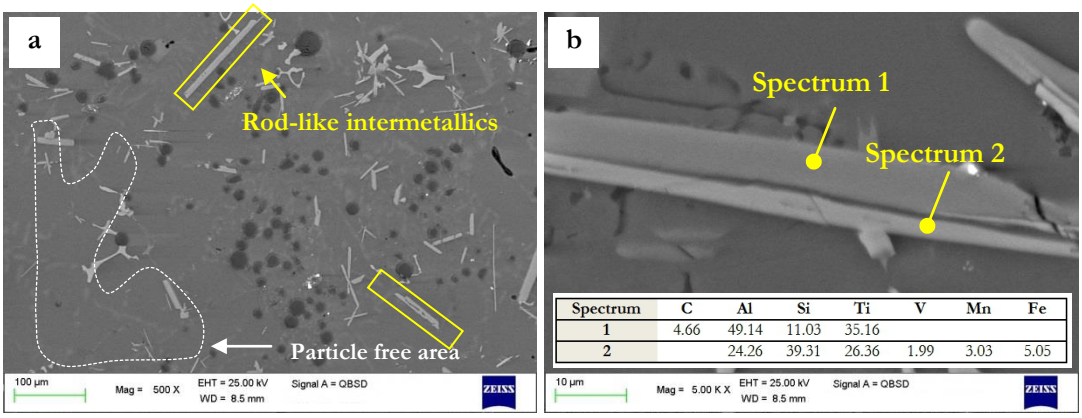

Figure 6.6. SEM images of (a) M5 composite showing a particles-depleted area and rod-like intermetallics; (b) SEM image at high magnification of Ti-rich rod-like phases with corresponding EDS chemical analyses.

Chemical analyses carried out on the particles revealed they consisted of Ti-based phases, containing also Al, Si, Fe and some other trace elements (among them, V). The reason of this should be linked to the dissolution of Ti from the ultrasonic probe during the treatment. During this phase, in fact, in view of the high temperature (730 °C), diffusive phenomena led to dissolution of Ti and V from the Ti6Al4V probe into the Al matrix. Microparticles were also observed to interact with the formation of coarse solidification intermetallic particles, which were sometimes observed to nucleate in correspondence of Al_2O_3 particles; in this case, Al_2O_3 particles were partially or even completely engulfed by the intermetallics itself. Representative SEM image and corresponding EDS maps of an engulfed Al_2O_3 particle are presented in Figure 6.7.

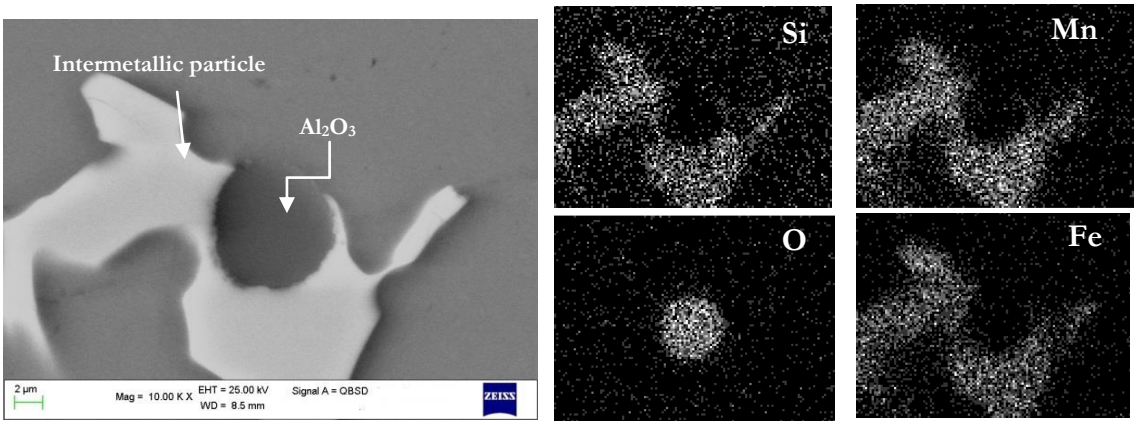

Figure 6.7. SEM image of Al_2O_3 microparticle engulfed inside an intermetallic particle; (b) EDS elemental maps showing the composition of the intermetallic particle (Al-Fe-Mn-Si).

Nanoparticles, on the contrary, are quite difficult to observe even at high magnification through electron microscopy, when homogeneously dispersed. Optical images of

composites containing 1 wt.% of nanoparticles and mixed 1 wt.% of nano - 3 wt.% microparticles (indicated as N1, M3N1, respectively) are therefore not reported. Even at FEG, documentation of single dispersed particles was quite challenging (Figure 6.8). A certain amount of clusterized particles was observed, as shown in Figure 6.8b, due to the great tendency to agglomeration of nanoparticles, due to the poor wettability and large surface-to-volume ratio. EDS analyses, as shown in Figure 6.9, confirmed the clusters consisted of agglomerated Al_2O_3 nanoparticles.

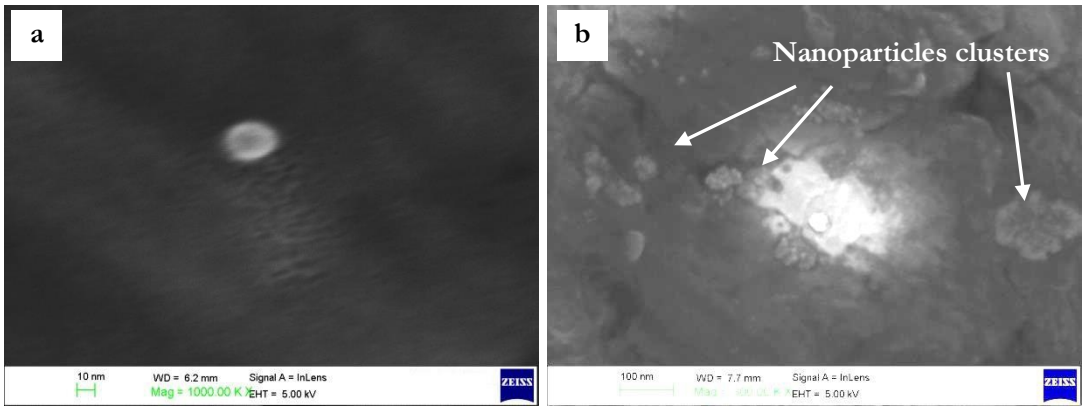

Figure 6.8. FEG images of (a) single dispersed nanoparticles observed in N1 composite and (b) Al_2O_3 nanoparticles clusters in the same sample.

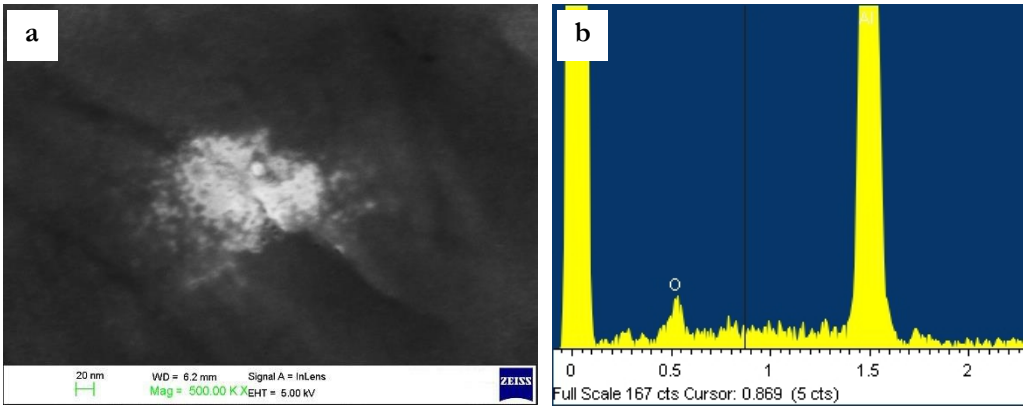

Figure 6.9. FEG image of (a) Al_2O_3 nanoparticles cluster and (b) corresponding EDS spectrum.

Since nanocomposites were processed at the same manner of microcomposites, Ti-based intermetallics were observed also in N1 and M3N1 samples. As concerning casting defects associated to nanoparticles, it must be highlighted that nanocomposites presented a higher quantity of pores and cavities in comparison to the composites containing micro-sized particles. In particular, Al_2O_3 clusterized particles were often observed on the cavity boundaries of pores. It is thought that agglomeration of nanoparticles, unavoidably associated to air entrapment, probably making difficult the interdendritic feeding, leads to the formation of internal voids. Representative images at increasing magnification of such

defects are shown in Figure 6.10, where it is possible to recognize Al_2O_3 agglomerated particles inside an interdendritic cavity.

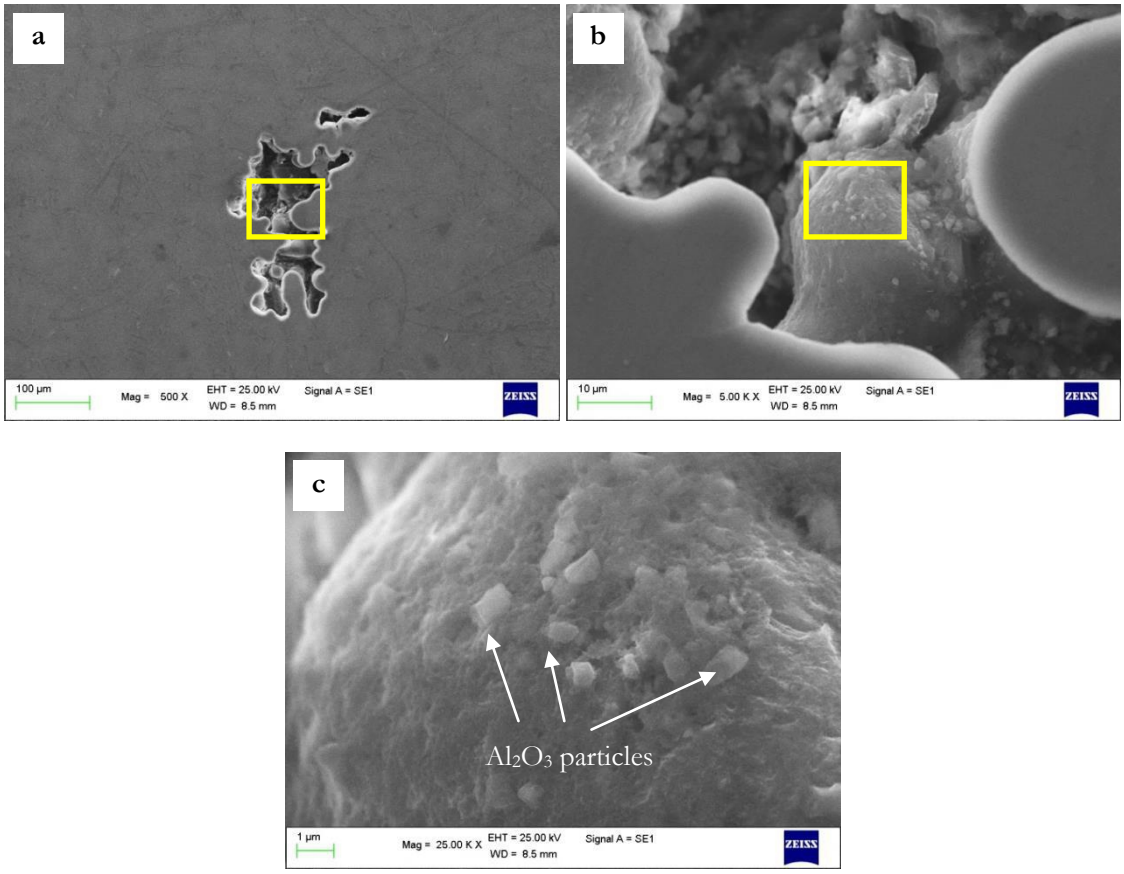

Figure 6.10. SEM images of casting defect associated to nanoparticles clusterization observed in the produced nanocomposite; (a) low magnification showing the typical morphology of interdendritic cavity, (b) high magnification of the previous image where it is possible to observe the distribution of Al_2O_3 particles on the internal boundary of the cavity and (c) high magnification of figure b, showing alumina clusters on the dendritic structure.

6.1.2 HARDNESS CHARACTERIZATION - EX SITU TECHNIQUE

Brinell hardness data measured on the composites are summarized in Figure 6.11. As expected, the base A356 alloy, unreinforced and unprocessed, shows the same hardness value of the ultrasonic treated alloy. The presence of microparticles dispersed within the matrix leads to a progressive and not negligible hardness increase. The maximum hardness was measured in M8 composite, containing the higher weight fraction of particles (8%). In this case, in comparison to the reference alloy (66 HB), an increase of about 17% was registered. On the other hand, also nanoparticles addition led to an increase of hardness; in particular, from the present investigation, 1 wt% of nanoparticles may confer to the alloy a hardness increase similar to that of the composite containing 2 wt.% or micro-reinforcement (71 HB). Also, M3N1 composite showed the same hardness of M5 composite.

It should be however pointed out that composites containing nanoparticles (namely M3N1 and N1), show higher dispersion in hardness data. This is due to the higher tendency of nanoparticles to form clusters and inducing related casting defects, in turn leading to a less even distribution of reinforcing phase.

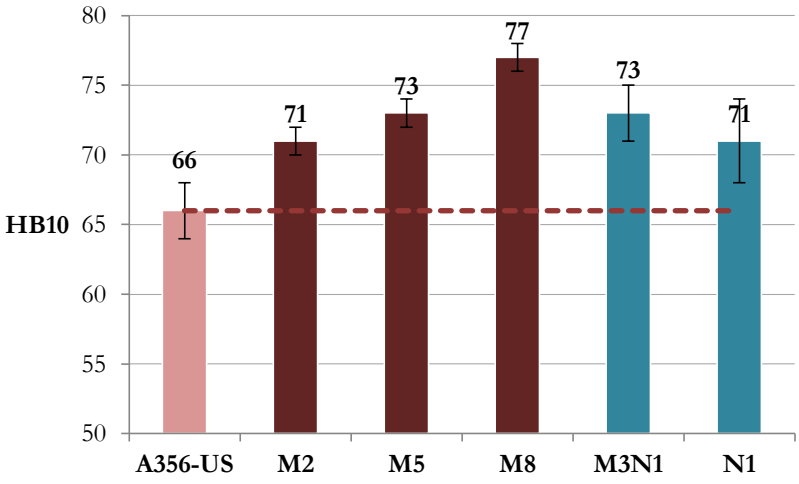

Figure 6.11. Brinell hardness (HB10 scale) measured on micro and nano reinforced composites. The red dotted line represents the reference, i.e. the unprocessed and unreinforced A356 matrix.

6.1.3 MICROSTRUCTURAL ANALYSIS - IN SITU TECHNIQUE

The produced composites, containing in total 5 and 10 wt% of salts, presented similar microstructure. Representative optical micrographs of 10wt% composite are reported in Figure 6.12a. The composites presented a typical α-Al dendritic microstructure, surrounded by a well modified eutectic structure; eutectic particles appeared in fact characterized by small size and globular morphology (Figure 6.12b). Also at low magnification (Figure 6.12a), some dark grey particles were observed within the eutectic structure. At higher magnification, these particles showed a highly fragmented morphology, differently from the usual appearance of intermetallic particles (Figure 6.12b). The presence of such phases was observed throughout the samples.

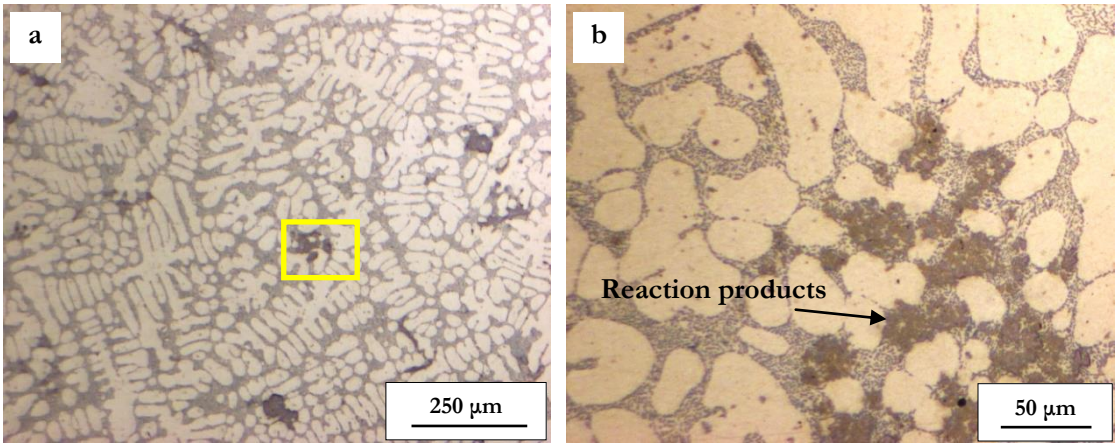

Figure 6.12. Optical images of the in situ processed composite containing 10 wt% of reactant salts; (a) low magnification image showing the dendritic structure, (b) higher magnification image where it is possible to observe the modified eutectic structure and reaction products in the eutectic region.

SEM-EDS analyses revealed the chemical composition of the unknown phases. As shown in Figure 6.13, EDS reported the concurrent presence of Al, Zr, Si and B particles, with eventual minor quantities of K and Ti, characterized by several different morphologies, mainly irregular and fragmented.

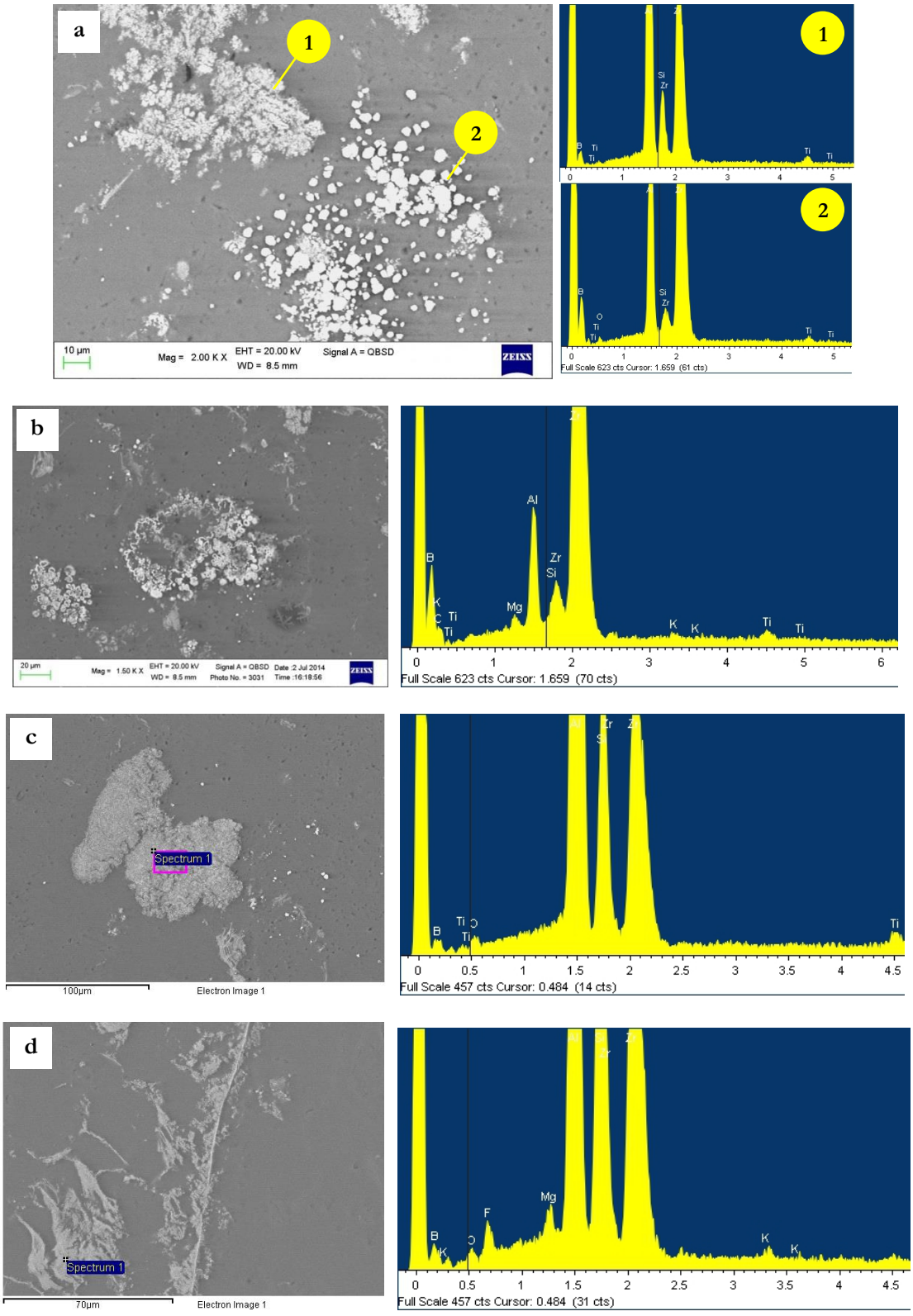

Figure 6.13. SEM images and corresponding EDS spectra carried out on unknown particles found in the eutectic structure of in-situ composites; Al, Si, Zr and B were detected in all the analyzed phases, while elements such as K, F and Ti were detected only occasionally.

The presence of such phases was somehow unexpected, since the few works investigating the same system found in the literature did not report similar findings[1,2]. On the contrary,

the presence of ZrB_2 and Al_3Zr particles was expected, as reported by Zhang[1], who claimed the production of a A356-Al_3Zr+ZrB_2 composite, working with the same reactants employing in this study. In particular, the proposed reactions to produce Al_3Z and ZrB_2 particles are the following[2]:

$$K_2ZrF_6 + 13/3Al \rightarrow Al_3Zr + 4/3AlF_3 + 2KF \quad (1)$$

$$2KBF_4 + 3Al \rightarrow AlB_2 + 2AlF_3 + 2KF \quad (2)$$

$$Al_3Zr + AlB_2 \rightarrow ZrB_2 + 4Al \quad (3)$$

According to equations 1-3, the theoretical mole ratio of salts required to produce one mole of ZrB_2 is, respectively, 1mol of K_2ZrF_6 and 2mol of KBF_4. In such a way, the only produced phase should be ZrB_2. However, a slightly higher quantity of KBF_4 with respect to the nominal 2:1 mole ratio was suggested by Dinharan et al.[2], aiming to suppress the formation of the brittle and needle-like Al_3Zr phase. This solution has therefore been adopted in the present investigation; the reactants were added in KBF_4/ K_2ZrF_6 2.4:1 mole ratio and 1.06 weight ratio. However, as a result of SEM-EDS analyses, none of the expected reaction products, neither ZrB_2 nor Al_3Zr, was detected. On the contrary, only the above mentioned phases, containing Al, Zr, Si, B, and sometimes also K and Ti, were produced. The morphology of such phases appeared quite irregular, fragmented and, unevenly dispersed within the composite microstructure.

6.1.4 HARDNESS CHARACTERIZATION - IN SITU TECHNIQUE

Brinell hardness of the in situ composites are shown in Figure 6.14. It is possible to affirm that both the composites, produced by adding 5 and 10 wt% of reactant salts to the molten matrix, present similar hardness. From the comparison with unreinforced matrix, processed at the same manner (stirring and casting procedure) of the composites, it was inferred that the salts addition led to a hardness decrease of about 22%, probably due to the irregular and fragmented morphology of the produced phases.

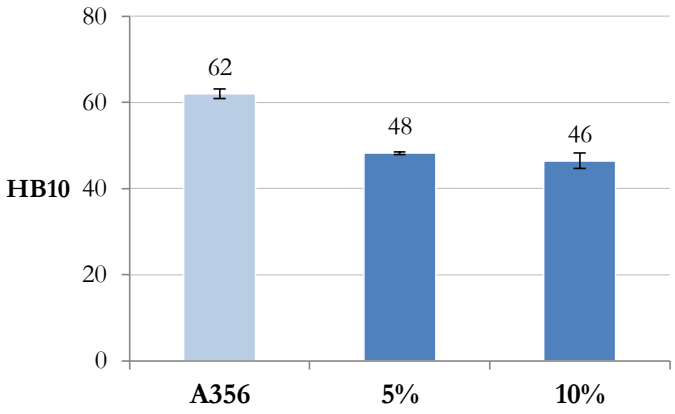

Figure 6.14. Brinell hardness (HB10 scale) of the in situ composites, produced by adding in total 5 and 10% of reactant inorganic salts (KBF_4, K_2ZrF_6). The reference value is the unreinforced A356 matrix, stirred and cast in the same way of the composites for comparison.

It should be pointed out that, in the present investigation, the presence of Si was observed in almost all the analyzed particles. Among other investigators, only Zhang et al.[1] employed an Al-Si alloy as matrix (i.e. A356 alloy), while other works were carried out on low Si alloys, namely AA6351 and AA6061 alloys[2,3]. Despite Zhang et al. did not report the formation of such phases, the interaction between reactants and Si could explain discrepancies between the attended reaction products and the actual results.

6.1.4 CONCLUSIONS

Laboratory scale production attempts were carried out to produce Al-based composites reinforced with micro- and nano-sized reinforcing phases. Different techniques, both ex situ and in situ were studied, respectively: (i) stir casting technique assisted with ultrasonic treatment of the melt, aiming to distribute Al_2O_3 micro and nanoparticles within A356 matrix, (ii) a reactive technique aimed to induce the formation of ZrB_2 nanoparticles by addition of reactant salts (KBF4-K2ZrF6) into A356 molten matrix. Experimental results may be summarized as follows:

- A356-Al_2O_3 ex situ composites were produced by stir casting technique assisted with ultrasonic treatment, by adding 2, 5, 8 wt% of micrometric Al_2O_3, 1 wt% of nanometric Al_2O_3 and a mixture of the two (3 wt% of micro and 1 wt% of nano particles). A good distribution of particles was achieved, especially in the case of micrometric reinforced composites. The lower wettability of nanoparticles was reflected in major tendency to voids formation and clusterization.
- Hardness enhancement was registered on the produced composites; nanoparticles showed a more significant contribution to composite strengthening in comparison to micro-sized ones. Despite this, casting defects associated to the poor wettability of nanoparticles were observed.
- The exploitation at the industrial scale of such technique for the production of Al-based nanocomposites seems still challenging, since a higher quantity of defects related to clusterization is expected for higher melt volumes, thus nanoparticles contents.
- In the investigated conditions, salts reactive route was reported to be ineffective; despite the results reported in the literature, no homogeneous distribution of particles was obtained, irrespectively of the salts fraction employed. Irregular, fragmented phases were observed in the interdendritic regions, containing Al, Si, Zr, B, K, F and Ti.
- Despite no significant casting macro-defects (pores, cavities) were detected, hardness of the composites produced by salt route significantly decreased from the reference value of the unreinforced matrix. Further studies are needed to understand the reason of the formation of undesired phases, thus allowing to adjust reactants amounts or properly modify the production process.

6.2 Results and Discussion – PART 2

Characterization of AA2024-Al_2O_3 FSP nanocomposites

6.2.1 MICROSTRUCTURAL ANALYSIS

Macrostructure of cast matrix alloy and nanocomposite are presented in Figure 6.15a,c. A higher amount of casting defects was detected in the nanocomposite in comparison to the as cast unreinforced matrix. The presence of such casting defects should be related to the addition of nanoparticles, characterized by poor wettability with the matrix alloy. Several studies reported similar finding, showing that, especially in liquid routes, agglomeration tendency and clusters-related entrapment of gas[4–10] is a common drawback of nanoparticles addition. Semi-solid state processing, on the other hand, is thought to induce a more uniform distribution of the reinforcing particles by increasing the wettability between particles and matrix in comparison to liquid routes, such as stir casting [11–16]

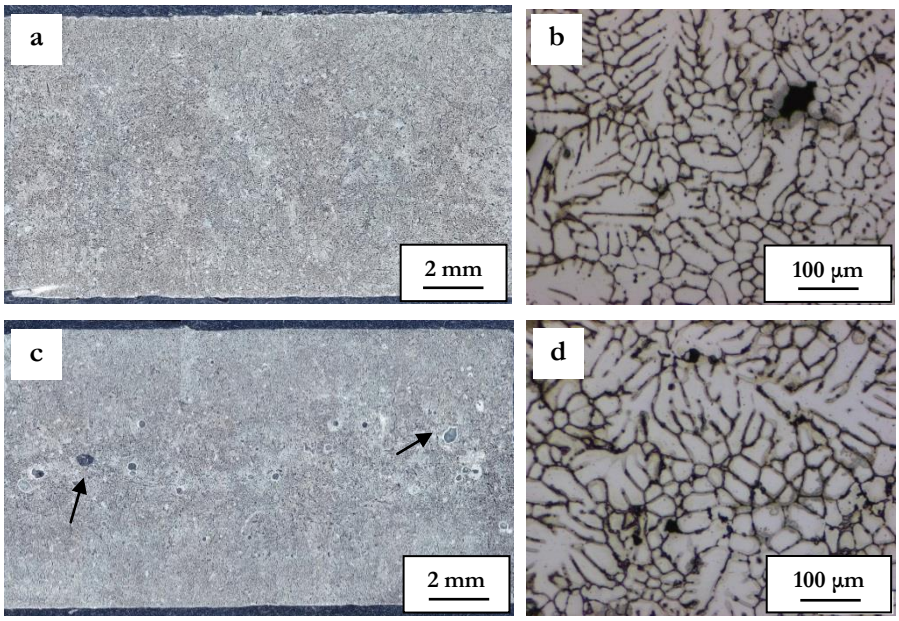

Figure 6.15. Macrographs and optical images of microstructure of semisolid-processed (a, b) AA2024 alloy and (c, d) AA2024-Al_2O_3 nanocomposite. Pores are highlighted by arrows.

Similar microstructure was observed in the as cast samples, consisting in quasi-globular α-Al dendrites, surrounded by the Al-Cu-Mg eutectic structure (Figure 6.15b,d).

The relation between porosities and nanoparticles was confirmed by SEM-EDS analyses. Clusters of Al_2O_3 nanoparticles were in fact observed on the internal boundaries of pores (Figure 6.16 a-c). Similarly, also interdendritic regions were characterized by the presence of

small alumina particle agglomerates (Figure 6.16d,e). The position of such clusters seems to indicate that the segregation of particles is the result of solidification process, in particular of the pushing action of the solidification front.

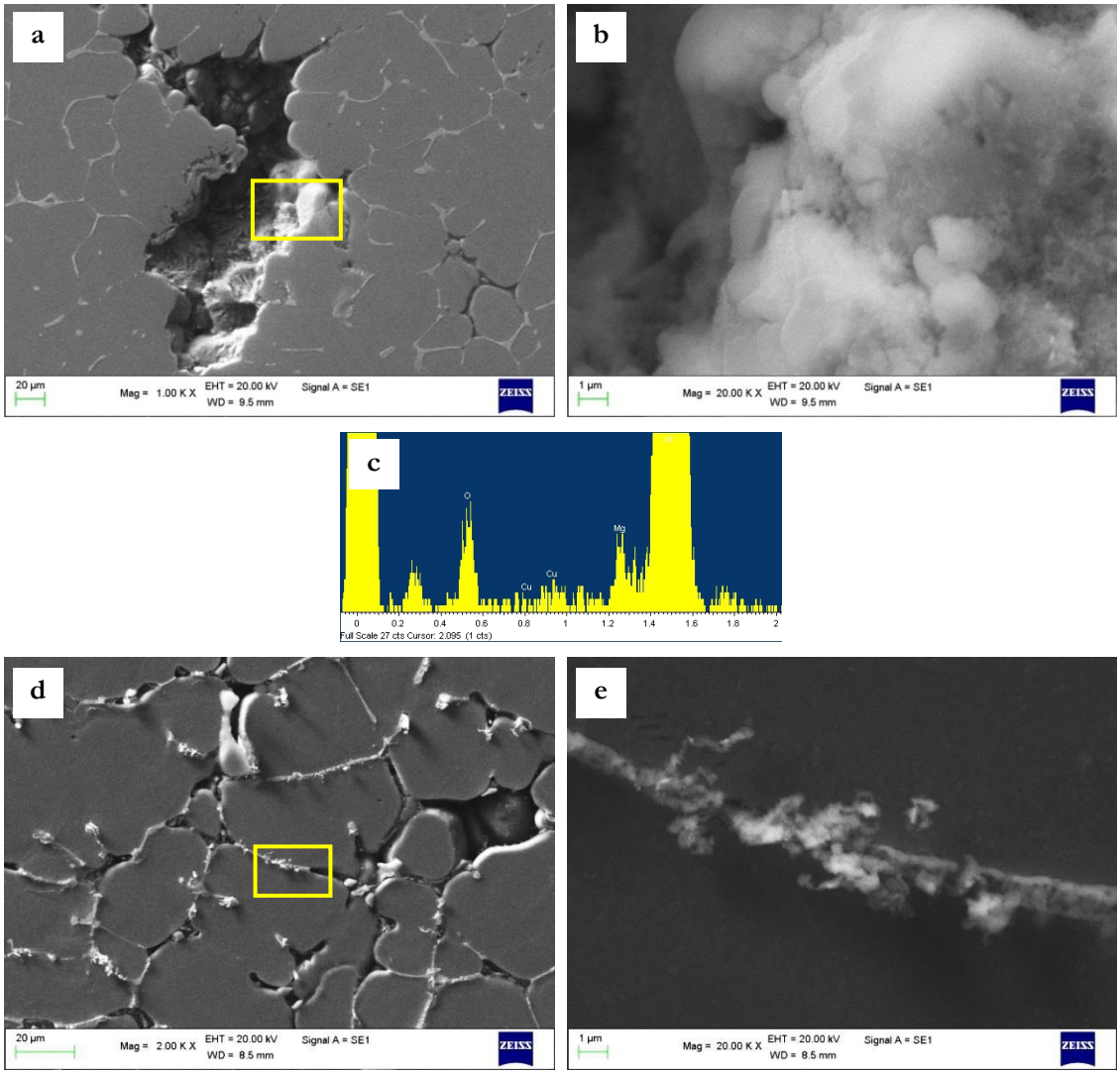

Figure 6.16. SEM images showing (a) the segregation of nanoparticles on cavities internal boundaries in the interdendritic regions, (b) high magnification image of clusterized Al_2O_3 particles and (c) EDS spectrum of Al_2O_3; (d) interdendritic distribution of small Al_2O_3 clusters and (e) higher magnification of the area highlighted in Fig. d.

By comparing unprocessed and FSPed nanocomposites (Figure 6.17c), it is possible to observe that FSP strongly reduced the quantity of casting defects associated to nanoparticles addition. Plastic deformation induced by the thermomechanical action of the pin allowed eliminating voids; as a consequence, particles are thought to be better dispersed by FSP. A different kind of interface between stirred zone and thermo-mechanically affected zone were observed at the advancing side (AS) and retreating side (RS), the first being characterized by a defined border and the latter a diffuse interconnected zone, due to

the pin rotation action, which causes material movement from the AS to the RS, where it is accumulated.

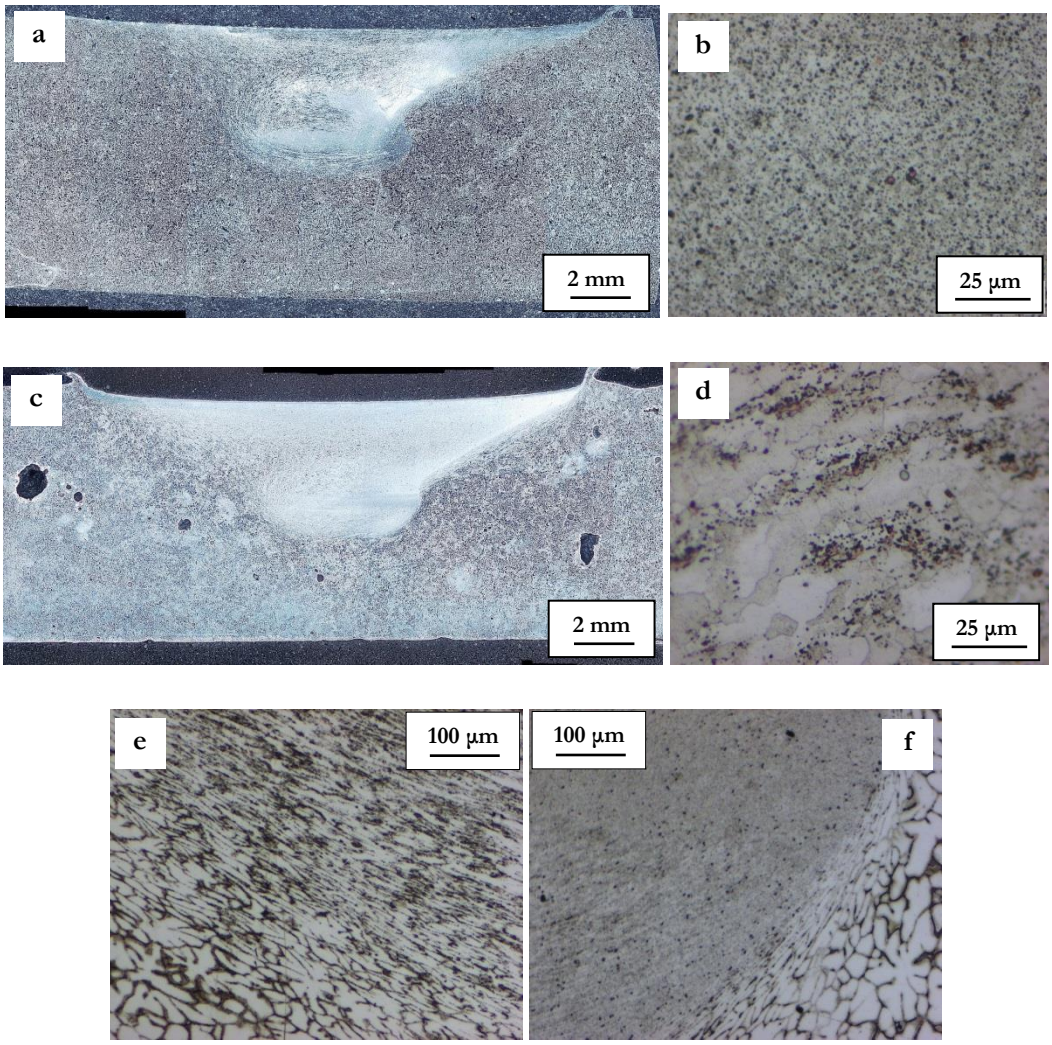

Figure 6.17. Macrographs and optical images of nugget zone microstructure of (a, b) FSP 2024 alloy and (c, d) FSP AA2024-Al_2O_3 nanocomposite. Optical images of the interface between nugget and (e) retreating side, (f) advancing side, in the FSP AA2024.

In both AA2024 and AA2024-Al_2O_3 FSP samples, the nugget zone is characterized by a noticeable grain refinement in comparison to the base material, due to recrystallization process induced by FSP, while the TMAZ presents elongated grains, as a result of deformation process.

The finer microstructure of the nugget zone in comparison to the unprocessed materials as a result of FSP dynamic recrystallization process was observed also by SEM-EDS, both in the FSP AA2024 alloy and nanocomposite (Figure 6.18). Together with microstructural refinement, the decrease in the size of intermetallic particles was registered. In the processed zone of the nanocomposite, no alumina cluster was observed. It is therefore

thought that the mechanical action of the pin is effective in void elimination and nanoparticles distribution.

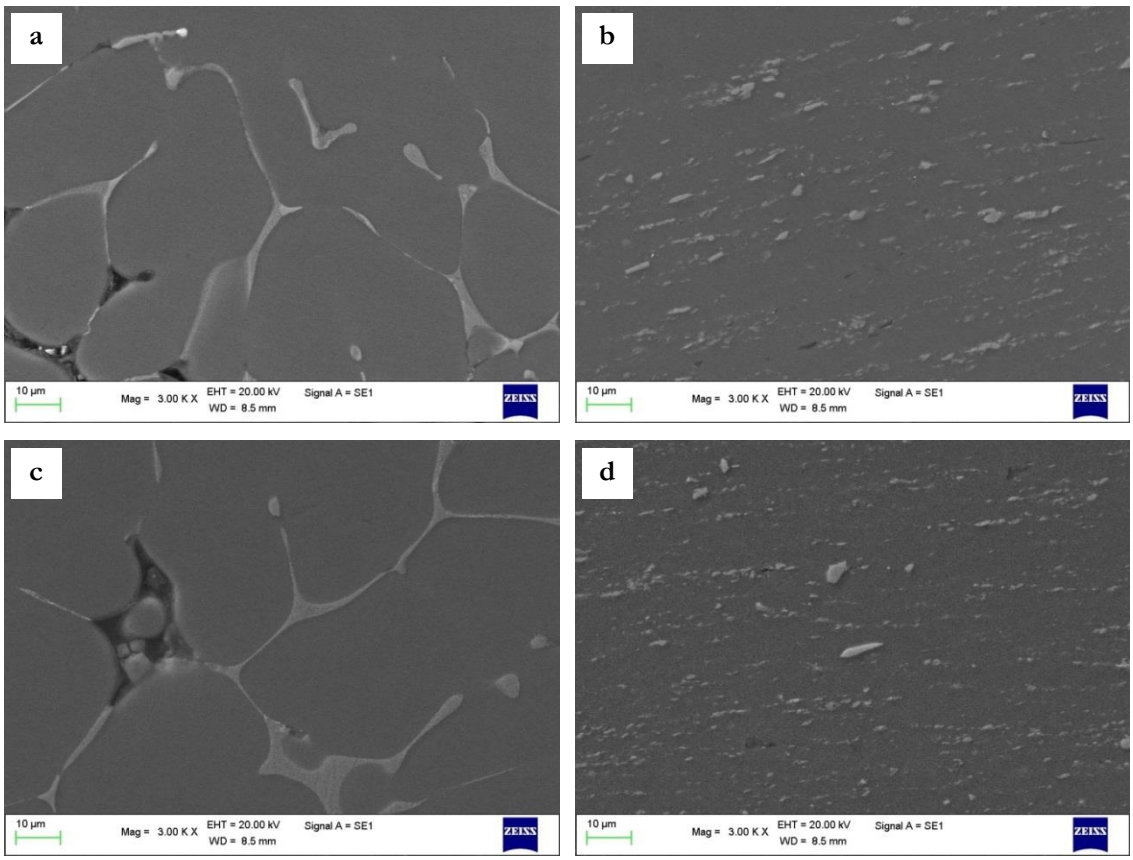

Figure 6.18. SEM images at equal magnification showing (a) base material and (b) nugget of the FSP AA2024 alloy, (c) base material and (d) nugget of the FSP 2024-Al_2O_3 nanocomposite; intermetallic particles are clearly refined in the nugget zone due to the mechanical action of the pin.

The average grain size calculated by EBSD analyses (Figure. 6.19) was similar between the FSP AA2024 alloy and AA2024-Al_2O_3 nanocomposite, being 8 and 11 µm, respectively.

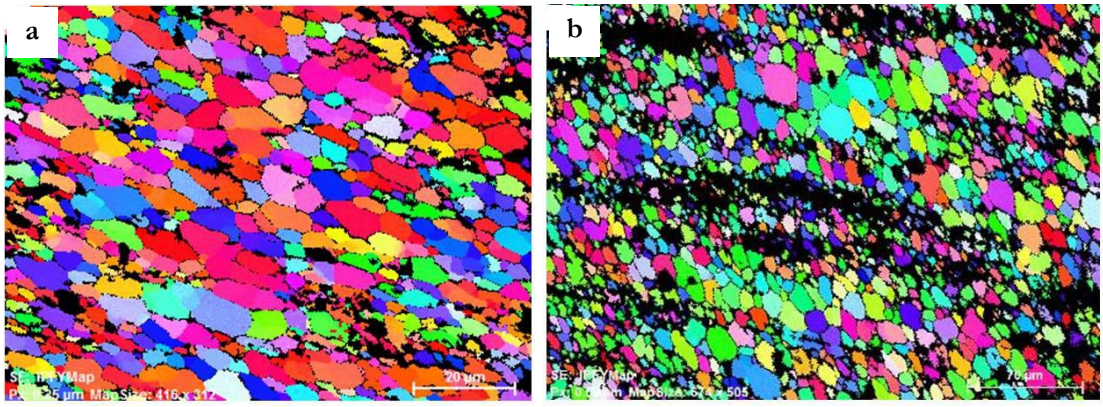

Figure 6.19. EBSD maps (IPF map relative to ND Y) for friction stir processed (a) AA2024 matrix and (b) AA2024-Al_2O_3 nanocomposite, carried out at different magnifications.

6.2.2 MECHANICAL CHARACTERIZATION

Microhardness of the FSP materials was compared to that of the unprocessed alloy/nanocomposite; comparison profiles are shown in Figure 6.20. The reference values of microhardness measured on as cast 2024 alloy and nanocomposite are 82 $HV_{0.5}$ ± 2 and 101 $HV_{0.5}$ ± 11, respectively. At 0,5 and 2,5 mm from the FSP surface, the higher hardness of both unreinforced and reinforced alloy registered within the nugget in comparison to the reference value, should be mainly related to the smaller grain size induced by FSP; precipitation hardening phenomena, are however expected to occur and to contribute to the hardness enhancement. The high temperatures reached in the nugget zone during FSP may in fact bring into solution Cu based particles, thus leading to natural age hardening. Differently, lower temperatures are reached in the TMAZ; as a result, the dissolution of alloying elements to form strengthening precipitates with natural aging is expected to be less pronounced. Nevertheless, the lower temperatures may induce overaging of hardening precipitates formed subsequently to casting from the slightly supersaturated α-Al phase, leading to a reduction of hardness. Hardness increase with respect to the base material, in the case of the FSP nanocomposite should also be related to the more even nanoparticles distribution induced by FSP, in comparison to the cast condition. The 5 mm profiles, corresponding to the bottom of the FSP zone, instead, does not show hardness increase in comparison to the corresponding cast condition. The reason could be the lower processing temperature reached in this area, which may have led to precipitate growth, thus overtaking both the strengthening effects of grain refinement for the unreinforced alloy and balancing the grain refinement and nano-reinforcement distribution in the nanocomposite.

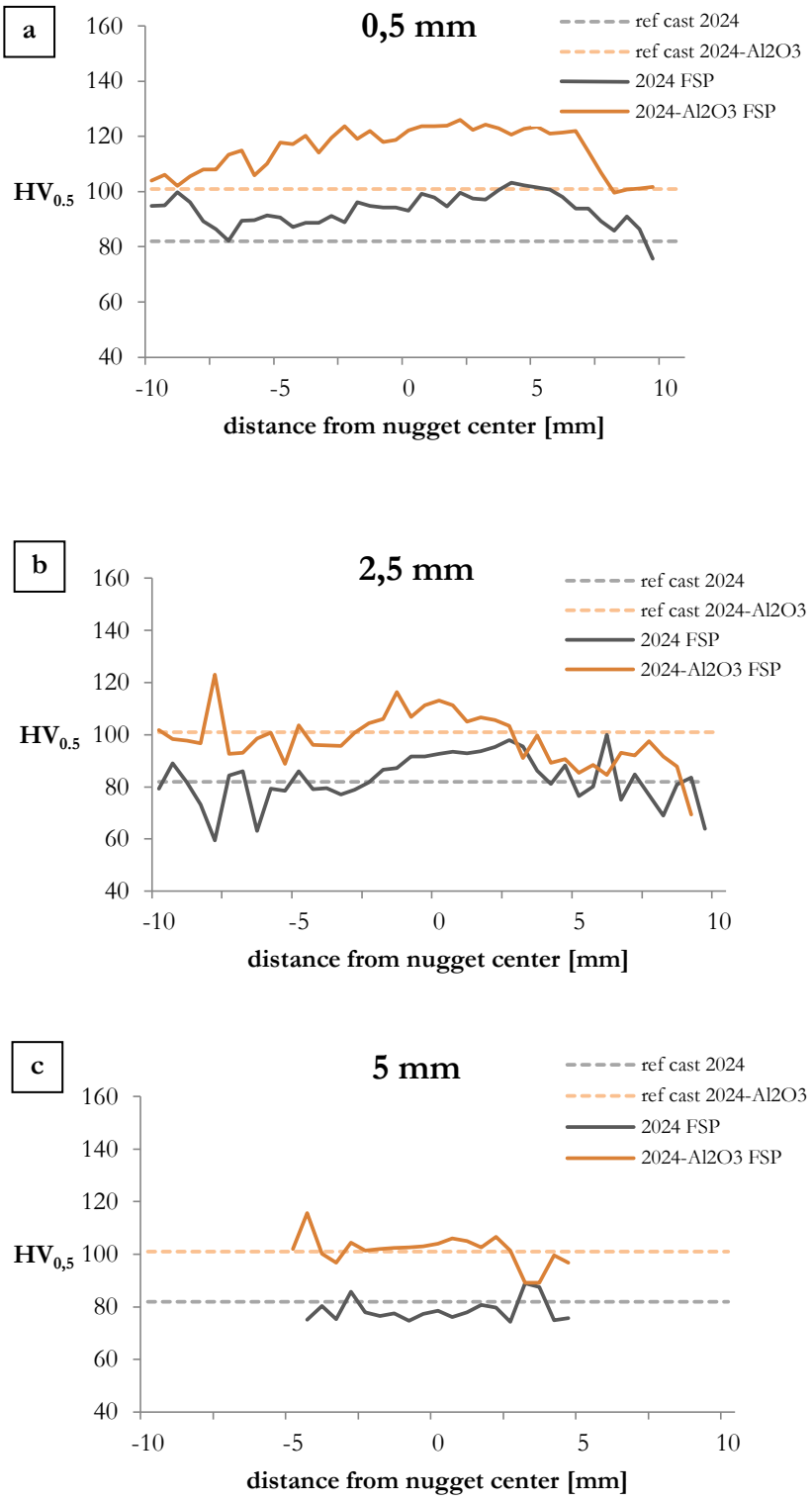

Figure 6.20 Vickers microhardness profiles of FSP unreinforced AA2024 alloy and AA2024/Al_2O_3 nanocomposite at (a) 0.5, (b) 2.5 and (c) 5 mm of depth from the FSP surface.

6.2.3 TENSILE TESTS

Results of tensile tests are summarized in Figure 6.21. The UTS of the semi-solid cast matrix (169 MPa) is strongly reduced (-70%) by the addition of nanoparticles. The reason of this decrease is due to particles clusterization, which is known to induce a general reduction of mechanical properties. Moreover, due to clusters and voids associated to nanoparticles, elongation to failure of the semisolid processed composite is basically absent. Similarly to a brittle material, tensile failure occurred without plastic deformation; it was therefore not possible to identify yield strength of the composite.

Friction stir processing applied to the unreinforced matrix led to a strong increase of YS and UTS, 25 and 52 % respectively. Both grain refinement and casting defects mitigation induced by the severe plastic deformation resulted in a noticeable increase of mechanical properties and elongation to failure (from 0.7 to 7.4%).

A strong increase of YS and UTS was observed also in the FSP composite, in comparison to the as cast condition. Moreover, it should be pointed out that UTS is increased of about 13 % in comparison to the FSP unreinforced matrix. It is therefore thought that FSP process allowed to exploit nanoparticle strengthening effect, by obtaining a more even distribution. Also in this case, elongation to failure was strongly increased in comparison to the as cast condition, reaching a value comparable to that of the FSP unreinforced matrix (7.2 and 7.4 %, respectively).

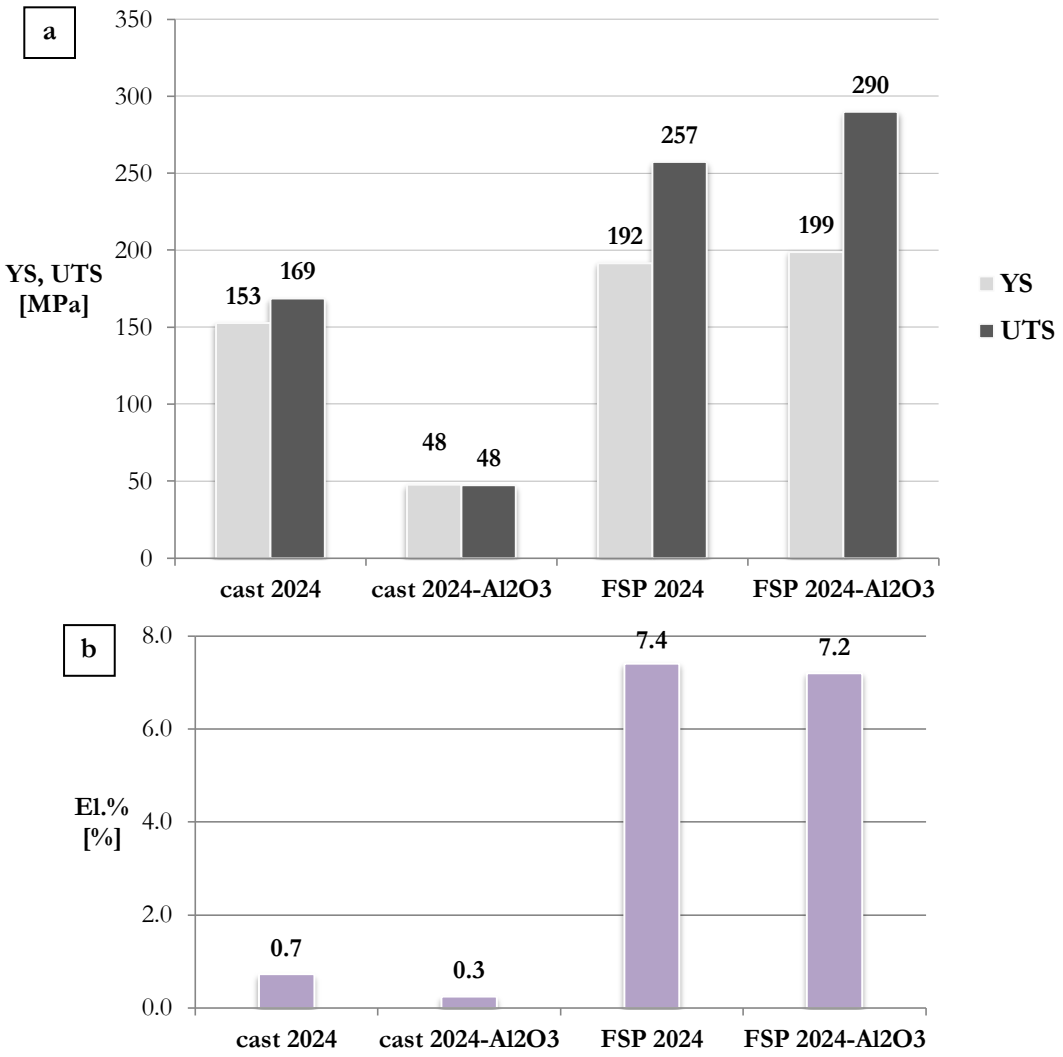

Figure 6.21. Tensile properties of 2024 alloy and 2024-Al_2O_3 nanocomposite in the as cast state and after FSP; (a)YS=Yield Strength, UTS=Ultimate Tensile Strength, (b) elongation to failure.

6.2.4 FRACTOGRAPHIC ANALYSES

Multifocal images of fracture surfaces are presented in Figure 6.22; SEM images at low and high magnification are reported in Figure 6.23 and 6.24, respectively. As previously discussed, the cast unreinforced matrix presented a negligible elongation to failure (0.7%). Oxide films and casting defects were in fact observed on the fracture surfaces, as shown in Figure 6.22a and 6.23a. The presence of films, pores and cavities led to the loss of microstructural cohesion, therefore to low plastic capacity of the matrix. Fracture surface morphology did not present typical ductile features, i.e. dimples. Fracture surfaces of the cast composites were characterized by the presence of nanoparticles clusters, together with several casting defects, namely porosities and cavities (Figure 6.22b, 6.23b and 6.24b) associated to the difficulties in obtaining an even dispersion of reinforcing phase by semi-

solid casting assisted with mechanical stirring. The presence of such casting defects explained the very low values of elongation to failure measured by tensile testing and the brittle-like behavior of the cast composite. While both the cast materials presented brittle fracture surface morphology, a typical ductile aspect was observed on FSP alloy and composite. Even though some oxide film was still found (Figure 6.22c,d), microstructural refinement led to a clear ductile morphology, characterized by small circular dimples (Figure 6.24c,d). As a results, elongation to failure increased from 0.7 and 0.3 % to 7.4 and 7.2% for the unreinforced alloy and composite, respectively. The beneficial effect of severe plastic deformation induced by the pin rotation on particle distribution led to absence of appreciable particles segregation and clusters.

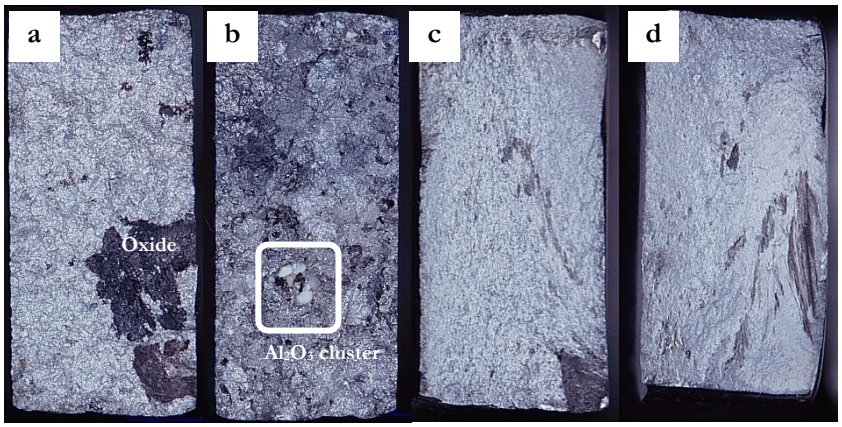

Figure 6.22. Multifocal images of fracture surfaces of (a) as cast 2024 alloy, (b) as cast AA2024-Al_2O_3 composite, (c) FSP 2024 alloy and (d) FSP AA2024-Al_2O_3 composite.

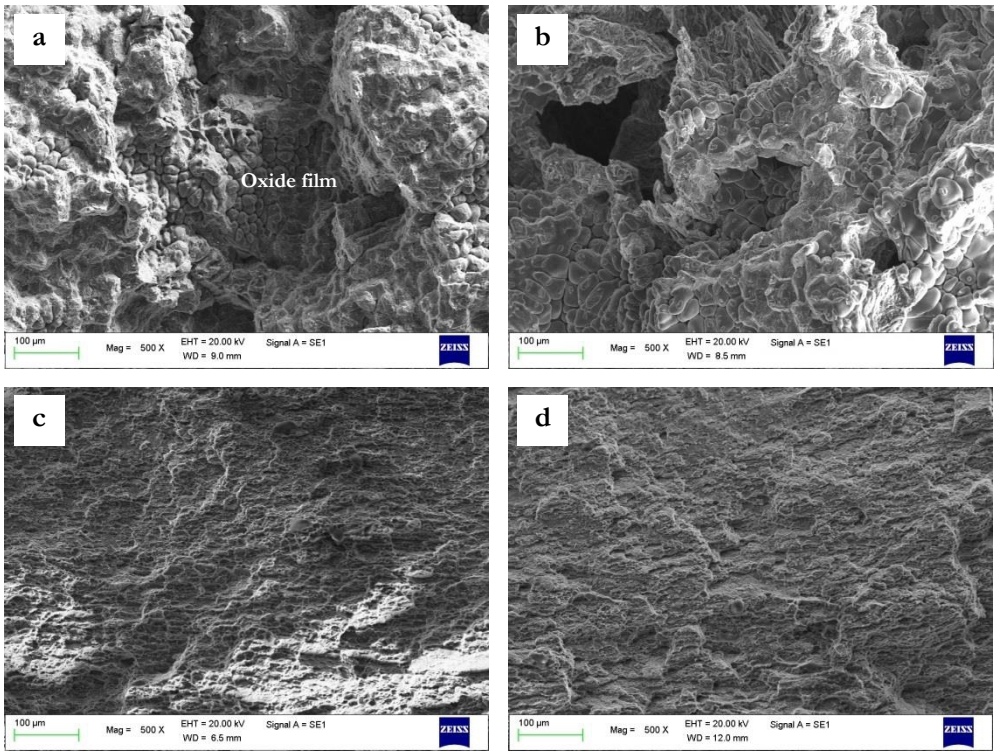

Figure 6.23. Fracture surfaces SEM images at low magnification of (a) as cast 2024 alloy, (b) as cast AA2024-Al_2O_3 composite, (c) FSP 2024 alloy and (d) FSP AA2024-Al_2O_3 composite.

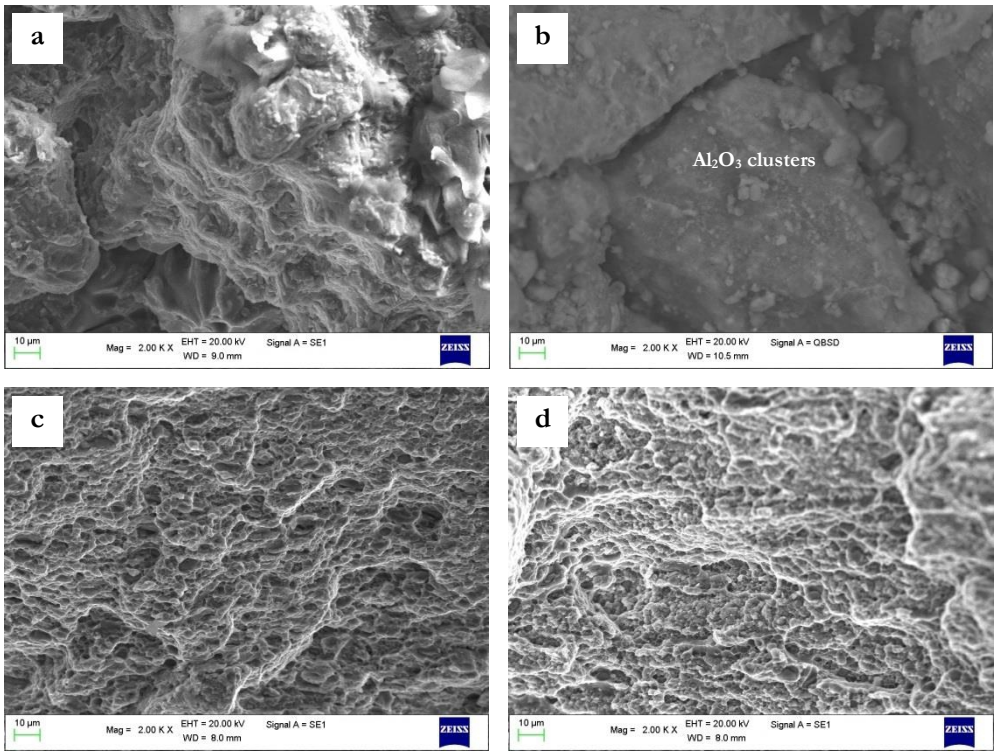

Figure 6.24. Fracture surfaces SEM images at high magnification of (a) as cast 2024 alloy, (b) as cast AA2024-Al_2O_3 composite, (c) FSP 2024 alloy and (d) FSP AA2024-Al_2O_3 composite.

6.2.5 CONCLUSIONS

AA2024-based nanocomposites containing 1 wt% of Al_2O_3 nanoparticles produced by semi-solid casting technique and processed by FSP were characterized from microstructural and mechanical point of view. Based on the experimental results of this activity, it was possible to conclude that:

- The sole semi-solid casting technique assisted by mechanical stirring, applied to the system AA2024-1wt%Al_2O_3, does not allow to fully distribute Al_2O_3 nanoparticles into the matrix. Low wettability of nanoparticles leads to particles clusterization and generation of casting defects such as cavities, pores and particle clusterization. In comparison to the composites described in Paragraph 6.1, prepared at the liquid state, in this case a higher amount of matrix, therefore of nanoparticles, has been processed; as a result, the observed higher amount of casting defects related to particles clusterization was expected.
- Friction stir processing led to noticeable grain refinement and microstructural homogenization through severe plastic deformation, therefore inducing an increase of both YS and UTS as well elongation to failure in the unreinforced alloy.
- Casting defects associated to nanoparticles addition were mitigated by FSP, by enabling the exploitation of nanoparticles strengthening effect, thus inducing in the FSPed composite a higher UTS in comparison to the similarly processed matrix. Besides yield and ultimate tensile strength increase, FSP induced a remarkable increase of elongation to failure, which was basically absent in the cast materials.

From the present investigation it was confirmed that for exploiting nanoparticles strengthening effect, a homogeneous distribution should be achieved; in this regard, a secondary process such as FSP seems to be a good candidate for increasing microstructural homogeneity and for enhancing particles distribution, therefore leading to increased mechanical properties.

6.3 Results and Discussion – PART 3

Characterization of AA7075-Al_2O_3 FSP nanocomposites

6.3.1 MICROSTRUCTURAL ANALYSIS

Multifocal images of the FSP nanocomposites processed by 1, 3 and 4 passes are shown in Figure 6.25. Images were taken on etched specimens. The nugget, i.e. the stirred zone, presented in all the processed samples a maximum depth of about 5 mm. Similarly to what has been observed on the study of application of FSP to AA2024 alloy and AA2024-Al_2O_3 nanocomposite, a difference between the interface between TMAZ and nugget at the advancing and retreating side exists. In particular, the border at the interface advancing side appears, in all the analysed samples, more clear and marked, in comparison to the retreating side, due to the different plastic flux at the two sides[17]. The most relevant feature that characterizes in particular the samples processed by 1 and 3 passes, is the presence of macroscopic Al_2O_3 clusters inside the nugget zone. However, an increased number of passes led to a decrease in the cluster size, as it is possible to observe from the comparison between Figure 6.25 a and b. It is therefore possible to affirm that neither 1 nor 3 FSP passes are sufficient to obtain a homogeneous distribution of nanoparticles within the processed zone. At this magnification, on the contrary, no agglomeration has been observed in the sample processed with 4 passes. Moreover, a tunnel was observed both in 1 and 3 passes samples. This defect was not found in the sample processed through 4 passes, confirming the effectiveness of increasing FSP passes in mitigating and eliminating processing defects, previously reported in the literature[18].

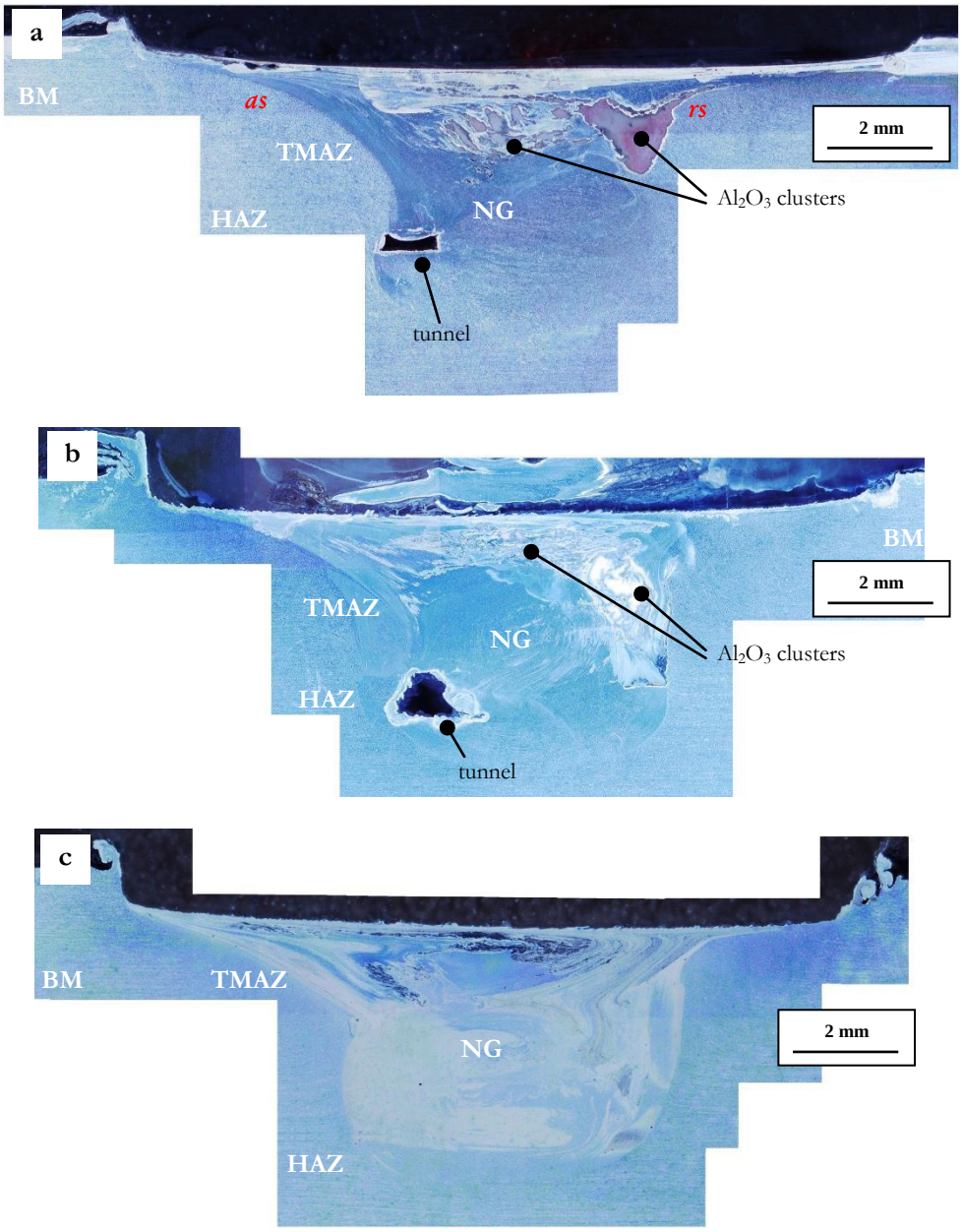

Figure 6.25. Multifocal images of AA7075-Al_2O_3 nanocomposites processed by (a) 1 FSP pass, (b) 3 FSP passes, (c) 4 FSP passes. Images were taken on etched samples.

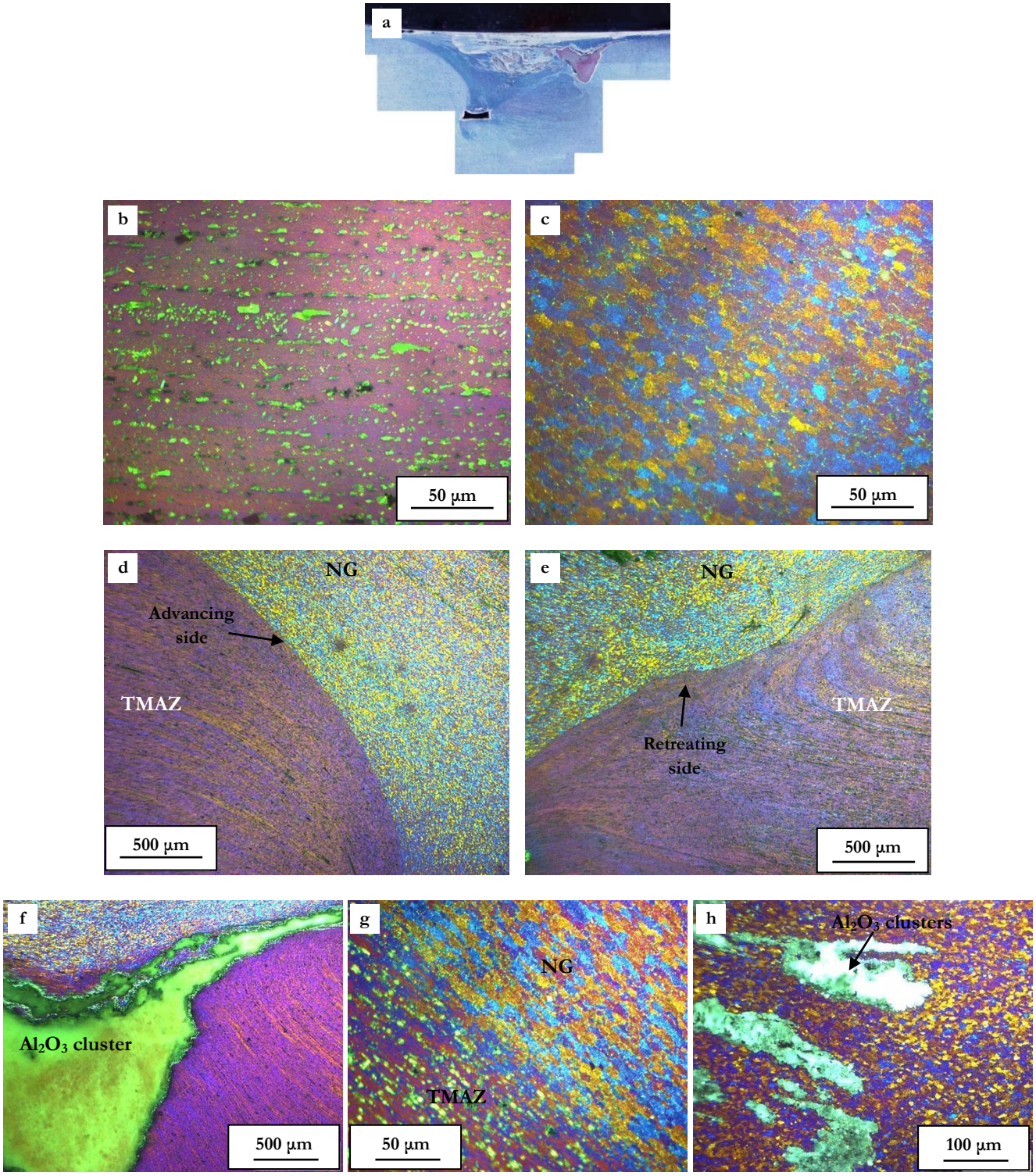

Figure 6.26. (a) Macro-multifocal image of 1 FSP AA7075-Al_2O_3 sample; optical images under polarized light, showing: (b) base material and (c) nugget, (d) advancing side, (e) retreating side, (f)Al_2O_3 cluster near retreating side, (g)high magnification of the interface between nugget and TMAZ at the advancing side and (h) Al_2O_3 clusters within the nugget zone.

Optical images under polarized light of the sample processed by 1 FSP pass are shown in Figure 6.26. Grain refinement induced by FSP process can be observed by comparing Figure 6.26 b and c. At this magnification, a remarkable difference between the microstructure of nugget and base material can be observed: the base material of AA7075-O alloy (Figure 6.26b) consists of elongated grains and intermetallic particles (in green) oriented with grains, i.e. along the matrix lamination direction. On the contrary, in the nugget center, grains appear mainly equiaxed and clearly refined, as a result of the action of the pin (Figure 6.26c). The stored energy contained into dislocations is supposed to drive the dynamic recovery and recrystallization processes, leading to a remarkably decreased of grain size. Moreover, a difference in the distribution of intermetallic particles may be observed between base material and processed zone. While coarse intermetallic particles are clearly recognizable in the base material, at the same magnification they are not observable in the nugget zone. It is thought that, as a result of the mechanical and thermal actions induced by FSP, intermetallic particles undergo fragmentation or even partial/complete dissolution. The above mentioned difference is even more clear at higher magnification in Figure 6.26d, showing the border between TMAZ and nugget at the advancing side. Grain size in the nugget zone was calculated by linear intercept method. Even though the average grain size may vary from zone to zone inside the nugget itself, an average value of 5.6 μm has been calculated. This dimensional range of recrystallized grain has been observed also in Al alloys subjected to FSP by several works[17,19,20]. The difference between the nugget/TMAZ interface at the advancing and retreating side is shown in Figure 6.26d and e. In both the images the TMAZ is clearly recognizable as strongly oriented microstructure, consisting of highly deformed grains as a consequence of the pin action; on the contrary, the nugget zone shows its typical recrystallized structure. The uniform plastic deformation at the advancing side is clearly observable, while at the retreating side a more turbulent plastic flux exists. Clusterized alumina nanoparticles appear yellow/green under polarized light, and are clearly recognizable in Figure 6.26f and h. The first one shows the largest cluster, found at the retreating side; recrystallized grains and the elongated grains of TMAZ are clearly recognizable on the top and on the right of the cluster, respectively. Nanoparticles agglomerates were however detected also inside the nugget, between 1 and 2 mm of depth from the FSP surface. High magnification of these Al_2O_3 clusters, surrounded by recrystallized grains, are reported in Figure 6.26h.

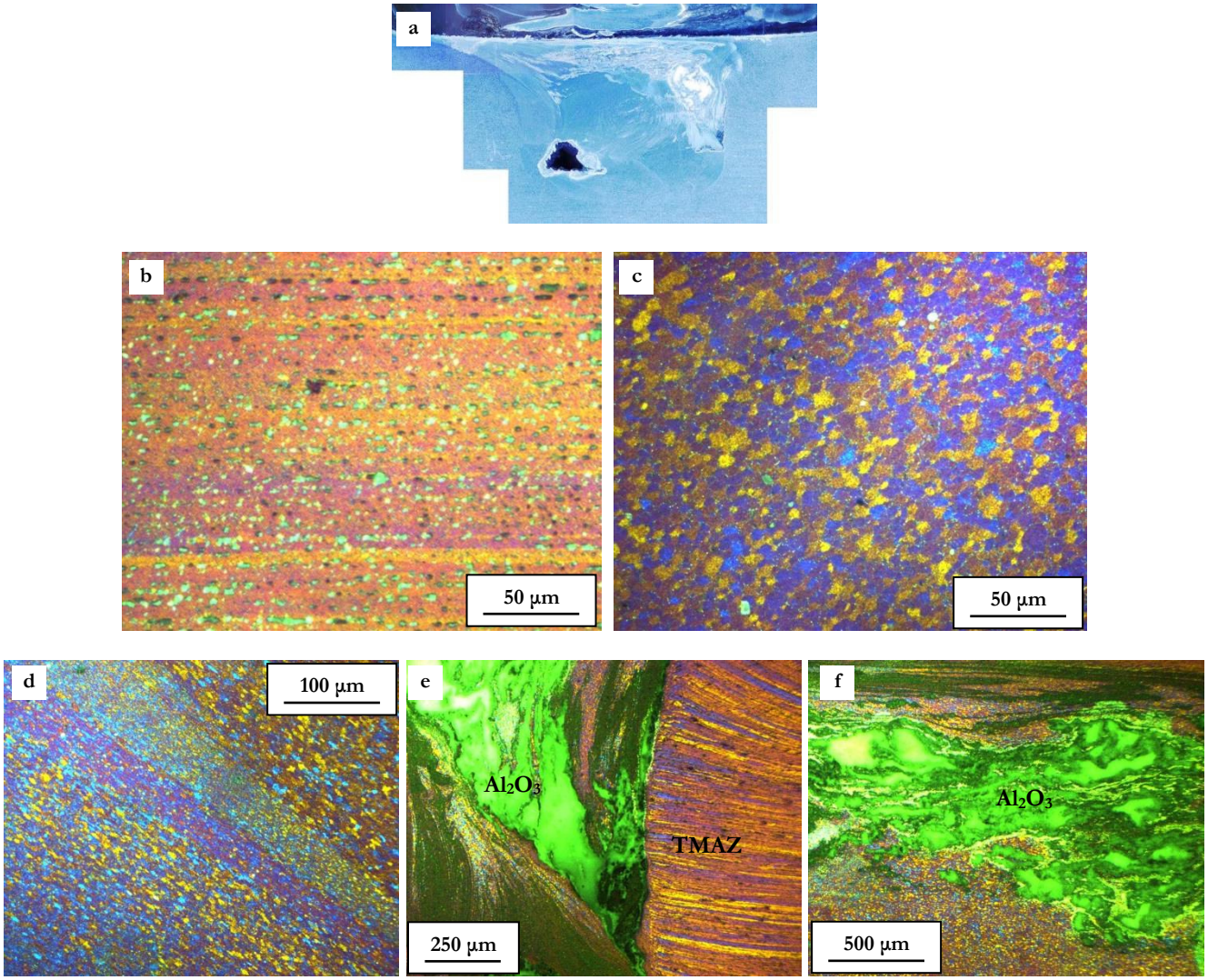

Figure 6.27. (a) Macro-multifocal image of 3 FSP passes AA7075-Al_2O_3 sample; optical images under polarized light, showing: (b) base material and (c) nugget zone, (d) recrystallized areas characterized by different grain sizes, (e) Al_2O_3 macro-clusters located at the interface between nugget and TMAZ and (f) near the sample surface, surrounded by recrystallized grains.

The presence of a remarkable amount of unevenly distributed nanoparticles indicates that one only FSP pass is not sufficient for a full exploitation of nanoparticles strengthening effect.

Optical images of the sample processed through 3 passes are shown in Figure 6.27. Similar differences between the base material and the nugget zone of 1 FSP sample were observed (Figure 6.27b and c). Also in this case a certain dispersion in grain size was observed not only at the boundary between processed and unprocessed zone (Figure 6.27d), but also inside the nugget zone. It is generally accepted that the dominant factor governing grain size is the peak temperature reached during the FSP thermal cycle[18,21]. In particular, grain size variation between top, bottom and side of the FSP line, was observed to correspond to a temperature distribution[22], also related to heat dissipation in the nugget zone. However, the average value was similar to that calculated on the samples processed with 1 pass, i.e. about 5.2 μm. The constant average grain size with increasing number of FSP passes has been previously reported in the literature[23,24]. Being the final grain size in the processed zone closely related to the welding temperature[23,25,26], it is thought that the similar temperature values from pass to pass should not induce strong variation in the average recrystallized grain size[24].

Intermetallics distribution, as a result of thermo-mechanical action of the pin, was affected by FSP similarly to the 1 pass sample; also in this case, in fact, the nugget zone was free from coarse particles.

Alumina clusters were observed also in this sample. In Figure 6.27 e and f nanoparticles agglomerates found at the TMAZ/NG interface and under the FSP surface are shown, respectively. In the first case, the elongated structure of TMAZ may be observed on the right side of the cluster, while in the nugget, recrystallized grains are present in the areas surrounding Al_2O_3 agglomerates.

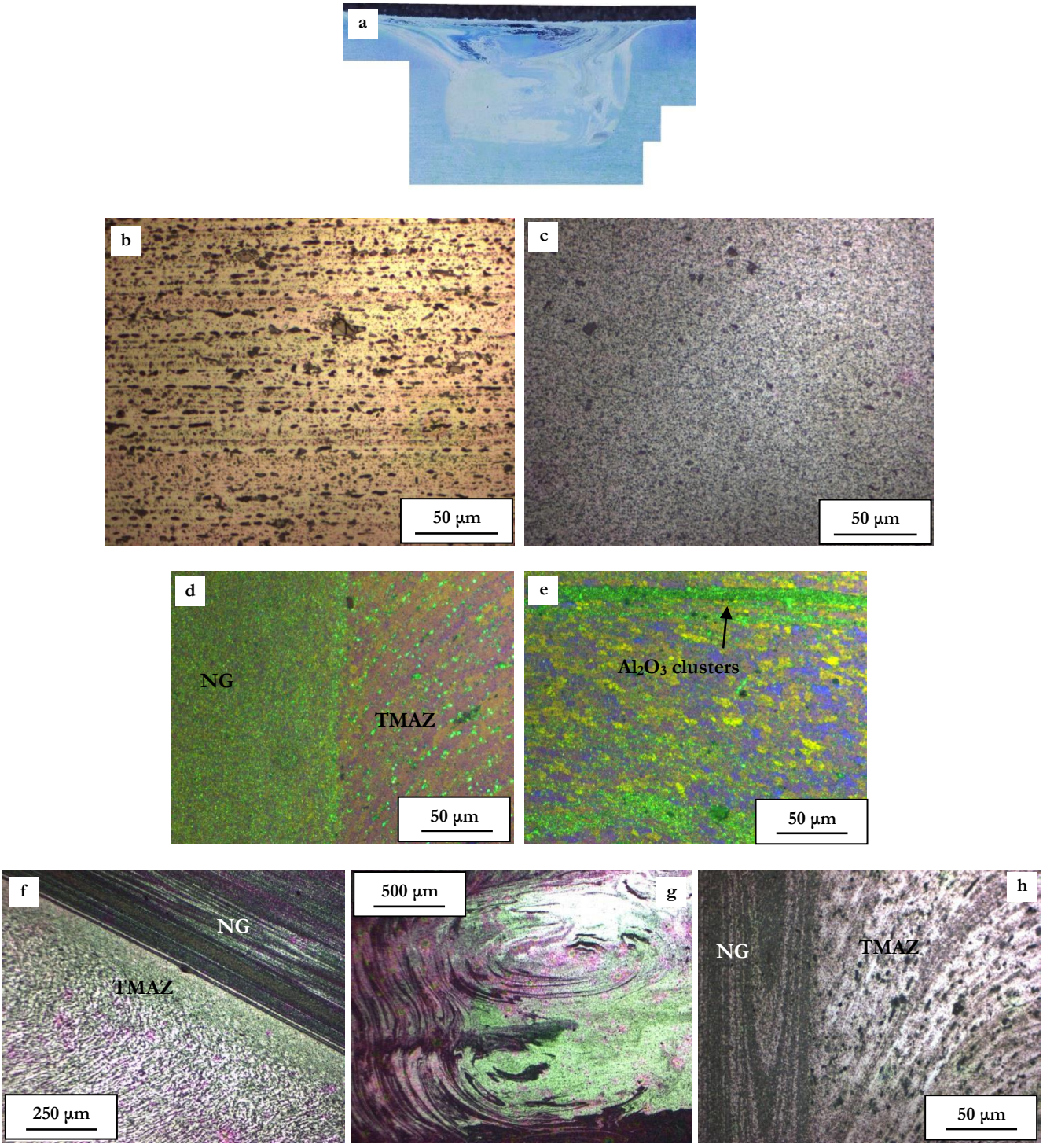

Figure 6.28. (a) Macro-multifocal image of 4 FSP passes AA7075-Al_2O_3 sample; optical images under polarized light, showing: (b) base material (c) nugget, (d) interface between nugget and TMAZ, (e) elongated superficial Al_2O_3 clusters within recrystallized microstructure, (f) low magnification of nugget-TMAZ interface at the advancing side, (g) onion rings observed within the nugget and (h) low magnification of nugget-TMAZ interface at the retreating side (RS).

Optical images of 4 passes sample are reported in Figure 6.28. The sample presented interesting differences compared to the previous analysed ones. First of all, no appreciable clusterization was observed through optical microscopy inside the nugget. Only small particles agglomerates were observed just underneath the FSP surface (Figure 6.28e). Moreover, no macroscopic defect such as the tunnel observed in samples processed with 1 and 3 passes was observed. Another important difference is in the average grain size. As it is possible to observe in Figure 6.28, the effect of etching on the sample microstructure was quite different from the previous ones; this sample seemed even over-etched. In particular, with exception of restricted and limited areas located near small Al_2O_3 clusters (Figure 6.28e), it was impossible to observe and quantify the average grain size in the nugget area, since grain boundaries were not recognizable. It is possible that in this case, the grain size remarkably decreased in comparison to 1 and 3 passes sample; as a result, the same etching time may have led to an over-etched microstructure, since a higher amount of grain boundaries are present. Fragmentation of intermetallics was registered also in this sample, as it is possible to observe by comparing the base material and the nugget zone (Figure 6.28b,c) and at the interface between nugget and TMAZ (Figure 6.28d). Onion ring structures were observed in the nugget (Figure 6.28g), as a result of extrusion process induced by the pin[18].

In conclusion, increasing the number of passes was observed to (i) enhance particles distribution, by strongly diminishing Al_2O_3 agglomeration, (ii) eliminate macroscopic defects and (iii) reducing the grain size of the nugget zone. The finer grain size registered (even if not calculated) in the sample processed by 4 FSP passes could be related to the enhanced nanoparticles distribution (indicated by the absence of particles clusters) induced by the 4 passes. Reinforcing particles are known to interact with grain size distribution; as reported by different investigators, particle stimulated nucleation (PSN) is supposed to occur during friction stir processing of Al-based MMCs[27–29]. Anyway, this mechanism is thought to act if dislocations accumulate around the particles during deformation[30], and this seems to be possible only when the average particle size exceeds 1 μm[30]. In view of this, some authors suggested the grain refining action induced by nanoparticles to be due to the pinning effect induced by nano-Al_2O_3 particles, which could slow the grain growth of the matrix[24]. In the present investigation it is therefore possible to hypothesize a similar effect; on the other hand, since some particles clusterization is still observed, it could also be possible that agglomerated particles, acting as single micrometric particles, could have, to some extent, led to stimulation nucleation effect.

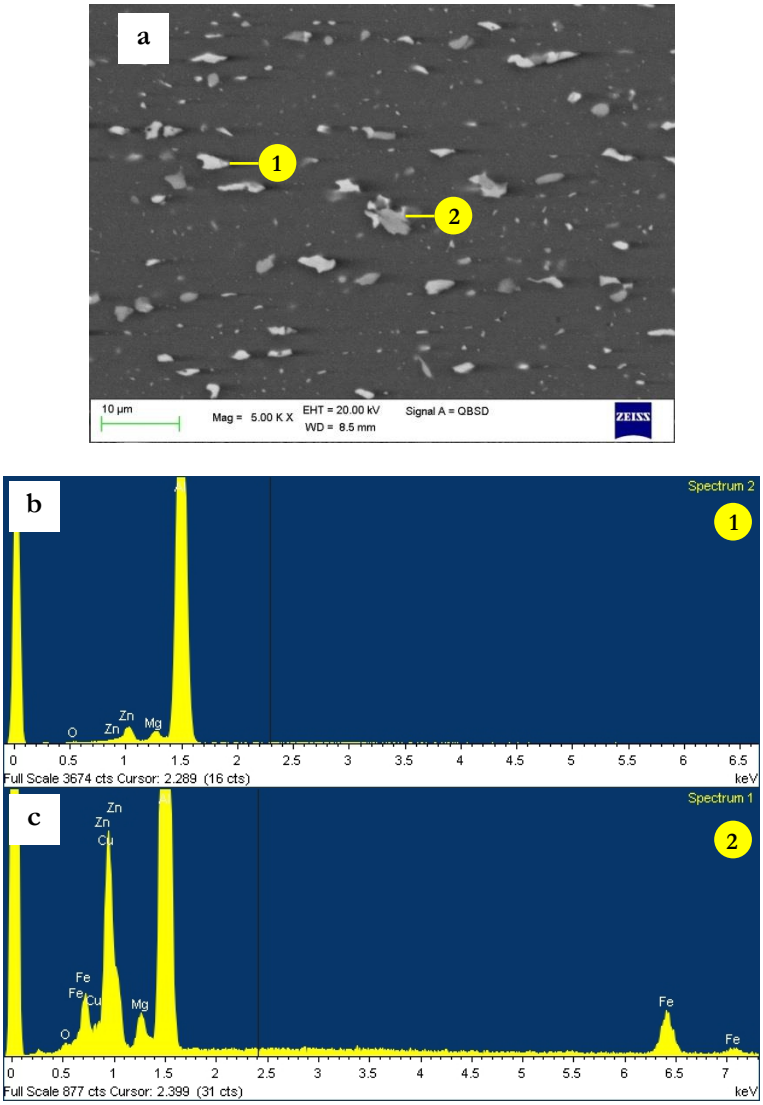

Figure 6.29. SEM image of (a) AA7075-Al_2O_3 composite base material, showing the distribution of intermetallic particles along lamination direction and (b, c) corresponding EDS spectra.

SEM-EDS analyses were carried out on the alloy base material (Figure 6.29) and in the nugget zones of AA7075- Al_2O_3 nanocomposites processed by 1 and 4 FSP passes (Figure 6.30 and Figure 6.32, respectively). The particles observed in the base material are clearly aligned along the lamination direction. EDS analyses revealed that the smaller particles contain both Mg and Zn, being probably the $MgZn_2$ phases. Nevertheless, also Fe and Cu containing phases were detected, generally characterized by bigger size that the previous ones.

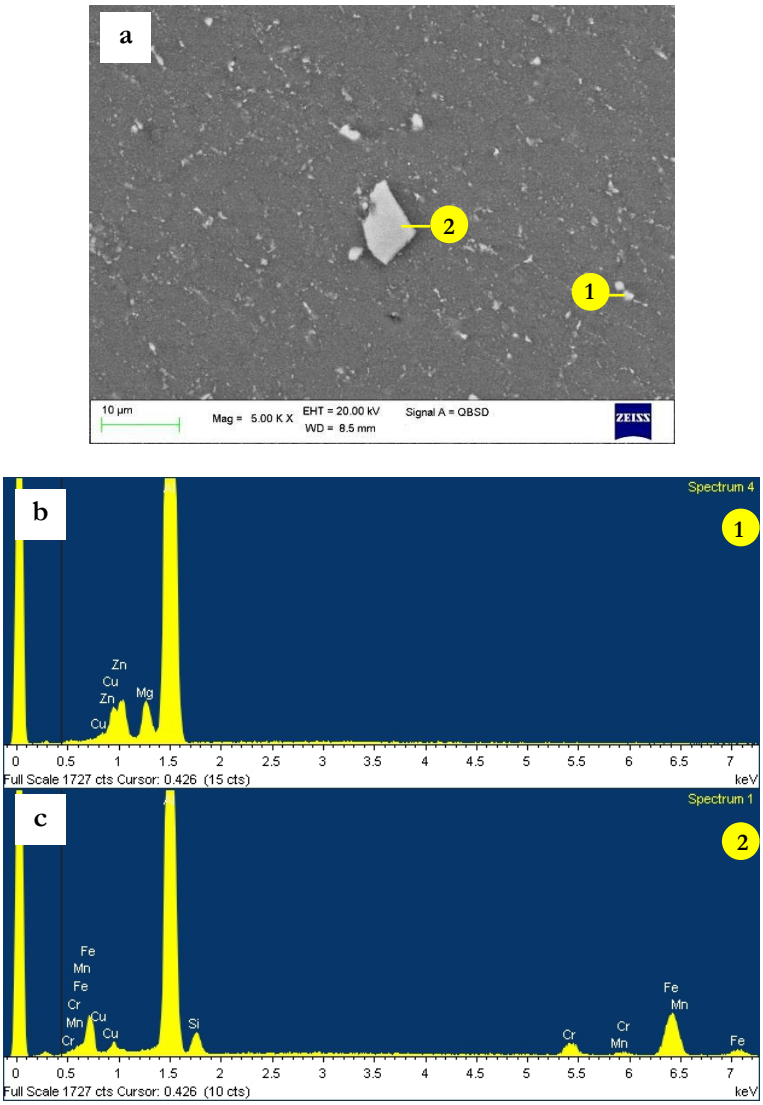

Figure 6.30. SEM image of (a) the nugget zone of AA7075-Al_2O_3 FSP sample processed by 1 single pass, showing the distribution of intermetallics and (b, c) corresponding EDS spectra.

In the nugget zone of the AA7075- Al_2O_3 sample processed by 1 FSP pass, it was possible to observe (i) a finer distribution on small, fragmented intermetallic particles in comparison to the base material (Figure 6.30) and (ii) large Al_2O_3 clusters (Figure 6.31), located in particular underneath the FSP surface and at the border between nugget and retreating side TMAZ.

Most of the observed intermetallic particles contained Fe and Cu. Very small and fragmented particles, containing Mg, Zn, Cu and Mn were also observed. The different size of intermetallic particles within the nugget zone is due, as known, to the thermo-mechanical action of the pin during FSP. Sometimes also Cr has been detected by EDS analyses in Fe containing particles; it is possible that the presence of Cr and Fe as well is due to the dissolution of small amounts of the pin tool during processing.

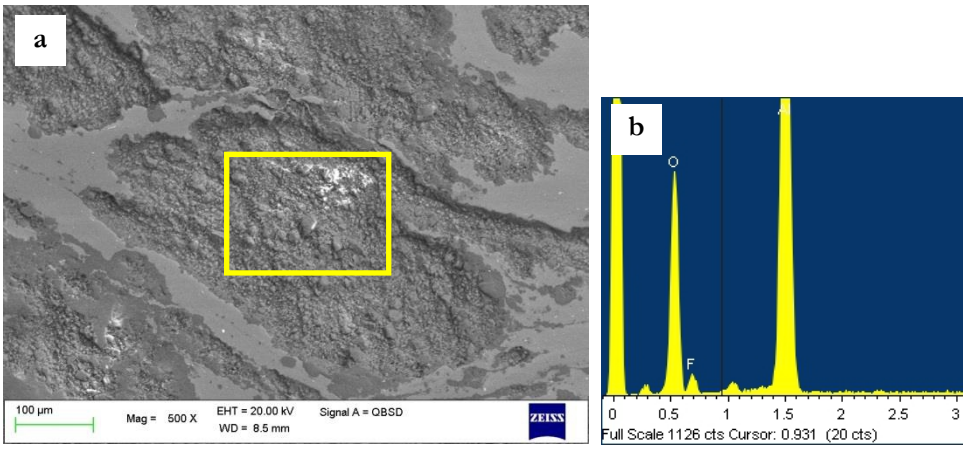

Figure 6.31. AA7075-Al_2O_3 nanocomposite processed by 1 FSP pass: (a) SEM image of a nanoparticles cluster and (b) EDS spectrum of the area highlighted in (a). Traces of F were due to the metallographic etching.

A minor quantity of coarse intermetallic particles within the nugget zone in comparison to the base material was observed also in the composite processed by 4 FSP passes. In particular, by comparing Figure 6.32a and Figure 6.30a, it is possible to observe that an increased number of FSP passes led to a decreased number of particles, probably due to the multiple thermo-mechanical action of the pin. Occasionally, some micrometric distributed black particles containing O were detected, being probably small Al_2O_3 nanoparticles agglomerates. Large clusters, similarly to the ones observed in the sample processed by 1 FSP pass, were not detected, with the exception of some small Al_2O_3 agglomerates under the FSP surface. An example is shown in Figure 6.33. Elements such as F, Ca and Na were absorbed by the sample during metallographic etching.

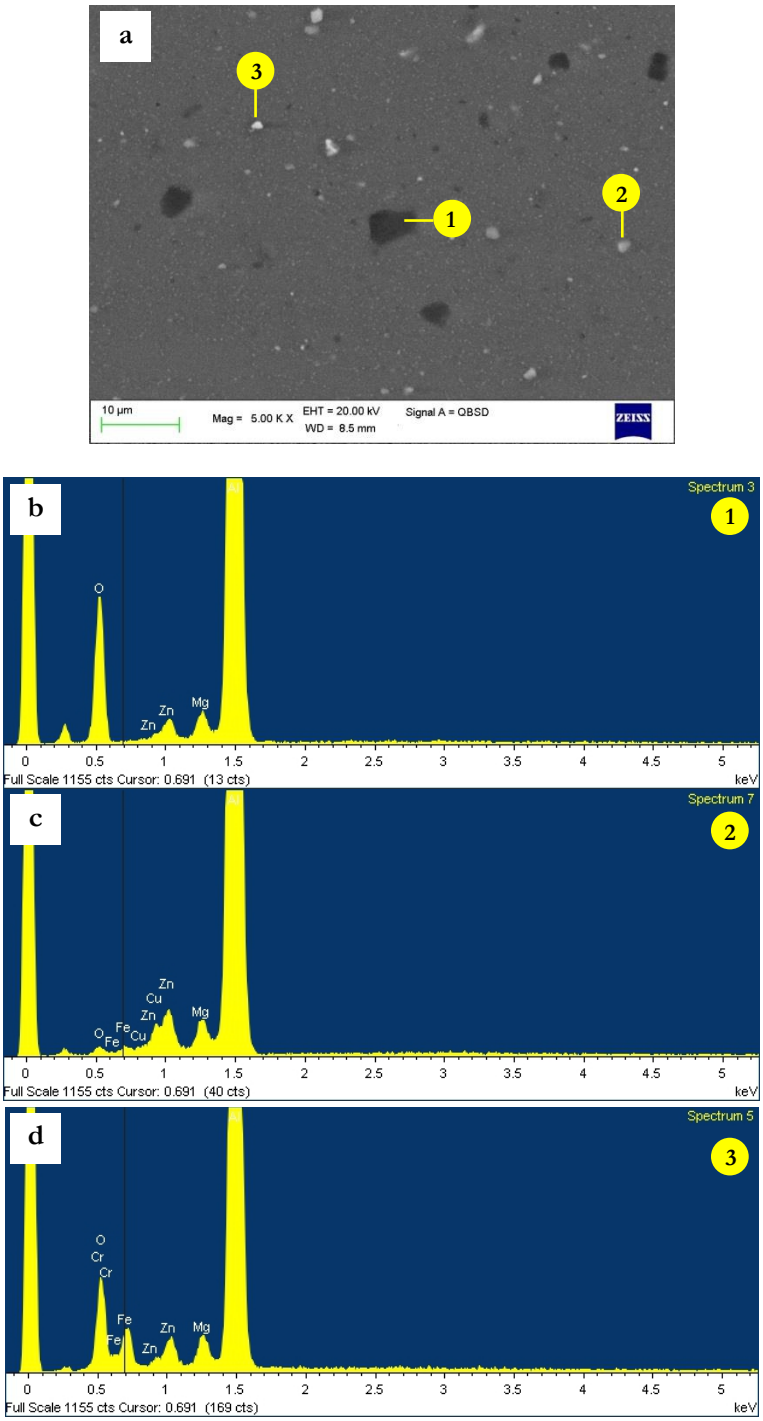

Figure 6.32. SEM image of (a) the nugget zone of AA7075-Al_2O_3 FSP sample processed by 4 passes, showing the distribution of intermetallics and (b, c, d) corresponding EDS spectra.

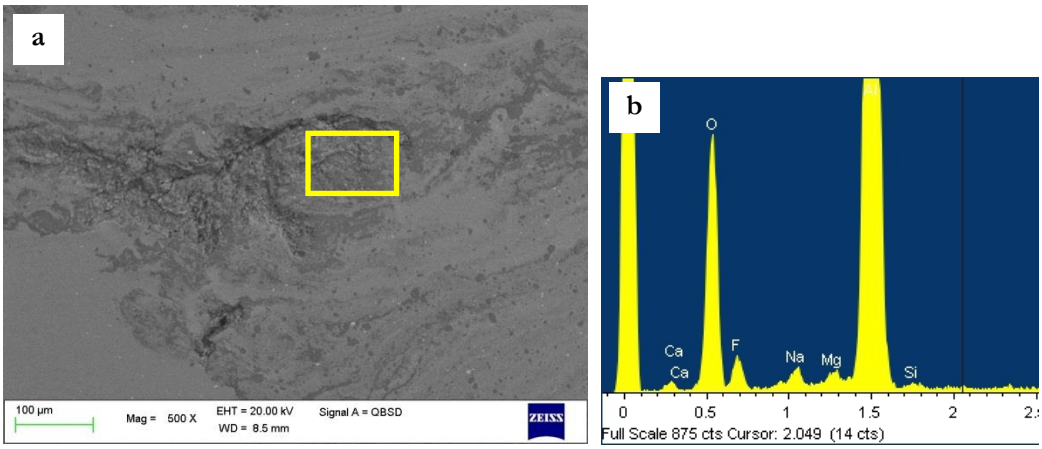

Figure 6.33. AA7075- Al_2O_3 sample processed by 4 passes: (a) SEM image of a Al_2O_3 nanoparticles cluster surrounded by the processed matrix and (b) EDS spectrum corresponding to the square area in (a).

6.3.2 MECHANICAL CHARACTERIZATION

Microhardness profiles carried out at different depths from the FSP surface of samples processed by 1, 3 and 4 FSP passes are shown in Figure 6.34. In comparison to the microhardness value measured on the base material (67 ± 3 $HV_{0.5}$), taken as a reference, it is possible to observe that in all the samples, FSP process leads to a general increase of hardness. The presence of large nanoparticles clusters made impossible, in some locations, to measure the hardness value. A dotted line has been used to indicate the presence of such defects. On 1 FSP pass, the lowest values of hardness associated to clusterization (indicated with the dotted line) were detected at 2 mm of depth from the FSP surface, in the right part of the nugget, in correspondence of the wide Al_2O_3 macro-clusters, observed both by optical and electron microscopy, as previously discussed (Figure 6.26 a, f, h). The most significant hardness increase was registered at 2 mm from the FSP surface, while a gradual decrease was registered up to 8 mm. In view of the substantial particle clusterization observed in this sample, it is thought that the most relevant action in hardness increase was played by grain refinement (probably slightly decreasing from the surface to the nugget bottom) induced by FSP. As concerning the distribution of hardness along each single profile, it should be pointed out that the highest hardness values were measured in correspondence of the FSP center line, in the central area of the nugget (about -5 to 5 mm from the center line).

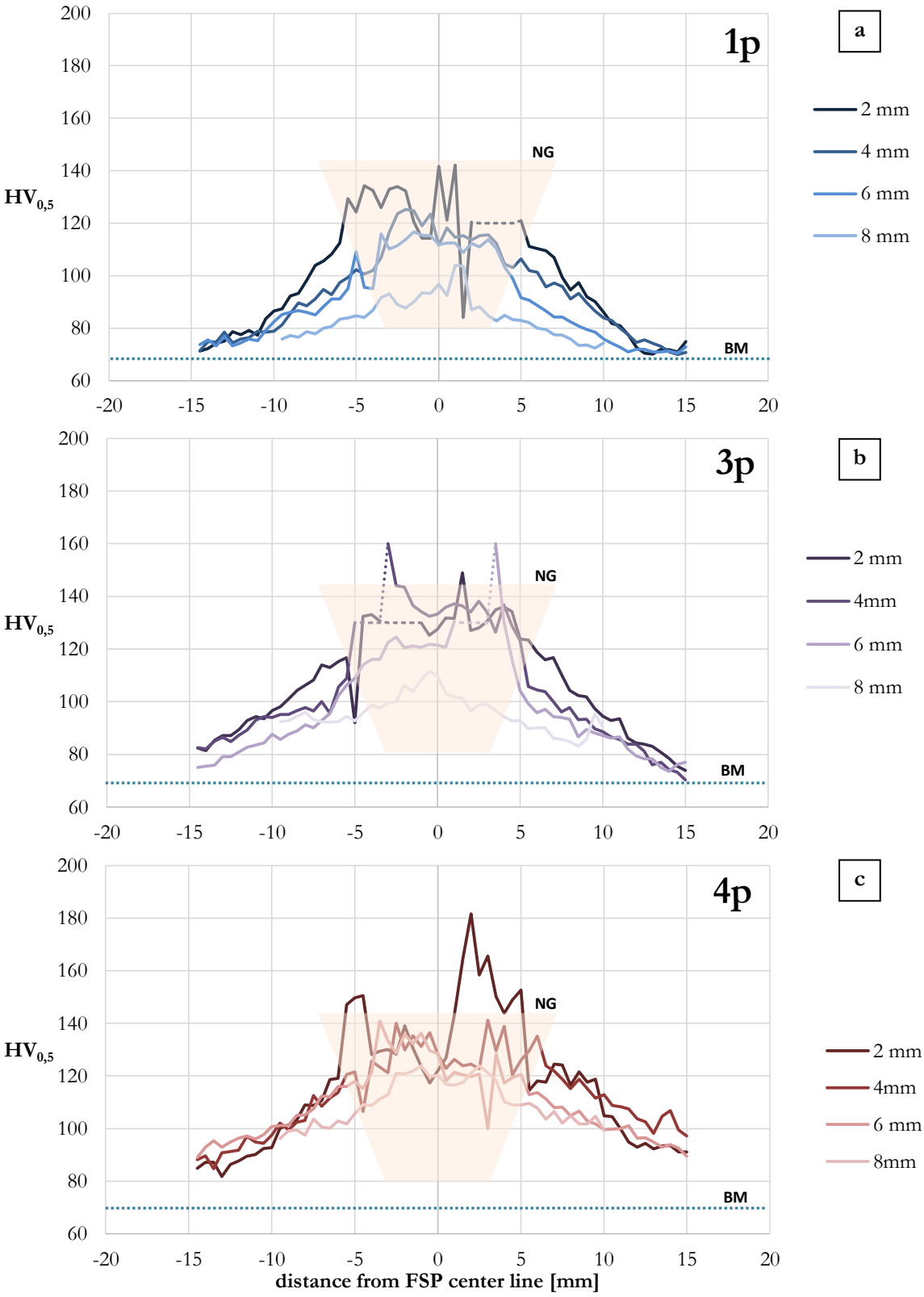

Figure 6.34. Vickers Microhardness profiles carried out on samples processed by (a) 1 FSP pass, (b) 3 FSP passes and (c) 4 FSP passes, at different depth from the FSP surface, namely 2, 4, 6 and 8 mm. The reference value (dotted line) is the microhardness measured on the base material.

This area, highlighted in the graphs, corresponds to the nugget zone of the sample. Microhardness gradually decreases in TMAZ and HAZ, up to the values of the base material. The sample processed by 3 FSP passes presented similar microhardness trends in comparison to 1 FSP pass sample. The most significant hardness increase was observed near the surface; in this sample, however, similar values at 2 and 4 mm depth were registered. While some particles cluster was still observed at these depth and despite no substantial grain size variation were detected between 1 and 3 FSP passes, it could be possible to think that an increased number of FSP passes leads to an increased level of microstructural and nanoparticles distribution homogenization, therefore leading to more homogeneous hardness values.

The positive effect of increasing the number of FSP passes is clearly outlined in Figure 6.34c: a general homogenization of hardness was achieved, since 2, 4, 6 and 8 mm profiles showed similar values; this could be due both to microstructural homogenization and grain refinement, but also to the enhanced nanoparticles distribution (no particle clusters were encountered during microhardness measurement).

The effect of FSP passes number on hardness distribution is summarized in Figure 6.35, where microhardness profiles at 2, 4, 6 and 8 mm are plotted.

In general, it is clear that increasing the number of passes leads to an enhancement in microhardness values within the nugget zone. The reason of this should be related both to the increased microstructural homogenization, leading to an more even distribution of nanoparticles and elimination of Al_2O_3 clusterization, and also to the increased grain refinement effect, as observed from microstructural analyses.

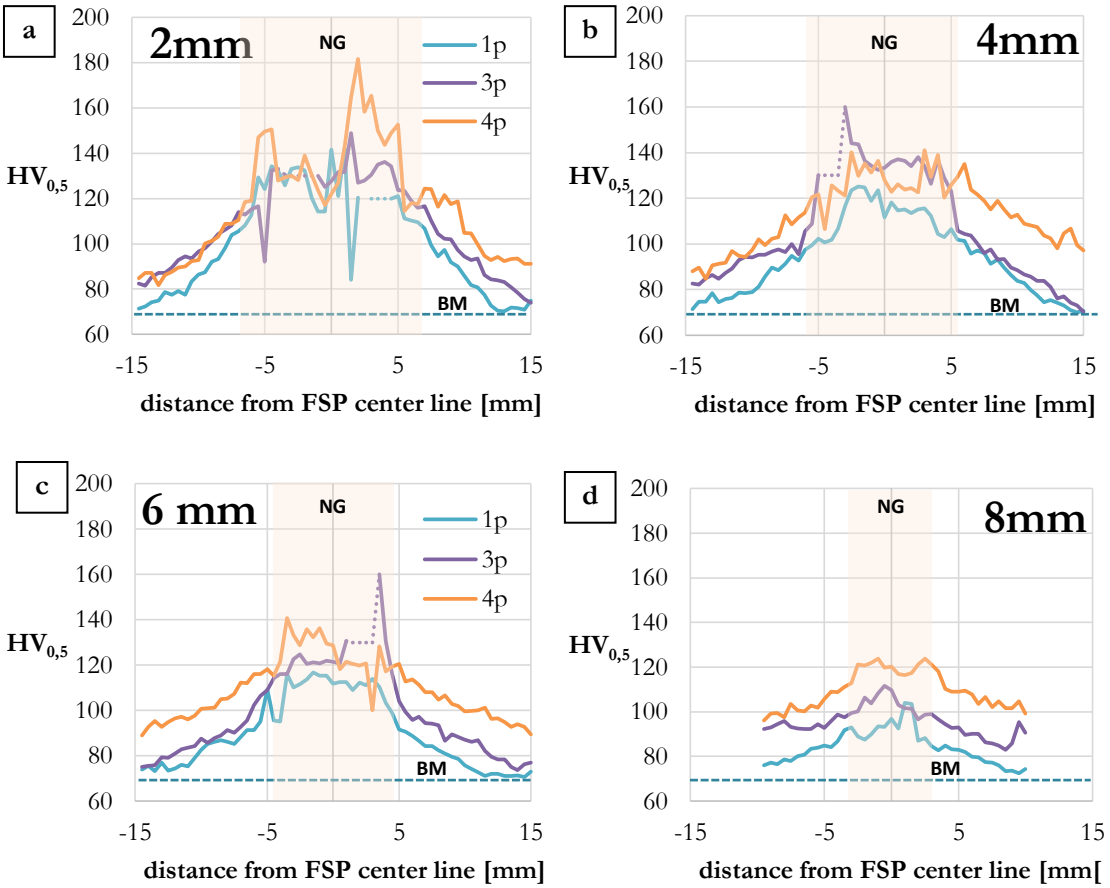

Figure 6.35. Vickers Microhardness profiles carried out at (a) 2, (b) 4, (c) 6 and (d) 8 mm depth from the FSP surface, on AA7075-Al_2O_3 nanocomposites processed by 1, 3 and 4 FSP passes, named 1p, 3p and 4p, respectively. The reference dotted line corresponds to the average microhardness measured on the base material.

6.3.3 CONCLUSIONS

AA7075-Al_2O_3 nanocomposites produced by FSP technique were characterized from microstructural point of view; preliminary mechanical characterization was carried out by microhardness profiles. Experimental results showed that:

- FSP technique allows the distribution of nanoparticles within the matrix at the solid state by exploiting severe plastic deformation mechanisms, provided that a sufficient number of tool passes is carried out. In this case study, 4 FSP passes were necessary to eliminate macro-sized nanoparticles clusters.
- Significant grain refinement was detected after 4 FSP passes, probably as a result of combined action of recrystallization processes related to FSP and to the action of nano-Al_2O_3 particles in slowing the grain growth of the matrix.
- Increasing the number of FSP passes led to an enhancement in microhardness values within the nugget zone, likely due to the increased microstructural homogenization and more even distribution of nanoparticles, together with the increased grain refinement effect.

REFERENCES – CHAPTER 6

[1] S. Zhang, Y. Zhao, G. Chen, X. Cheng, X. Huo, **2008**, *450*, 185.

[2] I. Dinaharan, N. Murugan, S. Parameswaran, *Mater. Sci. Eng. A* **2011**, *528*, 5733.

[3] G. Kumar, R. Narayanasamy, S. Natarajan, S. Kumaresh Babu, K. Sivaprasad, S. Sivasankaran, *Mater. Des.* **2010**, *31*, 1526.

[4] G. Cao, H. Choi, J. Oportus, H. Konishi, X. Li, *Mater. Sci. Eng. A* **2008**, *494*, 127.

[5] S. Donthamsetty, **2009**, *2*, 27.

[6] M. Karbalaei Akbari, O. Mirzaee, H. R. Baharvandi, *Mater. Des.* **2013**, *46*, 199.

[7] S. A. Sajjadi, H. R. Ezatpour, H. Beygi, *Mater. Sci. Eng. A* **2011**, *528*, 8765.

[8] J. Hashim, L. Looney, M. S. J. Hashmi, *J. Mater. Process. Technol.* **1999**, *93*, 1.

[9] A. Dehghan Hamedan, M. Shahmiri, *Mater. Sci. Eng. A* **2012**, *556*, 921.

[10] Y. Yang, J. Lan, X. Li, *Mater. Sci. Eng. A* **2004**, *380*, 378.

[11] M. R. Kamali Ardakani, S. Khorsand, S. Amirkhanlou, M. Javad Nayyeri, *Mater. Sci. Eng. A* **2014**, *592*, 121.

[12] B. Abbasipour, B. Niroumand, S. M. Monir Vaghefi, *Trans. Nonferrous Met. Soc. China* **2010**, *20*, 1561.

[13] A. Mazahery, M. . Shabani, *Strength Mater.* **2012**, *44*, 686.

[14] S. a. Sajjadi, H. R. Ezatpour, M. Torabi Parizi, *Mater. Des.* **2012**, *34*, 106.

[15] S. Tahamtan, a. Halvaee, M. Emamy, M. S. Zabihi, *Mater. Des.* **2013**, *49*, 347.

[16] L.-Y. Chen, J.-Y. Peng, J.-Q. Xu, H. Choi, X.-C. Li, *Scr. Mater.* **2013**, *69*, 634.

[17] R. S. Mishra, M. W. Mahoney, Eds., *Friction Stir Welding and Processing*, ASM International, **2007**.

[18] R. S. Mishra, Z. Y. Ma, *Mater. Sci. Eng. R Reports* **2005**, *50*, 1.

[19] P. Cavaliere, G. Campanile, F. Panella, a. Squillace, *J. Mater. Process. Technol.* **2006**, *180*, 263.

[20] S. Benavides, Y. Li, L. . Murr, D. Brown, J. . McClure, *Scr. Mater.* **1999**, *41*, 809.

[21] M. W. Mahoney, C. G. Rhodes, J. G. Flintoff, R. A. Spurling, W. H. Bingel, *Met. Mater. Trans. A* **1998**, *29*, 1955.

[22] Y. Li, L. Murr, J. McClure, *Mater. Sci. Eng. A* **1999**, *271*, 213.

[23] R. Brown, W. Tang, A. Reynolds, *Mater. Sci. Eng. A* **2009**, *513-514*, 115.

[24] J. F. Guo, J. Liu, C. N. Sun, S. Maleksaeedi, G. Bi, M. J. Tan, J. Wei, *Mater. Sci. Eng. A* **2014**, *602*, 143.

[25] Y. Sato, M. Urata, H. Kokawa, *Metall. Mater. Trans. A* **2002**, *33*, 625.

[26] K. A. . Hassana, A. . Normanb, D. A. Pricec, P. B. Prangnella, *Acta Mater.* **2003**, *51*, 1923.

[27] J. M. Root, D. P. Field, T. W. Nelson, *Metall. Mater. Trans. A* **2009**, *40*, 2109.

[28] R. A. Shahani, T. W. Clyne, *Mater. Sci. Eng. A* **1991**, *135*, 281.

[29] J. Guo, P. Gougeon, X. G. Chen, *Mater. Sci. Eng. A* **2012**, *553*, 149.

[30] F. J. Humphreys, M. Hatherly, in *Recryst. Relat. Annealing Phenom.*, Elsevier, **2004**, pp. 415–450.

CONCLUSIONS

In the framework of Al-Si cast alloys for the production of automotive components, two main research fields were explored, with common aim to investigate possible strategies to enhance mechanical properties, in particular after high temperature exposure (over-aging): (i) chemical modification of Al-Si cast alloys, aiming to induce the formation of thermally stable strengthening phases, (ii) addition of micrometric/nanometric ceramic particles (dispersoids) to Al-Si matrix, acting as effective obstacles to dislocation movement.

The research activities were focused, from one side, on the characterization, heat treatment study and chemical modification of quaternary Al-Si-Cu-Mg alloys for automotive components. In recent years, quaternary Al-Si-Cu-Mg alloys attracted large industrial interest for the production of lightweight and complex-shape castings. In view of the concurrent presence of Cu and Mg, these alloys are supposed not only to present enhanced mechanical properties at room temperature in comparison to traditional ternary Al-Si-Mg alloys, but also a higher thermal stability. The β-Mg_2Si and θ-Al_2Cu precipitates present in the heat treated Al-Si-Mg and Al-Si-Cu alloys, in fact, are known to undergo rapid coarsening and loss of coherency with long term high temperature exposure. As a result of the literature survey, it is thought that quaternary Q precipitates (containing Al, Si, Cu and Mg), on the contrary, possess higher coarsening resistance and capability to withstand long term exposure even to 300 °C.

Aiming to better understand the effect of Cu on microstructure and mechanical properties of cast Al-Si alloys, a first research activity was addressed to the study of two Al-Si-Cu-Mg alloys (A354 and C355) employed for engine parts. The effect of solidification rate (and therefore SDAS), secondary phases (intermetallic particles) and heat treatment condition (peak-aging or overaging) on the tensile and fatigue behavior, at room and elevated temperature, was investigated. Experimental results showed that SDAS strongly affects the mechanical behavior of the alloys, in particular UTS and elongation to failure, while its

effect on YS was less relevant. Room temperature fatigue behavior, under rotating bending conditions, was similarly influenced by SDAS, while at high temperature in the overaged condition no clear influence was observed. Solidification rate was reported to play a role also on coarse intermetallic phases size and aspect ratio. In particular, while in fine SDAS samples small π-$Al_8Mg_3FeSi_6$ and β-Al_5FeSi particles ($\leq$ 10 μm) were detected, coarse SDAS alloys were mostly characterized by large β-Al_5FeSi (100-150 μm). The presence of Cu was reflected on microstructure mainly in the presence of the quaternary Q-$Al_5Cu_2Mg_8Si_6$ phases found in coarse SDAS samples. It was inferred that an increased amount of Cu effectively leads to enhanced thermal stability: this was confirmed by the comparison of the tensile and fatigue properties of C355 and A354 alloys, characterized by different Cu content (1 and 1.5 wt.%, respectively) in the overaged condition, both at room and high temperature. Moreover, the superior coarsening resistance of quaternary alloys was observed by comparing their tensile behavior to that of the widely used A356 (AlSi7Mg0.3) alloy. In the overaged condition, while UTS and YS of A356 decreased of about 50% from the T6 condition, the loss in Cu-containing alloys, on the contrary, was limited to about 30 %.

Since the heat treatment of A354 alloy in the previously described experimental activity was derived from industrial practice, an optimization study was aimed to induce the maximum precipitation hardening effect while maintaining limited to a minimum treatment temperature and time. Differential thermal analyses, microstructural characterization and hardness tests allowed defining the new heat treatment parameters. A first solution phase was defined aiming to dissolve a low melting eutectic compound and prevent from its incipient melting at higher solution temperature, while a second phase was meant to further dissolve Cu and Mg atoms, to be exploited through precipitation hardening. Different aging temperatures were evaluated, allowing to identify the peak-aging condition. The optimized heat treatment conferred to the alloy higher mechanical properties (HB, YS, UTS) at room temperature, in comparison to the standard parameters, while maintaining good ductility. Moreover, benefits of the optimized heat treatment, in term of high temperature exposure resistance, were confirmed by tensile tests in the overaged condition.

Aiming to further enhance overageing response of A354 alloy, the addition of Mo as alloying element was evaluated. From the present investigation, the addition of Mo to A354 alloy was reflected in the formation of Mo-rich solidification intermetallics characterized by two types of morphology, probably formed during different solidification stages, and prevented from the formation of β-Fe phases. As a result of heat treatment study and preliminary tensile characterization, an increase of high temperature mechanical properties

was registered in the overaged condition in comparison to the base alloy. Even if further studies are necessary to better understand the role of Mo in such enhancement, the experimental results seem to be in agreement with recent literature works, reporting the formation of thermally stable quaternary Al-Fe-Mo-Si phases during solution treatment.

The addition of ceramic particles to Al-based alloys is another possible strategy to enhance room and high temperature mechanical behavior. Al-matrix Nanocomposites, in particular, gained much academic interest in the last years, in view of the high potential mechanical properties in comparison to the more traditional micro-reinforced composites. Moreover, the high weight fraction of microparticles which characterizes microcomposites, confer low ductility; the addition of low amounts of nanoparticles, is expected and to some extent reported to maintain good values of elongation to failure. The main processing techniques may be classified as (i) liquid/semi-solid state and (ii) solid state methods. Aiming to produce large-sized and low cost bulk components, liquid state routes seem to be the most attractive. Despite many researchers reported in the literature optimistic results in terms of nanoparticles distribution, difficulties associated to low wettability issues related to liquid state and semi-solid state processing techniques have been clearly outlined in this research activity.

Ex-situ stir casting technique assisted with ultrasonic treatment of the melt was used to distribute Al_2O_3 micro and nanoparticles within A356 matrix. A good distribution of microparticles (added in weight fractions up to 8 wt.%) was achieved, while the lower wettability of nanoparticles (added in 1 wt.%) led to the related formation of cavities and particles clusters. Good hardness enhancement was registered on the produced micro and nanocomposites. However, the exploitation at the industrial scale of liquid state stir casting technique for the production of Al-based nanocomposites seems still challenging, in view of the casting defects unavoidably induced by nanoparticles low wettability. From the experimental results, it is thought that strategies to enhance particles distribution of cast composites are needed. To this aim, the effectiveness of Friction Stir Processing (FSP) as secondary/primary process to promote nanoparticles distribution, was evaluated. As a secondary process, FSP was applied to a semi-solid cast AA2024-Al_2O_3 nanocomposite. Even if processing at the semi-solid state is reported in the literature to increase particles wettability in comparison to the fully liquid state, the as cast AA2024-1wt%Al_2O_3 composite presented a noticeable amount of particles agglomerates and porosity. The application of FSP induced grain refinement, microstructural homogenization and enhanced nanoparticles distribution, resulting in increased YS and UTS in comparison to the as-cast and FSP unreinforced matrix. FSP was also investigated as possible primary

method for distributing Al_2O_3 nanoparticles, deposited in a superficial groove of a AA7075 plate. Rotation of the tool was then applied to exploit severe deformation processes to distribute nano-alumina particles at the solid-state. As a results of microstructural characterization, it was revealed that, by applying a sufficient number of passes, severe plastic deformation allowed to distribute nano-sized particles and eliminating most of the macro-sized Al_2O_3 clusters, as well as process defects such as tunnels. Also in this case, the process led to significant grain refinement; after 4 FSP passes, in particular, the best combination of microstructural homogenization, grain refinement and microhardness increase were registered, probably due to the combined action of recrystallization processes and pinning effect of nano-Al_2O_3 particles.

As a conclusion, nanoparticles are indeed characterized by high strengthening potential as dispersoids, but to fully exploit their effectiveness in hindering dislocation movement, an even distribution must be achieved. The application of traditional casting technologies, even at the semi-solid state, for the production of large volume of composites seem at the moment still inapplicable; on the other hand, secondary processes, such as FSP, appear as promising methods to improve reinforcement distribution.

Appendix

Publications and Conference proceedings

International Journals

[1] L. Ceschini, Al. Morri, An. Morri, S. Toschi, S. Johansson, S. Seifeddine, *Effect of microstructure and overaging on the tensile behavior at room and elevated temperature of C355-T6 cast aluminum alloy,* ***Materials and Design,*** Vol. 83C (2015), 626-634.

[2] L. Ceschini, Al. Morri, S. Toschi, S. Johansson, S. Seifeddine, *Microstructural and mechanical properties characterization of heat treated and overaged cast A354 alloy with various SDAS at room and elevated temperature*, ***Materials Science and Engineering: A,*** Vol. 648 (2015), 340–349.

[3] L. Ceschini, Al. Morri, S. Toschi, S. Seifeddine, *Room and high temperature fatigue behaviour of the A354 and C355 (Al-Si-Cu-Mg) alloys: role of microstructure and heat treatment*, ***Materials Science and Engineering A***, Vol. 653 (2016), 129–138.

[4] W. Hoziefa, S. Toschi , M. M. Z. Ahmed, Al. Morri, A. A. Mahdy, I. El-Mahallawi, L. Ceschini, A. Atlam, *Effect of Friction Stir Processing on microstructure and mechanical properties of compocast AA2024/Al_2O_3 nanocomposite,* submitted to ***Composites Part A***, 2016.

International Conferences

[5] L. Ceschini, A. Jarfors, Al. Morri, An. Morri, F. Rotundo, S. Seifeddine, S. Toschi, *High temperature tensile behaviour of the A354 aluminum alloy,* 14th International Conference on Aluminium Alloys (ICAA), ***Materials Science Forum***, Trans Tech Publications, Switzerland, Vols. 794-796 (2014), 443-448

[6] L. Ceschini, A. Jarfors, Al. Morri, An. Morri, F. Rotundo, S. Seifeddine, S. Toschi, *Influence of SDAS on the high temperature tensile behavior of the C355 Al alloy*, ***Materials Science Forum*** Vols. 783-786, Trans Tech Publications, Switzerland, (2014), pp 228-233, 8th International Conference on Processing and Manufacturing of Advanced Materials, THERMEC 2013; Las Vegas, NV; United States; 2-6 December 2013

[7] M. Boselli, L. Ceschini, V. Colombo, E. Ghedini, M. Gherardi, A. Morri, F. Rotundo, P. Sanibondi, S. Toschi, *Cast Al-based nanocomposites reinforced with thermal plasma-synthesized ceramic nanoparticles*, ***Materials Science Forum*** Vols. 783-786, Trans Tech Publications, Switzerland, (2014), pp 1567-1572, 8th International Conference on Processing and Manufacturing of Advanced Materials, THERMEC 2013; Las Vegas, NV; United States; 2-6 December 2013

[8] L. Ceschini, Al. Morri, F. Rotundo, S. Toschi, *Gas-liquid in-situ production of ceramic reinforced aluminum matrix nanocomposites*, ***Materials Science Forum*** Vols. 783-786, Trans Tech Publications,

Switzerland, (2014) 2011-2015, 8th International Conference on Processing and Manufacturing of Advanced Materials, THERMEC 2013; Las Vegas, NV; United States; 2-6 December 2013

[9] M. Boselli, L. Ceschini, V. Colombo, E. Ghedini, M. Gherardi, A. Morri, F. Rotundo, S. Toschi, P. Sanibondi, *RF inductively coupled thermal plasma synthesis of ceramic nanoparticles for the production of Al-based metal matrix nanocomposites*, poster session at **ISPC21**, 4-9 August 2013, Cairns, Australia

National Journals

[10] L. Ceschini, Alessandro Morri, Andrea Morri, F. Rotundo, S. Toschi, *Heat treatment response and influence of overaging on mechanical properties of C355 cast aluminum alloy,* **La Metallurgia Italiana,** 106 (5) (2014), 11-17.

National Conferences

[11] L. Ceschini, Alessandro Morri, Andrea Morri, F. Rotundo, S. Toschi, *Miglioramento della stabilità termica di getti in lega di alluminio da fonderia per applicazioni motoristiche,* Atti del III Congresso Nazionale del Coordinamento della Meccanica Italiana **CDMI 2014**, Napoli 30 Giugno – 1 Luglio 2014. ISBN 88-902096-2-3, 1-7.

[12] L. Ceschini, Alessandro Morri, Andrea Morri, F. Rotundo, S. Toschi, *Risposta al trattamento termico e influenza del degrado sulle proprietà meccaniche della lega di alluminio C355,* **24° Convegno Nazionale Trattamenti Termici AIM**, Piacenza, 17-18 Ottobre 2013; ISBN: 978-88-85298-972.

[13] L. Ceschini, Al. Morri, F. Rotundo, S. Toschi *Produzione di nanocompositi a matrice di alluminio tramite stir-casting e trattamento ultrasonico*, Atti del **35° Convegno Nazionale AIM**, Roma, 5-7 Novembre 2014, ISBN: 978-88-98990-01-6, 1-7

[14] L. Ceschini, V. Colombo, E. Ghedini, M. Gherardi, A. Morri, F. Rotundo, S. Toschi, P. Sanibondi, A. Stancampiano, *Plasma assisted integrated production of cast Al-based metal matrix nanocomposites*, **Nanotech Italy** 2012, 21-23 Novembre 2012, Venezia.

Ringraziamenti

Si concludono dunque questi tre anni.. tre anni davvero importanti per me.

La lista delle persone da ringraziare sarebbe infinita.. Comincio però con la Prof.ssa Ceschini, che mi ha trasmesso la sua grandissima passione per la metallurgia ed è stata una guida "materna" in tutti questi anni. Grazie di cuore per avermi dato la possibilità di crescere dal punto di vista scientifico, per l'immensa disponibilità, ed anche per avermi spronata quando ce n'è stato bisogno!

Un grazie ad Alessandro, per il costante aiuto e per le riflessioni sull'alluminio; grazie a Fabio, per aver affrontato insieme il mondo dei nanocompositi, le ore spese sulla review, e per avermi insegnato tanto.

Come non ringraziare Iuri, per la sua gentilezza e per aver passato insieme tante ore al SEM a parlare di intermetallici e a ricercare introvabili nanoparticelle. Grazie a Fabrizio, per il supporto tecnico, o meglio, per il "software", fondamentale per tantissime attività sperimentali! E grazie mille anche ad Antonio, per tutte le volte che ha tornito e fresato per me.!

Un grazie poi a tutti gli altri metallurgisti: il Prof. Casagrande, per aver spesso provveduto al mio sostentamento alimentare e per aver tollerato le mie insalate, al Prof. Sambogna, per avermi sempre messo di buon umore, per la *strongness,* e per i suoi pezzoni su qualsivoglia argomento; grazie ad Andrea per le tante consulenze sulle prove meccaniche.

E poi, un grazie immenso a Vale, per i caffè, le risate, le stupidaggini, lo sharingan.. e per essere stato un collega ed un amico perfetto. Grazie anche ad Ele, per la sua dolcezza e per essermi stata vicina quando ne ho avuto bisogno.

Grazie a Carla e Cristina per la squisita gentilezza, la compagnia, le considerazioni a tema dolciario e per la serenità che mi hanno sempre trasmesso. Un grazie di cuore a Benni, per la sua amicizia, per tutti i the presi insieme e le grandi chiacchierate.

Un grazie poi a tutti coloro che hanno, in diverso modo, contribuito a questo lavoro di tesi, producendo gran parte del materiale da caratterizzare, e per la proficua collaborazione nella scrittura degli articoli: il Prof. Salem Seifeddine, la Prof.ssa Iman El-Mahallawi, il Prof. Mohamed Zaky Ahmed e Wael Hoziefa.

Un grande grazie anche a tutti gli studenti che, nel corso di questi anni, si sono succeduti in laboratorio; non solo per aver contribuito in prima persona al mio Dottorato, ma per avermi lasciato, ciascuno a modo suo, qualcosa di bello.

Terminati i ringraziamenti professionali…

… Grazie infinite ai miei genitori, per avermi supportata in tutti i modi possibili, per essersi spesi in qualunque modo pur di aiutarmi, in qualsiasi circostanza. Vi voglio bene.

Grazie infinite a Matti, l'essere più dolce e sensibile che esiste sulla faccia della terra. Grazie per essere così come sei, per tutto quello che abbiamo vissuto insieme e tutto quello che vivremo.

Un grazie immenso alle mie amiche Chiara ed Ilaria, per essermi state vicine, soprattutto in questo ultimo anno; siete state davvero fondamentali. Grazie per i the serali, i mille messaggi vocali e per i commenti sui gatti bianchi. Un grazie grandissimo anche all'Ely e Gale, per le nostre serate–giochi di società, per le infinite chiacchierate e per il supporto. Grazie poi a Emily ed Elisa: anche se ora siamo più distanti, mi basta solo pensarvi per sorridere; se mi sento oberata dalle cose da fare, penso a te Emily, e subito mi sento meglio!. Grazie alla mitica Vale per l'amicizia, passano gli anni e i chilometri, ma non l'affetto. Grazie a Giacomo, per i trekking e le giornate di osservazione (più o meno fallimentari e con ogni meteo), grazie a Matteo per la bella amicizia nata tra le nanoparticelle e grazie a Maria e Rossella per gli aperitivi al femminile.

A tutti voi un grazie di cuore.